

**INVESTIGATION OF INCIPIENT DYNAMIC STALL  
AT HIGH REYNOLDS NUMBERS**

**FINAL REPORT**

**Mukund Acharya, John W. Kiedaisch, & Angelis Bizos**

**January 10, 2000**

**Sponsored by**

**U. S. ARMY RESEARCH OFFICE**

**Grant No. DAAH04-94-G-0069**

**Fluid Dynamics Research Center  
Illinois Institute of Technology  
Chicago, IL**

**APPROVED FOR PUBLIC RELEASE;  
DISTRIBUTION UNLIMITED**

**DTIC QUALITY INSPECTED 4**

**20000628 059**

REPORT DOCUMENTATION PAGE					Form Approved OMB No. 0704-0188	
Public reporting burden for this collection of information is estimated to average 1 hour per response, including the time for reviewing instructions, searching data sources, gathering and maintaining the data needed, and completing and reviewing the collection of information. Send comments regarding this burden estimate or any other aspect of this collection of information, including suggestions for reducing this burden to Washington Headquarters Service, Directorate for Information Operations and Reports, 1215 Jefferson Davis Highway, Suite 1204, Arlington, VA 22202-4302, and to the Office of Management and Budget, Paperwork Reduction Project (0704-0188) Washington, DC 20503.						
PLEASE DO NOT RETURN YOUR FORM TO THE ABOVE ADDRESS.						
1. REPORT DATE (DD-MM-YYYY) 10-01-2000		2. REPORT DATE Final		3. DATES COVERED (From - To) 15-04-1994 to 31-08-1997		
4. TITLE AND SUBTITLE  Investigation of Incipient Dynamic Stall at High Reynolds Numbers				5a. CONTRACT NUMBER		
				5b. GRANT NUMBER DAAH04-94-G-0069		
				5c. PROGRAM ELEMENT NUMBER		
6. AUTHOR(S)  Acharya, Mukund Kiedaisch, John W. Bizos, Angelis				5d. PROJECT NUMBER		
				5e. TASK NUMBER		
				5f. WORK UNIT NUMBER		
7. PERFORMING ORGANIZATION NAME(S) AND ADDRESS(ES) Illinois Institute of Technology 3300 S. Federal St. Chicago, IL 60616				8. PERFORMING ORGANIZATION REPORT NUMBER		
9. SPONSORING/MONITORING AGENCY NAME(S) AND ADDRESS(ES) U. S. Army Research Office P. O. Box 12211 Research Triangle Park, NC 27709-2211				10. SPONSOR/MONITOR'S ACRONYM(S)		
				11. SPONSORING/MONITORING AGENCY REPORT NUMBER ARO 32489.1-EG		
12. DISTRIBUTION AVAILABILITY STATEMENT  Approved for public release; distribution unlimited						
13. SUPPLEMENTARY NOTES The views, opinions, and/or findings contained in this report are those of the author(s) and should not be construed as an official Department of the Army position, policy, or decision unless designated by other documentation.						
14. ABSTRACT In the first part of this study, surface shear-stress measurements were obtained on a NACA 0012 airfoil model, undergoing a pitch-up motion from 0° to 45° angle of attack at a constant rate, using an array of surface-mounted hot-film sensors. Dominant features in these data and in the standard deviations computed from these data were examined and related to events in the development and evolution of the unsteady separation over the suction surface. Results were compared with well-known features of the dynamic stall process seen in the surface-pressure distributions. Trends in the behavior of these features are presented for a range of non-dimensional pitch rates and chord Reynolds numbers. Significant changes were seen in the behavior of these features at high Reynolds numbers. The results suggest that these changes are due to transition in the shear layer at high pitch rates and quasi-steady behavior at low pitch rates. In the second part of this study, large amplitude sinusoidal motions were investigated for a wide range of Reynolds numbers and reduced frequencies. A combination of unsteady pressure and shear-stress data at the surface of the airfoil provided detailed information about the development and evolution of the flowfield. In particular, the formation of the dynamic stall vortex (DSV) during the upstroke of the motion profile was examined in detail as well as the reattachment process during the downstroke of the motion profile. Significant changes in behavior were seen with changing Reynolds number, reduced frequency, and amplitude of oscillation. The mean angle did not affect the development of the DSV except at the highest reduced frequency ( $k=0.4$ ). Amplitude of oscillation did not affect the development of the reattachment process. Reduced frequency had the greatest effect on the reattachment process, delaying or even preventing the onset of the process due to the presence of the dynamic stall vortex over the airfoil during the downstroke portion of the cycle.						
15. SUBJECT TERMS  Dynamic Stall, Unsteady Separation						
16. SECURITY CLASSIFICATION OF:			17. LIMITATION OF ABSTRACT		18. NUMBER OF PAGES	
a. REPORT	b. ABSTRACT	c. THIS PAGE			19a. NAME OF RESPONSIBLE PERSON	
U	U	U	UU		184	
						19b. TELEPHONE NUMBER (Include area code)



## ACKNOWLEDGMENT

We would like to express out sincere thanks to Mr. Craig Johnson and Mr. Ron Mashek of the MMAE Department Machine Shop, and Mr. Dominic Deluca of the MMAE Department Electronics Shop, for their skilled craftsmanship, patience, and advice. Also, we would like to express our thanks to Mr. David Grossman and Mr. Chris Evans who assisted very ably during various phases of this work.



## TABLE OF CONTENTS

	Page
ACKNOWLEDGMENT	iii
LIST OF TABLES	vi
LIST OF FIGURES	vii
NOMENCLATURE	xiv
ABSTRACT	xv
CHAPTER	
I. INTRODUCTION AND BACKGROUND	1
1.1 Introduction	1
1.2 Background	2
1.2.1 Unsteady Flow over 2-D Airfoils	3
1.2.2 Flow Control Techniques	6
1.3 Previous Work at IIT	7
1.4 Objectives	9
II. EXPERIMENTAL FACILITIES AND INSTRUMENTATION	12
2.1 Wind Tunnel Facilities	12
2.2 Airfoil Model and Motion Control System	13
2.3 Instrumentation	14
2.3.1 Pressure	14
2.3.2 Hot-Film Sensors	14
2.4 Computer Facilities	15
2.5 Measurement and Experimental Procedure	16
2.6 Experimental Parameters	18
 PART A. PITCH-UP MOTION EXPERIMENTS	 20
III. ANALYSIS OF HOT-FILM DATA	21
3.1 Features of the Shear Stress Data	21
3.2 Behavior of Dominant Flow Features	27

IV.	PITCH RATE AND REYNOLDS NUMBER EFFECTS	30
4.1	Effects of Changing Pitch Rate	30
4.2	Effects of Changing Reynolds Number	31
4.3	Discussion of Results	34
V.	CONCLUSIONS AND RECOMMENDATIONS, PART A	37
5.1	Conclusions	37
5.2	Recommendations	38
	PART B. OSCILLATORY MOTION EXPERIMENTS	40
VI.	SURFACE PRESSURE RESULTS	41
6.1	Steady Surface Pressure	41
6.2	Unsteady Surface Pressure Data	42
6.2.1	Frequency Effects	44
6.2.2	Reynolds Number Effects	46
VII.	HOT-FILM SHEAR STRESS RESULTS	49
7.1	Unsteady Hot-Film Surface Data	49
7.2	Frequency Effects	52
7.3	Reynolds Number Effects	54
VIII.	DISCUSSION OF RESULTS	58
IX.	CONCLUSIONS AND RECOMMENDATIONS, PART B	62
9.1	Conclusions	62
9.2	Recommendations	63
	APPENDIX	64
	PARTICIPATING SCIENTIFIC PERSONNEL	65
	PUBLICATIONS AND TECHNICAL REPORTS	66
	TABLES	67
	FIGURES	74
	BIBLIOGRAPHY	178

## LIST OF TABLES

Table	Page
1. Chordwise location of pressure ports.	68
2. Chordwise location of hot-film sensors (first configuration).	69
3. Chordwise location of hot-film sensors (second configuration).	70
4. Experimental parameters (Part B).	71
5. Maximum LESP.	72
6. DSV Formation.	73

## LIST OF FIGURES

Figure	Page
1. Parameter ranges of present and past experimental and computational studies of dynamic stall on pitching airfoils.	75
2. Plan view of the Andrew Fejer Unsteady Wind Tunnel Facility.	76
3. Plan view of the National Diagnostic Facility (NDF).	77
4. Airfoil model installed in the NDF test section.	78
5. Hot-film instrumentation for shear-stress measurements.	79
6a. Constant voltage amplifier circuit diagram.	80
6b. Signal conditioning circuit diagram.	81
7. Motion profiles of oscillation.	82
8. Normalized shear-stress variations during pitch-up for three regions on the airfoil suction surface ( $\alpha^+ = 0.036$ , $Re_c = 1.0 \times 10^6$ ).	84
9. Normalized shear-stress variations during pitch-up for three regions on the airfoil suction surface ( $\alpha^+ = 0.036$ , $Re_c = 1.1 \times 10^5$ ).	85
10. Normalized shear-stress variations during pitch-up for three regions on the airfoil suction surface ( $\alpha^+ = 0.036$ , $Re_c = 4.6 \times 10^5$ ).	86
11. Normalized shear-stress variations during pitch-up for three regions on the airfoil suction surface ( $\alpha^+ = 0.036$ , $Re_c = 2.0 \times 10^6$ ).	87
12. Normalized shear-stress variations during pitch-up for three regions on the airfoil suction surface ( $\alpha^+ = 0.010$ , $Re_c = 1.1 \times 10^5$ ).	88
13. Normalized shear-stress variations during pitch-up for three regions on the airfoil suction surface ( $\alpha^+ = 0.010$ , $Re_c = 4.6 \times 10^5$ ).	89
14. Normalized shear-stress variations during pitch-up for three regions on the airfoil suction surface ( $\alpha^+ = 0.010$ , $Re_c = 1.0 \times 10^6$ ).	90
15. Normalized shear-stress variations during pitch-up for three regions on the airfoil suction surface ( $\alpha^+ = 0.010$ , $Re_c = 2.0 \times 10^6$ ).	91

16. Normalized shear-stress variations during pitch-up for three regions on the airfoil suction surface ( $\alpha^+ = 0.150$ , $Re_c = 1.1 \times 10^5$ ).	92
17. Normalized shear-stress variations during pitch-up for three regions on the airfoil suction surface ( $\alpha^+ = 0.150$ , $Re_c = 4.6 \times 10^5$ ).	93
18. Normalized shear-stress variations during pitch-up for three regions on the airfoil suction surface ( $\alpha^+ = 0.150$ , $Re_c = 1.0 \times 10^6$ ).	94
19. Dominant features of the surface pressure distributions (from Acharya and Metwally <sup>39</sup> ).	95
20. Location and movement of the dominant shear stress features ( $\alpha^+ = 0.036$ , $Re_c = 1.1 \times 10^5$ ). LESP and DSVP data from Acharya and Metwally <sup>39</sup> .	96
21. Standard deviations of the hot-film sensor output voltages during pitch-up for three regions on the airfoil suction surface ( $\alpha^+ = 0.036$ , $Re_c = 1.0 \times 10^6$ ).	97
22. Standard deviations of the hot-film sensor output voltages during pitch-up for three regions on the airfoil suction surface ( $\alpha^+ = 0.036$ , $Re_c = 2.0 \times 10^6$ ).	98
23. Standard deviations of the hot-film sensor output voltages during pitch-up for three regions on the airfoil suction surface ( $\alpha^+ = 0.010$ , $Re_c = 1.0 \times 10^6$ ).	99
24. Standard deviations of the hot-film sensor output voltages during pitch-up for three regions on the airfoil suction surface ( $\alpha^+ = 0.150$ , $Re_c = 1.0 \times 10^6$ ).	100
25. Location and movement of the dominant shear stress and standard deviation features ( $\alpha^+ = 0.036$ , $Re_c = 1.0 \times 10^6$ ).	101
26. Location and movement of the dominant shear stress and standard deviation features ( $\alpha^+ = 0.036$ , $Re_c = 2.0 \times 10^6$ ).	101
27. Location and movement of the dominant shear stress and standard deviation features ( $\alpha^+ = 0.010$ , $Re_c = 1.0 \times 10^6$ ).	102
28. Location and movement of the dominant shear stress and standard deviation features ( $\alpha^+ = 0.150$ , $Re_c = 1.0 \times 10^6$ ).	102
29. Behavior of shear stress feature 1 with varying pitch rate.	103

30. Behavior of shear stress feature 2 with varying pitch rate.	105
31. Behavior of shear stress feature 4 with varying pitch rate.	107
32. Behavior of shear stress feature 1 with varying Reynolds number.	109
33. Behavior of shear stress feature 2 with varying Reynolds number.	111
34. Behavior of shear stress feature 4 with varying Reynolds number.	113
35. Pressure coefficient distributions on the airfoil suction surface during pitch-up ( $\alpha^+ = 0.150$ , $Re_c = 0.5 \times 10^6$ ).	115
36. Pressure coefficient distributions on the airfoil suction surface during pitch-up ( $\alpha^+ = 0.150$ , $Re_c = 1.0 \times 10^6$ ).	116
37. Pressure coefficient distributions on the airfoil suction surface during pitch-up ( $\alpha^+ = 0.036$ , $Re_c = 0.5 \times 10^6$ ).	117
38. Pressure coefficient distributions on the airfoil suction surface during pitch-up ( $\alpha^+ = 0.036$ , $Re_c = 1.0 \times 10^6$ ).	118
39. Pressure coefficient distributions on the airfoil suction surface during pitch-up ( $\alpha^+ = 0.010$ , $Re_c = 0.5 \times 10^6$ ).	119
40. Pressure coefficient distributions on the airfoil suction surface during pitch-up ( $\alpha^+ = 0.010$ , $Re_c = 1.0 \times 10^6$ ).	120
41. Changes in the normalized shear-stress variations during pitch-up with increasing Reynolds number at $x/c = 0.101$ .	121
42. Chordwise pressure distribution over an oscillating 2-D airfoil at selected angles for $Re_c = 1.1 \times 10^5$ , $k = 0.1$ , $\alpha_o = 10^\circ$ , $\alpha_m = 10^\circ$ .	122
43. Chordwise pressure distribution over an oscillating 2-D airfoil at selected angles for $Re_c = 1.1 \times 10^5$ , $k = 0.1$ , $\alpha_o = 10^\circ$ , $\alpha_m = 20^\circ$ .	123
44. Chordwise pressure distribution over an oscillating 2-D airfoil at selected angles for $Re_c = 1.1 \times 10^5$ , $k = 0.1$ , $\alpha_o = 20^\circ$ , $\alpha_m = 10^\circ$ .	124
45. Chordwise pressure distribution over an oscillating 2-D airfoil at selected angles for $Re_c = 1.1 \times 10^5$ , $k = 0.1$ , $\alpha_o = 20^\circ$ , $\alpha_m = 20^\circ$ .	125
46. Chordwise pressure distribution over an oscillating 2-D airfoil at selected angles for $Re_c = 1.1 \times 10^5$ , $k = 0.4$ , $\alpha_o = 10^\circ$ , $\alpha_m = 10^\circ$ .	126

47.	Chordwise pressure distribution over an oscillating 2-D airfoil at selected angles for $Re_c = 1.1 \times 10^5$ , $k = 0.4$ , $\alpha_o = 10^\circ$ , $\alpha_m = 20^\circ$ .	127
48.	Chordwise pressure distribution over an oscillating 2-D airfoil at selected angles for $Re_c = 1.1 \times 10^5$ , $k = 0.4$ , $\alpha_o = 20^\circ$ , $\alpha_m = 10^\circ$ .	128
49.	Chordwise pressure distribution over an oscillating 2-D airfoil at selected angles for $Re_c = 1.1 \times 10^5$ , $k = 0.4$ , $\alpha_o = 20^\circ$ , $\alpha_m = 20^\circ$ .	129
50.	Chordwise pressure distribution over an oscillating 2-D airfoil at selected angles for $Re_c = 4.6 \times 10^5$ , $k = 0.1$ , $\alpha_o = 10^\circ$ , $\alpha_m = 10^\circ$ .	130
51.	Chordwise pressure distribution over an oscillating 2-D airfoil at selected angles for $Re_c = 4.6 \times 10^5$ , $k = 0.1$ , $\alpha_o = 10^\circ$ , $\alpha_m = 20^\circ$ .	131
52.	Chordwise pressure distribution over an oscillating 2-D airfoil at selected angles for $Re_c = 4.6 \times 10^5$ , $k = 0.1$ , $\alpha_o = 20^\circ$ , $\alpha_m = 10^\circ$ .	132
53.	Chordwise pressure distribution over an oscillating 2-D airfoil at selected angles for $Re_c = 4.6 \times 10^5$ , $k = 0.1$ , $\alpha_o = 20^\circ$ , $\alpha_m = 20^\circ$ .	133
54.	Typical voltage output of hot-film sensors over an oscillating 2-D airfoil at selected chordwise locations for $Re_c = 1.1 \times 10^5$ , $k = 0.1$ , $\alpha_o = 10^\circ$ , $\alpha_m = 10^\circ$	134
55.	Typical voltage output of hot-film sensors over an oscillating 2-D airfoil at selected chordwise locations for $Re_c = 1.1 \times 10^5$ , $k = 0.1$ , $\alpha_o = 10^\circ$ , $\alpha_m = 20^\circ$	136
56.	Typical voltage output of hot-film sensors over an oscillating 2-D airfoil at selected chordwise locations for $Re_c = 1.1 \times 10^5$ , $k = 0.1$ , $\alpha_o = 20^\circ$ , $\alpha_m = 10^\circ$	138
57.	Typical voltage output of hot-film sensors over an oscillating 2-D airfoil at selected chordwise locations for $Re_c = 1.1 \times 10^5$ , $k = 0.1$ , $\alpha_o = 20^\circ$ , $\alpha_m = 20^\circ$	140
58.	Chordwise location and movement of Feature 1 for $Re_c = 1.1 \times 10^5$ , $k = 0.1$ .	142
59.	Chordwise location and movement of Feature 1 for $Re_c = 1.1 \times 10^5$ , $k = 0.2$ .	142
60.	Chordwise location and movement of Feature 1 for $Re_c = 1.1 \times 10^5$ , $k = 0.4$ .	143
61.	Chordwise location and movement of Feature 1 for $Re_c = 3.2 \times 10^5$ , $k = 0.1$ .	143

62.	Chordwise location and movement of Feature 1 for $Re_c=4.6 \times 10^5$ , $k=0.1$ .	144
63.	Chordwise location and movement of Feature 2 for $Re_c=1.1 \times 10^5$ , $k=0.1$ .	145
64.	Chordwise location and movement of Feature 2 for $Re_c=1.1 \times 10^5$ , $k=0.2$ .	145
65.	Chordwise location and movement of Feature 2 for $Re_c=1.1 \times 10^5$ , $k=0.4$ .	146
66.	Chordwise location and movement of Feature 2 for $Re_c=3.2 \times 10^5$ , $k=0.1$ .	146
67.	Chordwise location and movement of Feature 2 for $Re_c=4.6 \times 10^5$ , $k=0.1$ .	147
68.	Chordwise location and movement of Feature 2 for $Re_c=0.5 \times 10^6$ , $k=0.1$ .	147
69.	Chordwise location and movement of Feature 2 for $Re_c=1.0 \times 10^6$ , $k=0.1$ .	148
70.	Chordwise location and movement of Feature 4 for $Re_c=1.1 \times 10^5$ , $k=0.1$ .	149
71.	Chordwise location and movement of Feature 4 for $Re_c=1.1 \times 10^5$ , $k=0.2$ .	149
72.	Chordwise location and movement of Feature 4 for $Re_c=1.1 \times 10^5$ , $k=0.4$ .	150
73.	Chordwise location and movement of Feature 4 for $Re_c=3.2 \times 10^5$ , $k=0.1$ .	150
74.	Chordwise location and movement of Feature 4 for $Re_c=4.6 \times 10^5$ , $k=0.1$ .	151
75.	Chordwise location and movement of Feature 4 for $Re_c=0.5 \times 10^6$ , $k=0.1$ .	151
76.	Chordwise location and movement of Feature 4 for $Re_c=1.0 \times 10^6$ , $k=0.1$ .	152
77.	Chordwise location and movement of Feature 5 for $Re_c=1.1 \times 10^5$ , $k=0.1$ .	153
78.	Chordwise location and movement of Feature 5 for $Re_c=1.1 \times 10^5$ , $k=0.2$ .	153
79.	Chordwise location and movement of Feature 5 for $Re_c=1.1 \times 10^5$ , $k=0.4$ .	154
80.	Chordwise location and movement of Feature 5 for $Re_c=3.2 \times 10^5$ , $k=0.1$ .	154
81.	Chordwise location and movement of Feature 5 for $Re_c=4.6 \times 10^5$ , $k=0.1$ .	155
82.	Chordwise location and movement of Feature 5 for $Re_c=0.5 \times 10^6$ , $k=0.1$ .	155
83.	Chordwise location and movement of Feature 5 for $Re_c=1.0 \times 10^6$ , $k=0.1$ .	156
84.	Chordwise location and movement of Feature 6 for $Re_c=1.1 \times 10^5$ , $k=0.1$ .	157



85. Chordwise location and movement of Feature 6 for  $Re_c=1.1 \times 10^5$ ,  $k=0.2$ . 157
86. Chordwise location and movement of Feature 6 for  $Re_c=1.1 \times 10^5$ ,  $k=0.4$ . 158
87. Chordwise location and movement of Feature 6 for  $Re_c=3.2 \times 10^5$ ,  $k=0.1$ . 158
88. Chordwise location and movement of Feature 6 for  $Re_c=4.6 \times 10^5$ ,  $k=0.1$ . 159
89. Chordwise location and movement of Feature 6 for  $Re_c=0.5 \times 10^6$ ,  $k=0.1$ . 159
90. Chordwise location and movement of Feature 6 for  $Re_c=1.0 \times 10^6$ ,  $k=0.1$ . 160
91. Effects of reduced frequency on Feature 2 for  $Re_c = 1.1 \times 10^5$ ,  $\alpha_o = 10^\circ$ ,  $\alpha_m = 10^\circ$ . 161
92. Effects of reduced frequency on Feature 2 for  $Re_c = 1.1 \times 10^5$ ,  $\alpha_o = 10^\circ$ ,  $\alpha_m = 20^\circ$ . 161
93. Effects of reduced frequency on Feature 2 for  $Re_c = 1.1 \times 10^5$ ,  $\alpha_o = 20^\circ$ ,  $\alpha_m = 20^\circ$ . 162
94. Effects of reduced frequency on Feature 4 for  $Re_c = 1.1 \times 10^5$ ,  $\alpha_o = 10^\circ$ ,  $\alpha_m = 10^\circ$ . 163
95. Effects of reduced frequency on Feature 4 for  $Re_c = 1.1 \times 10^5$ ,  $\alpha_o = 10^\circ$ ,  $\alpha_m = 20^\circ$ . 163
96. Effects of reduced frequency on Feature 4 for  $Re_c = 1.1 \times 10^5$ ,  $\alpha_o = 20^\circ$ ,  $\alpha_m = 10^\circ$ . 164
97. Effects of reduced frequency on Feature 4 for  $Re_c = 1.1 \times 10^5$ ,  $\alpha_o = 20^\circ$ ,  $\alpha_m = 20^\circ$ . 164
98. Effects of reduced frequency on Feature 5 for  $Re_c = 1.1 \times 10^5$ ,  $\alpha_o = 10^\circ$ ,  $\alpha_m = 10^\circ$ . 165
99. Effects of reduced frequency on Feature 5 for  $Re_c = 1.1 \times 10^5$ ,  $\alpha_o = 10^\circ$ ,  $\alpha_m = 20^\circ$ . 165
100. Effects of reduced frequency on Feature 5 for  $Re_c = 1.1 \times 10^5$ ,  $\alpha_o = 20^\circ$ ,  $\alpha_m = 10^\circ$ . 166
101. Effects of reduced frequency on Feature 5 for  $Re_c = 1.1 \times 10^5$ ,  $\alpha_o = 20^\circ$ ,  $\alpha_m = 20^\circ$ . 166

102.	Effects of reduced frequency on Feature 6 for $Re_c = 1.1 \times 10^5$ , $\alpha_o = 10^\circ$ , $\alpha_m = 10^\circ$ .	167
103.	Effects of reduced frequency on Feature 6 for $Re_c = 1.1 \times 10^5$ , $\alpha_o = 10^\circ$ , $\alpha_m = 20^\circ$ .	167
104.	Effects of reduced frequency on Feature 6 for $Re_c = 1.1 \times 10^5$ , $\alpha_o = 20^\circ$ , $\alpha_m = 10^\circ$ .	168
105.	Effects of reduced frequency on Feature 6 for $Re_c = 1.1 \times 10^5$ , $\alpha_o = 20^\circ$ , $\alpha_m = 20^\circ$ .	168
106.	Effects of Reynolds number on Feature 2 for $k=0.1$ , $\alpha_o = 10^\circ$ , $\alpha_m = 10^\circ$ .	169
107.	Effects of Reynolds number on Feature 2 for $k=0.1$ , $\alpha_o = 20^\circ$ , $\alpha_m = 10^\circ$ .	169
108.	Effects of Reynolds number on Feature 2 for $k=0.1$ , $\alpha_o = 20^\circ$ , $\alpha_m = 20^\circ$ .	170
109.	Effects of Reynolds number on Feature 4 for $k=0.1$ , $\alpha_o = 10^\circ$ , $\alpha_m = 10^\circ$ .	171
110.	Effects of Reynolds number on Feature 4 for $k=0.1$ , $\alpha_o = 10^\circ$ , $\alpha_m = 20^\circ$ .	171
111.	Effects of Reynolds number on Feature 4 for $k=0.1$ , $\alpha_o = 20^\circ$ , $\alpha_m = 10^\circ$ .	172
112.	Effects of Reynolds number on Feature 4 for $k=0.1$ , $\alpha_o = 20^\circ$ , $\alpha_m = 20^\circ$ .	172
113.	Effects of Reynolds number on Feature 5 for $k=0.1$ , $\alpha_o = 10^\circ$ , $\alpha_m = 10^\circ$ .	173
114.	Effects of Reynolds number on Feature 5 for $k=0.1$ , $\alpha_o = 10^\circ$ , $\alpha_m = 20^\circ$ .	173
115.	Effects of Reynolds number on Feature 5 for $k=0.1$ , $\alpha_o = 20^\circ$ , $\alpha_m = 10^\circ$ .	174
116.	Effects of Reynolds number on Feature 5 for $k=0.1$ , $\alpha_o = 20^\circ$ , $\alpha_m = 20^\circ$ .	174
117.	Effects of Reynolds number on Feature 6 for $k=0.1$ , $\alpha_o = 10^\circ$ , $\alpha_m = 10^\circ$ .	175
118.	Effects of Reynolds number on Feature 6 for $k=0.1$ , $\alpha_o = 10^\circ$ , $\alpha_m = 20^\circ$ .	175
119.	Effects of Reynolds number on Feature 6 for $k=0.1$ , $\alpha_o = 20^\circ$ , $\alpha_m = 20^\circ$ .	176
120.	Flow visualization showing development of the DSV over a pitching airfoil in laminar flow ( $\alpha^+ = 0.31$ , $Re_c = 30,000$ , spanwise smoke wire positioned at nose) (Karim <sup>12</sup> , 1992).	177

## NOMENCLATURE

Symbol	Term
$c$	airfoil chord length
$C_p$	pressure coefficient, $2(p - p_\infty)/(\rho U_\infty^2)$
$f$	frequency of oscillation
$k$	dimensionless reduced frequency, $(\pi f c)/U_\infty$
$p$	surface pressure
$p_\infty$	reference static pressure
$Re_c$	chord Reynolds number, $(U_\infty c)/\nu$
$t$	time
$t_p$	time period for pitch-up motion through an angle $\Delta\alpha$
$U_\infty$	free-stream velocity
$\alpha$	angle of attack
$\alpha^+$	dimensionless pitch rate, $(\Delta\alpha c)/(t_p U_\infty)$
$\alpha_o$	mean angle of oscillation
$\alpha_m$	amplitude of oscillation
$\Delta\alpha$	change in angle of attack during oscillation
$\rho$	fluid density
$\tau$	surface shear stress
$\tau_{\alpha=0}$	surface shear stress at 0 deg. angle of attack
$\nu$	fluid kinematic viscosity
$\langle \rangle$	ensemble-averaged value

## ABSTRACT

In the first part of this study, surface shear stress and pressure measurements were obtained on a NACA 0012 airfoil model, undergoing a pitch-up motion from  $0^\circ$  to  $45^\circ$  angle of attack at a constant rate, using an array of surface-mounted hot-film sensors. Dominant features in these data and in the standard deviations computed from these data were examined and related to events in the development and evolution of the unsteady separation over the suction surface. Results were compared with well-known features of the dynamic stall process seen in the surface-pressure distributions. Trends in the behavior of these features are presented for a range of non-dimensional pitch rates ( $0.010 < \alpha^+ < 0.150$ ) and chord Reynolds numbers ( $1.1 \times 10^5 < Re_c < 2.0 \times 10^6$ ). Significant changes were seen in the behavior of these features at high Reynolds numbers. The results suggest that these changes are due to transition in the shear layer at high pitch rates and quasi-steady behavior at low pitch rates.

In the second part of this study, the unsteady flow field over a NACA 0012 airfoil model undergoing large amplitude sinusoidal motion was investigated for a wide range of chord Reynolds numbers and reduced frequencies. A combination of unsteady pressure and shear stress data at the surface of the airfoil provided detailed information about the development and evolution of the flowfield over the surface of the airfoil during its sinusoidal motion. In particular, the formation of the dynamic stall vortex during the upstroke of the motion profile was examined in detail as well as the reattachment process during the downstroke of the motion profile. The effects of Reynolds number, reduced frequency, mean angle of attack, and amplitude of oscillation were examined. In the current investigation, significant changes in behavior were seen with changing Reynolds number, reduced frequency, and amplitude of oscillation, while the mean angle did not appear to play any role in the evolution and development of this vortex except for the highest reduced frequency ( $k=0.4$ ). Amplitude of oscillation did not appear to be a factor in the development of the reattachment process. Reduced frequency had the greatest affect on the reattachment process, delaying or even preventing the onset of the process. This was caused by the presence of the dynamic stall vortex over the airfoil during the downstroke portion of the cycle.

# CHAPTER I

## INTRODUCTION AND BACKGROUND

### 1.1 Introduction

The unsteady flow over a pitching or oscillating airfoil is dominated by the development of a large vortical structure known as the dynamic-stall vortex (DSV). The formation and subsequent separation of this vortex results in the phenomenon known as dynamic stall. Interest in the study of this process has been largely motivated by the need for a better understanding of helicopter blade aerodynamics. More recently, motivation has come from interest in improving the maneuverability of aircraft. There has been a great deal of work devoted to the investigation of this complicated unsteady flow phenomenon. The reviews by McCroskey<sup>1</sup>, Gad-el-Hak<sup>2</sup>, Ericsson and Reding<sup>3</sup>, and Doligalski et al.<sup>4</sup> summarize a large portion of this work. Although some of this work examined the mechanisms responsible for the formation of the DSV, most of the results pertain to the evolution of the flowfield once the vortex has formed and the detachment of the vortex, which leads to dynamic stall.

There is great interest in the development of systems for controlling DSV formation and detachment on helicopter rotor blades and on wings of highly maneuverable aircraft. In helicopter applications, complete suppression of the DSV is desired, while in aircraft applications, it is desirable to allow the DSV to form and delay its detachment from the suction surface to take advantage of the lift enhancement it provides. The capability to accomplish both of these goals has been demonstrated in the work by Karim and Acharya<sup>5</sup> and by Alrefai and Acharya<sup>6</sup> through the use of leading-edge suction. However, to improve and optimize these techniques and develop new control schemes, a better understanding of the unsteady flow mechanisms that play a part in the very early stages of DSV formation, as well as the mechanisms responsible for DSV detachment, is essential. Specifically, it is of interest to determine how the events that lead to DSV formation, the movement of the DSV, and the subsequent detachment of the DSV scale with pitch rate and Reynolds number. Metwally<sup>7</sup> investigated these

relationships for a range of pitch rates at low Reynolds numbers, but it is unclear if these relationships hold at high Reynolds numbers or at very low pitch rates.

## 1.2 Background

The dynamic features of the flow associated with rapid variations in incidence of an airfoil were first identified by Kramer<sup>8</sup> in 1932. However, after this early investigation very little attention was given to these phenomena until the 1960s, when they were identified on the retreating blades of helicopters. Since then, great progress has been made in identifying the features associated with dynamic stall.

In the early seventies, Johnson & Ham<sup>9</sup> (1972) were among the first to theorize about the development of the DSV in oscillating airfoils. They believed that the vortex originated by the bursting of a laminar separation bubble formed on the suction side of the airfoil. McAlister, Carr & McCroskey<sup>10,11</sup> (1976-78) performed extensive tests in order to determine the events that lead to the DSV using hot-film sensors (shear stress), hot wire probes, pressure data and visualization techniques. In their studies, they used a NACA 0012 model with various leading edge modifications as well as an ONERA 0012 airfoil. Their findings concluded that there was no direct relation between the laminar separation bubble and the DSV. In all but two of the cases examined, the DSV was attributed to the progression of the trailing edge flow reversal. The progression of the flow reversal towards the leading edge was followed by an abrupt breakdown of the turbulent boundary layer in the forward portion of the airfoil, which in turn, fed vorticity into the DSV prior to its being shed off the airfoil. In only two of the cases studied, the DSV was attributed to the bursting of the leading edge separation bubble. Recent investigation by Karim<sup>12</sup> 1992 proved that there is no direct connection between trailing flow reversal and the dynamic stall vortex. He concluded that the separation of the dynamic stall vortex was initiated by local reversed flow in the leading edge region of the airfoil.

The primary goal of present studies is concentrated in the early stages of evolution of the dynamic stall vortex as well as the separation of this vortex from the surface of the

airfoil leading to stall conditions. In addition, great emphasis is placed on controlling the evolution of the dynamic stall vortex (Karim<sup>12</sup> and others<sup>7,13,14,15,16</sup>).

Prandtl in 1904 was the first to explain the mechanism of separation for a two-dimensional boundary layer. The characteristic of flow separation is the thickening of the boundary layer, the ejection of vorticity and the vanishing of wall shear at a point or line. Subsequently, design of helicopter blades, rapidly pitching airfoils, and turbomachines based on steady separation has not improved the performance of these devices, indicating a difference between steady and unsteady separation. The breakthrough in the unsteady separation was achieved by three researchers working independently, Moore<sup>17</sup>, Rott<sup>18</sup>, and Sears<sup>19</sup>. They all arrived at the same conclusion, stating that the unsteady separation point (or line) is the point (or line) in the boundary layer at which both shear stress as well as velocity vanish as seen by an observer moving with the separation velocity.

1.2.1 Unsteady Flow over 2-D Airfoils. The last three decades of investigation into the effects of unsteady motion of two-dimensional airfoils has yielded an impressive body of work. Through the use of pressure and velocity measurement in combination with visualization techniques, a great deal of understanding in the effects of reduced frequency, amplitude etc. has resulted.

The most extensive body of work on oscillating airfoils was performed by the U.S. Army Aeromechanics Laboratory in 1970s. They utilized flow visualization, hot-film and hot-wire data, as well as surface pressure distributions. These experiments were concentrated on small amplitude oscillations around low mean angles of attack. They provided, however, a large portion of our current understanding of the DSV. In a recent review on dynamic stall, McCroskey<sup>1</sup> summarized most of the work in the field related to unsteady airfoil flows. It has been found that the nature of motion has a strong effect on the dynamic stall process with reduced frequency being the dominant parameter in oscillating airfoils. This parameter has been heavily investigated in the past decade by several researchers<sup>20,21,22</sup>. The majority of the present work has been confined to steady flows over oscillating airfoils, since this model arrangement has been found to be similar to the flows over real configurations for large Reynolds numbers.

For an oscillating airfoil in a uniform flow, the reduced frequency is defined as

$$k = \frac{\pi f c}{U_{\infty}}$$

where  $f$  is the frequency of oscillation,  $c$  is the chord length of the airfoil and  $U_{\infty}$  is the free stream velocity. Change of the frequency of oscillation causes a shift or delay in the evolution of dynamic stall within the cycle of oscillation (McCroskey, Carr and McAlister<sup>10</sup>). In addition, these experimentalists also reported a delay of the flow reversal from the trailing edge, which propagates upstream with increasing reduced frequency. This event results in a significant lift overshoot followed by a sudden loss of lift (stall) and a surge in the pitching moment. Their experiments also revealed the velocity of the shed vortex over the upper surface of the airfoil, on the order of  $1/3$  to  $1/2$  of  $U_{\infty}$ .

Chandrasekhara and Brydges<sup>23</sup> in 1990 studied the effects of amplitude on dynamic stall of an oscillating airfoil. Results showed a significant influence in the development of dynamic stall. The airfoil was able to provide additional lift to higher angles of attack for higher amplitudes, with the vortex still attached to the surface. This was attributed to the additional vorticity generation due to surface acceleration and local streamwise pressure gradient.

Chandrasekhara, Wilder, and Carr<sup>24</sup> in 1996, conducted experiments to determine the influence of Reynolds number on 2-D compressible flows. They determined that Reynolds number effects indicate an increase in the airfoil suction peak, smaller laminar bubble, increase in dynamic stall onset angle, and an increased ability to withstand adverse pressure gradients in the flow.

Ahmed and Chandrasekhara<sup>25</sup> in 1991 investigated an important feature of the dynamic stall cycle, the reattachment of the boundary layer over the surface of the airfoil during the downstroke of a motion profile. The results showed that the reattachment begins close to the static stall angle and continues down to about 6 degrees. The completion of the reattachment process is also indicated through the disappearance of the laminar separation bubble formed above the airfoil.

Similar investigations have been conducted in recent years using hold-pitch-hold motions after interest in highly maneuverable aircraft was initiated. This work shows that



the processes involved in the formation and evolution of the DSV depend strongly on pitch rate, which can be related to reduced frequency in the oscillating case. The dimensionless pitch rate ( $\alpha^+$ ) is the key parameter that affects the behavior of this unsteady flow, and is defined as

$$\alpha^+ = \frac{\Delta\alpha c}{t_p U_\infty}$$

where  $\Delta\alpha$  is the change in angle of attack (in radians) and  $t_p$  is the pitch time. In other words, this parameter is the ratio of the tip velocity of the pitching airfoil to the free-stream velocity. At higher pitch rates, the processes of DSV formation and detachment are delayed to higher angles of attack. As the pitch rate is decreased, the unsteady effects become weaker, and shear-layer instabilities begin to occur further upchord on the airfoil surface. The mechanisms leading to the DSV formation occur at earlier angles of attack, the shear-layer roll up becomes more gradual, and the hold time of the DSV above the suction surface is greatly reduced. After a certain pitch rate, the hold time is no longer distinguishable, and the DSV appears to propagate downchord as it forms. It has also been shown that as the pitch rate is reduced, the adverse pressure gradient over the suction surface increases, which allows transition to turbulence to occur at earlier angles of attack.

In recent years, increasing interest has been placed on computational studies by many investigators (Ekaterinaris<sup>26</sup>, Visbal<sup>27</sup>, Ghia<sup>28</sup>, Okong'o and Knight<sup>29</sup>). Visbal in 1990 explained the vortex formation as the process of accumulation of fluid in the leading edge underneath the shear layer caused by a thin reverse flow. The thickening of the reverse flow causes the shear layer to lift up away from the wall where the adverse pressure gradient combined with the outer flow initiates the rollup of the shear layer into the vortical structure known as dynamic stall vortex. The increase in the pitch rate studied resulted in a more coherent vortex closer to the leading edge. In addition, the computational work of Visbal revealed that the reverse flow initiating the dynamic stall process is of a local nature that originates in the leading edge of the airfoil. The above was proven by visualization studies performed by Karim<sup>12</sup> in 1992. Yang in 1994 studied the dynamic stall over oscillating/pitching airfoils at high Reynolds numbers. The results

indicated that for a Mach number of 0.4, the local flow near the nose of the airfoil becomes supersonic. Under these conditions a weak shock forms, inducing boundary-layer separation at earlier angles of attack than for subsonic flows. He also concluded that for the same pitch rate, an increase in the Mach number results in an increase of the drag coefficient. Further investigation by Okong'o and Knight in 1997, indicated that the principal effect of increasing Reynolds number causes the primary recirculation region (vortex) to be formed at lower angles of attack, closer to the leading edge.

The influence of Reynolds number on the DSV formation process is not well understood. As the chord Reynolds number ( $Re_c$ ) increases, the boundary layer becomes thinner and the inertial effects are greater. Earlier transition to turbulence in the boundary layer, especially at lower pitch rates, becomes an important factor and adds complexity to the unsteady flow. However, at higher pitch rates, it has been shown that certain critical flow mechanisms in the unsteady flow evolution are insensitive to changes in Reynolds number for Reynolds numbers ranging in order from  $10^4$  to  $10^5$ . The work by Acharya, Karim, and Metwally shows very similar flow development over this range of Reynolds number for higher pitch rates ( $\alpha^+ \geq 0.1$ ). Also, they show that the occurrence of the local leading-edge flow reversal and shear-layer lift-up are not affected by changing Reynolds number over this range.

**1.2.2 Flow Control Techniques.** The need to reduce undesirable effects, such as flutter, buffeting, and dynamic stall has motivated different techniques in controlling flow over airfoils. In addition, the need to expand the operational envelope of fighting helicopters and highly maneuverable aircraft has renewed the interest in control techniques. Nelson<sup>30</sup> in 1989, used vortex generators upstream of the separation point (or line) in an attempt to mix the free stream flow with the retarded boundary-layer flow. The results of this passive technique were discouraging, however, due to the fact that the vortices generated were very weak compared to the vortices produced by the unsteady motion. Therefore, no significant change in the location or formation time of the dynamic stall vortex was detected. A different approach using active controls was demonstrated by Huang, Bryant, and Maestrello<sup>13</sup> in 1987. The effectiveness of acoustic forcing on the

steady flow field in the leading edge of the airfoil emanating from a narrow gap at the surface of the airfoil was investigated. The results indicated a drastic reduction in separation of the shear-layer, increased lift, and stall delay to higher angles of attack by sound emanating at twice the shedding frequency of the shear layer. Hsiao and Shyo<sup>14</sup> showed that acoustic excitation is most effective when placed near the vicinity of separation. Freymuth<sup>31</sup> in 1989 demonstrated unsteady flow separation without dynamic stall, using an airfoil equipped with a rotating leading edge. This approach showed that dynamic stall depends on the ratio of circumferential speed of the rotated cylinder with the flow speed. This ratio needed to be increased as the pitch angle increased. Another approach in active control is through the use of suction. Karim and Acharya<sup>5</sup> in 1994 demonstrated that leading edge suction can be used effectively to suppress the formation of the DSV. This approach was based on the removal of reverse flowing fluid before shear lift up was initiated. Further investigation by Alrefai and Acharya<sup>6</sup> on the effects of suction has revealed additional information allowing the development of different control strategies.

### 1.3 Previous Work at IIT

The IIT Fluid Dynamics Research Center has placed great emphasis on the understanding of the mechanism involved in the formation of DSV as well as in control techniques for suppressing it. Koga<sup>15</sup> in 1983 carried out an experimental study to determine the effects of large vortical structures on separated flows. The interaction of the vortical structures energized the separated region, thus, greatly reducing the mean separation length of the separated region. Encouraged by the results of Koga, Reisenthel<sup>32</sup> continued the work with emphasis on identifying the parameters involved. His findings confirmed the results of Koga and determined that under optimum conditions one could reduce the reattachment length by half. Ramiz<sup>33</sup> in 1989 looked into a non-intrusive technique for unsteady flow detection. He studied different criteria based on unsteady pressure measurements. The signature of wall pressure data with a preset value was compared, as well as the derivative of the wall pressure signal. He concluded that the unsteadiness in the flow could be detected using these techniques. Metwally<sup>7</sup> in 1990

investigated the events that occurred during the formation and evolution of the DSV. Using unsteady pressure measurements, Metwally identified the presence of the leading edge suction peak, and the constant pressure region, followed by another pressure peak associated with the formation of the DSV. Vorticity calculations identified the source and location of vorticity fed to the dynamic stall vortex. His experiments provided new information in the development and detachment of DSV. He also investigated the effects on leading edge suction as a controlling mechanism for suppressing the vortex formation. Karim<sup>12</sup> in 1992, investigated the near wall flow structure using visualization and he also investigated the effect of suction flow control on a pitching airfoil. He determined that local flow reversal, close to the leading edge of the airfoil, caused the vortex to separate. These investigations helped form the current description of the origin of the DSV. Computational work by Visbal<sup>34</sup> provided additional insight into this process. This work shows that the vorticity present in the DSV originates from a concentrated source near the leading edge on the pressure surface of the airfoil. This vorticity is transported to the suction surface in a thin shear layer. A thin region of reverse-flowing fluid in the leading edge region accumulates beneath this shear layer, causing it to lift away from the surface. This reverse flow near the surface is produced by the increasing adverse pressure gradient over the suction surface as the angle of attack increases. The initial flow reversal occurs just downstream of the leading edge region on the suction surface, and is independent of the reverse flow initiated at the trailing edge. As the airfoil continues to pitch up, accumulation of vorticity in the shear layer downchord of the reverse-flow region interacts with the outer flow, causing the shear layer to roll up and form the DSV. The DSV remains attached to the suction surface of the airfoil over a range of angles of attack, enhancing the unsteady lift force. The abrupt detachment of the DSV, due to a secondary flow eruption, causes this lift enhancement to be lost, resulting in dynamic stall.

Using the experimental knowledge obtained from the above, Alrefai<sup>35</sup> in 1995 studied the unsteady flow over two-dimensional airfoils using controlled leading edge suction. He developed a technique for identifying flow states to meet the desired objective. Based on the information provided by the work of Alrefai, Kawthar-Ali<sup>36</sup> developed a neural-network to predict the required suction flow rate for the given

objective. Recently Karim<sup>37</sup> investigated the unsteady flow over a pitching swept airfoil. The unsteady pressure and vorticity flux were analyzed studying the effects of cross flow on the development of unsteady flow; in addition, the feasibility of suction in the dynamic stall vortex was investigated.

#### 1.4 Objectives

Most practical applications involve low pitch rates ( $\alpha^+ = 0.01-0.2$ ) and high Reynolds numbers ( $Re_c > 2.5 \times 10^6$ ). The flow mechanisms which lead to the formation of the DSV described in the previous section are only well understood for pitch rates greater than  $\alpha^+ = 0.1$ . Also, there is very little or no information about the nature of the unsteady flowfield for Reynolds numbers greater than 500,000. Figure 1 shows a summary of the  $Re_c$  and  $\alpha^+$  values at which past experimental and computational investigations were carried out. This figure only shows investigations where a pitch-up motion profile was used. The solid circles represent the proposed research, while the open symbols represent past experiments and the small solid symbols represent past computations. Clearly, a detailed investigation of the unsteady flow development at low pitch rates and higher Reynolds numbers is needed to close the gap between research and applications and to answer a number of fundamental questions about the nature of this process. First, it is unclear if the same mechanisms and events that lead to the formation of the DSV at higher pitch rates contribute in the same way or behave in a similar manner at lower pitch rates. Also, it is not known if the flow reversal and shear-layer roll-up events remain independent of chord Reynolds number at higher Reynolds numbers. It is not known if transition in the shear layer is an important factor. As mentioned earlier, transition occurs at earlier angles of attack as the non-dimensional pitch rate decreases, and it occurs closer to the leading edge of the airfoil as the chord Reynolds number increases. Previous investigations, which modeled the effects of transition at low Reynolds number using boundary-layer trips, proved to be difficult. An investigation of these effects at high Reynolds numbers, where transition occurs naturally, would be of value. Finally, the importance of viscous-inviscid interactions between the shear layer and the outer flow, such as the interaction between the laminar separation bubble and the outer flow

described by early investigations at low Reynolds numbers, needs to be studied at high Reynolds numbers.

As mentioned earlier, past experimental investigations have used flow visualization and surface pressure measurements to obtain information about the flowfield. However, at higher Reynolds numbers, conventional flow visualization is no longer possible. In addition, the frequency response of pressure measurements is limited when long transmission lines are used. Furthermore, the range of Reynolds number for which current computational techniques can be applied is limited, and suitable computational models for transition to turbulence and unsteady turbulent shear layer evolution are still being developed. In order to obtain additional detailed information about the flow development over the surface of the airfoil, new experimental techniques are necessary. In this study, a technique for measuring relative changes in the surface shear stress using hot-film sensor arrays will be developed. Using this technique, which will be described later, important features in the shear stress data will be identified. These features will then be related to flow events through comparison with the flow visualization of Karim and Acharya<sup>5</sup> and the pressure measurements of Acharya and Metwally<sup>7,39</sup>.

The main objective of the first part of the proposed research (Part A) is to develop a better understanding of the physical mechanisms and processes that lead to DSV formation on an airfoil undergoing a constant amplitude pitch-up motion through a systematic experimental investigation of the effects of pitch rate and Reynolds number on certain key flow quantities. The ranges of pitch rate and Reynolds number selected will bridge the gap between past experimental investigations and actual aircraft applications (see Figure 1). This information will aid in the development of improved or new flow control systems. More specifically, the first objective is to investigate the effects of chord Reynolds number on DSV development by extending the range of  $Re_c$  to  $2.0 \times 10^6$ . The events that lead to DSV formation will be examined in detail for a wide range of  $Re_c$ , from  $1.1 \times 10^5$  to  $2.0 \times 10^6$ . Unsteady surface pressure and surface shear-stress measurements will be used to identify the mechanisms involved and identify key flow features. Relationships between the events that lead to DSV formation and these flow

features will be investigated. Secondly, this work will examine the effects of pitch rate and how these effects change over the entire range of  $Re_c$  studied. The focus will be on low pitch rates ( $0.01 \leq \alpha^+ \leq 0.15$ ), for a constant-velocity pitch-up motion profile.

In order to accomplish these objectives, a number of specific tasks will be performed. A motion control system will be designed that will allow the desired motion profile and the desired range of pitch rates to be achieved over the entire range of Reynolds numbers. This includes hardware selection and motion control software development. Hot-film sensor instrumentation required to measure the unsteady surface shear stress will be designed and developed. This involves designing the hot-film sensor array that will be placed on the airfoil surface and developing the constant-voltage amplifiers and signal-conditioning circuitry required to operate the sensors. The unsteady shear-stress variations in the leading-edge region of the airfoil will be measured for the entire range of pitch rate and Reynolds number using the hot-film sensors. Finally, the unsteady surface-pressure distributions at the higher Reynolds numbers will be measured and compared to the shear stress results. At lower Reynolds numbers, pressure data is already available (see Metwally<sup>7</sup>).

The objectives of the second part of this project (Part B) are to identify the effects of Reynolds number, reduced frequency, mean angle, and amplitude of oscillation on the development and evolution of the DSV for an airfoil undergoing an oscillatory motion. In addition, the influence of the above parameters on the reattachment process during the downstroke portion of the cycle will be investigated. The information obtained will provide additional insight into the complex phenomenon of dynamic stall, thus helping us determine the best combination of controlling parameters for suppressing or delaying the DSV.

To accomplish these above objectives, unsteady pressure data above the surface of the airfoil in conjunction with the acquisition of shear stress data at the surface will be again be used to get a unique picture of the processes involved. The current investigation provides higher shear stress spatial resolution in the leading edge of the airfoil, while events above the surface of the airfoil (unsteady pressure) will be related to events on the surface of the airfoil (shear stress).



## CHAPTER II

### EXPERIMENTAL FACILITIES AND INSTRUMENTATION

#### 2.1 Wind Tunnel Facilities

The current research was performed in two experimental facilities located at the Illinois Institute of Technology Fluid Dynamics Research Center. The first facility used was the Andrew Fejer Unsteady Wind Tunnel shown in Figure 2. A detailed description of this facility can be found in Koga<sup>15</sup>. It is a closed circuit, low speed facility with a free stream turbulence level of 0.03% at the maximum velocity of 40 m/s. The wind tunnel cross sectional testing area is 0.61 x 0.61m and 3.1m in length. Special features of this facility are its ability to introduce unsteady oscillation in the flow by a computer controlled shutter mechanism located downstream of the test section. This feature was not used in these experiments. In addition, the front and top walls of the test section are made out of clear Plexiglas to aid in flow visualization. The removable hatches on the test section floor provide access (if needed) to the test section. The airfoil, positioned horizontally in the test section, was supported on the back wall by a ball bearing and the motor, while a needle bearing supported the front end.

The second experimental facility used, was the National Diagnostics Facility (NDF) shown in Figure 3. This facility is a closed-return subsonic wind tunnel designed to have nearly uniform flow with low levels of velocity, temperature, and pressure fluctuations. The facility and flow quality are described in detail in the paper by Nagib et al.<sup>48</sup> The wind tunnel incorporates several flow control features which make it very well suited to high Reynolds number research. The low-rpm variable speed fan has adjustable blade pitch, which allows precise adjustment of the flow speed. The fan is driven by a 2000 hp constant speed electric motor through a variable speed electromagnetic clutch. This combination allows free-stream velocities up to 120 m/s (400 ft/s) that can be adjusted to within 0.1 m/s (0.3 ft/s) and can be held to within  $\pm 0.1$  m/s (0.3 ft/s). The test section is 1.22 m x 1.52 m x 10.3 m (4' x 5' x 34') long with a multi-panel moveable ceiling that can be adjusted to give the desired pressure gradient. Upstream of the test section, the flow passes through a honeycomb, six screens, and a 6.25:1 area ratio fifth-order contraction, which provide the turbulence manipulation. As a result, free-stream



turbulence intensity in the test section ranges between 0.03% and 0.08%, depending on the free-stream velocity. For this experiment, an additional fifth-order contraction was installed in the test section. The airfoil model was mounted vertically in this contraction as shown in Figure 4. The cross-section of the test section downstream of the additional contraction was 0.61 m x 1.52 m (2' x 5'). This contraction allows free-stream velocities up to 150 m/s (500 ft/s) to be reached. Free-stream flow cooling is provided by pumping chilled water through passages in the turning vanes of turns one and three of the wind tunnel. Temperature in the test section can be controlled to within 0.1°C (0.2°F) and can be held to within  $\pm 0.1^\circ\text{C}$  (0.2°F) over several hours of operation. In turn two of the wind tunnel, the pressure sides of the turning vanes are lined with an acoustically absorbent material that decreases the effect of fan noise.

## 2.2 Airfoil Model and Motion Control System

The airfoil model used in this research was the one described by Acharya and Metwally<sup>39</sup>. It has a NACA 0012 profile, a chord length of 30 cm, and a span of 60 cm. The model pitch axis was located at the quarter-chord point. The airfoil is a hollow design that provides valuable internal space for instrumentation. Access to the model interior is given through a removable panel on the side of the airfoil. The instrumentation connecting leads were fed through the hollow shaft that connects the airfoil to the servomotor outside the tunnel. The airfoil motion was driven via a 14.4 HP, low inertia, high torque, brushless servo controlled DC motor, model MPM1903FRMM-BM, manufactured by Custom Servo Motors, Inc. The servomotor incorporates resolver feedback and was controlled by a PC-based Compumotor AT6250 servo controller and a Custom Servo Motors MPA-75 analog servo amplifier. The motion profile and the servomotor tuning parameters are software-programmable. A Gateway 2000 486 personal computer was equipped with AT6250 card and Compumotor Motion Architect Software. For the constant-amplitude pitch-up motion profiles, a control program was written using National Instruments LabVIEW software along with Compumotor Motion Toolbox software. The motion profile for oscillation was created using C++ code after the reduced frequency, mean angle, amplitude, Reynolds number, and number of oscillations was provided. The angle of attack was varied in a sinusoidal manner described by the

equation  $\alpha = \alpha_o + \alpha_m \sin(\omega t)$ . Once the motion profile was generated, it was downloaded in the controller and executed. The square wave encoder signal obtained from the motion controller provided positional information accurate to within 0.09 degrees. For the high-Reynolds number tests performed in the NDF, the motor was equipped with an ultra-precision 3:1 planetary gear drive, which provided the torque multiplication needed to overcome the high aerodynamic loads (approximately 255 Nm at 1200 RPM). With the gear drive installed, the angular resolution was increased to  $\pm 0.03$  degrees.

## 2.3 Instrumentation

2.3.1 Pressure. The model is instrumented with a single row of 21 pressure ports located at half-span on the suction surface. The location of these ports is shown in Table 1. The ports are spaced progressively closer to allow greater spatial resolution in the leading-edge region. The pressure ports are connected to a single, externally located Setra model 239 pressure transducer through a 24-port Scanivalve mounted inside the airfoil model. Two Setra 239 pressure transducers were used for the acquisition of the pressure data. The Setra 239 with sensitivity of 2.5 volts per 2.5" of water was used for the Reynolds number range of  $1.1 \times 10^5$  to  $3.2 \times 10^5$ . For higher Reynolds numbers the second pressure transducer with resolution 2.5 volts per 15" of water was used. The pressure transducers were placed outside the tunnel section as close as possible to minimize dampening effects. The tubing used had an inner diameter of 0.063 inches, connecting the pressure transducer to the output port of the scanivalve, while the reference port on the pressure transducer was connected to a static pressure tap on the sidewall of the tunnel test section. The total length of the vinyl tubing from the scanivalve to the pressure transducer was  $< 2$  m, providing a frequency response of approximately 80 Hz (Metwally<sup>7</sup>). The individual pressure ports along the surface of the airfoil were connected to the scanivalve with 0.040-inch inner diameter vinyl tubing approximately 0.2 m long. The scanivalve was remotely controlled with a CTLR 10P/S2-S6 controller accompanied by a model number CTR2/OETM-BINY counter.

2.3.2 Hot-Film Sensors. The leading edge of the airfoil model is also instrumented with a multi-element array of microthin hot-film sensors adhered to the airfoil surface,

shown in Figure 5a. This array consists of a single row of 50 nickel sensors spaced 2.54 mm apart and deposited on a 0.05 mm thin flexible polyimide substrate. Each sensor has two 18.4 cm long copper leads to which the electrical connections are made. The nominal cold resistance of these sensors was approximately 9.0 Ohms with an average size of 1.5 mm long (spanwise direction) and 0.15 mm wide (streamwise direction). The row of sensors is oriented parallel to the row of pressure ports approximately two inches from half-span, and wrapped around the leading edge of the airfoil from 13% of chord on the pressure surface to 25% of chord on the suction surface, as shown in Figure 5b. The locations of these sensors are given in Tables 2 and 3. (Note that the sensor configuration was changed for the final oscillation tests performed in the NDF due to damage to the first configuration.) The remaining surface area of the airfoil is covered with blank substrate material so that no discontinuities or steps exist which could disturb the flow. Each sensor was connected to its own constant voltage amplifier circuit, designed and constructed at IIT, which gave the proper overheat ratio and frequency response. A schematic of the amplifier circuit is shown in Figure 6a. In order to obtain the shear stress data, all 50 sensors were operated at an overheat ratio of about 1.2. The amplifier outputs were low-pass filtered at 1000 Hz, offset to obtain a zero mean, amplified by a gain of 50, and acquired pseudo-simultaneously at 3000 Hz by a PC-based data acquisition system. A schematic of the signal conditioning circuit is shown in Figure 6b. It should be noted that hot-film sensors of this type have been and are currently being used successfully by other researchers to characterize unsteady boundary-layer transition<sup>21</sup> and to detect flow features such as laminar-to-turbulent transition regions, separation and reattachment points, and stagnation points<sup>49,50</sup>.

#### 2.4 Computer Facilities

A combination of two computers was required for the acquisition of the pressure and the shear stress data. One computer was dedicated for the acquisition of the data, while the other computer was controlling the servomotor. For tests done in the Fejer tunnel, the data acquisition was performed using a National Instruments model AT-MIO-16X analog-to-digital converter board installed in a Gateway 2000 486 66MHz PC. The resolution of this board was 16-bit with a maximum aggregate-sampling rate of 100 kHz.

The board had 16 single-ended analog input channels (8 differential) with an input of 0 to 10 volts for unipolar mode and -10 to +10 volts for bipolar mode. In addition, the board had two analog output channels and eight digital input/output channels. One of the digital output channels was used to synchronize the two computers. The EXTRIG was used to receive the signal, initiating the start of the acquisition 0.1 seconds prior to the start of the motion profile. The data acquisition was performed with the use of a DOS based data acquisition program at a sampling rate of 11 kHz required to resolve the encoder signal correctly. Due to the high rate of acquisition, only eight sensors were acquired at a time.

For the high Reynolds number data taken in the NDF, a 12-bit board with a sampling frequency of 500 kHz (National Instruments model AT-MIO-16E-2) was installed in a Dell-Dimension 100 MHz Pentium PC. Two analog multiplexer boards (National Instruments model AMUX-64T) allowed the acquisition of all 43 sensors pseudo-simultaneously at a sampling frequency of 11 kHz. A new data acquisition program was written for this purpose using LabVIEW software. The triggering mechanism remained the same as before. The addition of the gear reducer, however, increased the required acquisition frequency needed to decode the encoder signal to 35 kHz. This prevented the acquisition of both encoder and sensors at the same time. The motion profiles were found to be very repeatable, however, so the tuned motion profile was acquired separately and a timing pulse signal acquired from the motion controller was used to synchronize the motion files with the data files.

## 2.5 Measurement and Experimental Procedure

The initial portion of the proposed research was carried out in the Fejer wind tunnel at low Reynolds numbers ( $1.1 \times 10^5 \leq Re_c \leq 4.6 \times 10^5$ ) for the entire range of pitch rates. For Part A of this project, unsteady shear-stress variations were acquired and used as a baseline for the remaining measurements. Analysis of the shear stress data involved ensemble averaging multiple realizations and plotting the variations with angle of attack for different flow and motion parameters. Ten realizations were acquired for each case, which were then aligned and ensemble averaged. The shear stress data were compared with the flow visualization and surface pressure data obtained by Metwally<sup>7</sup> and Karim<sup>12</sup>. This comparison allowed characterization of the shear stress signatures corresponding to

the flow features seen in the flow visualization and pressure data and described by Metwally and Karim. Once identified, the progression of these features along the airfoil surface was tracked for different pitch rates and Reynolds numbers.

For Part B of this project, unsteady pressure and shear stress data were acquired for a range of oscillation amplitudes and reduced frequencies. The pressure data were acquired one port at a time throughout the cycling of the airfoil motion. Once all the ports were acquired, the data records were split into individual cycles and were ensemble averaged. It should be noted that the first two cycles of each data file were dropped to minimize any initial transient effects before 'steady' oscillating conditions were reached. The calculated pressure coefficient was plotted against the non-dimensional chord length ( $x/c$ ). The hot-film shear-stress data were handled in a similar manner. Once the data were recorded, they were split into individual cycles and ensemble averaged (dropping the first two cycles). The shear-stress variations were then plotted vs. angle of attack and the key features were identified and tracked.

The second portion of this work took place in the NDF. For both Part A (pitch-up motion) and Part B (oscillatory motion), surface shear stress and pressure data were acquired for the entire range of pitch rates (Part A) and reduced frequencies (Part B) at high Reynolds numbers ( $0.5 \times 10^6 \leq Re_c \leq 2.0 \times 10^6$ ). These results were compared to the baseline results to identify significant trends with increasing Reynolds number.

The output voltage of the constant-voltage amplifier circuit used to power the hot-film sensors is related to the variation of the sensor resistance due to convective heat transfer by the flow. The circuit detects changes in the current required to compensate for resistance variations due to variations in the surface shear stress, and the output voltage of the CVA is proportional to changes in the current. High output voltages indicate high shear stresses at the wall, while low voltages would indicate low shear stresses. For example, a vortical structure in close proximity to a wall would produce high shear stress levels (high voltages) indicating position and strength, while a separation point would give low shear stress levels (low voltages). However, it should be noted that it is not possible to calibrate these hot-film sensors in place on the airfoil model. Therefore, values for the shear stress were obtained by assuming that the sensors obey a general calibration law of the form:

$$E = A + B\tau^{1/3}$$

where  $E$  is the amplifier output voltage,  $\tau$  is the shear stress, and  $A$  and  $B$  are calibration constants. In these experiments,  $A$  was adjusted to zero, and normalization eliminated  $B$ . Therefore, the shear stress is proportional to the circuit output voltage cubed. An explanation of this relationship is given by Sarma<sup>51</sup>. The shear stress data presented in this report are normalized by the shear stress values at the onset of the airfoil motion for each case ( $\alpha = 0^\circ$  for the pitch-up motion). The assumptions made and this normalization give accurate information on the relative variations in shear stress at each location, allowing comparisons to be made for various airfoil motions and flow conditions. While it is possible that the structure of the boundary layer over the airfoil renders the assumptions made invalid during some stages of the unsteady separation, it is believed that although the shear stress values obtained may not be exact during these periods, these measurements do correctly indicate the trends in shear stress behavior.

It was found that the hot-film sensors were sensitive to changes in the free stream temperature. Therefore, in order to prevent drifts in the acquired data, the free stream temperature was closely monitored. In the Fejer tunnel, where no free stream temperature control existed, the tunnel was run until a 'steady' state (small change in temperature with time) was reached. This technique eliminated any effects changes in temperature would have on the data.

The data acquired were of extremely high quality and repeatable. For the oscillatory motion data, the main concern was the presence of hysteresis, which would interfere with the normalization process. No hysteresis was present in the data acquired in the Fejer tunnel, however there was a small amount present in the NDF data. The addition of the gearbox on the motor prior to the NDF experiments was identified as one of the sources (backlash). The maximum amount of hysteresis in the data did not exceed 0.7 degrees through the complete set of cycles, and it was only present at the highest Reynolds number of  $1.0 \times 10^6$ .

## 2.6 Experimental Parameters

For Part A of this project, five non-dimensional pitch rates are studied ( $\alpha^+ = 0.01, 0.018, 0.036, 0.072, \text{ and } 0.15$ ). The motion of the airfoil was a constant-velocity pitch-up

from zero degrees to 45 degrees angle of attack. Surface pressure and surface shear-stress data were taken at seven chord Reynolds numbers ( $1.1 \times 10^5$ ,  $3.2 \times 10^5$ ,  $4.6 \times 10^5$ ,  $0.5 \times 10^6$ ,  $1.0 \times 10^6$ ,  $1.5 \times 10^6$ , and  $2.0 \times 10^6$ ). The first three Reynolds numbers were investigated in the Fejer tunnel and the remaining four were investigated in the NDF. Due to the extreme motion characteristics and high aerodynamic loading at high flow speeds, all five pitch rates could not be achieved at the higher two Reynolds numbers. At  $Re_c = 1.5 \times 10^6$ , the lowest four pitch rates were examined, and at  $Re_c = 2.0 \times 10^6$ , the lowest three pitch rates were examined.

For Part B of this project, the experimental parameters tested shown in Table 4, indicate a wide range of Reynolds numbers, reduced frequencies, and combinations of mean angles and amplitudes required to satisfy the objectives set by the current research. The Reynolds number was varied from  $1.1 \times 10^5$  up to  $1.0 \times 10^6$  at a fixed reduced frequency of  $k = 0.1$ . This allowed the examination of the Reynolds number effects on the flow-field for the four different motion profiles executed (Figure 7). Detailed analysis on the effects of reduced frequency on the unsteady flow field was also conducted for a range of  $k = 0.1$  to  $k = 0.4$  at the Reynolds number of  $1.1 \times 10^5$ . The oscillating profiles used in the current investigation were generated based on mean angle and amplitude of  $10^\circ$  and  $20^\circ$ .

## **PART A**



## CHAPTER III

### ANALYSIS OF HOT-FILM DATA

#### 3.1 Features of the Shear Stress Data

The relationship between the output voltage of the hot-film sensor amplifier circuits and the change in surface shear stress was mentioned in the last chapter. The analysis of this data and the shear stress variations for different flow conditions and pitch rates will be presented in this chapter. The shear stress variations with angle of attack provide a picture of the structure of the flow field above the surface of the airfoil for each pitch rate and Reynolds number. These shear stress variations will be discussed first. In the figures presented in this report, the quantity  $\langle \tau / \tau_{\alpha=0} \rangle$  represents the ensemble-averaged normalized shear stress at the airfoil surface. To obtain this quantity, the "shear stress" was computed by taking the cube of the hot-film sensor amplifier output voltage. This value was normalized by the "shear stress" value at the  $0^\circ$  angle of attack position for each  $x/c$  location. The results were then ensemble averaged over the ten realizations acquired for each case. Therefore, this quantity reflects the change in shear stress locally during the pitch-up motion, relative to the value at  $\alpha = 0^\circ$ . As mentioned in the last chapter, it is believed that the assumptions made regarding the relationship between the hot-film amplifier output voltage and the shear stress, along with the normalization described, will give accurate information on the relative variations in shear stress at a location, allowing comparisons to be made for various pitch-up motions and flow conditions.

Figure 8 shows the normalized, ensemble-averaged shear-stress variations on the suction surface of the airfoil during a pitch-up motion for  $\alpha^+ = 0.036$  and  $Re_c = 1.0 \times 10^6$ . Once again, each curve in this figure shows the relative change in shear stress at a given  $x/c$  location during the pitch-up motion, not absolute magnitudes of shear stress. By examining the shear stress variations such as these for each pitch rate and Reynolds number, several key features and trends were identified and related to events occurring in the dynamic stall process. These features are indicated in Figures 8a and 8b. For this discussion, the instrumented portion of the suction surface may be divided into three

regions, each exhibiting different behavior related to the unsteady flowfield development and evolution. Five  $x/c$  locations in each region are shown in Figure 8.

Figure 8a shows the ensemble-averaged shear-stress variations at five chordwise locations very close to the leading edge of the airfoil ( $x/c < 3\%$ ). At the sensor location nearest to the leading edge ( $x/c = 0.003$ ), the shear stress initially rises to a maximum before rapidly decreasing as the angle of attack increases. This maximum is referred to as Feature 1 (F1). At the next two sensor locations ( $x/c = 0.008$  and  $0.014$ ), this peak occurs at progressively earlier angles of attack. At  $x/c = 0.029$  and beyond, this feature is no longer seen. Therefore, this feature occurs very close to the leading edge early in the pitch-up motion and propagates further upchord as the angle of attack increases. It is believed that Feature 1 is the signature of the leading-edge suction peak (LESP), which is a feature seen in pressure variations over the suction surface by several researchers, and is associated with the acceleration and deceleration of the flow close to the leading edge. A more detailed comparison to the pressure data of Acharya and Metwally<sup>39</sup> will be made later in this chapter.

At sensor locations further from the leading edge, the shear stress decreases to a minimum as the airfoil is pitched up. This minimum is referred to as Feature 2 (F2), and is indicated in Figures 8a and 8b. For each case, this feature is seen at all sensor locations except those very close to the leading edge. This feature occurs at low angles of attack at the highest  $x/c$  location ( $x/c = 0.209$ ), and it propagates upchord towards the leading edge as the angle of attack increases, as seen in Figures 8b and 8c. It is believed that this feature is a precursor to the arrival of the thin region of reverse-flowing fluid just above the surface underneath the shear layer. The flow visualizations described in detail by Karim and Acharya<sup>5</sup> show this flow reversal clearly. Investigations of unsteady boundary layer separation<sup>52,53</sup> have shown that under unsteady conditions, the point of zero shear stress does not indicate separation. Instead, it was seen that the leading edge of a thin reverse-flow region exists just downstream of this point.

Immediately after Feature 2, the shear stress rapidly increases, indicating that the shear layer has been lifted away from the surface by the region of reverse-flowing fluid. This rapid rise in shear stress is indicated as Feature 3 (F3) in Figure 8b. Following the

rapid increase, the shear stress remains at an elevated level for a range of angles of attack. At higher  $x/c$  locations, this range grows in magnitude and width. This behavior is believed to be associated with the unsteady events occurring underneath the shear layer just prior to the roll-up of the shear layer into the dynamic-stall vortex (DSV). At the end of this range, a distinct shear-stress peak is seen, which is indicated as Feature 4 (F4) in Figure 8b. For most cases, as will be discussed later, this feature corresponds to the roll-up of the separated shear layer into a coherent dynamic-stall vortex (DSV). A comparison with the pressure data of Acharya and Metwally<sup>39</sup> will be made later in this chapter which reveals the connection between Feature 4 and the DSV. Similar connections were made by Schreck, et al.<sup>21</sup> Once this feature is seen, it propagates downchord and increases in magnitude as the angle of attack increases. This is seen in Figure 8b and 8c. Also, at higher  $x/c$  locations, Feature 4 is more easily distinguished from the range of elevated shear stress following Feature 3. Following this peak, the shear stress decreases to a low level, indicating the fully stalled state that exists after the DSV has detached from the surface and convected downstream. At certain pitch rates and Reynolds numbers, a small, broad peak is seen at very high angles of attack following F4. This is indicated as Feature 5 (F5) in Figure 8b. At this point, it is unclear what this feature indicates. It may be an indication of a secondary structure induced by the DSV before it detaches and convects downstream, or it may indicate the arrival of trailing-edge reverse flow in the leading edge region.

Figures 9-11 show normalized shear-stress variations for the same pitch rate and sensor locations at a different Reynolds numbers. The same shear-stress features are seen, however there are some interesting differences. Figures 9 and 10 show two lower Reynolds number cases,  $1.1 \times 10^5$  and  $4.6 \times 10^5$ , respectively. At these Reynolds numbers, the same shear-stress features are seen, but they occur at  $x/c$  locations further from the leading edge. In Figure 9, for the lowest Reynolds number, F2 and F3 are not seen upchord of  $x/c \approx 0.06$ , and F4 is not seen upchord of  $x/c \approx 0.10$ . Also, the shear stress no longer exhibits a sharp peak at F3, and F4 occurs at a much earlier angle of attack. This results in a smaller range of  $\alpha$  between F3 and F4. In Figure 10 ( $Re_c = 4.6 \times 10^5$ ) the

behavior is similar to that shown in Figure 8, but the features occur slightly further downchord on the airfoil surface.

Figure 11 shows the behavior at the highest Reynolds number studied ( $Re_c = 2.0 \times 10^6$ ) for the same pitch rate ( $\alpha^+ = 0.036$ ). At this Reynolds number, the shear-stress minimum (F2) and the distinct shear-stress peak (F4) are seen very close to the leading edge, as indicated by the arrow in Figure 11a. Further downchord, we start to see a small shear-stress peak at angles of attack immediately ahead of F4, as indicated by the arrow in Figure 11b. At even higher  $x/c$  locations, shown in Figure 11c, a second small peak develops just after the first. (These will be referred to as F4a and F4b, respectively, in the subsequent discussion.) Both of these peaks propagate downchord as the angle of attack increases once they form. Explanations for these differences at higher Reynolds numbers will be offered later in this discussion.

Figures 12-15 show the normalized shear-stress variations at the same four Reynolds numbers for the lowest pitch rate,  $\alpha^+ = 0.010$ . Overall, the behavior at this pitch rate is similar to that shown in Figures 8-11, but in each case, the shear-stress features occur at earlier angles of attack. Also, F4 is not as distinct and is smaller in magnitude compared to the region of elevated shear stress preceding it.

Figures 16-18 show normalized shear-stress variations for the highest pitch rate,  $\alpha^+ = 0.150$ . Three Reynolds numbers are shown,  $1.1 \times 10^5$  (Fig. 16),  $4.6 \times 10^5$  (Fig. 17), and  $1.0 \times 10^6$  (Fig. 18). In each case, the flow behavior is much different than for the lower pitch rates. Figure 16 shows that at the lowest Reynolds number, F4 appears to have a much higher magnitude compared to the region of elevated shear stress following F3. In Figures 16 and 17, there are large fluctuations in the shear stress and angles of attack preceding and following F4. In Figure 18, where the Reynolds number is higher, all shear stress features are significantly delayed to higher angles of attack. (In the cases presented previously, F2 and F3 appeared at nearly the same  $\alpha$ .) Reasons for this large delay will be discussed later in this chapter and in the next chapter. For all Reynolds numbers at the higher pitch rates, the shear stress appears to level out following F3, rather than forming a peak at it did in the lower pitch rate cases.

Figure 19 shows two typical pressure variations over the pressure and suction surfaces of the airfoil model taken from Acharya and Metwally<sup>39</sup>. Pressure variations are shown for two different angles of attack for the same pitch rate, and the dominant features are identified. The first feature is the leading-edge suction peak (LESP). This feature develops in the forward region of the airfoil suction surface ( $x/c < 3\%$ ) immediately after motion is initiated. It is associated with acceleration of flow around the nose of the airfoil from the stagnation point. With increasing angle of attack, the peak increases in magnitude and moves closer to the airfoil leading edge. The second feature is the constant pressure plateau (CPP). This feature is linked to the accumulation of reverse-flowing fluid on the suction surface of the airfoil resulting in shear layer lift-up prior to DSV formation. The third feature is the dynamic stall vortex peak (DSVP). It was shown that this peak corresponds to the location of the DSV above the suction surface of the airfoil. By tracking this peak in the pressure data, it was shown that once the DSV forms, it remains bound to the suction surface of the airfoil for a period of time dependent on the pitch rate and chord Reynolds number. During this period, as the pitch-up motion continues, the DSVP moves to higher  $x/c$  locations until a secondary event causes the DSV to detach and convect downstream. When this occurs, the DSVP disappears.

In order to compare the current shear-stress data to the pressure results, the location and movement of shear stress Features 1, 2, and 4 were tracked over the suction surface for  $0.003 \leq x/c \leq 0.209$ ,  $\alpha^+ = 0.036$ , and  $Re_c = 1.1 \times 10^5$ . The results are shown in Figure 20 together with data on the location of the LESP and DSVP from Acharya and Metwally<sup>39</sup>. It is clear from this comparison that Feature 1 is related to the LESP and Feature 4 is related to the DSVP. This figure summarizes some of the key features involved in DSV formation and evolution. At low angles of attack, a LESP appears at about 3% of chord. This peak moves toward the leading edge as  $\alpha$  continues to increase. The signature of this LESP is a corresponding peak that first appears in the wall shear stress signature at around 3% chord and at successively later instants in these signatures at locations progressing upchord toward the nose.

The second characteristic feature is a minimum in the shear stress-time (or equivalently,  $\alpha$ ) signature. It is first seen for these flow conditions at  $\alpha = 8^\circ$  at  $x/c =$

20.9%. The appearance of this minimum in the shear stress signatures propagates very rapidly upchord, and is seen at  $x/c = 8.5\%$  at  $\alpha = 10^\circ$ . Thereafter, its upchord movement begins to slow down. This feature is a precursor to the initiation of a thin region of reverse-flowing fluid traveling upchord underneath the shear layer. The progression of this fluid slows as it begins to accumulate just above the airfoil surface, resulting in a lift-up of the shear layer. This region of accumulating fluid has also been described as a "bubble" by other researchers. After the upchord movement of Feature 2 begins to slow down, and after the LESP and Feature 1 are no longer seen near the leading edge, the DSVP first appears in the pressure data, as does shear stress feature 4, at around  $\alpha = 15.5^\circ$ . Also note that the DSVP and Feature 4 first appear at about the same  $x/c$  location where the movement of Feature 2 begins to slow ( $x/c = 9\%$ ). As the pitch-up continues, the DSVP and Feature 4 move downchord rapidly. The present shear-stress data track the movement of the DSV to  $x/c = 20.9\%$  where the sensor array ends. The pressure data track the DSV and its progression over the suction surface to about  $\alpha = 20^\circ$ ,  $x/c = 35\%$  for this pitch rate and Reynolds number<sup>39</sup>. Similar descriptions of the flowfield behavior for other pitch rates and Reynolds numbers will be presented in Section 3.2.

The degree of fluctuation in the shear stress data was examined by computing the standard deviations of the sensor output voltages for the ten realizations acquired for each pitch rate and Reynolds number. Examples of the standard deviation histories obtained are shown in Figures 21-24. Figure 21 shows the standard deviation variations during the pitch-up motion at three  $x/c$  locations for  $\alpha^+ = 0.036$ ,  $Re_c = 1.0 \times 10^6$ . Two main features in these variations were identified in each case. At higher  $x/c$  locations, the standard deviation is low initially until a distinct, sharp peak is seen. This is indicated as Sv1 in Figure 21a. At  $x/c$  locations further upchord, this peak occurs at higher angles of attack, indicating upchord propagation during the pitch-up motion. This can be seen by comparing  $x/c$  locations 0.209 (Figure 21c) and 0.029 (Figure 21a). As the leading edge of the airfoil is approached, this peak disappears. For the case shown in Figure 21a, it is no longer seen at  $x/c = 0.014$ . For all cases studied, the standard deviation returns to a low value following Sv1, and it remains low for a range of angles of attack. This range is terminated by an abrupt increase in the standard deviation, indicated as Sv2 in Figure 21a.

Following this abrupt increase, the standard deviation remains at a relatively high value for the rest of the pitching motion. This sudden increase in standard deviation is seen at all sensor locations, and at locations very close to the leading edge, it appears as a sharp peak (see  $x/c = 0.014$  in Figure 21a).

The standard deviation histories were very similar for all pitch rates and Reynolds numbers studied in this work, and they each exhibited these two features. Figure 22 shows the standard deviation histories for the same pitch rate,  $\alpha^+ = 0.036$ , for the highest Reynolds number,  $2.0 \times 10^6$ . This case exhibits the same behavior, but the features are delayed to higher angles of attack. Figure 23 and 24 show the lowest ( $\alpha^+ = 0.010$ ) and highest ( $\alpha^+ = 0.150$ ) pitch rates, respectively, for  $Re_c = 1.0 \times 10^6$ . Again, the same standard deviation features are seen, but the behavior is different as the leading edge is approached. At the lower pitch rate (Fig. 23), Sv1 is not seen at  $x/c$  locations close to the leading edge, and it occurs at earlier angles of attack than for  $\alpha^+ = 0.036$  (Fig. 21). At the higher pitch rate (Fig. 24), both Sv1 and Sv2 are significantly delayed to higher angles of attack, as was seen for the shear-stress features at the same  $\alpha^+$  and  $Re_c$ . Also, close to the leading edge, the standard deviation levels preceding and following Sv1 are higher than in the lower pitch rate/lower Reynolds number cases. It is believed that this is an indication of transition to turbulence in the attached shear layer very close to the leading edge. This will be discussed further in the next chapter.

### 3.2 Behavior of Dominant Flow Features

To help in understanding the sequence of events that occur in the dynamic stall process, the primary features in the shear stress and standard deviation variations were tracked over the airfoil surface during the pitch-up motion for each Reynolds number and pitch rate, as shown earlier for  $\alpha^+ = 0.036$ ,  $Re_c = 1.1 \times 10^5$ . The changes in behavior of these events with changing pitch rate and Reynolds number are summarized in Figures 25-28. Figures 25 and 26 show the location and movement of the dominant features for the cases of  $\alpha^+ = 0.036$ ,  $Re_c = 1.0 \times 10^6$  (Fig. 25) and  $\alpha^+ = 0.036$ ,  $Re_c = 2.0 \times 10^6$  (Fig. 26). These figures map out the location and movement of features F1, F2, F4, and F5 from the shear stress data and features Sv1 and Sv2 from the standard deviation histories. It should be noted



that due to the level of fluctuations in the data, features F1, F5, and Sv2 were the most difficult to pick out of the variations with a high degree of certainty. Therefore, it is estimated that the maximum error associated with the tracking process for these features is approximately  $\pm 2$  degrees. On the other hand, features F2, F4, and Sv1 were very distinct and easier to pick out of the variations. Therefore, the error associated with these features is estimated to be less than 1 degree.

In both Figures 25 and 26, F1 initially appears at low angles of attack near the airfoil leading edge. It moves even closer to the leading edge as the angle of attack increases. At about the same time, F2 appears at the sensor furthest downchord and rapidly moves upchord. This upchord propagation dramatically slows as it approaches the leading edge. Feature Sv1 closely follows the movement of F2, and is offset to a slightly higher angle of attack. The location and movement of Sv1 also corresponded well with shear stress feature F3 (the rise in shear stress following F2), therefore F3 is not shown in these figures. Other researchers<sup>21</sup> attribute a peak in the standard deviation (Sv1) accompanied by a rapid increase in shear stress (F3) to transition to turbulence in the boundary layer above the airfoil surface. However, Sv1 always occurs after F2 (which is a precursor to shear layer lift up due to the approaching reverse flow). It is unclear if a surface hot-film sensor under these conditions can detect transition in the shear layer, which may no longer be in contact with the airfoil surface. We believe that this peak in the standard deviation is an indication of the location of the leading edge of the thin region of reverse-flowing fluid underneath the shear layer. Whether the shear layer undergoes transition at this point is unclear, however other indications of transition in the shear layer will be described later in this discussion.

At an angle of attack shortly after F1 and F2 are no longer seen, Sv2 appears. As shown in both Figures 25 and 26, Sv2 occurs at approximately the same angle of attack for all x/c locations, for a given pitch rate and Reynolds number. It was noticed that as the pitch rate and Reynolds number increased, this feature was delayed to higher angles of attack. However, in all cases, Sv2 preceded all other remaining features seen in the shear stress variations. This suggests that between Sv1 and Sv2, a thin, quiescent reverse-flow region exists above the airfoil surface under the shear layer. This region grows, covering a



larger range of  $x/c$  as the angle of attack increases. Therefore, Sv2, which represents a sudden increase in the standard deviation, indicates the point at which coherent vortical structures begin to form in this reverse-flow region. In Figure 25, at approximately the same angle at which Sv2 is seen, shear stress feature F4 appears between 3 and 4% chord and propagates downchord as the angle of attack increases. This represents the movement of the DSV over the airfoil surface. Also, at angles of attack after the DSV is seen, F5 appears. In Figure 26, which is for a higher Reynolds number, F4 occurs very close to the leading edge at an angle of attack somewhat higher than the angle at which Sv2 appears, and it propagates rapidly downchord. Also, the second and third peaks described earlier (F4a and F4b) first appear further downchord at about the same angle as Sv2. These features also propagate downchord as the angle of attack increases. The major difference between this case and the case at the lower Reynolds number shown in Figure 25 is that the range of angles of attack between Sv1 and Sv2 is smaller for this case. This represents a shorter period of time between the arrival of the flow reversal and the development of vortical structures in the flow. This decrease in range was only seen at the higher pitch rates and Reynolds numbers ( $\alpha^+=0.150$  at  $Re_c=1.0 \times 10^6$ ,  $\alpha^+=0.072$  at  $Re_c=1.5 \times 10^6$ , and  $\alpha^+=0.036$  at  $Re_c=2.0 \times 10^6$ ), and is the result of a delay in shear layer lift-up by the reverse-flow region (delay of F2 and Sv1 to higher angles of attack) for these cases. Reasons for this delay will be discussed in the next chapter.

Figures 27 and 28 show the location and movement of the dominant shear-stress and standard deviation features for the same  $Re_c$  shown in Figure 25 ( $1.0 \times 10^6$ ) for the lowest ( $\alpha^+=0.010$ ) and highest ( $\alpha^+=0.150$ ) pitch rates, respectively. At the lowest pitch rate (Fig. 27), the behavior of each feature is similar to that shown in Figure 25, but all events occur at earlier angles of attack. Figure 28 shows the differences that occur at higher pitch rates and higher Reynolds numbers; a significant delay of all events to higher angles of attack and a decrease in the range of  $\alpha$  between Sv1 (shear layer lift-up) and Sv2 (formation of vortical structures in the flow).

## CHAPTER IV

### PITCH RATE AND REYNOLDS NUMBER EFFECTS

#### 4.1 Effects of Changing Pitch Rate

Figure 29 shows the behavior of F1 (corresponding to the LESP) with varying  $\alpha^+$  for four different Reynolds numbers. For each case, this feature is delayed to higher angles of attack as the pitch rate increases. This is consistent with the expectation that unsteady effects become more pronounced with increasing pitch rate, and delay the evolution of the flow to higher angles of attack. In addition, this feature occurs over the same range of  $x/c$  ( $0 < x/c < 1.5\%$ ) for all pitch rates. These results are consistent with the pressure data of Acharya and Metwally<sup>39</sup> and others.

Figure 30 shows changes in the location and propagation of F2 (the shear-stress minimum related to local flow reversal) with varying  $\alpha^+$  for four different  $Re_c$ . As expected, this feature is delayed to higher angles of attack as the pitch rate is increased for each Reynolds number studied due to the stronger unsteady effects at higher pitch rates. It is interesting to note that this delay is significantly greater at the higher Reynolds numbers (Figures 30c and 30d). Reasons for this behavior will be discussed in the next section. For each pitch rate, this feature moves progressively upchord approaching the leading edge as the angle of attack increases. Also, the propagation speed of this feature increases as the pitch rate increases. (The propagation speed was observed by converting the angle of attack to time for each pitch rate.) This is shown, for example, in Figure 30a for  $Re_c = 1.1 \times 10^5$ . This figure shows the increasing slope of the lines in the range  $0.04 \leq x/c \leq 0.21$ , indicating more rapid upchord propagation. At  $\alpha^+ = 0.15$  in Figure 30a, this feature occurs almost simultaneously over this region of the suction surface. The appearance of this feature is delayed dramatically, however, at  $x/c$  locations closer to the leading edge, indicating a delay in the first occurrence of flow reversal in this region.

In Figure 31, the location of F4 (the shear stress peak associated with the DSV) is plotted against angle of attack for the five pitch rates studied in the present work. Again, four different Reynolds numbers are shown. For all Reynolds numbers, increasing the pitch rate delays F4 to higher angles of attack, as expected. In each case, this feature

moves downchord as angle of attack increases. For Reynolds numbers of  $1.0 \times 10^6$  and lower, this movement is progressively slower with increase in pitch rate. This indicates that as the pitch rate increases, the DSV remains bound to the airfoil surface over a larger range of  $\alpha$  for lower Reynolds numbers. Also, for Reynolds numbers less than  $1.0 \times 10^6$ , F4 first appears at lower  $x/c$  locations (closer to the leading edge) as the pitch rate increases. At the highest two Reynolds numbers ( $1.5 \times 10^6$  and  $2.0 \times 10^6$ ), this was not apparent, as seen in Figure 31d. By converting the angle of attack to time, the propagation speed of F4 appeared to remain the same for the entire range of pitch rates at a given Reynolds number. At the low pitch rates, the propagation speed appeared to remain the same for all Reynolds numbers. However at the higher pitch rates, the propagation speed appeared to slightly decrease at the lowest Reynolds numbers.

#### 4.2 Effects of Changing Reynolds Number

As mentioned in the objectives of this work, the main interest is how increasing Reynolds number effects the development of the flow field. Some interesting changes in the flow features were seen at the higher Reynolds numbers studied in this investigation. The following figures will illustrate these changes. Figure 32 shows the location and movement of shear stress feature F1 at three different pitch rates; the lowest pitch rate studied ( $\alpha^+ = 0.010$ , Fig. 32a), a moderate pitch rate ( $\alpha^+ = 0.036$ , Fig. 32b), and the highest pitch rate studied ( $\alpha^+ = 0.150$ , Fig. 32c). For the lower two pitch rates, the tracking of this feature is shown at seven chord Reynolds numbers. For the highest pitch rate, only five Reynolds numbers were studied, as mentioned earlier. These figures show that this feature is delayed to higher angles of attack as the chord Reynolds number increases, and, over the range of Reynolds numbers studied in the present work, this feature occurs over the same range of  $x/c$ . At the lower pitch rates, however, the delay to higher angles of attack is not as pronounced.

Figure 33 shows the location and movement of shear stress feature F2 at the same three pitch rates. Figure 33a shows that at the lowest pitch rate, F2 appears at about the same angle of attack for all seven Reynolds numbers. Also, the region of accumulation of this fluid is pushed to  $x/c$  locations closer to the leading edge as  $Re_c$  increases, as

indicated by the point at which the upchord movement of F2 begins to slow. This indicates the quasi-steady behavior observed by other researchers<sup>5,39</sup> at low pitch rates. At low pitch rates, the unsteady effects are weaker, events occur at lower angles of attack, and the process is less sensitive to transition in the shear layer. Acharya and Metwally<sup>39</sup> found that the dynamic stall process was insensitive to Reynolds number for the low range of Reynolds numbers they investigated. Figure 33a shows that at low pitch rates, the process remains Reynolds number independent. As the pitch rate increases, however, as shown in Figures 33b and 33c, this Reynolds number independence is not maintained. At these higher pitch rates, F2 is clearly delayed to higher angles of attack at the higher Reynolds numbers. In Figure 33b ( $\alpha^+ = 0.036$ ), the behavior of F2 is independent of Reynolds number for  $Re_c < 1.5 \times 10^6$ , while at  $\alpha^+ = 0.150$  (Fig. 33c), it remains independent of Reynolds number for  $Re_c < 0.5 \times 10^6$ . This indicates that at higher Reynolds numbers and pitch rates, shear layer lift-up (reverse-flow initiation) occurs later. At higher pitch rates, unsteady effects are greater, and the unsteady separation process is more sensitive to transition in the shear layer. At the higher Reynolds numbers, transition occurs in the shear layer before the reverse-flow region causes the shear layer to lift away from the surface. Therefore, there is more energy in the shear layer and it resists lifting away from the surface. This is what causes the delay of F2 to higher angles of attack at the higher pitch rates and Reynolds numbers. Further substantiation of this result can be seen by examining the standard deviation histories at angles of attack before Sv1 is seen. While no other distinct standard deviation peak is seen, the overall standard deviation levels at low angles of attack appear slightly higher at x/c locations near the first appearance of Sv1 for the highest pitch rates at each Reynolds number ( $\alpha^+ = 0.150$  at  $Re_c = 0.5 \times 10^6$ ,  $\alpha^+ = 0.072$  and  $0.150$  at  $Re_c = 1.0 \times 10^6$ ,  $\alpha^+ = 0.072$  at  $Re_c = 1.5 \times 10^6$ , and  $\alpha^+ = 0.018$  and  $0.036$  at  $Re_c = 2.0 \times 10^6$ ). An example of this was previously shown in Figure 24a, which shows the standard deviation histories for  $\alpha^+ = 0.150$  and  $Re_c = 1.0 \times 10^6$  in the leading edge region. Here, there is a notable increase in the standard deviation at low angles of attack for x/c locations between 0.008 and 0.029. This may be an indication that the shear layer undergoes transition before it lifts away from the surface for these cases.

Recent work by other researchers seems to indicate that the local flow reversal under the shear layer near the leading edge of the airfoil may occur at slightly earlier angles of attack as the Reynolds number increases for lower Reynolds numbers. Computations performed by Okong'o and Knight<sup>29</sup> support these observations. Similar trends with pitch rate and Reynolds number were also seen by Schreck, et al.<sup>21</sup> The behavior of F2, which is related to this flow reversal event, shown in Figure 33 shows very little variation in angle of attack with Reynolds number for lower Reynolds numbers, but it is possible that F2 occurs at slightly earlier angles of attack with increasing Reynolds number at low pitch rates, as shown in Figure 33a.

Figure 34 shows how the location and movement of shear stress feature F4 changes with increasing Reynolds number for the same three pitch rates. For each pitch rate, F4 is delayed to higher angles of attack with increasing Reynolds number for low Reynolds numbers. Figure 34c shows that this same trend continues at the higher Reynolds numbers for  $\alpha^+ = 0.150$ , but Figures 34a and 34b indicate that this trend does not hold at higher Reynolds numbers for the lower pitch rates. In Figure 34a, where  $\alpha^+ = 0.010$ , and Figure 34b, where  $\alpha^+ = 0.036$ , F4 is delayed to higher angles of attack for all Reynolds numbers except  $2.0 \times 10^6$ . For this Reynolds number, F4 actually occurs at an earlier angle of attack. Also, at the two highest Reynolds numbers, F4 first appears very close to the leading edge, and the magnitude of this peak in the shear stress variations was noticeably smaller than at the other Reynolds numbers. Again, this may be due to the quasi-steady nature of the flow at these low pitch rates. This may indicate that at these low pitch rates and high Reynolds numbers, a well-defined DSV does not form above the airfoil surface. Instead, the shear layer undergoes unsteady separation and vortical structures are formed which do not coalesce into a coherent DSV. This may also explain the presence of the second and third shear stress peaks (F4a and F4b) seen for certain cases. This will to be investigated further by examining the unsteady surface pressure results. For all pitch rates, F4 first appeared closer to the leading edge as  $Re_c$  increased, and for a given pitch rate, it was present above the airfoil surface for approximately the same range of angles of attack for all  $Re_c$ . Also, the propagation velocity remains

relatively unchanged for the range of  $Re_c$  examined. This indicates that the propagation velocity of the DSV is a stronger function of pitch rate than  $Re_c$ .

Figures 35-40 show surface pressure coefficient distributions on the suction surface of the airfoil for various angles of attack during the pitching motion. Figures 35 and 36 show pressure distributions for the highest pitch rate,  $\alpha^+ = 0.150$  for two Reynolds numbers,  $0.5 \times 10^6$  and  $1.0 \times 10^6$ . These high pitch rate cases show distributions that are very similar to those described by Metwally<sup>7</sup>. The lower Reynolds number case shown in Figure 35 exhibits the features shown in Figure 19, the LESP, CPP and DSVP. These features develop early in the pitch-up motion (low angles of attack). At the higher Reynolds number, shown in Figure 36, these events are harder to see and occur much later in the pitch-up motion (higher angles of attack). Figures 37 and 38 show pressure distributions at the same two Reynolds numbers for  $\alpha^+ = 0.036$ . At this lower pitch rate, the pressure distributions are similar to those at  $\alpha^+ = 0.150$ . For both Reynolds numbers, however, the events occur at earlier angles of attack at this lower pitch rate. This is clearly seen by comparing Figures 36 and 38, which are both at  $Re_c = 1.0 \times 10^6$ . These results are consistent with the high pitch rate, low Reynolds number behavior described by Metwally<sup>7</sup>. Significant differences are seen, however, at the lowest pitch rate,  $\alpha^+ = 0.010$ , shown for the same two Reynolds numbers in Figures 39 and 40. For these cases, the unsteady separation events occur very early in the pitch-up motion, and a clear DSVP is not seen. This supports the previous discussion about the behavior of shear stress Feature 4 at low pitch rates and high Reynolds numbers.

#### 4.3 Discussion of Results

The major changes seen in the shear stress behavior resulting from variation of the pitch rate and Reynolds number can be described by examining the normalized shear-stress variations with angle of attack at four of the chord Reynolds numbers examined, for three non-dimensional pitch rates ( $\alpha^+ = 0.010$ ,  $0.036$ , and  $0.150$ ) at a chordwise location in the region of the surface where the DSV forms. The data shown in Figure 41 are at  $x/c = 10\%$ . At  $\alpha^+ = 0.010$  (Figure 41a), a large region of elevated shear stress (F3) follows a shear stress minimum (F2) at all four Reynolds numbers. As  $Re_c$  increases, the

relatively unchanged for the range of  $Re_c$  examined. This indicates that the propagation velocity of the DSV is a stronger function of pitch rate than  $Re_c$ .

Figures 35-40 show surface pressure coefficient distributions on the suction surface of the airfoil for various angles of attack during the pitching motion. Figures 35 and 36 show pressure distributions for the highest pitch rate,  $\alpha^+ = 0.150$  for two Reynolds numbers,  $0.5 \times 10^6$  and  $1.0 \times 10^6$ . These high pitch rate cases show distributions that are very similar to those described by Metwally<sup>7</sup>. The lower Reynolds number case shown in Figure 35 exhibits the features shown in Figure 19, the LESP, CPP and DSVP. These features develop early in the pitch-up motion (low angles of attack). At the higher Reynolds number, shown in Figure 36, these events are harder to see and occur much later in the pitch-up motion (higher angles of attack). Figures 37 and 38 show pressure distributions at the same two Reynolds numbers for  $\alpha^+ = 0.036$ . At this lower pitch rate, the pressure distributions are similar to those at  $\alpha^+ = 0.150$ . For both Reynolds numbers, however, the events occur at earlier angles of attack at this lower pitch rate. This is clearly seen by comparing Figures 36 and 38, which are both at  $Re_c = 1.0 \times 10^6$ . These results are consistent with the high pitch rate, low Reynolds number behavior described by Metwally<sup>7</sup>. Significant differences are seen, however, at the lowest pitch rate,  $\alpha^+ = 0.010$ , shown for the same two Reynolds numbers in Figures 39 and 40. For these cases, the unsteady separation events occur very early in the pitch-up motion, and a clear DSVP is not seen. This supports the previous discussion about the behavior of shear stress Feature 4 at low pitch rates and high Reynolds numbers.

#### 4.3 Discussion of Results

The major changes seen in the shear stress behavior resulting from variation of the pitch rate and Reynolds number can be described by examining the normalized shear-stress variations with angle of attack at four of the chord Reynolds numbers examined, for three non-dimensional pitch rates ( $\alpha^+ = 0.010, 0.036, \text{ and } 0.150$ ) at a chordwise location in the region of the surface where the DSV forms. The data shown in Figure 41 are at  $x/c = 10\%$ . At  $\alpha^+ = 0.010$  (Figure 41a), a large region of elevated shear stress (F3) follows a shear stress minimum (F2) at all four Reynolds numbers. As  $Re_c$  increases, the



minimum occurs at lower angles of attack and the region of elevated shear stress spreads over a larger range of  $\alpha$ , after which the flow over the airfoil becomes fully stalled. The shear stress peak associated with the DSV (F4) is not seen at all at the lowest value of  $Re_c$ , and is barely distinguishable at  $Re_c = 4.6 \times 10^6$ . At  $Re_c = 1.0 \times 10^6$ , F4 is a distinct peak, while at the highest Reynolds number,  $2.0 \times 10^6$ , it becomes difficult to see at this low pitch rate. This corresponds well with previous work<sup>5,39</sup> which show that as pitch rate decreases, the unsteady effects become weaker, the DSV is less coherent and identifiable, and convects downstream soon after its formation. As discussed in the previous section, at very low pitch rates and Reynolds numbers, the DSV may not even form above the suction surface of the airfoil. Figure 41b, where  $\alpha^+ = 0.036$ , shows large differences in the shear-stress variations with increasing  $Re_c$ . At  $Re_c = 1.1 \times 10^5$ , F4 is just beginning to emerge from F3, while at the three higher Reynolds numbers, F4 is more easily distinguished. Again, as Reynolds number increases, F4 is delayed to higher angles of attack, as is the onset of a fully stalled state. However, at this pitch rate, a change in the behavior of F2 is seen. For the lower two Reynolds numbers, F2 occurs at this location at lower angles of attack as  $Re_c$  increases, but at the higher two Reynolds numbers, F2 is significantly delayed to higher angles of attack. As mentioned in the previous section, it is believed that this is caused by transition to turbulence in the attached shear layer before the local reverse-flowing fluid accumulating under it lifts it away from the surface. This moderate pitch rate represents a transition of the unsteady flow development over this range of  $Re_c$  from that characteristic of low pitch rates to behavior seen at high pitch rates. In Figure 41c, where  $\alpha^+ = 0.150$ , F4 is well defined and occurs at higher angles of attack as  $Re_c$  increases. At the lower Reynolds number, F3 appears as a small shear stress peak, while at the two higher Reynolds numbers, it appears as a plateau extending from an angle just after the shear-stress minimum (F2) to an angle just prior to F4. As stated earlier, this feature is believed to correspond to events occurring underneath the shear layer prior to the formation of the DSV. Prior work<sup>5,39</sup> has shown that as the pitch rate increases, the formation of the DSV is delayed to higher angles of attack. This high pitch rate behavior results in the spreading of F3 over a larger range of  $\alpha$ . Another characteristic of high pitch rate behavior seen in Figure 41c is the delay of the fully



stalled state to much higher angles of attack. Again, at the higher Reynolds number,  $Re_c = 1.0 \times 10^5$  in this case, F2 is significantly delayed to a higher angle of attack due to transition in the shear layer before lift-up. Changes in  $\alpha^+$  and  $Re_c$  do not significantly affect the behavior of F1.

## CHAPTER V

### CONCLUSIONS AND RECOMMENDATIONS, PART A

#### 5.1 Conclusions

A NACA 0012 airfoil model was instrumented with an array of 50 hot-film sensors, each connected to a constant-voltage anemometer, in order to obtain wall shear stress information as the airfoil was pitched up from  $\alpha = 0^\circ$  to  $\alpha = 45^\circ$  at a constant rate. The voltage output of each anemometer was related to shear stress without calibration of the sensors. It is believed that this approach provides an accurate description of the changes in shear stress and shows trends in the flow behavior. Dominant features in the shear-stress data and in the standard deviation histories calculated from this data were identified and related to key events in the evolution of the unsteady separation on the suction surface of the airfoil. Significant differences were seen as the chord Reynolds number was increased to  $2.0 \times 10^6$ .

To summarize these results, a shear-stress peak that corresponded with the leading-edge suction peak (LESP) in the pressure measurements developed very early during the pitch-up motion at  $x/c$  locations very close to the leading edge of the airfoil. This peak propagated upchord as  $\alpha$  increased and was delayed to higher  $\alpha$  as  $\alpha^+$  and  $Re_c$  increased. Slightly later in the pitch-up motion, a shear stress minimum was seen around 20% of chord that also moved upchord on the airfoil surface as  $\alpha$  increased. It is believed that this minimum is related to the local flow reversal which occurs underneath the shear layer and is responsible for shear layer lift-up prior to DSV formation. This minimum occurred at higher  $\alpha$  as  $\alpha^+$  increased, and it occurred at slightly lower  $\alpha$  as  $Re_c$  increased. The minimum was followed by a rapid rise in the shear stress and a region of elevated shear stress. This region appeared as a peak at lower  $\alpha^+$  and  $Re_c$ , and as a plateau at higher  $\alpha^+$  and  $Re_c$ . This feature is related to events underneath the shear layer after it has lifted up and before DSV formation. A sharp shear-stress peak was seen to emerge from this region of elevated shear stress. This peak is related to the fully formed DSV, and was seen to propagate downchord as  $\alpha$  increased. As  $\alpha^+$  increased, this peak was delayed to higher  $\alpha$  and its propagation slowed. It was also delayed to higher  $\alpha$  as  $Re_c$  increased.

The first significant feature seen in the shear-stress data is a minimum (F2), which occurs downchord at low angles of attack and rapidly moves upchord as the angle of attack increases. As it approaches the leading edge, its movement dramatically slows. This shear-stress minimum is followed closely by a distinct peak in the standard deviation (Sv1). The occurrence of these two features at a particular x/c location indicates the arrival of a thin region of reverse-flowing fluid above the airfoil surface at that location. This reverse-flow region causes the shear layer to lift away from the surface. It is not believed that the standard deviation peak (Sv1) is an indication of transition in the shear layer, as reported by other researchers. At low pitch rates, the location and movement of F2 was independent of Reynolds number, indicating quasi-steady behavior. At higher pitch rates, this feature was clearly delayed to higher angles of attack at higher Reynolds numbers. This delay may be caused by the occurrence of transition in the shear layer before the arrival of the reverse flow.

The second key shear-stress feature is a distinct peak (F4), which occurs at low x/c locations at a certain angle of attack and propagates downchord as the angle of attack increases. The angle at which this feature first appears follows an abrupt increase in the standard deviation (Sv2), and this angle occurs shortly after the disappearance of F2 and Sv1. At higher pitch rates and lower Reynolds numbers, this peak corresponds to the presence of the DSV above the surface of the airfoil. At low pitch rates and high Reynolds numbers, however, there are indications that a well-defined DSV does not form, and this peak, along with other shear stress features seen downchord of F4 at slightly earlier angles of attack, correspond to vortical structures which form after the unsteady separation. Examination of unsteady pressure results helps substantiate this result.

## 5.2 Recommendations

The results of this study provide a better understanding of the flowfield development over a pitching airfoil at higher Reynolds numbers, however further studies are suggested to gain a deeper understanding and confirm the interpretation of the results presented here. These include:

- Measurement of near-wall flow direction in the leading-edge region using the 'thermal tuft' technique or another suitable technique. This will help pinpoint the location of local flow reversal on the airfoil suction surface.
- Further investigation of the role played by transition to turbulence by using leading-edge boundary layer trips to force transition in the shear layer prior to lift-up and roll-up into the dynamic-stall vortex.
- Investigation of length-scale effects by using airfoil models with different chord lengths to produce different flow conditions in the leading-edge region for the same chord Reynolds number. This will provide a better understanding of the observed Reynolds number effects and help determine if the chord is the appropriate length scale for the dynamic stall events.

Another recommended extension of this work is to use the results of this study to develop a feedback control system for suppressing or delaying the formation of the dynamic stall vortex. The flow features identified in this study and the shear-stress sensors used could be implemented in a variety of different flow control systems, such as those used by Karim<sup>12</sup>, Alrefai<sup>35</sup>, and Kawthar-Ali<sup>36</sup>. Sensors of this type could be used to trigger the flow control mechanism and could provide feedback about the effectiveness of the applied control. The high spacial resolution of these sensors provides detailed information about the flow state, allowing more precise control timing and more efficient control implementation.

## **PART B**

## CHAPTER VI

### SURFACE PRESSURE RESULTS

#### 6.1 Steady Surface Pressure

The static pressure distribution has been documented by many experimentalists<sup>7,54</sup> and others with the airfoil held steady at various angles of attack in order to establish a base line to be used for comparison to the unsteady pressure measurements. Metwally<sup>7</sup> in 1990 and Karim<sup>12</sup> in 1992, included flow visualization in an attempt to further understand the various features.

The dimensionless pressure coefficient ( $C_p$ ) is used for both steady and unsteady pressure distributions. At  $0^\circ$  angle of attack, the flow above the airfoil is fully attached with no evidence of separation. Characteristic of the flow at  $0^\circ$  angle of attack is the acceleration of the flow around the nose of the airfoil from the stagnation point at  $x/c=0$  to a maximum velocity at about  $x/c = 0.025$ . This property is very commonly used to verify the alignment of symmetric airfoils inside the tunnels. Increasing the angle of attack to  $5^\circ$  generates a suction peak near the leading edge due to the highly accelerated flow around the nose of the airfoil. This peak increases in magnitude with increasing angle of attack. Downstream of this suction peak, the adverse pressure gradient also increases causing a rapid pressure recovery. Detailed visualization photographs<sup>7</sup> indicate attached flow until  $13^\circ$  for a Reynolds number of  $1.2 \times 10^5$ . For angles of attack greater than  $5^\circ$  but less than the stall angle  $13^\circ$ , the pressure distribution is characterized by the presence of a separation bubble defined by the extent of a constant pressure region. Downstream of this region a sharp pressure rise followed with a pressure recovery to the pressure levels of  $0^\circ$ . At these angles of attack, the boundary layer encounters an adverse pressure gradient of sufficient magnitude to cause separation close to the leading edge. Downstream of this location, the resultant shear layer undergoes transition to turbulent and reattaches, thus, forming the separation bubble<sup>7,55</sup>. Flow visualization by Metwally, Karim and others shows that the turbulent boundary layer moves upchord as a result of the increase in the adverse pressure gradient. In addition, it was found that the extent of the constant pressure region decreases, moving closer to the leading edge for increasing the angles of attack prior to stall. At angles past the stall angle of  $13^\circ$ , a flattening of the

pressure distribution above the surface of the airfoil was detected. This is an indication of complete separation above the airfoil. Visualization records by Karim and Metwally indicate separated flow over the entire airfoil.

## 6.2 Unsteady Surface Pressure Data

The unsteady evolution of the pressure field above an oscillating airfoil was investigated in detail for the range of parameters tested (Section 2.6). In Figures 42-53, the dimensionless pressure coefficient is plotted against the dimensionless position along the chord of the airfoil ( $x/c$ ). In addition, the data presented are assembled averages of ten oscillations, where the first two oscillations were dropped to minimize transient effects until 'steady' oscillating conditions were reached. The quality of the data was extremely good with minimum hysteresis effects up to a Reynolds number of  $5.0 \times 10^5$ . The data presented in Figures 42-53 are used to represent unsteady pressure distributions with increasing angle (a) upstroke and decreasing angle (b) downstroke.

The main features in the unsteady pressure flow field above the oscillating airfoil were the Leading Edge Suction Peak (LESP), the Constant Pressure Plateau (CPP), and the Dynamic Stall Vortex Peak (DSVP) during the upward profile motion (Figure 42a). In addition, the LESP followed by the CPP were also formed during the downstroke portion of the cycle (Figure 42b). These features in combination with the Hot-Film shear data were used to identify and explain some of the essential features in the formation and evolution of the dynamic stall vortex.

LESP is associated with the acceleration of the flow over the nose of the airfoil during pitch up. It forms in the first 5% chord of the airfoil quickly moving to within 1% chord with increasing incidence past  $10^\circ$ . In addition, the maximum magnitude of the LESP followed by recovery of the pressure levels were delayed with increasing Reynolds number as well as with increasing reduced frequency. A secondary parameter in the maximum levels of LESP was the amplitude of oscillation. It was the dominant parameter at low reduced frequencies of  $k = 0.1$ . The mean angle effects appeared to influence the maximum LESP levels and time (angle of attack), only at the highest reduced frequency of  $k = 0.4$ .

In detail, the max LESP for  $Re_c 1.1 \times 10^5$ ,  $k = 0.1$  occurs at  $14^\circ$ ,  $x/c = 0.008$  for an amplitude of  $10^\circ$ , while a delay of three degrees was obtained with an increase in amplitude to  $20^\circ$ . Similar delays are recorded for Reynolds number of  $3.2 \times 10^5$ ,  $k = 0.1$  where max LESP occurs at  $17^\circ$ ,  $x/c = 0.008$  for  $10^\circ$  amplitude, delayed to  $20^\circ$ ,  $x/c = 0.008$  for an amplitude of  $20^\circ$ . The next two Reynolds numbers tested yielded the same position and incidence angle, as they should, although there was a small increase in the Reynolds number from  $4.6$  to  $5.0 \times 10^5$ . The main difference between the two was the fact that they were achieved in two different experimental facilities discussed in Chapter 2. Maximum value for LESP was achieved at  $18^\circ$  for an amplitude of  $10^\circ$  at  $x/c = 0.008$  and  $22^\circ$  for an amplitude of  $20^\circ$  at the same  $x/c$  location. The dominance of the amplitude of oscillation over the range of Reynolds number tested for reduced frequency of  $k = 0.1$  was stunning. Increasing the reduced frequency to  $k = 0.4$  allowed the effects of the mean angle to become more obvious in the development of this feature. For a Reynolds number of  $1.1 \times 10^5$ ,  $k = 0.4$ , the location of LESP max were:  $19^\circ$  at  $x/c = 0.008$  for  $\alpha_o = 10^\circ$   $\alpha_m = 10^\circ$ ,  $25^\circ$  at  $x/c = 0.000$  for  $\alpha_o = 20^\circ$   $\alpha_m = 10^\circ$ ,  $28^\circ$  at  $x/c = 0.000$  for  $\alpha_o = 10^\circ$   $\alpha_m = 20^\circ$ , and  $32^\circ$  at  $x/c = 0.000$  for  $\alpha_o = 20^\circ$   $\alpha_m = 20^\circ$ . The results presented above have also been tabulated in Table 5. It should also be noted that there is a strong relation between the incidence angle, the maximum LESP, and the DSV. The delays in the maximum levels of LESP indicate a delay in the movement of the DSV.

The second region of interest following the LESP is the CPP. This region is associated with the accumulation of vorticity generated and determines the extent of the recirculation zone (CPP) prior to the formation of the DSV. After the DSV forms, the CPP region behaves in one of two fashions. First, increasing the Reynolds number for low reduced frequencies causes the CPP levels to increase until it is no longer distinguishable from the LESP. The only indication of the DSV is the change in the adverse pressure gradient indicating the convection of the vortex downstream. As the airfoil progresses in motion, the pressure distribution spreads rapidly along the surface of the airfoil resulting in growth and subsequent detachment of the dynamic stall vortex (Figure 53a).



At high reduced frequencies of  $k = 0.4$  the CPP levels increase in magnitude with increasing angle of attack, changing into the DSVP or 'valley' before reaching the same pressure levels of the LESP. The DSVP indicates a well-developed vortex above the surface of the airfoil coexisting with the LESP. The DSV remains close to the leading nose of the airfoil until the LESP pressure levels start to decrease. At that instance, the DSV begins to grow in extent shown in Figure 49a evidenced by the broadening of the surface pressure curvature and movement of the DSVP.

Figures 42-45 show selected pressure distributions above the surface for  $Re_c$  of  $1.1 \times 10^5$ ,  $k = 0.1$  and combinations of mean angles and amplitudes. For  $\alpha_o = 10^\circ$  and  $\alpha_m = 10^\circ$  (Figure 42), the DSV becomes noticeable at  $14^\circ$  for  $x/c = 0.75$  at the end of the CPP region the instant the maximum LESP level has being reached. The pressure levels afterward quickly recover as the vortex extends to over 40% chord at  $18^\circ$  prior to stall. Increasing the amplitude to  $20^\circ$  delays the onset of DSV to  $17^\circ$  at  $x/c = 0.075$  with the vortex quickly moving to about 30% chord where a deep valley forms. Further increase in the angle of attack moves the vortex to over 50% chord at  $28^\circ$ . The increase of the mean angle to  $20^\circ$  for an amplitude of  $10^\circ$  does not change the onset of the DSV which remains at  $14^\circ$  with subsequent growth leading to complete stall at  $23^\circ$  and 40% chord. The increase of both mean angle and amplitude to  $20^\circ$  again does not affect the starting location and time (angle) of the DSV. The DSV grows rapidly to about 30% chord where a very well defined valley is formed (DSVP) followed by stall (separation) at about 35 to  $36^\circ$  and 50% chord Figure 10. The ability of the DSV to remain attached to the surface of the airfoil for higher angles of attack with increasing amplitude is attributed to the additional vorticity generated by the larger amplitude oscillations (Chandrasekhara and Brydges<sup>23</sup>).

**6.2.1 Frequency Effects.** Increasing the reduced frequency to 0.4 for the same  $Re_c$  of  $1.1 \times 10^5$  shown in Figures 46-49 effectively prevented separation or stall over the airfoil. The DSV remained above the surface of the airfoil within 30% chord in all cases studied, while the DSV was also seen on the downstroke of the airfoil pressure distributions and was pushed quickly downstream with decreasing angle of attack. In

addition, the effects of mean angle of attack appeared to influence the development and evolution of the DSV, breaking the dominance of amplitude.

In particular, for  $Re_c$  of  $1.1 \times 10^5$ ,  $k = 0.4$ ,  $\alpha_o = 10^\circ$  and  $\alpha_m = 10^\circ$  shown in Figure 46a, the LESP pressure levels were increasing up to the maximum angle of attack allowed by the cycle, while the vortex remained in the leading edge of the airfoil within 20% chord. Looking at the downstroke portion of the cycle Figure 46b, the DSV was located at about 25% chord, being pushed quickly downstream into the flow with decreasing angle of attack. Complete pressure recovery was delayed until  $2^\circ$ .

Increasing the amplitude to  $20^\circ$  (Figure 47a), moves the CPP region closer to the leading edge. The DSV remained within 22% chord until the maximum angle of attack  $30^\circ$  was reached. The onset of the downstroke portion of the cycle found the DSV where it was left about 23% chord. Decreasing the angle of attack pushed the DSV into the flow and downstream.

In Figure 48a the unsteady pressure flow field above the surface of the airfoil for  $Re_c = 1.1 \times 10^5$ ,  $k = 0.4$ ,  $\alpha_o = 20^\circ$ , and  $\alpha_m = 10^\circ$  is shown. LESP reached a maximum at  $25^\circ$  indicating the start of the DSV movement. The DSV forms at about  $x/c = 0.075$  where it grows in strength until it starts moving downchord with increasing angle of attack after the LESP reached a maximum. The DSV at the end of the upstroke had moved to about 25% chord. On the downstroke Figure 48b, the location of the DSV appears to be about 30% chord at  $28^\circ$ , being pushed quickly into the flow field with decreasing angle of attack.

Figure 49a depicts the behavior of the pressure evolution for  $Re_c = 1.1 \times 10^5$ ,  $k = 0.4$ ,  $\alpha_o = 20^\circ$ , and  $\alpha_m = 20^\circ$ , over the surface of the airfoil during the upstroke of the motion profile. The CPP region slowly curves into the DSV at about  $23^\circ$  and  $x/c = 0.60$ . It remains at that location and grows in size and magnitude until the maximum LESP value is reached at which point it starts moving slowly downstream. The maximum DSV value is reached at 14% chord and  $35^\circ$  expanding quickly afterwards. At the end of the upstroke, the DSV was located at about 30% chord. Figure 49b verifies the location of the DSV in the downstroke portion of the cycle at about 35% chord pushed quickly into the flow stream with decreasing angle.

6.2.2. Reynolds Numbers Effects. Increasing the Reynolds number from  $1.1 \times 10^5$  to  $3.2 \times 10^5$ ,  $4.6 \times 10^5$ ,  $5.0 \times 10^5$  at  $k = 0.1$ , allows the investigation of Reynolds number effects on the pressure flow distribution above the airfoil. With increasing Reynolds number, a delay in the maximum LESP levels was detected leading to a delay in the DSV convection downstream. However, once the maximum LESP pressure was reached initiating the movement of the DSV, the vortex moved quickly downstream leading to stall conditions. The DSVP valley was hardly detectable for the  $Re_c$  of  $3.2 \times 10^5$  at the amplitude of  $20^\circ$ , while there was no indication for the two higher Reynolds numbers at all. The signature of the DSV moving was detected by the widening of the pressure field with increasing incidence.

Figure 50a, shows the pressure distribution for selected angles over the surface of the airfoil for  $Re_c = 4.6 \times 10^5$ ,  $k = 0.1$ ,  $\alpha_o = 10^\circ$ , and  $\alpha_m = 10^\circ$ . The pressure coefficient increased in magnitude until the maximum LESP level was reached followed by stall at  $19^\circ$  over the whole airfoil length. The DSV once released at the end of the CPP region travels very quickly downstream leading to stall conditions. Figure 50b, depicts the flow above the surface for the downstroke portion of the motion profile with LESP forming in a similar fashion in the first 3% chord of the airfoil and the CPP region closely afterwards. The formation of a recirculation zone (CPP) on the downstroke of the cycle influences the reattachment of the boundary layer seen more clearly in the shear data.

Figure 51a, depicts the pressure distribution for  $Re_c = 4.6 \times 10^5$ ,  $k = 0.1$ ,  $\alpha_o = 10^\circ$ , and  $\alpha_m = 20^\circ$ . There is a progressive increase in  $C_p$  values until  $22^\circ$ , followed by a decrease in the pressure levels indicating movement of the DSV together with a widening in the pressure field. The shape of the pressure distribution shown in Figure 51b indicates the recovery of pressure with decreasing angle of attack. At about  $10^\circ$ , LESP is detected followed by the formation of the CPP region in the first 10% chord indicating the onset of reattachment.

Figure 52a, shows the pressure distribution for  $Re_c = 4.6 \times 10^5$ ,  $k = 0.1$ ,  $\alpha_o = 20^\circ$ , and  $\alpha_m = 10^\circ$ . The LESP and CPP regions grow in magnitude until they reach a maximum at  $18^\circ$ , followed by steady pressure recovery and convection of the DSV downstream. The pressure distribution approaches stall conditions at the end of the

motion profile  $28^\circ$ . During the downstroke of the cycle, the pressure levels were gradually decreasing with an indication of CPP region formation at about  $12^\circ$ .

Figure 53a, shows the pressure distribution for  $Re_c = 4.6 \times 10^5$ ,  $k = 0.1$ ,  $\alpha_o = 20^\circ$ , and  $\alpha_m = 20^\circ$ . The LESP grows in magnitude until it reaches a maximum at  $23^\circ$  followed by a gradual decrease in the pressure levels. The increase in amplitude to  $20^\circ$  delays the release of the DSV to higher angles of attack. Stall conditions were detected at the end of the motion  $37^\circ$ . On the downstroke of the motion profile, the pressure field indicated stall conditions slowly decreasing in magnitude until around  $10^\circ$  when LESP followed by the CPP region formed indicating the reattachment process of the boundary layer on the surface of the airfoil.

In summary, the features identified above provide valuable information in the development and evolution of the unsteady flow field over the airfoil. The maximum LESP indicates the onset of movement of the DSV while the widening of the pressure field at the end of the CPP region indicates the movement of the DSV. The DSVP indicating the location of the DSV above the surface of the airfoil was clearly identified in the low Reynolds number for all reduced frequencies tested, while increasing the Reynolds number at the reduced frequency tested prevented the formation of DSVP. In addition, the CPP region shrank with increasing Reynolds number, while the DSV formed closer to the leading edge of the airfoil. The absence of the DSVP with increasing Reynolds number indicated the downstream movement of the DSV at higher rates. Also, increasing the amplitude of oscillation added additional vorticity into the flow, further delaying the maximum LESP level to higher angles of attack. In addition, amplitude effects dominated over mean angle effects across the Reynolds number tested for the low frequency of 0.1.

Increasing the reduced frequency delayed the formation of the DSV to higher angles of attack in addition to the delay in the onset of movement indicated by the maximum levels of LESP. However, increasing the reduced frequency allowed the mean angle effects to become more pronounced, breaking the dominance of amplitude effects on the unsteady pressure field. The formation of the DSV and its location indicated by the DSVP are very well pronounced in the unsteady pressure distributions. Increasing the reduced frequency substantially delayed the convection of the DSV downchord, while at

the highest reduced frequency of  $k = 0.4$ , the DSV was located above the surface of the airfoil within 30% chord from the leading edge even during the initial part of the downstroke portion of the cycle.

The reattachment process was indicated by the formation of the CPP region on the downstroke portion of the cycle around the static stall angle of 13 degrees, while complete reattachment was achieved at around 6-5 degrees shown by the disappearance of the CPP region. At the highest reduced frequency tested  $k = 0.4$ , the presence of the DSV above the surface of the airfoil during the downstroke greatly affected the pressure distribution, delaying or even preventing the reattachment process until smaller angles of attack or even 0 degrees incidence.

## CHAPTER VII

### HOT-FILM SHEAR STRESS RESULTS

#### 7.1 Unsteady Hot-Film Surface Data

Typical normalized output voltages of the hot film sensors used in the present work is shown in Figures 54-57 for different combinations of mean angle and amplitudes. In these figures, the normalized voltages are presented instead of the shear stress levels to provide a better picture of some of the features associated with the unsteady evolution above an oscillating airfoil. The abscissa in these figures represents the instantaneous output voltage obtained during the oscillating cycle normalized by the output voltage at  $0^\circ$  angle of attack for each  $x/c$  location. The data presented are normalized ensemble averages of ten oscillations, from which the first two oscillations were dropped to minimize transient effects as done for the unsteady pressure case. Parts a, b, and c, of Figure 54 illustrate typical characteristics (features) at different chordwise locations during the upstroke portion of the motion profile, while parts d, e, and f demonstrate the behavior of the same  $x/c$  locations during the downstroke portion of an oscillating cycle.

Figure 54c shows the voltage variation (shear-stress) at four chordwise locations close to the leading edge of the airfoil (less than 3% chord). For  $x/c = 0.03$ , the shear stress level increases to a maximum at  $13^\circ$ , quickly decreasing afterwards. This shear rise will be identified as Feature 1 (F1) hereafter. F1 is associated with the acceleration of the flow around the leading edge of the airfoil and is related to the LESP discussed in the pressure data.

Figures 54a, and b show selected  $x/c$  locations ranging from  $x/c = 0.068$  to  $x/c = 0.209$  during the upstroke portion of the cycle. The minimum voltage level, identified as Feature 2 (F2), indicates low shear stress levels believed to be the precursor to flow reversal traveling upstream towards the leading edge of the airfoil. It is detected at the last sensor at 21% chord and is tracked up to 3% chord, at which point it terminates. Features 3 (F3), and Feature 4 (F4), shown in Figure 54b, start closely together, F3 being the first shear rise peak while F4 being the shear peak prior to drop in the shear levels. The two peaks indicate the extent of influence on the unsteady flow field above the airfoil. It is believed that the first shear rise peak in the shear data indicates the initial

time (angle of attack) at which a transition occurs when the shear layer detaches from the surface and rolls into the DSV. The first indication of these two features follows the end of the CPP region in the pressure data. More precisely, it follows the location and angle of the change in the adverse pressure gradient. Figure 54d, e, and f, show Feature 5 (F5) and Feature 6 (F6), which are present during the downstroke of the cycle. Feature F5 starts to emerge at about 3 to 5% chord followed by a minimum (F6) shortly afterwards. F5 is believed to be the onset of the reattachment process during the downstroke portion of the cycle, while F6 would correspond to fully reattached flow over the airfoil surface for a given  $x/c$  location.

The data presented below will be discussed in the following fashion. The Reynolds number of  $1.1 \times 10^5$  at the reduced frequency of  $k = 0.1$  will be analyzed first in order to provide a base line for comparison across the reduced frequency and Reynolds number ranges tested. Based upon this comparison, conclusions will be drawn with respect to frequency and Reynolds number effects. It should also be noted that the sensors placed on the pressure side of the airfoil did not provide any useful information in regard to the DSV development and evolution. In addition, the uncertainty in the data was negligible, small fluctuation in the data presented did not alter the trend seen in the development and evolution of the dynamic stall process.

Figure 58 shows the chord wise location and movement of F1 for  $Re_c = 1.1 \times 10^5$  and  $k = 0.1$  for combinations of mean angles and amplitudes. Feature 1 appears to be greatly influenced by the amplitude of oscillation in the same fashion LESP was affected. Increasing the amplitude to  $20^\circ$  delayed the appearance of F1 to higher angles of attack with no apparent influence from the mean angle. F1 was detected at about 3% chord and  $\alpha = 6.5^\circ$  for  $\alpha_o = 10^\circ$  and  $\alpha_m = 10^\circ$  closely following the same trend as the LESP plotted on the same plot up to the leading edge of the airfoil. An increase of the mean angle to  $20^\circ$ , did not influence the behavior of F1, which was identified and traced matching exactly with the previous case. Increasing both amplitude and mean angle to  $20^\circ$  delayed the angle of attack the feature first appears by about  $2^\circ$  to  $8^\circ$ . Decreasing the mean angle to  $10^\circ$  with amplitude of  $20^\circ$  altered the starting location of F1 but not the trend, which matched to the previous one.

Feature 2's chordwise location and movement for  $Re_c$  of  $1.1 \times 10^5$  and  $k = 0.1$  are shown in Figure 63. The nature of the feature to appear and propagate toward the leading edge at an early incidence prevented the tracking of the feature for  $\alpha_o = 20^\circ$  and  $\alpha_m = 10^\circ$ . F2 seen in Figures 63, appears at 21% chord and moves towards the leading edge with increasing angle of attack up to 3% chord, at which point it terminates. F2 initiates the shear layer lift up, resulting in a recirculation region (CPP), causing the roll up of the boundary layer into the DSV. The speed of the feature moving upchord remains the same for the different amplitudes and mean angles tested. However, the starting angle at which F2 is first detected appears to be influenced by both the amplitude and mean angle of oscillation, with the greatest delay of  $2^\circ$  obtained for  $\alpha_o = 20^\circ$  and  $\alpha_m = 10^\circ$ . A smaller delay of only  $1^\circ$  occurs when both the mean and amplitude of oscillation are raised to  $20^\circ$ , compared to the incidence angle of  $7.7^\circ$  when amplitude and mean angle are 10 degrees.

Feature 3 was not tracked due to the unclear nature of the feature. However, it is believed that while F3 is caused by the transition from the lift-up in the shear layer (caused by F2), it does not indicate or have anything to do with the DSV location. In addition, F3 appears first at 21% chord right after F2, and they progress together towards the leading edge of the airfoil, reaching the point where the DSV is formed.

Feature 4, which represents what is believed to be the location of the DSV, is shown in Figure 70 for  $Re_c$  of  $1.1 \times 10^5$  and  $k = 0.1$ . F4's appearance corresponds well with the end of CPP region. The dominance of amplitude on this feature is overwhelming, while the mean angle appears to have no affect on the location or movement of this feature. At an amplitude of  $10^\circ$ , the stating location and angle of attack are at  $x/c = 0.068$  and  $14^\circ$ . Increasing the amplitude to  $20^\circ$  delays the angle of attack the DSV forms to  $15^\circ$ , while at the same time it also delays the speed the DSV moves downstream.

Feature 5, believed to be the reattachment process of the flow during the downstroke portion of the cycle, first appears at about  $14^\circ$  and 6% chord as shown in Figure 77 for the  $Re_c$  of  $1.1 \times 10^5$  and  $k = 0.1$ . The reattachment process of the flow above the airfoil is not affected by the mean angle or amplitude of oscillation. As one would expect, the reattachment process starts at the leading edge and moves downstream with



decreasing angles until the flow attaches completely over the entire surface of the airfoil when the incidence angle is  $0^\circ$ . It is quite interesting to notice that the reattachment process takes place at about the same  $x/c$  location at which the DSV first appeared.

Feature 6, shown in Figure 84 for the  $Re_c$  of  $1.1 \times 10^5$  and  $k = 0.1$ , indicates fully attached flow on the downstroke portion of the cycle. This feature did not appear to be influenced by either the amplitude or the mean angle of attack. It was first detected at 1% chord, and  $\alpha = 22^\circ$ , moving downchord with decreasing angle of attack. At about 3% chord it starts moving faster until the end of the sensor array (21% chord), as can be seen from the slope in Figure 84.

## 7.2 Frequency Effects.

The effects of reduced frequency on F1, seen in Figures 59 and 60 for  $Re_c$  of  $1.1 \times 10^5$ , are hard to determine precisely due to the limited number of sensors in the leading edge region of the airfoil. Increasing the reduced frequency to  $k = 0.2$  introduces the mean angle effects into the development of F1 in addition to the  $2^\circ$  delay in the incidence angle at which F1 first appears. A further increase in reduced frequency to 0.4 forces F1 to within 1% chord, making it harder to determine the effects of reduced frequency on the starting angle of F1. There is, however a delay in the time that is required for this feature to approach the leading edge of the airfoil ( $x/c = 0.00$ ).

The effects of reduced frequency on F2 for  $Re_c = 1.1 \times 10^5$ ,  $k = 0.1$ ,  $\alpha_o = 10^\circ$ , and  $\alpha_m = 10^\circ$  are shown on Figure 91. Increasing the reduced frequency does not only delay the angle of incidence at which F2 appears, it also increases the speed with which this feature propagates upchord. There is an almost  $2^\circ$  delay from the starting angle of  $7.7^\circ$  for  $k = 0.1$  to  $9.5^\circ$  for  $k = 0.2$  to an additional  $3^\circ$  for  $k = 0.4$  to  $12.7^\circ$ . Increasing the amplitude to  $20^\circ$  (Figures 92) further delays the starting time of F2 from  $9.7^\circ$  for  $k = 0.1$  to  $13^\circ$  for  $k = 0.2$  and to  $17.5^\circ$  for  $k = 0.4$ . The unsteady effects of reduced frequency are so pronounced for  $k = 0.4$  that F2, which should be propagating towards the leading edge, appears to be reversed for an amplitude of  $20^\circ$ . Identical findings are recorded for  $\alpha_o = 20^\circ$  and  $\alpha_m = 20^\circ$  (Figure 93), indicating the dominance of amplitude over mean angle of attack.

Feature 4 is also greatly affected by the increase in reduced frequency. Figures 94-97 display the effects of reduced frequency for the different cases studied. In addition to Figures 94-95, the initial locations and angles of attack the DSV first appeared throughout the experimental range tested are tabulated in Table 6. For  $Re_c = 1.1 \times 10^5$ ,  $\alpha_o = 10^\circ$ , and  $\alpha_m = 10^\circ$  (Figure 94), the starting incidence angle at which F4 first appears for  $k = 0.1$  is  $14^\circ$ . It is delayed to  $16^\circ$  for  $k = 0.2$  and to  $18.5^\circ$  for  $k = 0.4$ . The convection speed of this feature appears to be the same for all reduced frequencies for  $\alpha_o = 10^\circ$  and  $\alpha_m = 10^\circ$ . Increasing the amplitude of oscillation to  $20^\circ$  (Figure 95) does not only delay the starting angle at which F4 appears, it also delays the speed DSV (F4) moves downstream. The starting angles DSV first appears are  $15^\circ$  for  $k = 0.1$ ,  $18^\circ$  for  $k = 0.2$ , and  $22.5^\circ$  for  $k = 0.4$ . For  $\alpha_o = 20^\circ$  and  $\alpha_m = 10^\circ$  the starting angles are  $14.2^\circ$  for  $k = 0.1$ ,  $17.2^\circ$  for  $k = 0.2$ , and  $19.5^\circ$  for  $k = 0.4$ . When both mean angle and amplitude are  $20^\circ$ , the starting angles for DSV are  $15.5^\circ$  for  $k = 0.1$ ,  $18.5^\circ$  for  $k = 0.2$ , and  $22^\circ$  for  $k = 0.4$ .

Figures 98-102 show the location and movement of F5 with decreasing angle. For an amplitude of  $10^\circ$ , the reattachment process appears to initiate for  $k = 0.1$  at  $13^\circ$  and 6% chord, moving downchord with decreasing angle of attack. An increase in the reduced frequency to 0.2 delays the reattachment until  $11^\circ$  at 13% chord, while at the reduced frequency of 0.4, the reattachment of the boundary layer does not occur until  $4^\circ$  at 16% chord. Increasing the amplitude to  $20^\circ$  depicts similar results. For  $k = 0.1$ , reattachment begins at  $14.5^\circ$ , 7% chord, while for  $k = 0.2$  it does not start until  $9^\circ$ , 11% chord. For the reduced frequency of 0.4, the peak associated with reattachment was not detected. Similarly for  $\alpha_o = 20^\circ$  and  $\alpha_m = 10^\circ$  the reattachment process starts at  $13.5^\circ$ , 6% chord for  $k = 0.1$  at and  $12.5^\circ$ , 7% chord for  $k = 0.2$ . Again, the reattachment was not detected for  $k = 0.4$ . Finally for  $\alpha_o = 20^\circ$  and  $\alpha_m = 20^\circ$  the reattachment process starts at  $12^\circ$ , 7% chord for  $k = 0.1$ ,  $11.5^\circ$  for  $k = 0.2$ , and  $11^\circ$  for  $k = 0.4$ . While for the first two reduced frequencies the reattachment process appears to be gradual, for the case of  $k = 0.4$ , the process takes place almost instantaneously up to 15% chord. The inability to track feature 5 in some of the cases presented is related to the influence of the DSV on the unsteady pressure field during the downstroke portion of the cycle.

Figures 102-105 depict the effects of reduced frequency on the development and movement of Feature 6. For  $\alpha_o = 10^\circ$  and  $\alpha_m = 10^\circ$  there is a  $2^\circ$  delay from  $k = 0.1$  to  $k = 0.2$  and an additional  $4^\circ$  delay to  $k = 0.4$  at 1% chord, starting from  $18.5^\circ$  for  $k = 0.1$  to  $16.5^\circ$  for  $k = 0.2$  and to  $12.5^\circ$  for  $k = 0.4$ . Increasing the amplitude to  $20^\circ$  simply shifts the abscissa to the left  $2.5^\circ$ , while the difference between the reduced frequencies remains the same. Figure 103 shows the effects of reduced frequency for  $\alpha_o = 20^\circ$  and  $\alpha_m = 10^\circ$ . A  $1.5^\circ$  delay exists initially at 1% chord with  $k = 0.1$  starting at  $21.7^\circ$  and  $k = 0.2$  at  $20.2^\circ$ . The curves appear identical up to about 7.5% chord at  $10^\circ$ . Increasing both mean angle and amplitude to  $20^\circ$  (Figure 105) indicates a change from  $k = 0.1$  to  $k = 0.2$ , while no further change appears between  $k = 0.2$  and  $k = 0.4$ .

### 7.3 Reynolds Number Effects

An increase in the Reynolds number results in higher output voltages for F1, which is in agreement with the higher LESP levels seen in the pressure data. In addition, dynamic stall is delayed to higher angles off attack, while the recirculation region shrinks in size. The DSV forms at the end of the CPP region (recirculation region) closer to the leading edge at about 3 to 4% chord for a  $Re_c$  of  $5.0 \times 10^5$  to  $1.0 \times 10^6$ , compared to 7% chord at the  $Re_c$  of  $1.1 \times 10^5$ . The reattachment process is also delayed during the downstroke portion of the motion profile with increasing Reynolds number. Amplitude effects dominate in the development of the DSV moving downstream over the mean angle throughout the range of Reynolds number tested.

It is interesting to note that while the reversed flow (F2), shown in Figures 106-108, occurs at earlier angles of attack for higher Reynolds numbers, the ability of the boundary layer to withstand higher adverse pressure gradients delays the onset of dynamic stall. In addition, the speed at which the reverse flow travels towards the leading edge of the airfoil is increased with higher Reynolds numbers.

Figure 109 depicts the effects of Reynolds numbers for  $\alpha_o = 10^\circ$  and  $\alpha_m = 10^\circ$  over the range of Reynolds numbers tested for both experimental facilities. As was mentioned earlier, a shift of about  $3^\circ$  between the results obtained at the two experimental facilities appears in the data. The movement of DSV appears to be constant (no change in

slope) with increasing Reynolds number. For the  $Re_c$  of  $1.1 \times 10^5$ , the DSV first appears at  $14.2^\circ$ , 8% chord. It appears at  $16^\circ$ , 3% chord for  $Re_c$  of  $3.2 \times 10^5$  and at  $17.5^\circ$ , 3% chord for the  $Re_c$  of  $4.6 \times 10^5$ . A similar change of  $1^\circ$  occurs between the data acquired at the NDF. Increasing the amplitude of oscillation to  $20^\circ$  (Figure 110) delays the DSV to  $15^\circ$ , 7% chord for  $Re_c$  of  $1.1 \times 10^5$ ,  $17.5^\circ$ , 3% chord for  $Re_c$  of  $3.2 \times 10^5$ ,  $19.2^\circ$ , 3% chord for  $Re_c$  of  $4.6 \times 10^5$ ,  $16.5^\circ$ , 3% chord for  $Re_c$  of  $5.0 \times 10^5$ , and  $17.5^\circ$ , 2% chord for  $Re_c$  of  $1.0 \times 10^6$ . For  $\alpha_o = 20^\circ$  and  $\alpha_m = 10^\circ$  (Figure 111), the DSV starting locations are  $14.2^\circ$ , 7% chord for  $Re_c$  of  $1.1 \times 10^5$ ,  $15.8^\circ$ , 4% chord for  $Re_c$  of  $3.2 \times 10^5$ ,  $17.4^\circ$ , 3% chord for  $Re_c$  of  $4.6 \times 10^5$ ,  $15^\circ$ , 3% chord for  $Re_c$  of  $5.0 \times 10^5$ , and  $17.5^\circ$ , 2% chord for  $Re_c$  of  $1.0 \times 10^6$ . Finally for  $\alpha_o = 20^\circ$  and  $\alpha_m = 20^\circ$  (Figure 112), the DSV starting locations are  $15.6^\circ$ , 8% chord for  $Re_c$  of  $1.1 \times 10^5$ ,  $17.9^\circ$ , 3% chord for  $Re_c$  of  $3.2 \times 10^5$ ,  $19.1^\circ$ , 3% chord for  $Re_c$  of  $4.6 \times 10^5$ ,  $16.5^\circ$ , 3% chord for  $Re_c$  of  $5.0 \times 10^5$ , and  $19^\circ$ , 2% chord for  $Re_c$  of  $1.0 \times 10^6$ . The above information is also available in Table 6.

The reattachment process (F5) is shown in Figures 113-115 for the different combinations of mean angles and amplitudes used over the range of Reynolds numbers tested. It is interesting to note that the reattachment process starts around the static stall angle, which for a NACA 0012 airfoil is about  $13^\circ$ . Increasing the Reynolds number slightly delays the onset of the process, and there is a difference in the speed with which the feature propagates downstream. For the Reynolds numbers of  $5.0 \times 10^5$  and  $1.0 \times 10^6$ , the reattachment process progresses at a faster rate than at the lower Reynolds numbers. For  $\alpha_o = 10^\circ$  and  $\alpha_m = 10^\circ$  the reattachment process starts at  $12.5^\circ$  for  $Re_c$  of  $1.1 \times 10^5$  followed closely by the other Reynolds numbers within  $1^\circ$  delay. Only the Reynolds number of  $1.0 \times 10^6$  appears to be separated from the pack. The reattachment process starts closer to the leading edge with increasing Reynolds number (smaller CPP region) and it progresses to 21% chord by  $9-6^\circ$ . Increasing the amplitude to  $20^\circ$  does not affect the angle at which the reattachment process starts for the range of Reynolds numbers tested. Reattachment starts around the static stall angle for the low Reynolds number of  $1.1 \times 10^5$ , followed by a small delay of less than  $1^\circ$  by the higher Reynolds numbers. Only for  $\alpha_o = 20^\circ$ ,  $\alpha_m = 10^\circ$  and Reynolds number of  $1.1 \times 10^5$ , the reattachment process started before the static stall angle by a small advance of  $1^\circ$ . In addition, only the Reynolds number of

$5.0 \times 10^5$  exceeded reattachment over the surface greater than 20% chord at the minimum angle of  $10^\circ$  followed by 17% chord reattachment for  $Re_c = 1.1 \times 10^5$ , and 13% chord reattachment for  $Re_c = 3.2 \times 10^5$ ,  $Re_c = 4.6 \times 10^5$  and  $Re_c = 1.0 \times 10^6$ .

Feature 6, shown in Figures 116-119, appears at about  $18^\circ$  for an amplitude of  $10^\circ$ , moving slowly in the first 2% chord, as can be seen by the slope in the leading edge of the airfoil. Past 2% chord, this feature moves faster downchord until  $4^\circ$ , 21% chord where the sensor array ends. Increasing the Reynolds number causes an additional increase in the movement of this feature. Raising the amplitude to  $20^\circ$  makes F6 to appear earlier during the downstroke portion of the cycle at about  $21^\circ$ . Again, a slow movement is observed between 1 and 2% chord, while past 2% chord, F6 changes slope, moving at a higher rate until the array ends at 21% chord and  $4^\circ$ .

In summary, the overview of the dynamic stall process based on the information obtained from the unsteady pressure and shear stress data agrees well with the sequence of events described by Karim<sup>12</sup> in 1992 for single pitch up motion profiles. The vorticity generated between the stagnation point and the leading edge suction peak (LESP) during the upstroke of the cycle is transported to the suction surface of the airfoil in a thin shear layer. As the angle of attack increases, the adverse pressure gradient in the downchord region of the LESP causes the fluid in the shear layer to slow down. Further increase in the adverse pressure gradient with increasing angle of attack allows the low-momentum fluid close to the wall to slow down sufficiently, producing a region of local reverse flow (Feature 2). This reverse fluid moves upchord with increasing angle of attack, causing the lift up of the shear layer from the surface of the airfoil. Once the reverse fluid approaches the LESP, causes a recirculation region to form in the leading edge of the airfoil. The accumulation of reverse fluid in combination with the clockwise vorticity caused by the adverse pressure gradient interacts with the outer flow-field initiating the roll up of the shear layer at the end of the recirculation region. This roll up of the shear layer into a coherent vortical structure indicates the birth of the dynamic stall vortex (Feature 4). Visualization records by Karim (Figure 120) show the development of the DSV for a selected Reynolds number and pitch rate. The DSV initially remains above the surface of the airfoil where it grows in size until it detaches itself from the surface of the airfoil. Subsequently increase in the angle of attack causes the DSV to convect downstream

leading to stall conditions. The timing of the actual events depends on the experimental parameters used and varies accordingly as was seen in the data presented above.

## CHAPTER VIII

### DISCUSSION OF RESULTS

The events involved in the development and evolution of dynamic stall and subsequent reattachment in the downstroke of the cycle over an oscillating airfoil will be discussed for the range of Reynolds numbers, reduced frequencies, mean angles and amplitudes tested. The flow model describing the dynamic stall events will be based on the understanding obtained from both measurement techniques utilized in the present research.

In the current investigation, a two-dimensional airfoil was oscillated about a mean angle of 10-20 degrees with amplitude of 10 and 20 degrees. This resulted in four motion profiles based on the various possible combinations (Figure 7). The Reynolds number based on chord length was varied between  $1.1 \times 10^5$  and  $1.0 \times 10^6$ . Although in most practical applications the Reynolds number is considerably higher, the range investigated provided valuable information in the behavior of dynamic stall process. The reduced frequency used across the Reynolds numbers tested was  $k = 0.1$ . At the lower Reynolds number of  $1.1 \times 10^5$  the reduced frequency was varied between  $k = 0.1$  and  $k = 0.4$ .

The mechanisms responsible for the evolution and development of the dynamic stall vortex were identified using unsteady pressure measurements in combination with shear stress data. The shear stress data were obtained through an array of hot-film sensors attached in the leading edge of a NACA 0012 airfoil. The well-established features developed in the unsteady pressure field over the surface of an airfoil were used to supplement the results from the shear stress sensors in building the model explaining the development of the dynamic stall vortex.

The unsteady pressure measurements carried out over the range of Reynolds numbers tested indicated an increase in the leading edge suction peak while the constant pressure plateau shrank in size. Chandrasekhara, Wilder and Carr<sup>24</sup> reported similar findings. The leading edge suction peak maximum was delayed to higher angles of attack with increased Reynolds numbers. Once the maximum peak was reached, the dynamic stall vortex moved quickly downstream. The formation of DSV was however initiated before the maximum LESP was reached, seen by a change in the slope of the pressure

gradient. The change in the pressure gradient from increasing to decreasing is consistent with the effects a vortex would have on the surrounding flow field. For the Reynolds number of  $1.1 \times 10^5$ , the pressure gradient is gradually curved (widened), indicating the movement of DSV downchord. In addition, increasing the amplitude of oscillation allows the DSV to grow in strength and size as seen by the extent in curvature in Figures 43 and 45. The additional vorticity fed into the vortex generated by the larger amplitude allows the coexistence of both the LESP and DSV, delaying movement of the vortex to higher angles of attack. This curvature of the pressure distribution (DSVP) above the surface of the airfoil was not seen at the higher Reynolds numbers, indicating a quick movement of the DSV downstream. In addition, an increase in the amplitude of oscillation delayed the formation and release of the dynamic stall vortex, dominating over the mean angle effects. Similar results of the effects of the amplitude of oscillation on the DSV were obtained by Chandrasekhara and Brydges<sup>23</sup>.

During the downstroke portion of the cycle, a suction peak was formed in the leading edge followed by a constant pressure plateau. The adverse pressure gradient caused by the leading edge suction peak initiated the reattachment process at the end of the CPP region around the static stall angle. The CPP region disappeared with decreasing angle of attack once complete reattachment was achieved. Similar results were reported by Ahmed and Chandrasekhara<sup>25</sup>.

Increasing the reduced frequency effectively delayed the movement of the dynamic stall vortex over the airfoil, 'holding' the vortex in the leading edge of the airfoil to progressively higher angles of attack. The DSV was formed in a similar fashion at the end of the CPP region, but with increasing frequency, the CPP region curved into the DSVP as shown clearly in Figures 46-49. In addition, at the reduced frequency of  $k = 0.4$ , the mean angle effects were introduced into the location and movement of the DSV. At the reduced frequency of  $k = 0.4$ , stall was prevented with the DSV 'pinned' in the leading edge of the airfoil within 30% chord at the end of the upward portion of the cycle. The vortex effects were also noticeable on the downstroke portion of the cycle, greatly delaying the reattachment process to later angles of attack.

Using the above information in cross-reference to the shear stress data, the mechanism behind the formation of the dynamic stall vortex starts to emerge. The end of



the CPP region (or recirculation region) is the location where the DSV is formed, as was seen by the results in the pressure data. These locations and angles of attack were also traced in the shear stress data, where a very precise match was made between the emergence of the first shear stress peak, and the change in the slope of the pressure gradient at the end of the CPP region. From that point on, the shear peak associated with the DSV was traced through the increasing angles of attack and  $x/c$  locations, as was shown in Chapter VII. The cause of formation of the DSV underlies, however, in F2, or reverse flow indicated by the minimum in the voltage levels. F2 first appeared at 21% chord at the last sensor in the array and quickly traveled upchord. This feature was also identified by Karim and others as a local reversed flow in the leading edge region of the airfoil. Based on the current information obtained from the data, a definite conclusion cannot be made about the origins of this feature. It is believed, however, to be a local event, due to early angles at which it appears (less than  $\alpha = 10$  degrees for  $k = 0.1$ ). F2 travels upstream followed by a transition in the shear layer seen by the shear rise moving along in the same direction closely afterwards (Feature 3). When F2 initiates the lift up of the shear layer resulting in the recirculation region (CPP), F3 lags behind until the roll up of the boundary layer into what is known as the dynamic stall vortex (Feature 4) occurs. From that point on, shown in Figures 54-57, the history of events through time (angle of attack) is clearly displayed. Secondary peaks in the region between Features 3 and 4 are believed to be secondary vortices moving downstream. The delay between the time F2 first lifts up the shear layer and the roll up of the boundary layer into the DSV (about 3 degrees) depends on the boundary layer's ability to withstand higher adverse pressure gradients. Thus, there is a delay in the onset of dynamic stall with increasing Reynolds numbers and reduced frequencies.

The reattachment of the boundary layer on the surface of the airfoil, shown in Figures 54-57 parts d, e, and f, is not effected by the amplitude or mean angle of attack at the low reduced frequency. Interestingly, the angle of attack at which the reattachment process began was close to the static stall angle for this particular airfoil. The delays recorded at the high reduced frequencies were caused by the dynamic stall vortex presence during the downstroke portion of the cycle, altering the pressure distribution above the surface. This prevented the formation of the LESP or, in some cases,

eliminating it altogether. Reynolds number increase had a minimal effect on the reattachment time the process initiated. It did, however, influence the  $x/c$  location at which the process began. In addition, the reattachment process appeared to progress faster with increasing Reynolds number.

The results presented above are in good agreement with previous work performed by many experimentalists. The model presented for the formation of dynamic stall vortex coincides with the explanation given by Karim<sup>12</sup> in 1992, stating that separation is initiated due to local reversed flow underneath the boundary layer. The work presented in Part A of this report indicated similar trends for a range of non-dimensional pitch rates and Reynolds Numbers. Direct comparison between the findings reported for different Reynolds number at the pitch rate of  $\alpha^+ = 0.036$ , corresponding to a reduced frequency of  $k = 0.1$ , are made for similar amplitudes. The dynamic stall vortex starting locations and angles of attack is identical in all cases for the Reynolds numbers of  $1.1 \times 10^5$ ,  $3.2 \times 10^5$ , and  $4.6 \times 10^5$ . However, the additional vorticity generated by the oscillation of the airfoil delays the downstream movement of the dynamic stall vortex. A substantial delay of  $2^\circ$  by 21% chord for the range of Reynolds numbers tested was recorded. For example, for the pitch up at  $Re_c = 1.1 \times 10^5$  the starting angle was  $15^\circ$ , while the recorded angle at 21% chord was  $16^\circ$ . Similarly, for the oscillating case, the starting angle was  $15^\circ$  and  $18^\circ$  respectfully. Although there was a difference between the pitch-up and oscillation, as was expected, the changes with respect to the events within the two cases indicated similar results.

## CHAPTER IX

### CONCLUSIONS AND RECOMMENDATIONS, PART B

#### 9.1 Conclusions

A wide range of experimental parameters, such as Reynolds number, reduced frequency, and amplitude of oscillation, was employed to study the evolution of the dynamic stall vortex over an oscillating airfoil. In addition, the reattachment progress in the downstroke of motion profile was studied.

Increasing the reduced frequency had the greatest effect on the evolution and development of dynamic stall. At the highest frequency used,  $k = 0.4$ , stall was prevented while the dynamic stall vortex remained above the surface of the airfoil within 30% chord for all cases studied.

Increasing the Reynolds number effectively delayed the onset of dynamic stall to higher angles of attack, while the convective speed of the vortex moving downstream was increased. In addition, the recirculation region (CPP) shrank in size with increasing Reynolds number. The shrinking of the recirculation region caused the dynamic stall process to start closer to the leading edge of the airfoil while higher leading edge suction peaks were present in the pressure data.

Amplitude effects were quite dominant over the mean angle effects during the development of the dynamic stall vortex. Throughout the Reynolds numbers tested, amplitude dominated, with no sign of any influence by the mean angle. Only with increasing the frequency of oscillation, the dominance of amplitude was broken with the mean angle contributing in the development and evolution of the dynamic stall vortex. Increasing the amplitude resulted in an additional delay to the onset of the dynamic stall process.

The reattachment process on the downstroke portion of the cycle was not affected by the mean angle or amplitude of oscillation, while the reattachment process began close to the static stall angle. The reattachment process involved the formation of a recirculation region during the downstroke portion of the motion profile. Reynolds number effects on the formation of the recirculation region were similar to those on the upstroke, with the reattachment process starting closer to the leading edge while

progressing at a higher rate downstream. Reduced frequency greatly effected the reattachment process delaying the process to smaller angles.

Based on the results, presented the prevention or delay of the reversed flow from reaching the end of the CPP region (bubble) appears to be a promising controlling mechanism in the onset of the dynamic stall vortex. A proper combination of reduced frequency and delay in the movement of Feature 2 would, perhaps, effectively delay stall conditions while providing additional lift needed by today's highly maneuverable aircraft and helicopters.

## 9.2 Recommendations

A number of uncertainties arose through the course of the current investigation, some of which could be resolved through the implementation of a number of improvements such as:

- The increase in the spatial resolution of the pressure ports in the CPP region to get a more precise picture of the pressure gradient involved in what is believed to be the birth of the dynamic stall vortex.
- The use of additional sensors downstream of 21% chord used in the current investigation to determine if Feature 2 was a local event or not.
- The reacquisition of the data in the NDF facility without the gear reducer to determine the effects of the backlash on the hysteresis seen at the higher Reynolds number.
- The purchase of a higher data acquisition card to allow the simultaneously acquisition of all 50 sensors together with the encoder signal.

## **APPENDIX**

## **PARTICIPATING SCIENTIFIC PERSONNEL**

1. Dr. Mukund Acharya, Principal Investigator
2. Mr. Angelis Bizo, Graduate Research Assistant (awarded MS degree, May 1998)
3. Mr. John W. Kiedaisch, Graduate Research Assistant (PhD degree expected May, 2000)

## **PUBLICATIONS AND TECHNICAL REPORTS**

1. Kiedaisch, J. W. and Acharya, M., "Investigation of Incipient Dynamic Stall over Pitching Airfoils using Hot-Film Sensors," AIAA Paper 97-0656, 35<sup>th</sup> Aerospace Sciences Meeting, Reno, NV, January 1997.
2. Kiedaisch, J. W. and Acharya, M., "Investigation of Unsteady Separation over Pitching Airfoils at High Reynolds Numbers," AIAA Paper 98-2975, 29<sup>th</sup> AIAA Fluid Dynamics Conference, Albuquerque, NM, June 1998.

Copies of any additional manuscripts submitted for publication will be forwarded to the ARO as soon as they are available.

## TABLES



Table 1 Chordwise location of pressure ports.

$(x/c)_{z=0}$	$(x/c)_{z=0.25''}$
-0.017	0.008
0.000	0.031
0.017	0.061
0.046	
0.075	
0.106	
0.138	
0.179	
0.221	
0.263	
0.317	
0.381	
0.444	
0.506	
0.568	
0.631	
0.693	
0.756	
0.818	

Table 2 Chordwise location of hot-film sensors (first configuration).

$x/c$	Sensor	Resistance (Ohms)
0.209	6	8.46
0.201	7	9.34
0.184	9	9.24
0.176	10	9.66
0.167	11	10.22
0.159	12	10.00
0.151	13	9.29
0.142	14	9.35
0.134	15	9.42
0.126	16	9.45
0.118	17	9.27
0.109	18	9.30
0.101	19	9.30
0.093	20	7.46
0.085	21	7.88
0.077	22	9.05
0.068	23	8.90
0.060	24	9.98
0.052	25	9.43
0.044	26	9.28
0.037	27	9.41
0.029	28	9.35
0.014	30	9.37
0.008	31	9.31
0.003	32	8.79
0.000	33	8.73
-0.003	34	8.75
-0.008	35	9.40
-0.014	36	9.39
-0.021	37	9.52
-0.029	38	9.42
-0.037	39	9.50
-0.044	40	9.59
-0.052	41	9.46
-0.060	42	9.71
-0.068	43	9.57
-0.077	44	9.67
-0.085	45	9.42
-0.093	46	9.26
-0.101	47	9.62
-0.109	48	9.10
-0.118	49	9.20
-0.126	50	9.57

Table 3 Chordwise location of hot-film sensors (second configuration).

x/c	Sensor	Resistance (Ohms)
0.209	24	9.17
0.201	25	9.21
0.184	27	9.51
0.176	28	9.24
0.167	29	12.55
0.159	30	9.14
0.151	31	9.19
0.142	32	9.16
0.134	33	9.44
0.126	34	10.87
0.118	35	9.43
0.109	36	9.12
0.101	37	9.44
0.093	38	9.72
0.077	40	9.53
0.068	41	9.16
0.060	42	11.30
0.052	43	8.76
0.044	44	8.00
0.037	45	8.42
0.029	46	8.01
0.021	47	8.02
0.014	48	8.05
0.008	49	8.20
0.003	50	8.09
0.000	51	8.07
-0.003	52	8.20
-0.008	53	8.05
-0.014	54	8.02
-0.021	55	8.10
-0.029	56	8.01
-0.037	57	8.94
-0.044	58	8.04
-0.052	59	8.09
-0.060	60	8.41
-0.068	61	8.00
-0.077	62	8.07
-0.085	63	8.02
-0.093	64	7.96
-0.101	65	8.12
-0.109	66	7.95
-0.118	67	8.56
-0.126	68	7.99

Table 4 Experimental parameters (Part B).

$Re_c$	$k$	$\alpha_o$	$\alpha_m$
$1.1 \times 10^5$	0.1	10	10
		10	20
		20	10
		20	20
	0.2	10	10
		10	20
		20	10
		20	20
	0.4	10	10
		10	20
		20	10
		20	20
$3.2 \times 10^5$	0.1	10	10
		10	20
		20	10
		20	20
$4.6 \times 10^5$	0.1	10	10
		10	20
		20	10
		20	20
$5.0 \times 10^5$	0.1	10	10
		10	20
		20	10
		20	20
$1.0 \times 10^6$	0.1	10	10
		10	20
		20	10
		20	20

Table 5 Maximum LESP.

	$\alpha_o=10^\circ \alpha_m=10^\circ$	$\alpha_o=10^\circ \alpha_m=20^\circ$	$\alpha_o=20^\circ \alpha_m=10^\circ$	$\alpha_o=20^\circ \alpha_m=20^\circ$
$Re_c=1.1 \times 10^5$ $K=0.1$	$14^\circ$ $x/c=0.008$	$17^\circ$ $x/c=0.008$	$14^\circ$ $x/c=0.008$	$17^\circ$ $x/c=0.008$
$Re_c=1.1 \times 10^5$ $K=0.2$	$16^\circ$ $x/c=0.008$	$24^\circ$ $x/c=0.000$	$18^\circ$ $x/c=0.008$	$24^\circ$ $x/c=0.000$
$Re_c=1.1 \times 10^5$ $K=0.4$	$19^\circ$ $x/c=0.008$	$25^\circ$ $x/c=0.000$	$28^\circ$ $x/c=0.000$	$32^\circ$ $x/c=0.000$
$Re_c=3.2 \times 10^5$ $K=0.1$	$17^\circ$ $x/c=0.008$	$20^\circ$ $x/c=0.008$	$17^\circ$ $x/c=0.008$	$20^\circ$ $x/c=0.008$
$Re_c=4.6 \times 10^5$ $K=0.1$	$18^\circ$ $x/c=0.008$	$22^\circ$ $x/c=0.008$	$18^\circ$ $x/c=0.008$	$22^\circ$ $x/c=0.008$
$Re_c=5.0 \times 10^5$ $K=0.1$	$18^\circ$ $x/c=0.008$	$22^\circ$ $x/c=0.008$	$18^\circ$ $x/c=0.008$	$22^\circ$ $x/c=0.008$

Table 6 DSV formation.

	$\alpha_o=10^0 \alpha_m=10^0$	$\alpha_o=10^0 \alpha_m=20^0$	$\alpha_o=20^0 \alpha_m=10^0$	$\alpha_o=20^0 \alpha_m=20^0$
$Re_c=1.1 \times 10^5$ $K=0.1$	$14.2^0$ $x/c=0.068$	$15^0$ $x/c=0.068$	$14.2^0$ $x/c=0.068$	$15.6^0$ $x/c=0.068$
$Re_c=1.1 \times 10^5$ $K=0.2$	$16^0$ $x/c=0.077$	$18^0$ $x/c=0.068$	$17.2^0$ $x/c=0.077$	$18.5^0$ $x/c=0.068$
$Re_c=1.1 \times 10^5$ $K=0.4$	$18.5^0$ $x/c=0.093$	$22.5^0$ $x/c=0.068$	$19.5^0$ $x/c=0.052$	$22^0$ $x/c=0.068$
$Re_c=3.2 \times 10^5$ $K=0.1$	$16^0$ $x/c=0.029$	$17.5^0$ $x/c=0.029$	$15.8^0$ $x/c=0.037$	$17.9^0$ $x/c=0.029$
$Re_c=4.6 \times 10^5$ $K=0.1$	$17.5^0$ $x/c=0.029$	$19.2^0$ $x/c=0.029$	$17.4^0$ $x/c=0.029$	$19.1^0$ $x/c=0.029$
$Re_c=5.0 \times 10^5$ $K=0.1$	$18.5^0$ $x/c=0.029$	$16.5^0$ $x/c=0.029$	$15^0$ $x/c=0.029$	$16.5^0$ $x/c=0.029$
$Re_c=1.0 \times 10^6$ $K=0.1$	$17.3^0$ $x/c=0.021$	$17.5^0$ $x/c=0.021$	$17.5^0$ $x/c=0.021$	$19^0$ $x/c=0.021$

## **FIGURES**

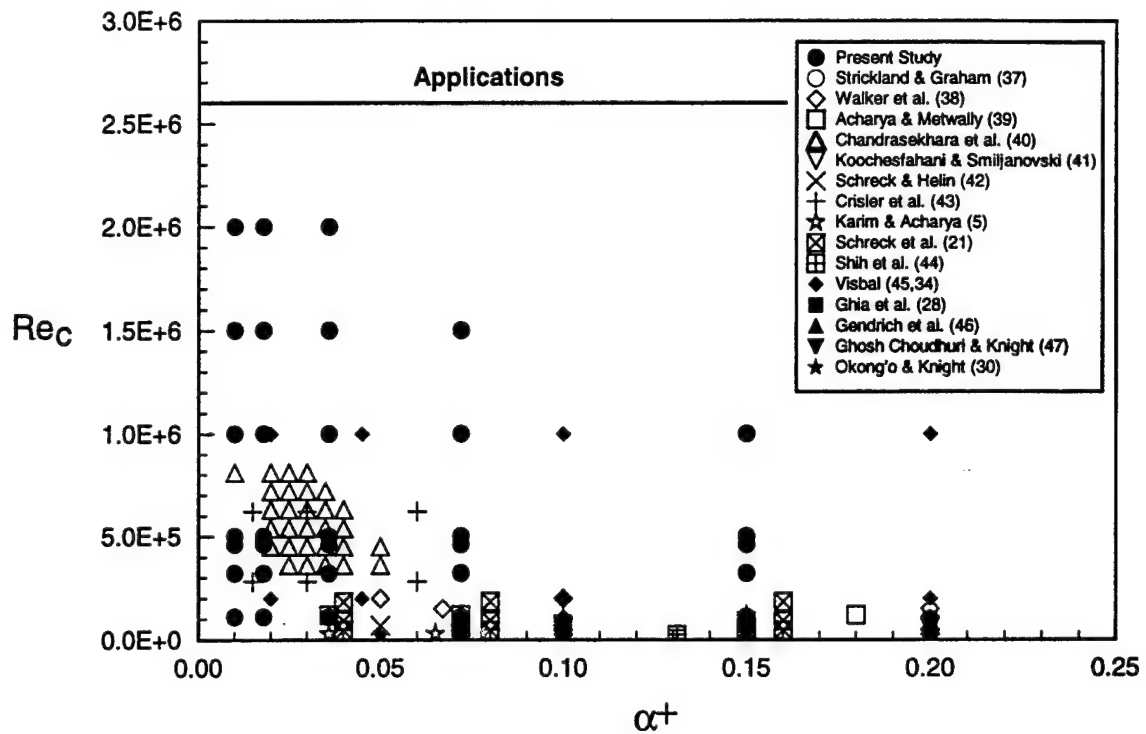


Figure 1 Parameter ranges of present and past experimental and computational studies of dynamic stall on pitching airfoils.



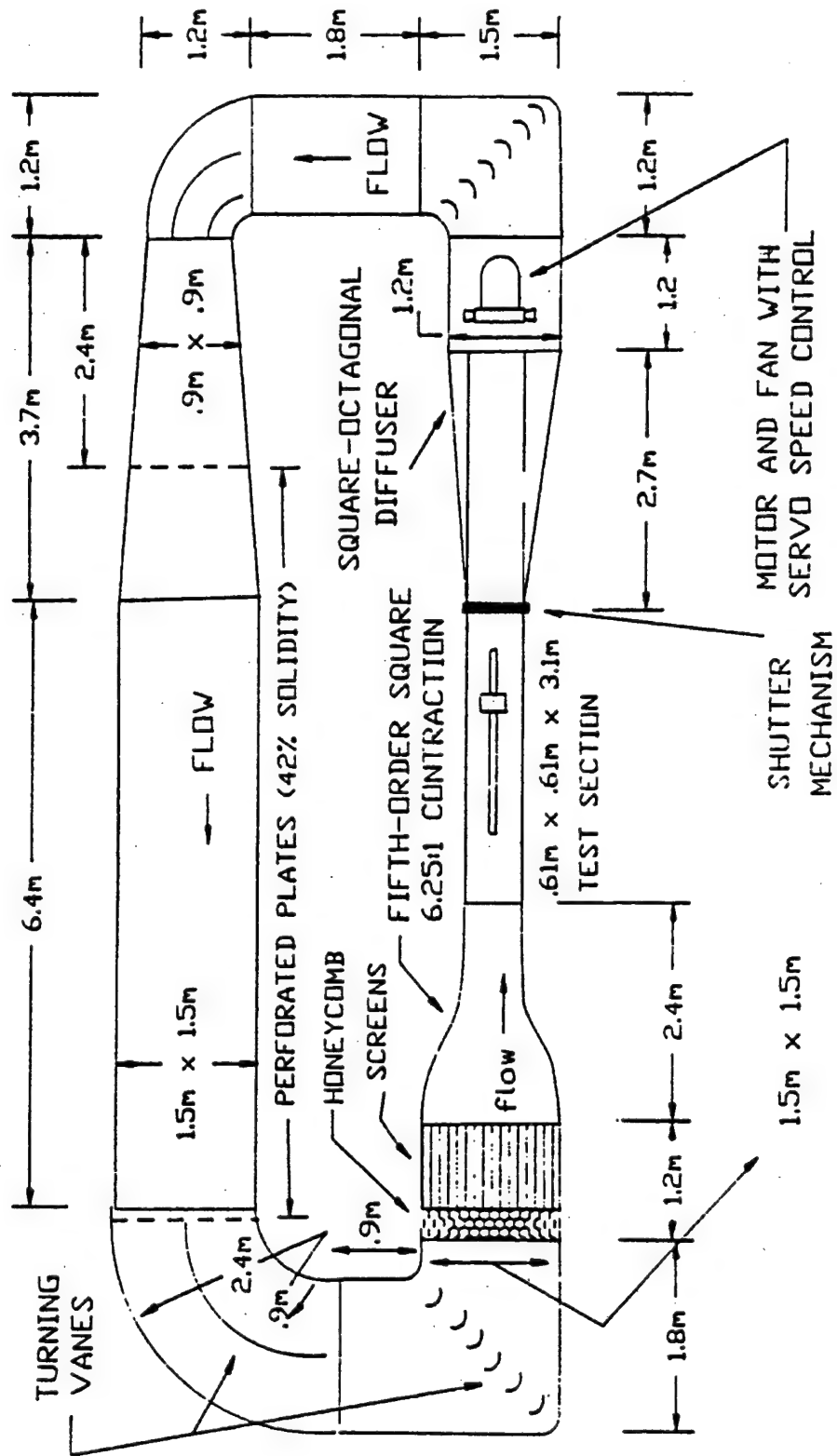


Figure 2 Plan view of the Andrew Fejer Unsteady Wind Tunnel facility.

# National Diagnostic Facility

Illinois Institute of Technology

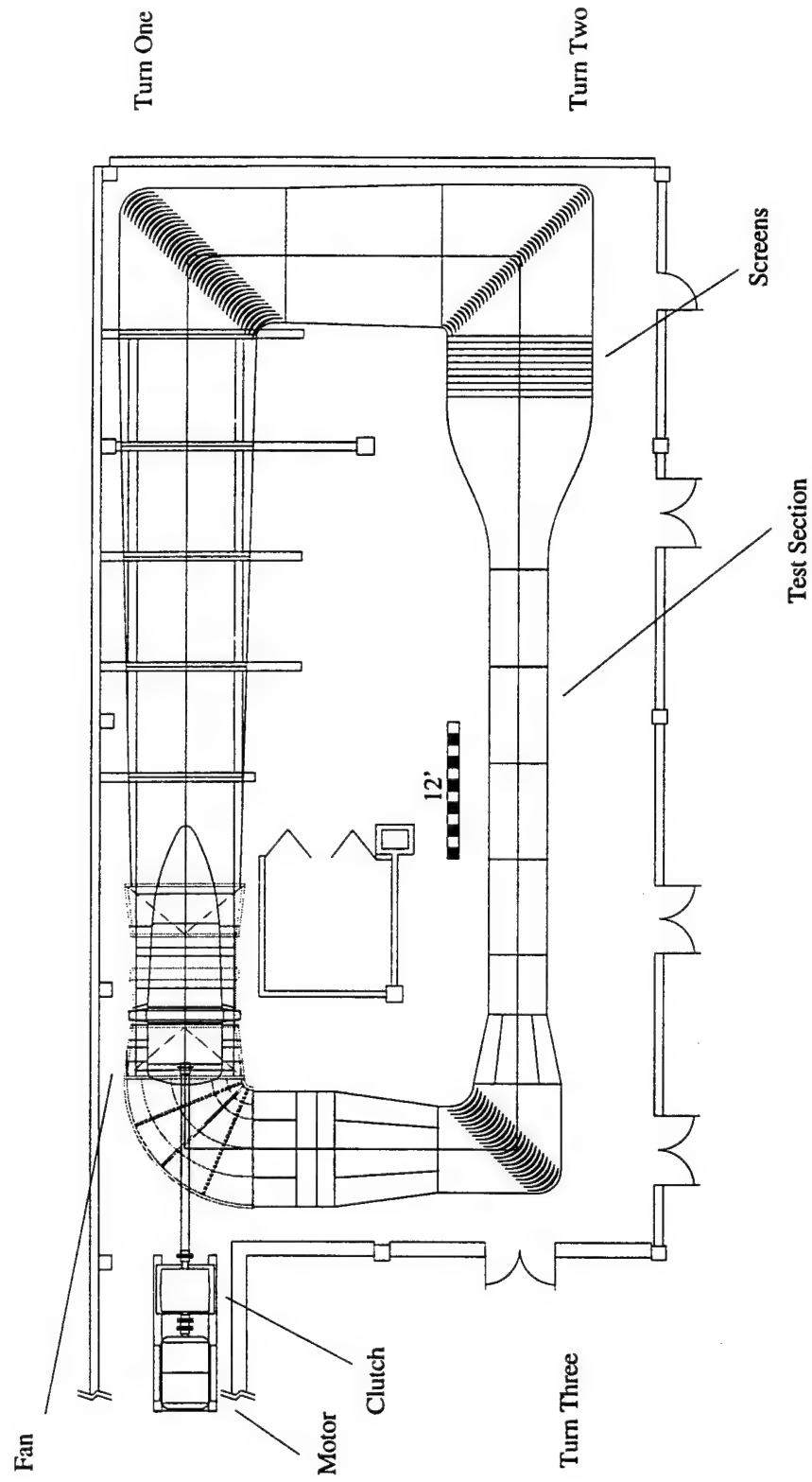


Figure 3 Plan view of the National Diagnostic Facility (NDF).

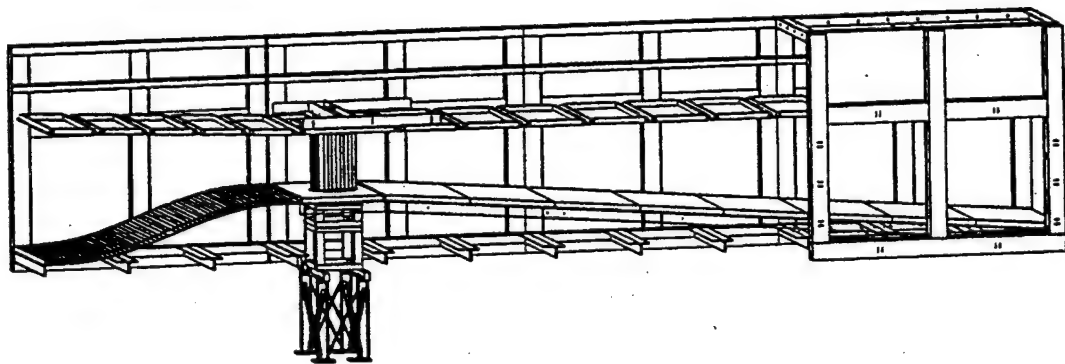
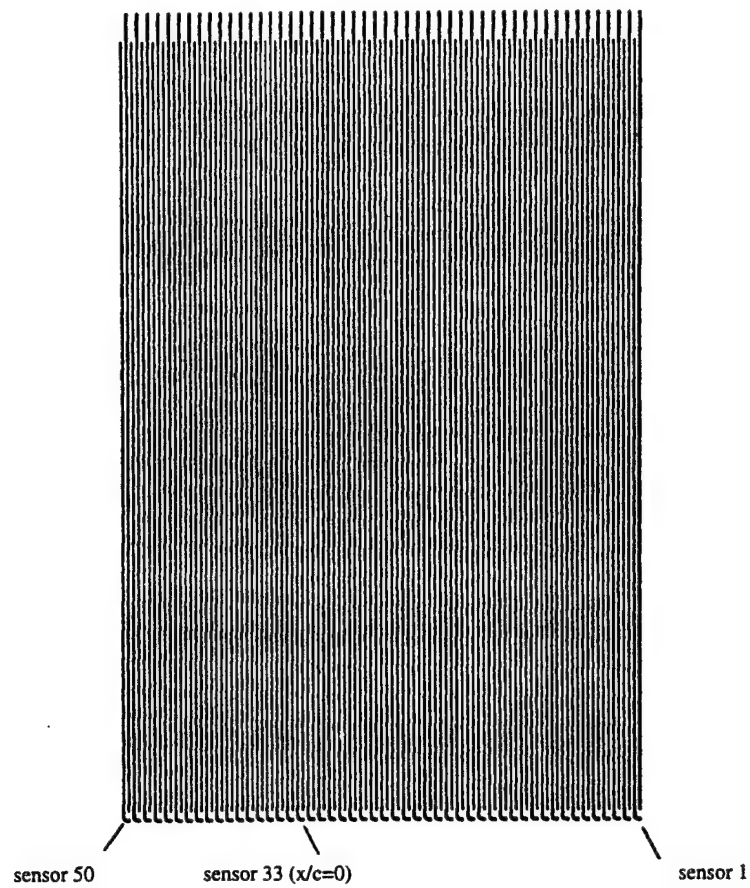
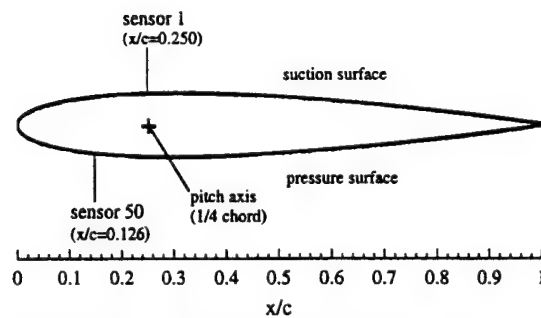


Figure 4 Airfoil model installed in the NDF test section.



(a) Hot-film sensor array.



(b) Position of array on airfoil model.

Figure 5 Hot-film instrumentation for shear-stress measurements.

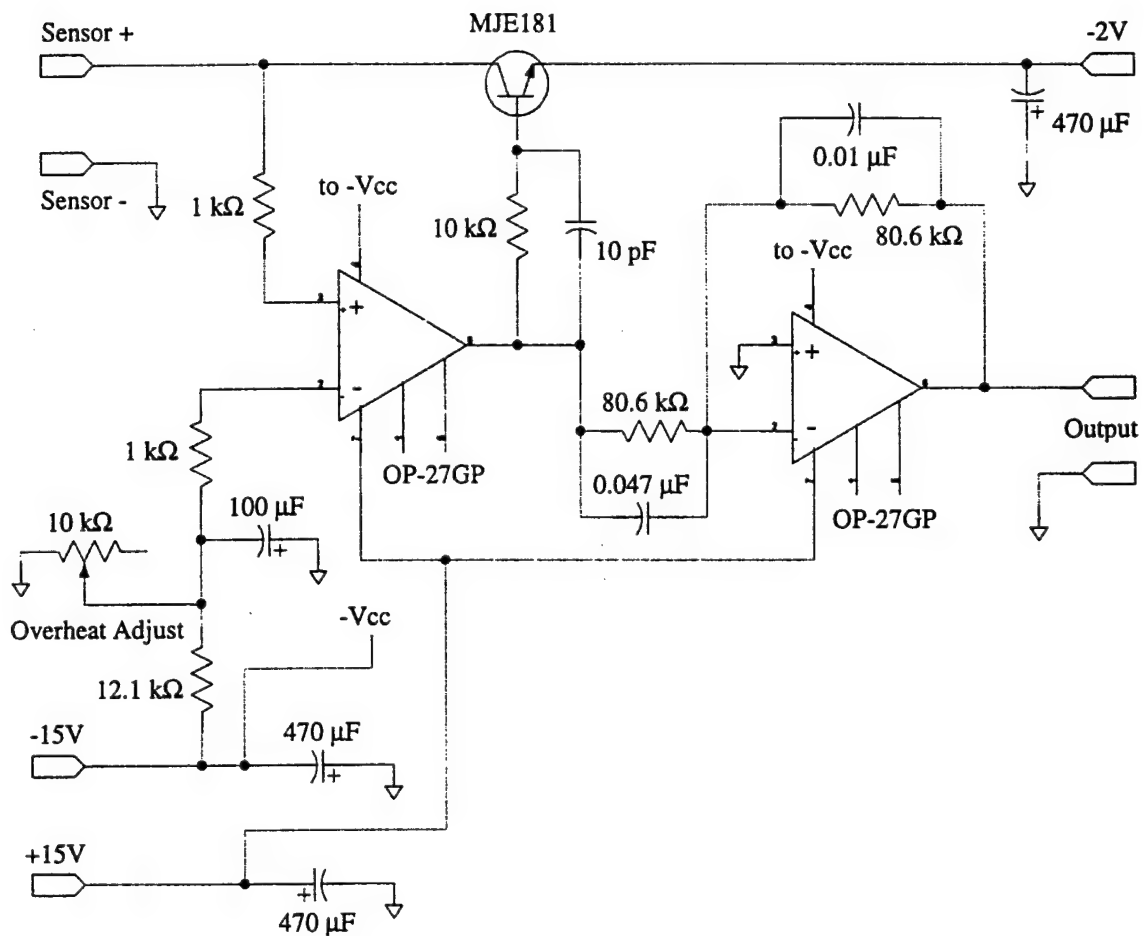


Figure 6a Constant voltage amplifier circuit diagram.

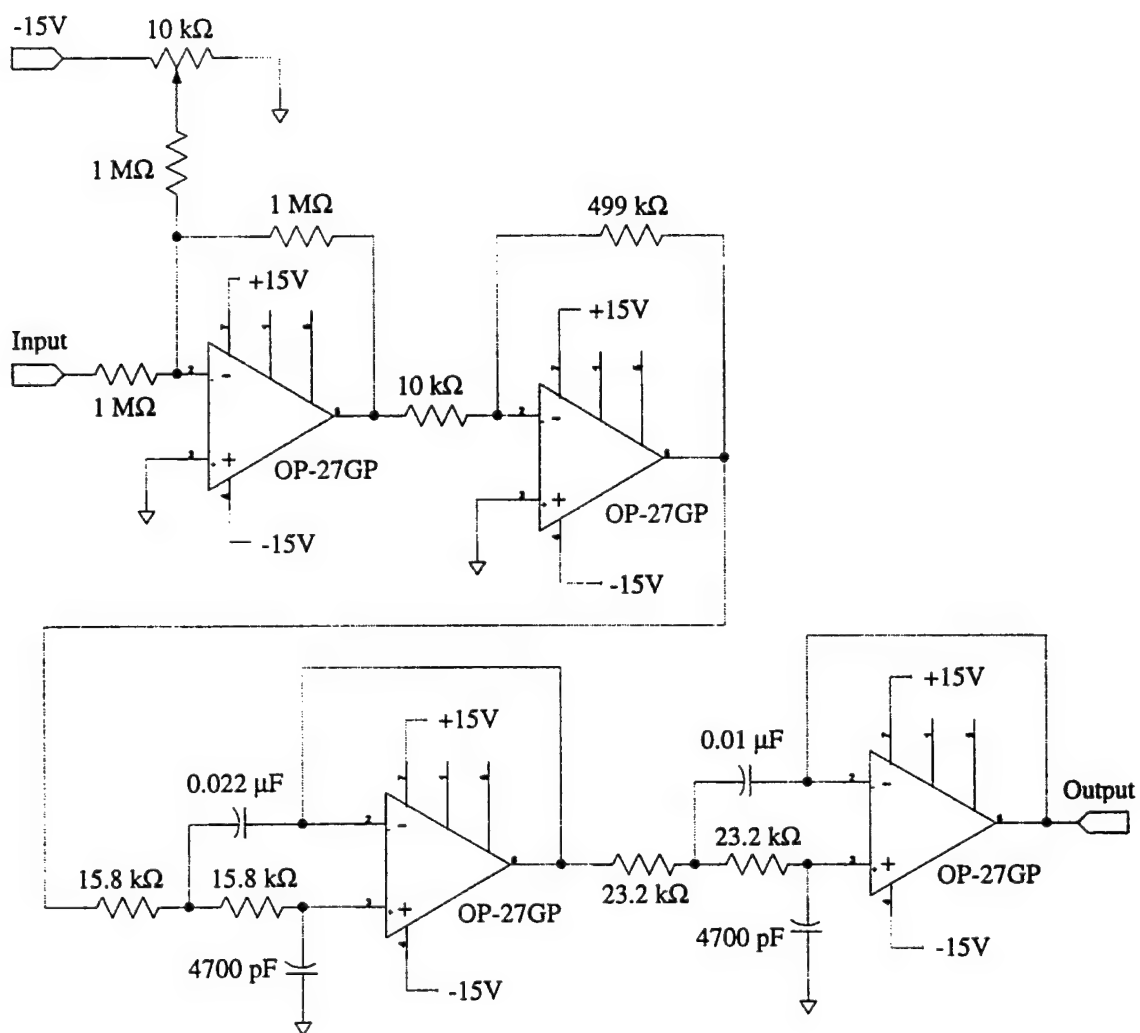


Figure 6b Signal conditioning circuit diagram.

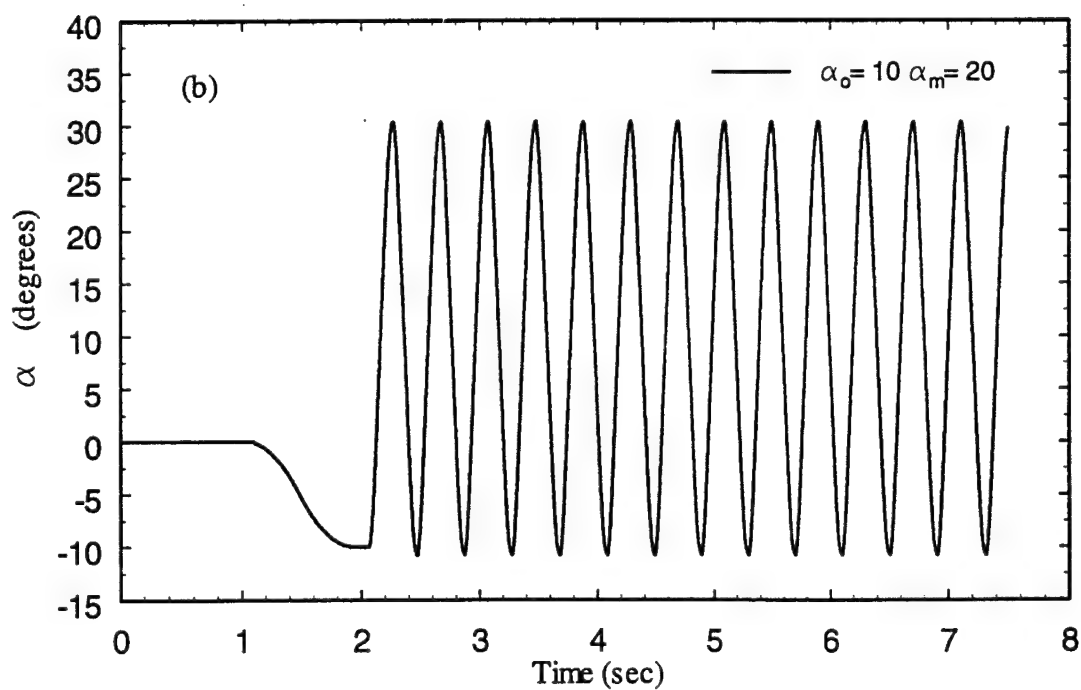
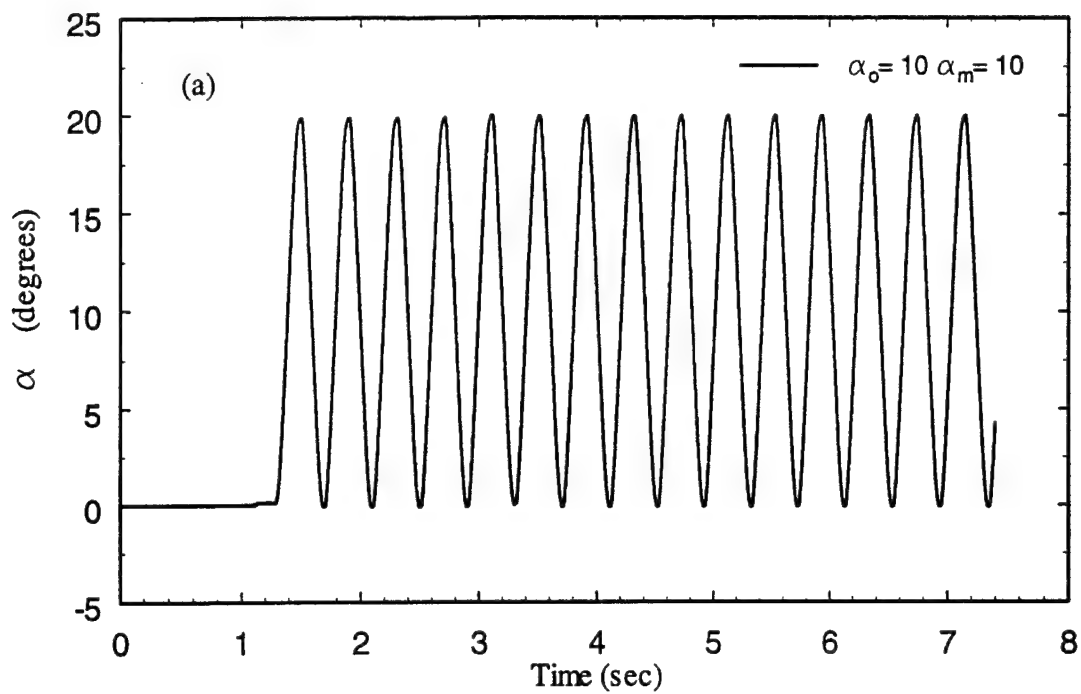


Figure 7 Motion profiles of oscillation (page 1 of 2).

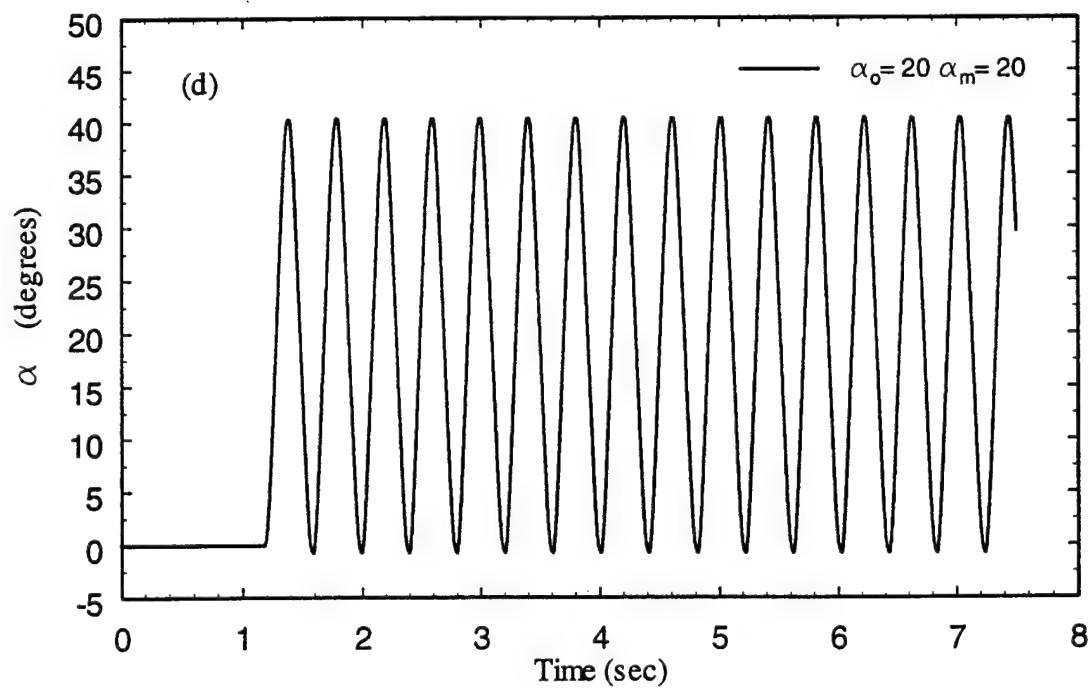
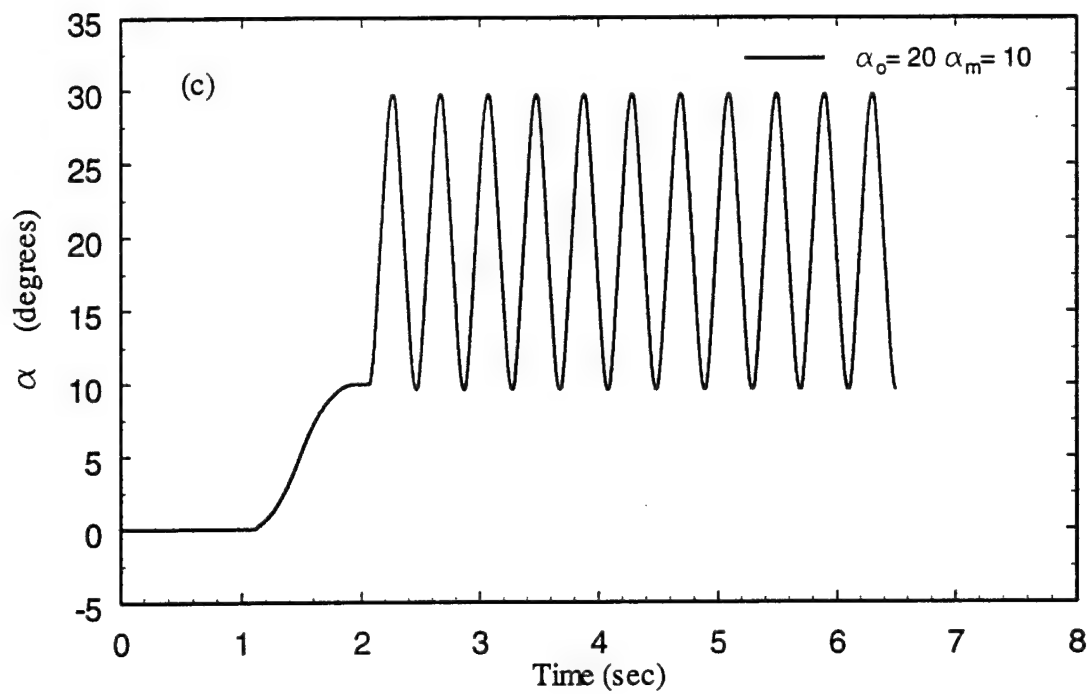


Figure 7 (concluded).



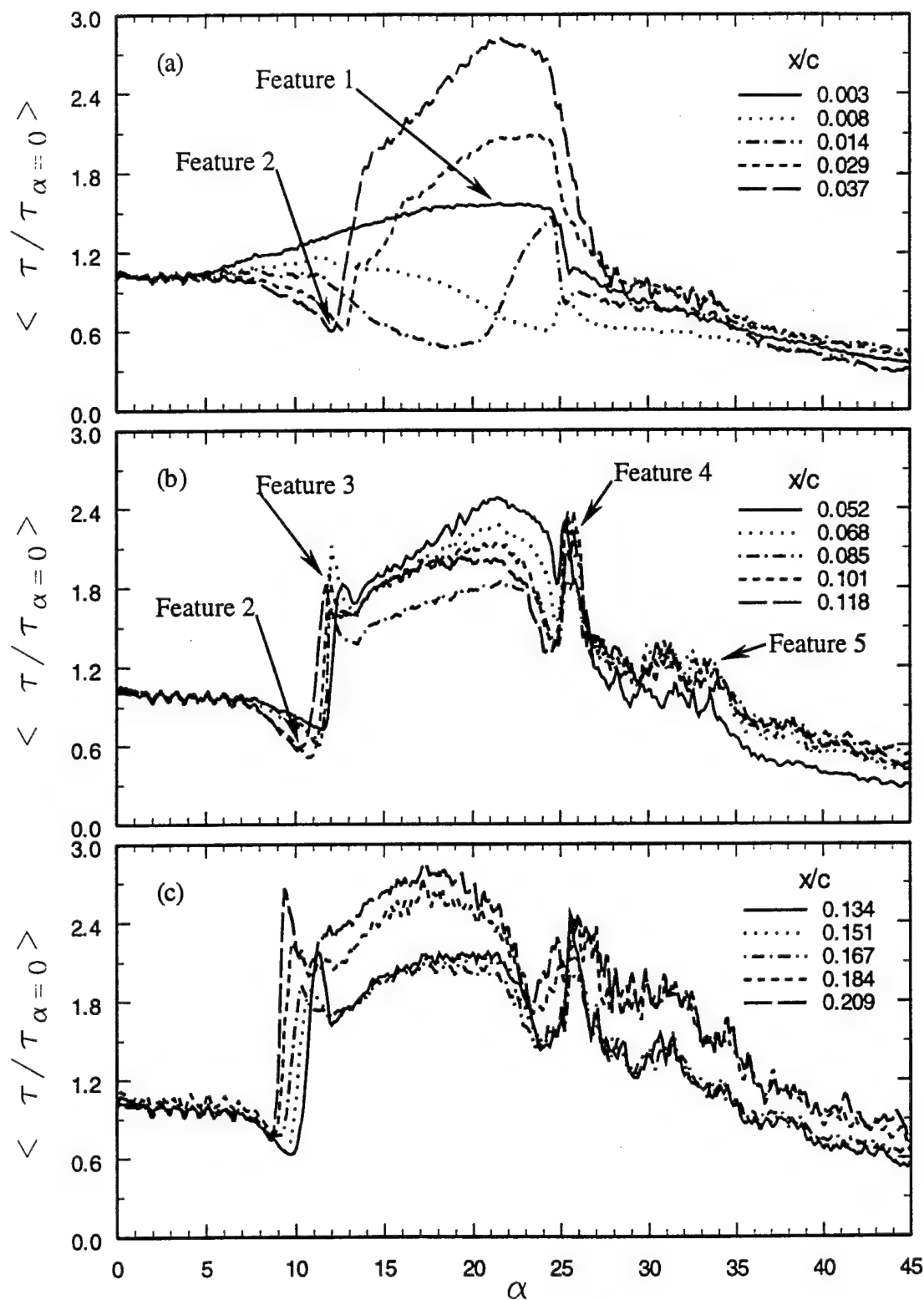


Figure 8 Normalized shear-stress variations during pitch-up for three regions on the airfoil suction surface ( $\alpha^+ = 0.036$ ,  $Re_c = 1.0 \times 10^6$ ).

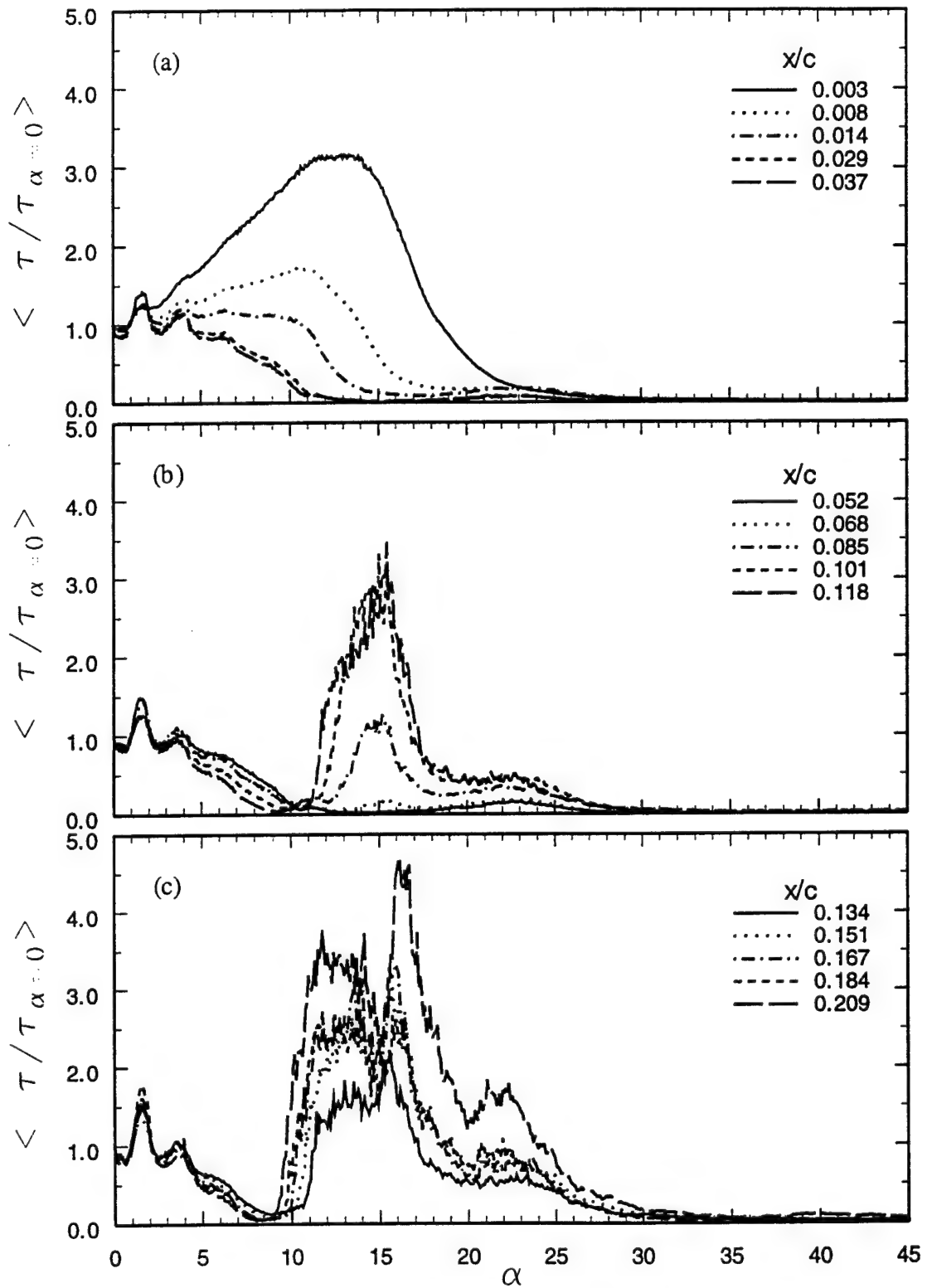


Figure 9 Normalized shear-stress variations during pitch-up for three regions on the airfoil suction surface ( $\alpha^+ = 0.036$ ,  $Re_c = 1.1 \times 10^5$ ).

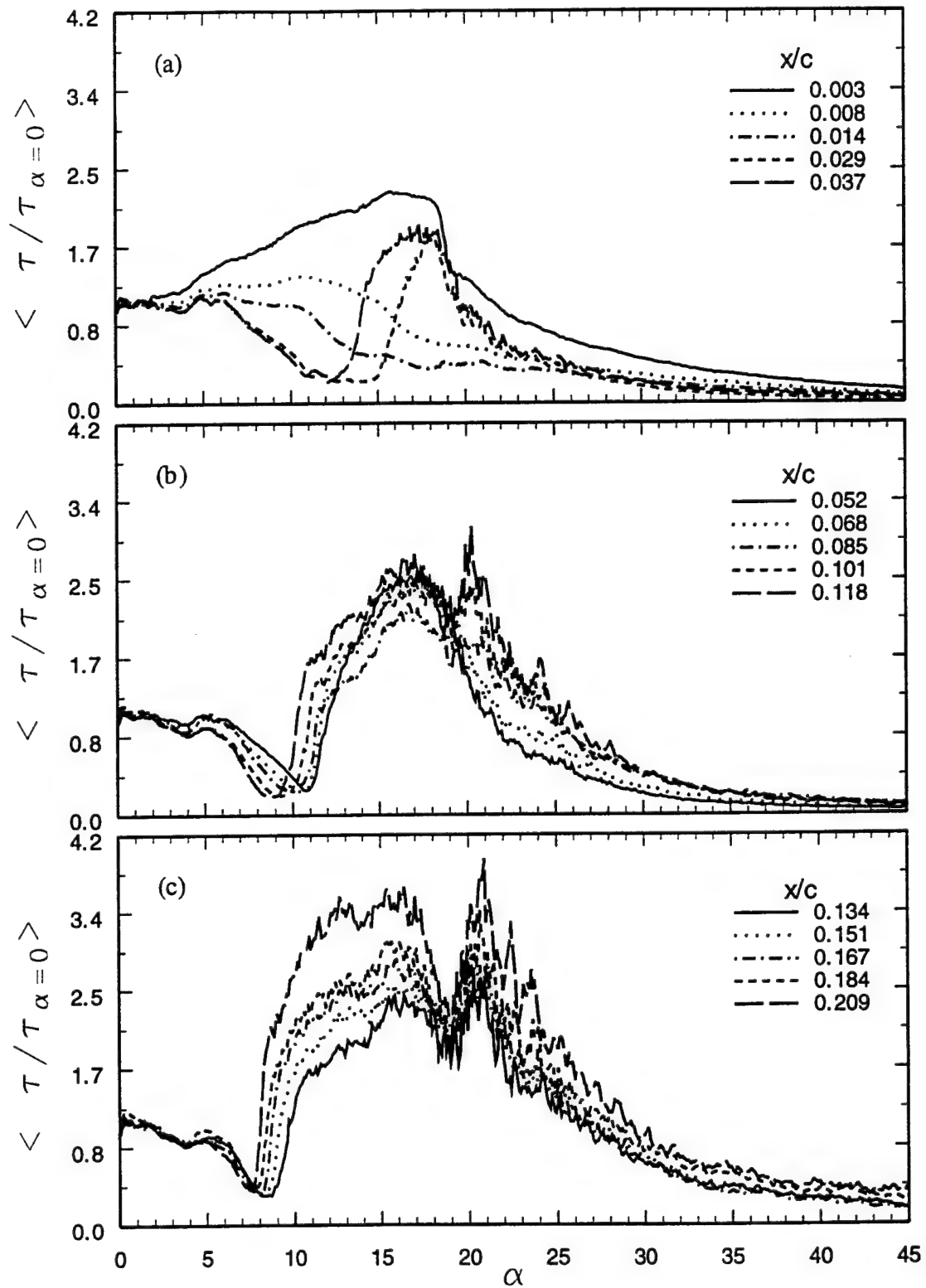


Figure 10 Normalized shear-stress variations during pitch-up for three regions on the airfoil suction surface ( $\alpha^+ = 0.036$ ,  $Re_c = 4.6 \times 10^5$ ).

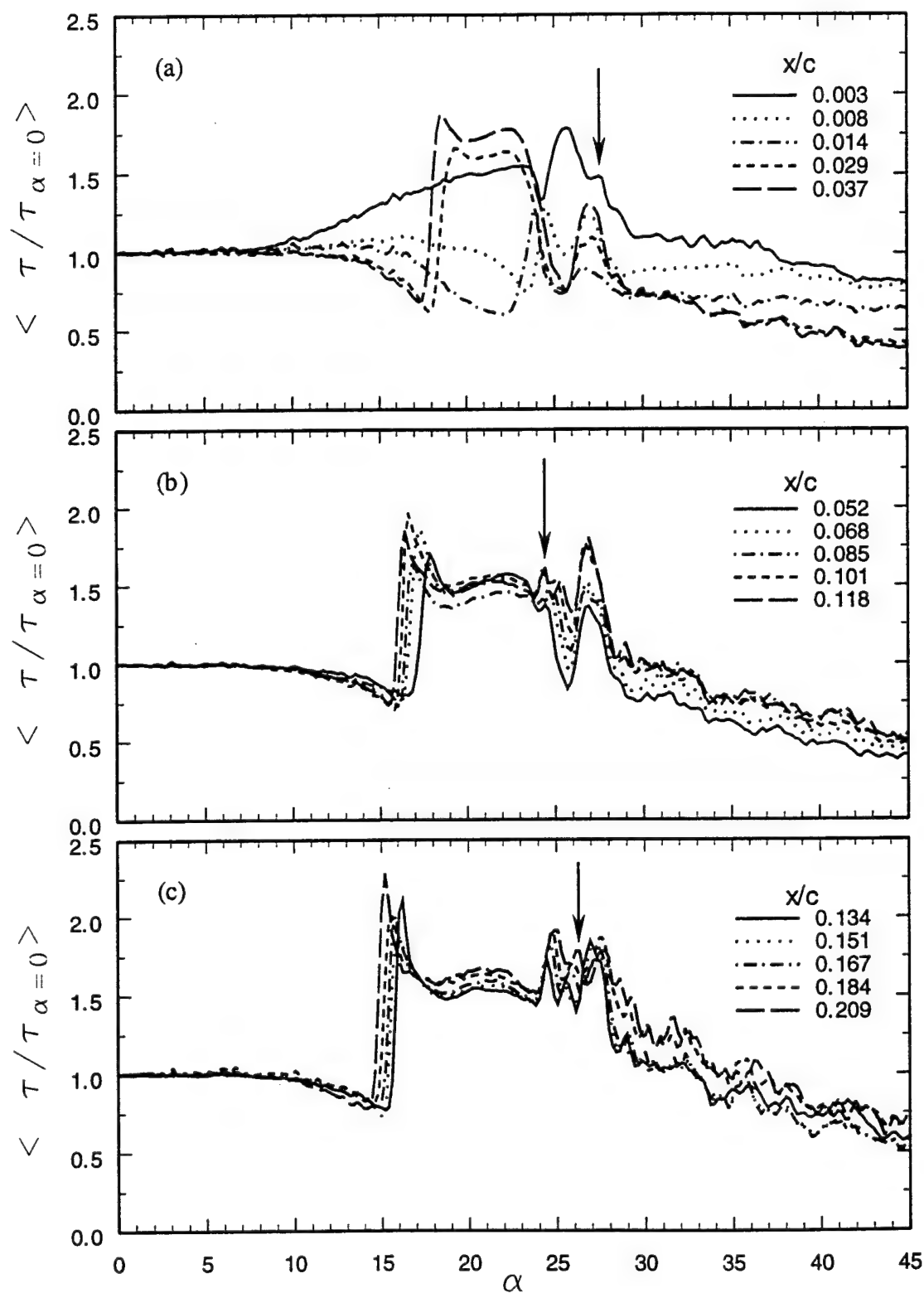


Figure 11 Normalized shear-stress variations during pitch-up for three regions on the airfoil suction surface ( $\alpha^+ = 0.036$ ,  $Re_c = 2.0 \times 10^6$ ).

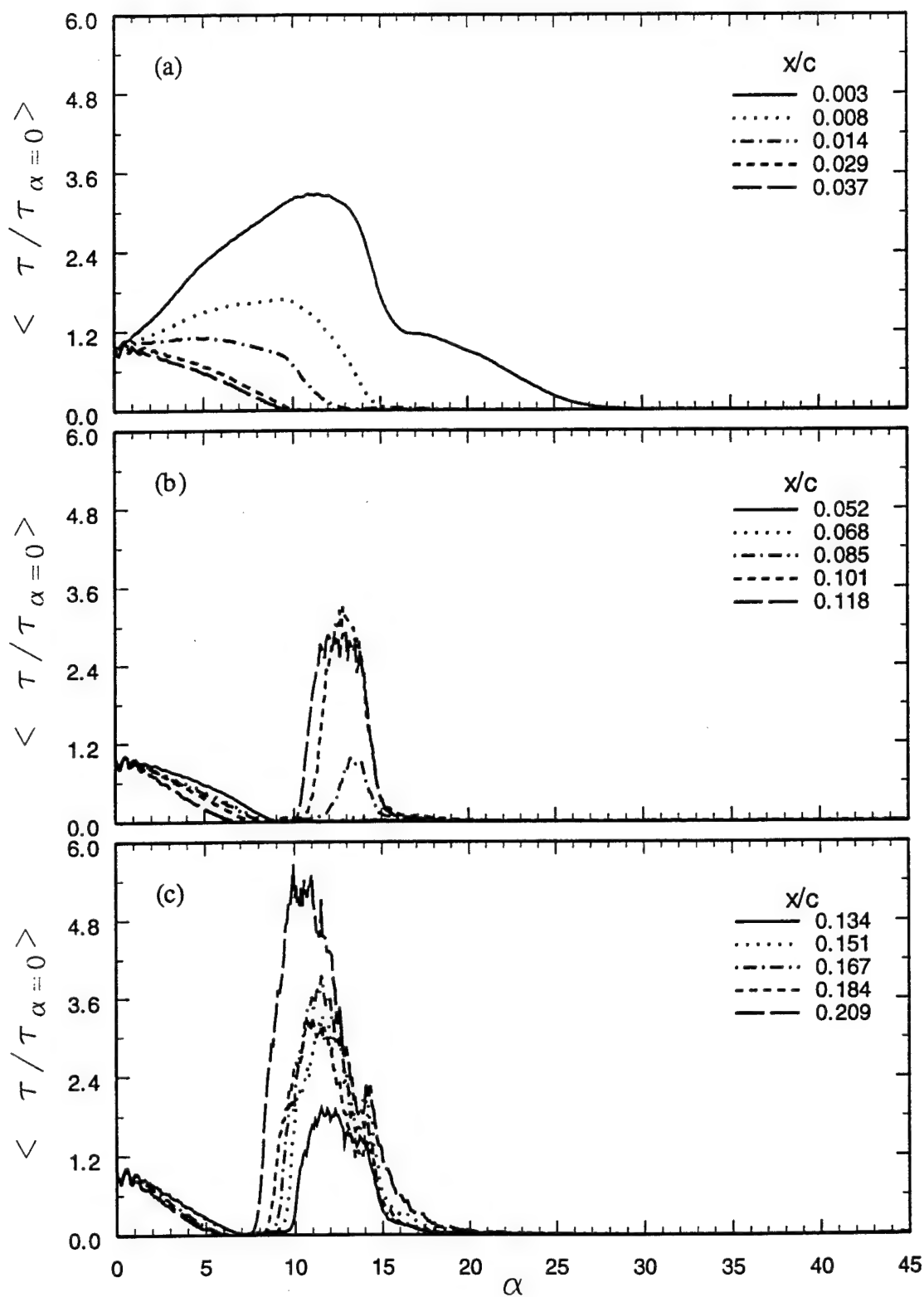


Figure 12 Normalized shear-stress variations during pitch-up for three regions on the airfoil suction surface ( $\alpha^+ = 0.010$ ,  $Re_c = 1.1 \times 10^5$ ).

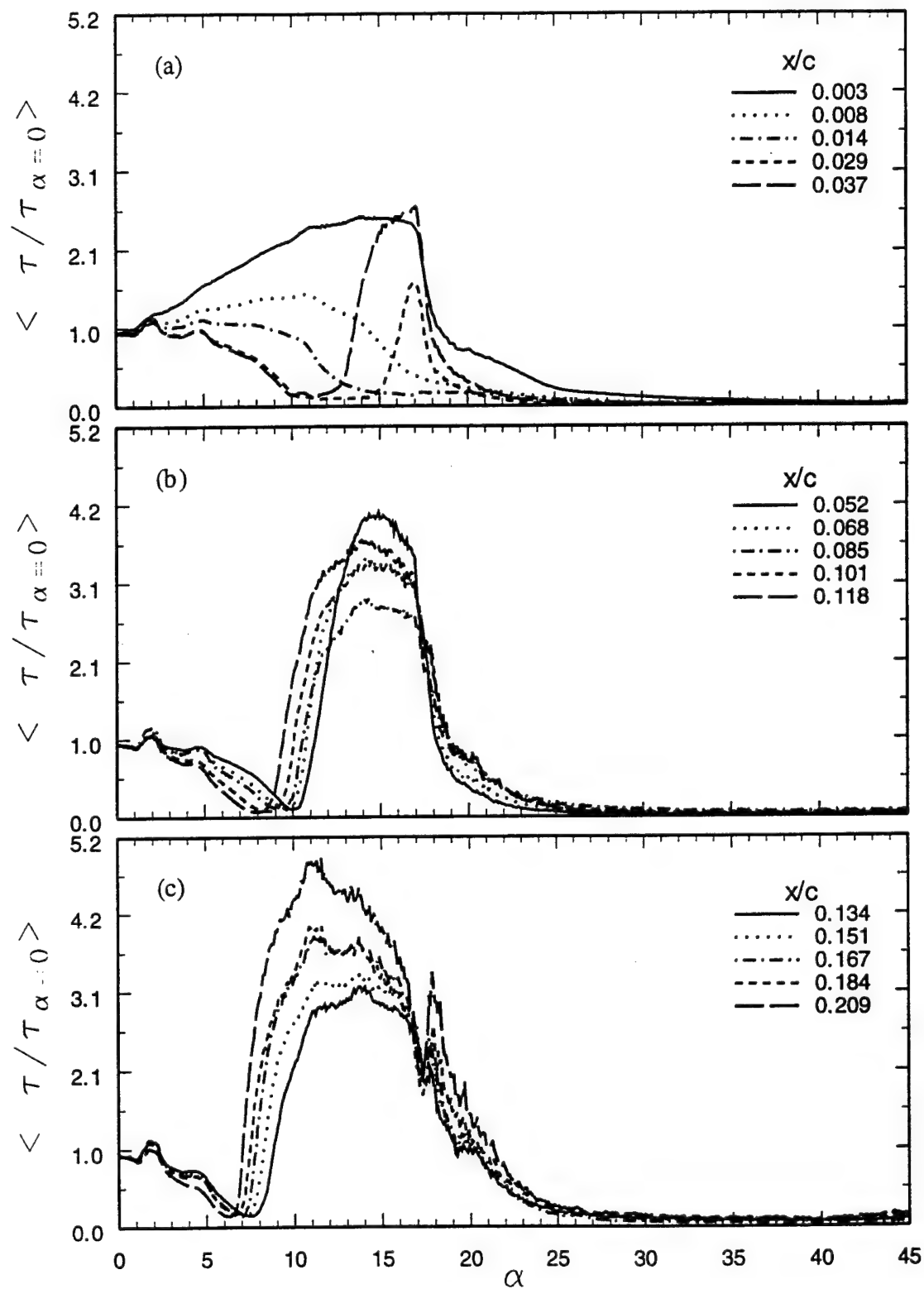


Figure 13 Normalized shear-stress variations during pitch-up for three regions on the airfoil suction surface ( $\alpha^+ = 0.010$ ,  $Re_c = 4.6 \times 10^5$ ).

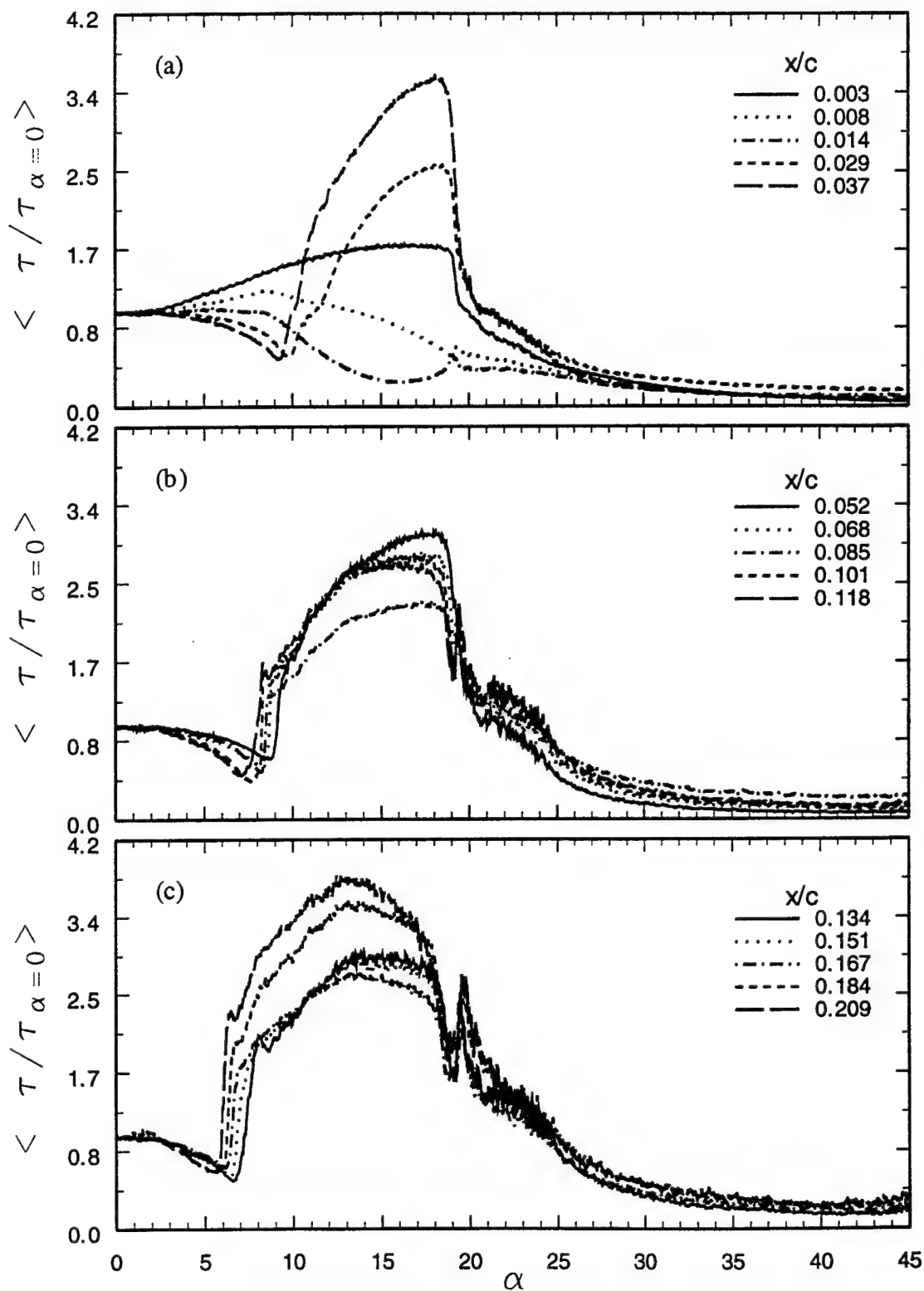


Figure 14 Normalized shear-stress variations during pitch-up for three regions on the airfoil suction surface ( $\alpha^+ = 0.010$ ,  $Re_c = 1.0 \times 10^6$ ).

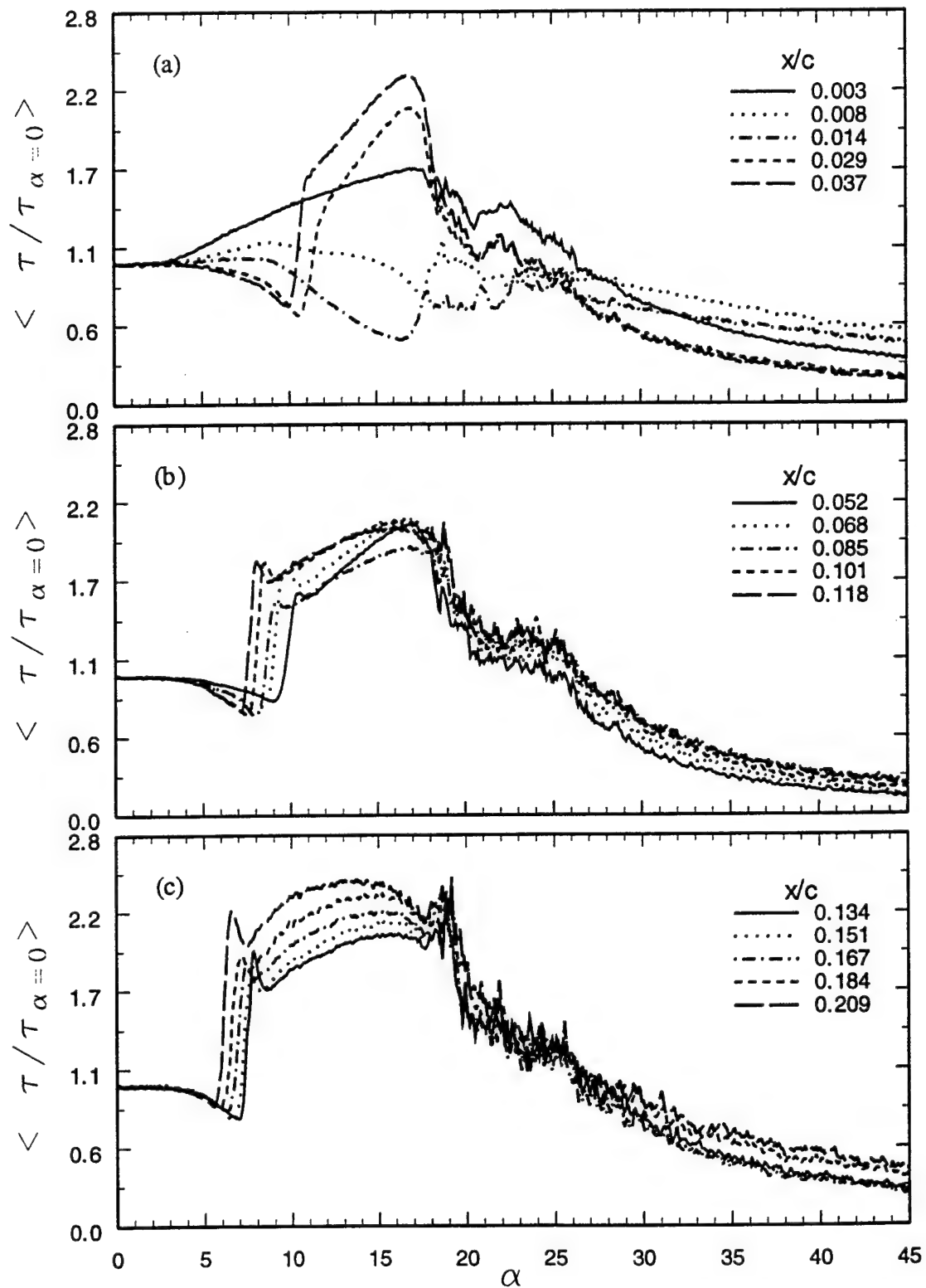


Figure 15 Normalized shear-stress variations during pitch-up for three regions on the airfoil suction surface ( $\alpha^+ = 0.010$ ,  $Re_c = 2.0 \times 10^6$ ).



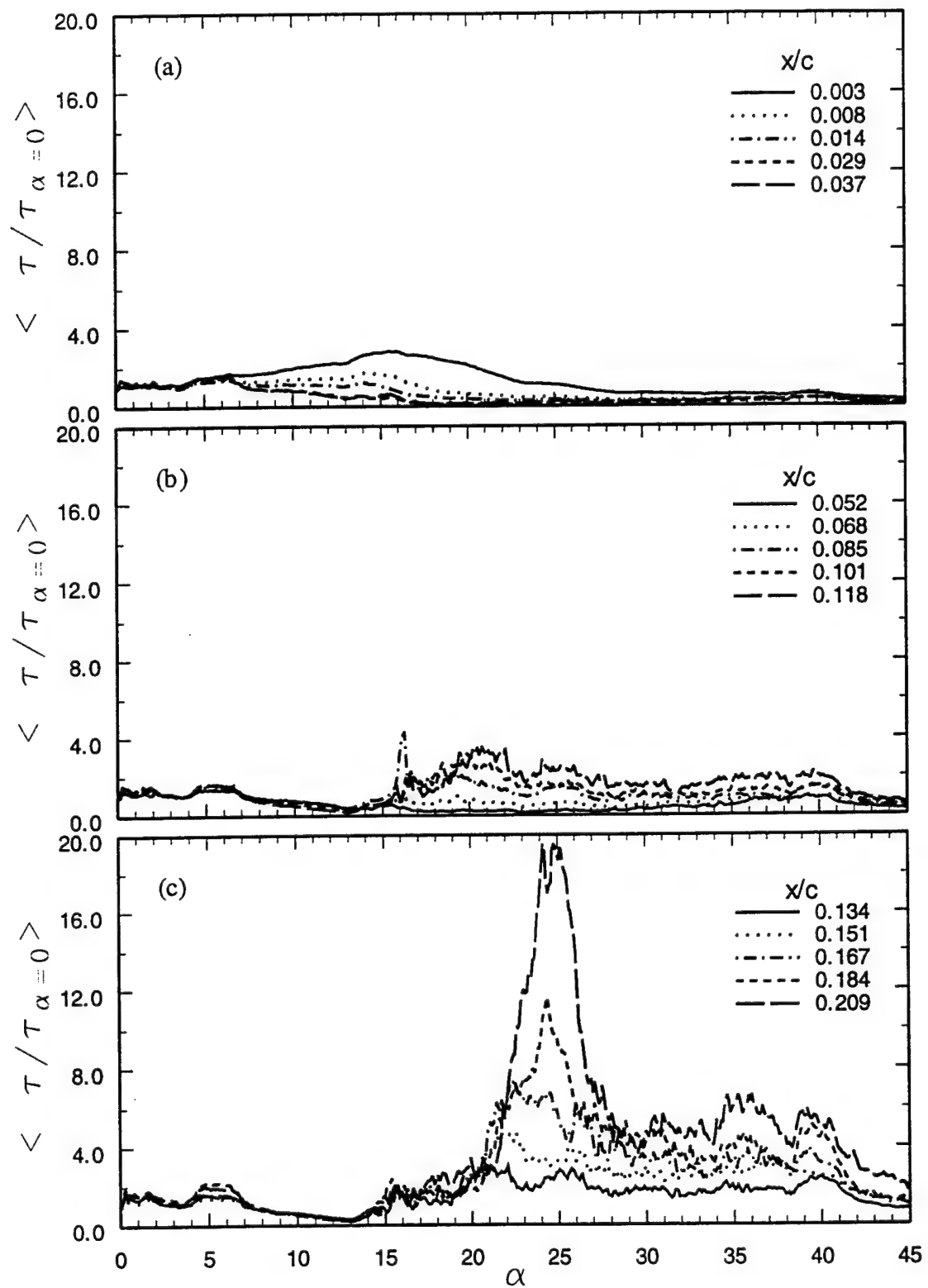


Figure 16 Normalized shear-stress variations during pitch-up for three regions on the airfoil suction surface ( $\alpha^+ = 0.150$ ,  $Re_c = 1.1 \times 10^5$ ).

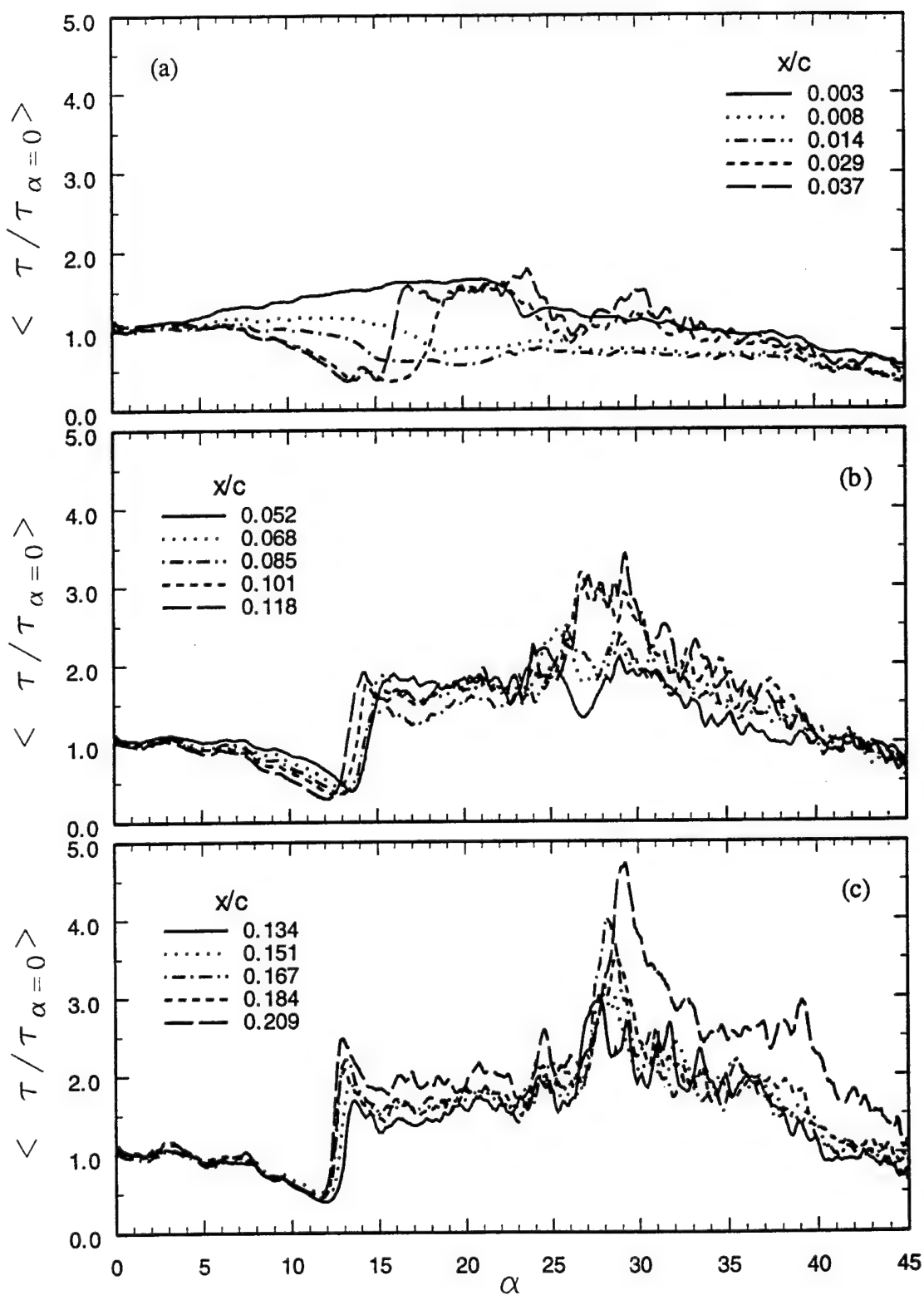


Figure 17 Normalized shear-stress variations during pitch-up for three regions on the airfoil suction surface ( $\alpha^+ = 0.150$ ,  $Re_c = 4.6 \times 10^5$ ).

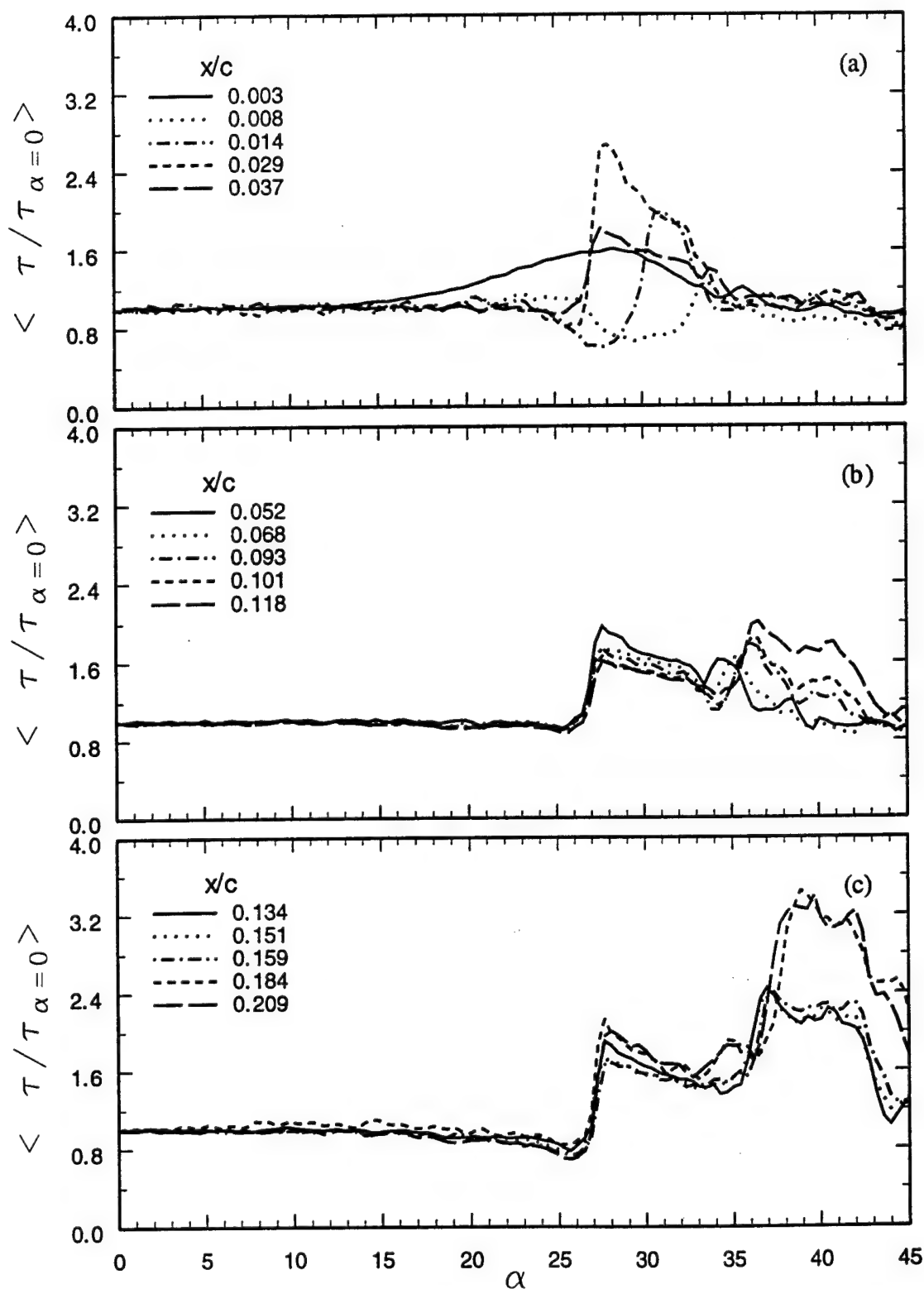


Figure 18 Normalized shear-stress variations during pitch-up for three regions on the airfoil suction surface ( $\alpha^+ = 0.150$ ,  $Re_c = 1.0 \times 10^6$ ).

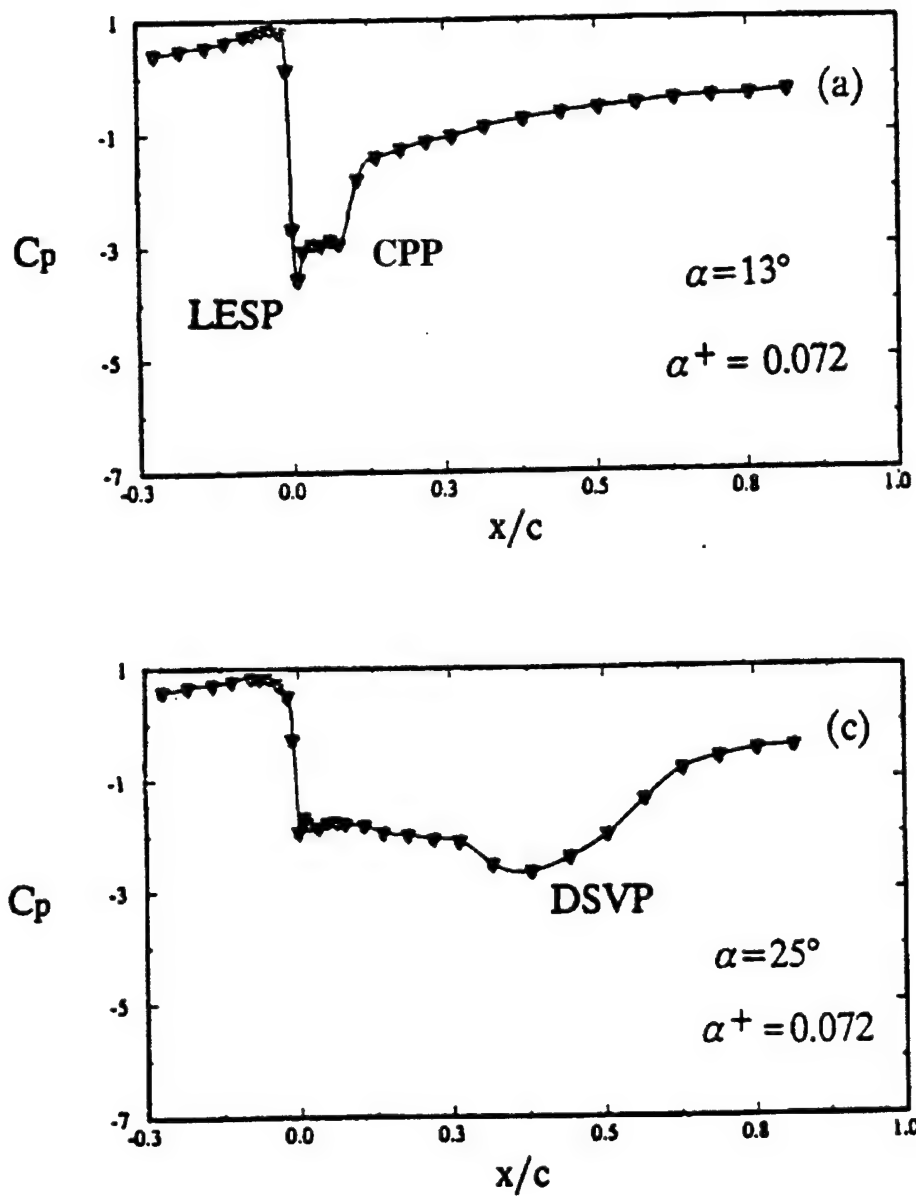


Figure 19 Dominant features of the surface pressure distributions (from Acharya and Metwally<sup>39</sup>).

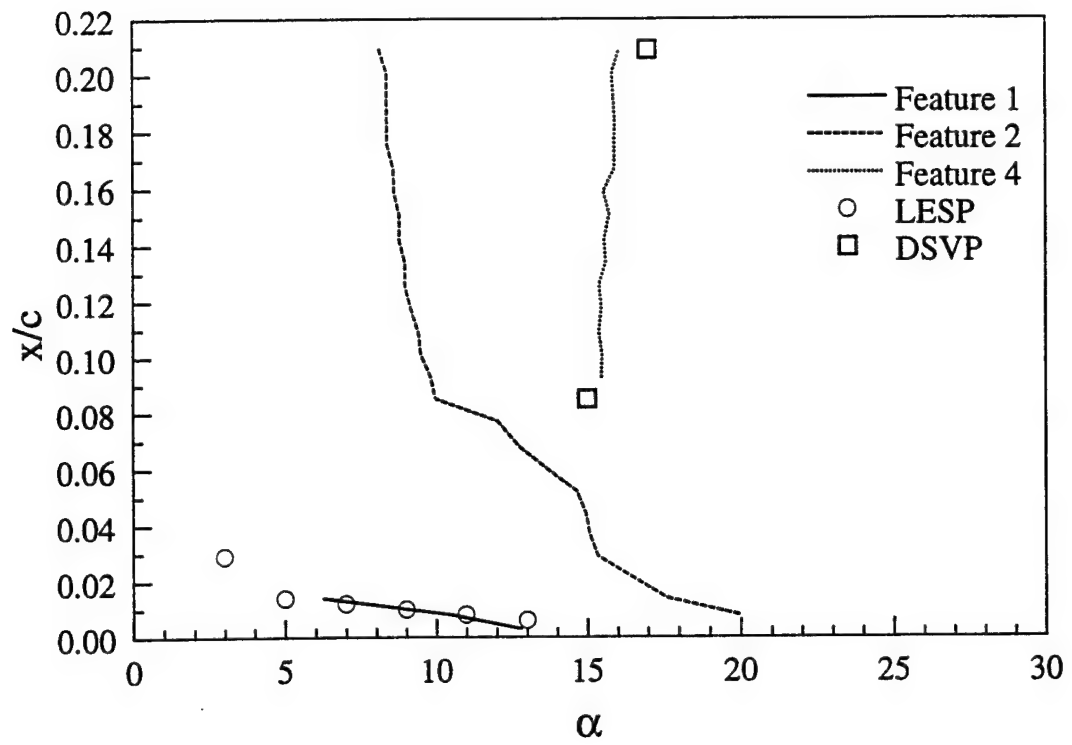


Figure 20 Location and movement of the dominant shear stress features ( $\alpha^+ = 0.036$ ,  $Re_c = 1.1 \times 10^5$ ). LESP and DSVP data from Acharya and Metwally<sup>39</sup>.

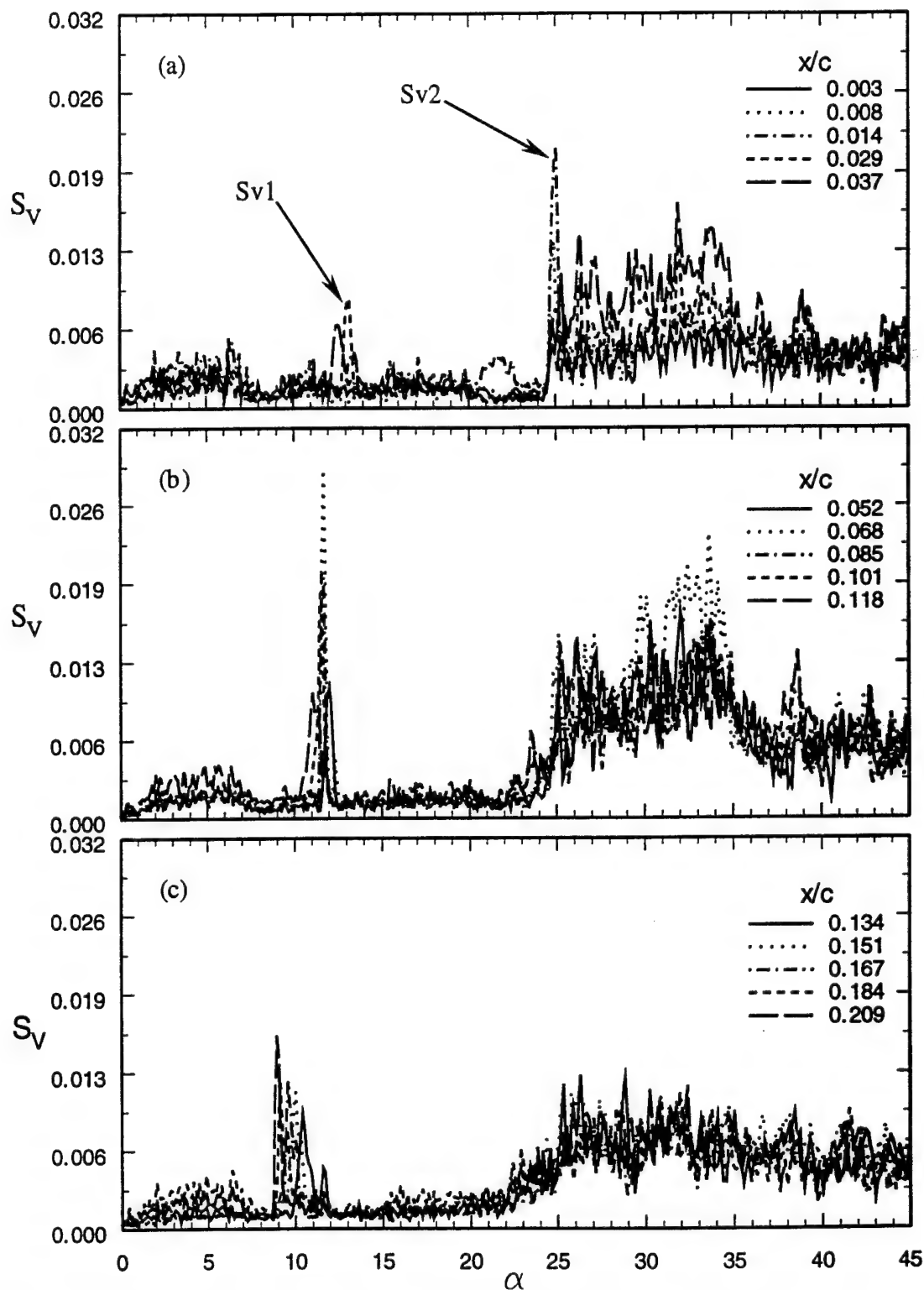


Figure 21 Standard deviations of the hot-film sensor output voltages during pitch-up for three regions on the airfoil suction surface ( $\alpha^+ = 0.036$ ,  $Re_c = 1.0 \times 10^6$ ).

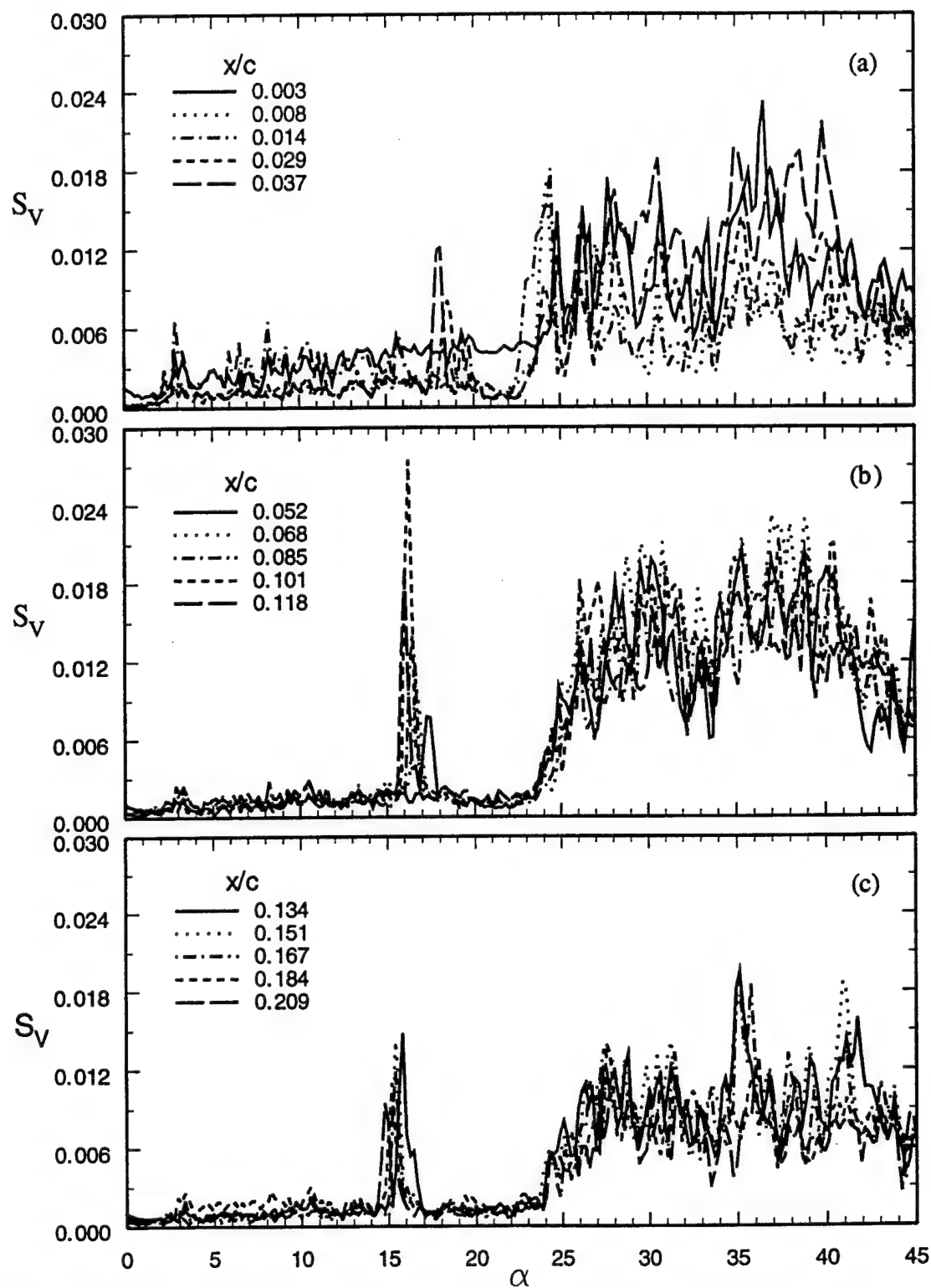


Figure 22 Standard deviations of the hot-film sensor output voltages during pitch-up for three regions on the airfoil suction surface ( $\alpha^+ = 0.036$ ,  $Re_c = 2.0 \times 10^6$ ).

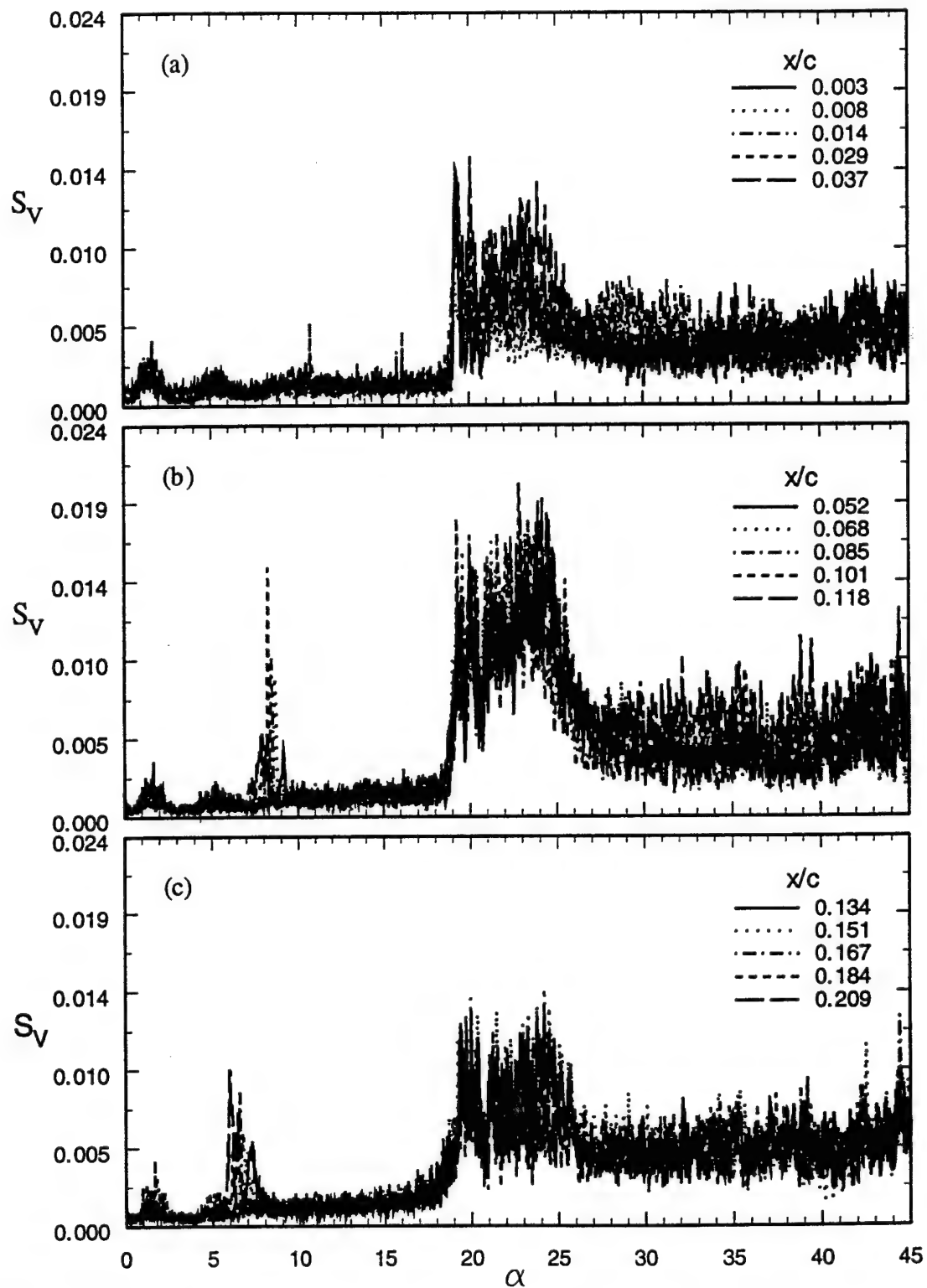


Figure 23 Standard deviations of the hot-film sensor output voltages during pitch-up for three regions on the airfoil suction surface ( $\alpha^+ = 0.010$ ,  $Re_c = 1.0 \times 10^6$ ).



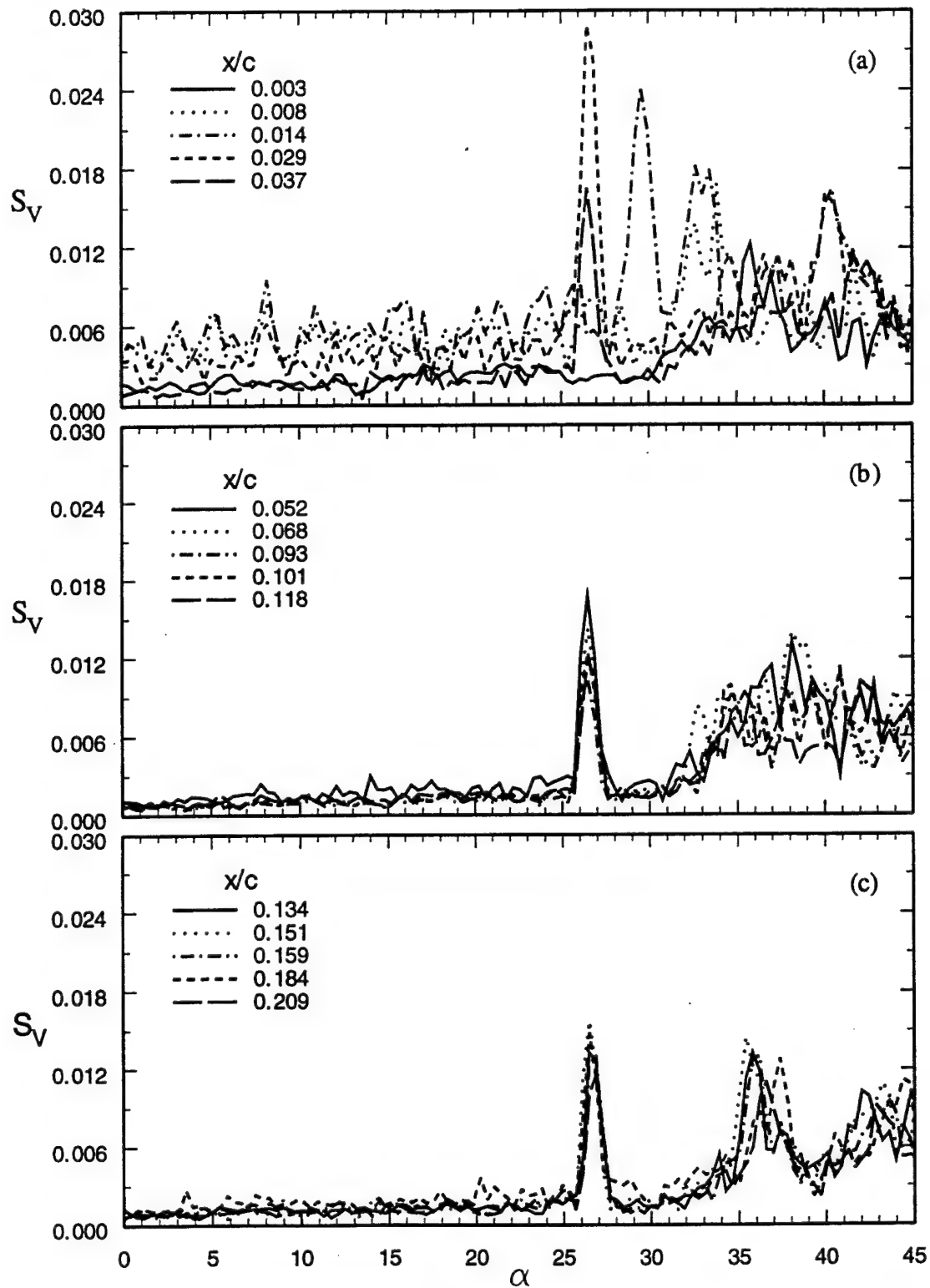


Figure 24 Standard deviations of the hot-film sensor output voltages during pitch-up for three regions on the airfoil suction surface ( $\alpha^+ = 0.150$ ,  $Re_c = 1.0 \times 10^6$ ).

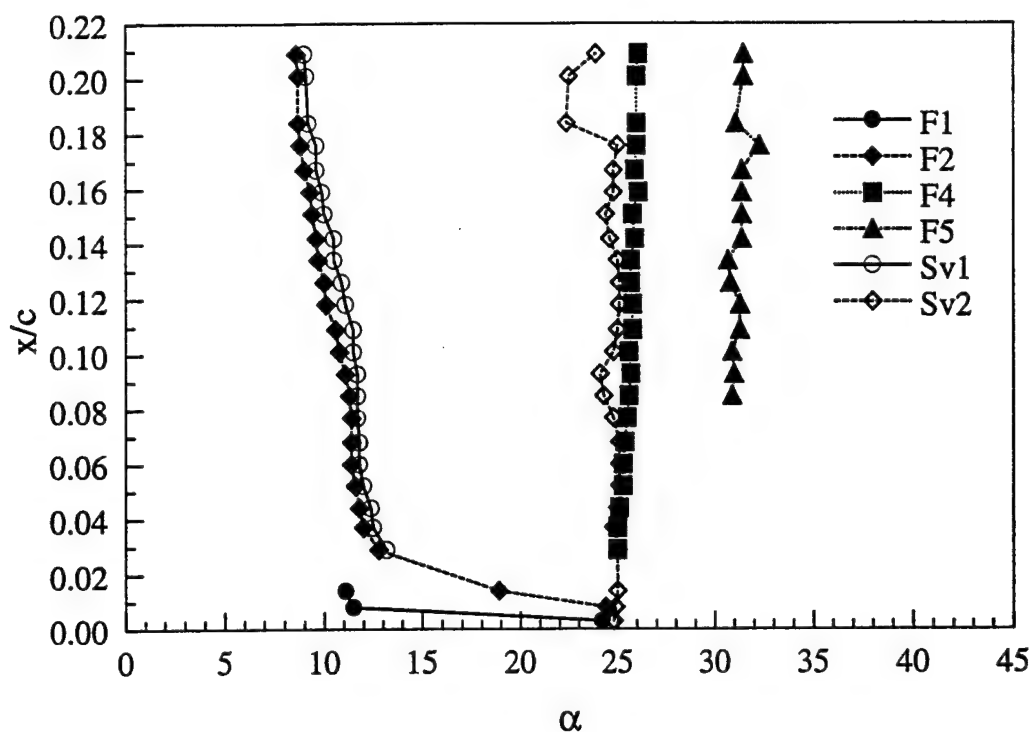


Figure 25 Location and movement of the dominant shear stress and standard deviation features ( $\alpha^+ = 0.036$ ,  $Re_c = 1.0 \times 10^6$ ).

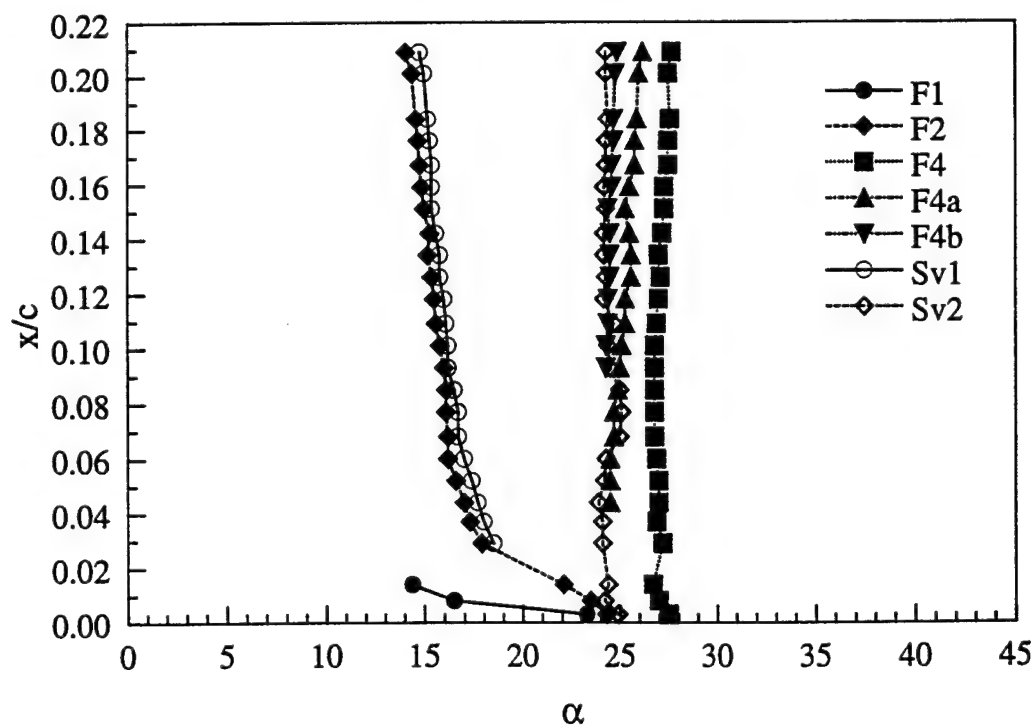


Figure 26 Location and movement of the dominant shear stress and standard deviation features ( $\alpha^+ = 0.036$ ,  $Re_c = 2.0 \times 10^6$ ).

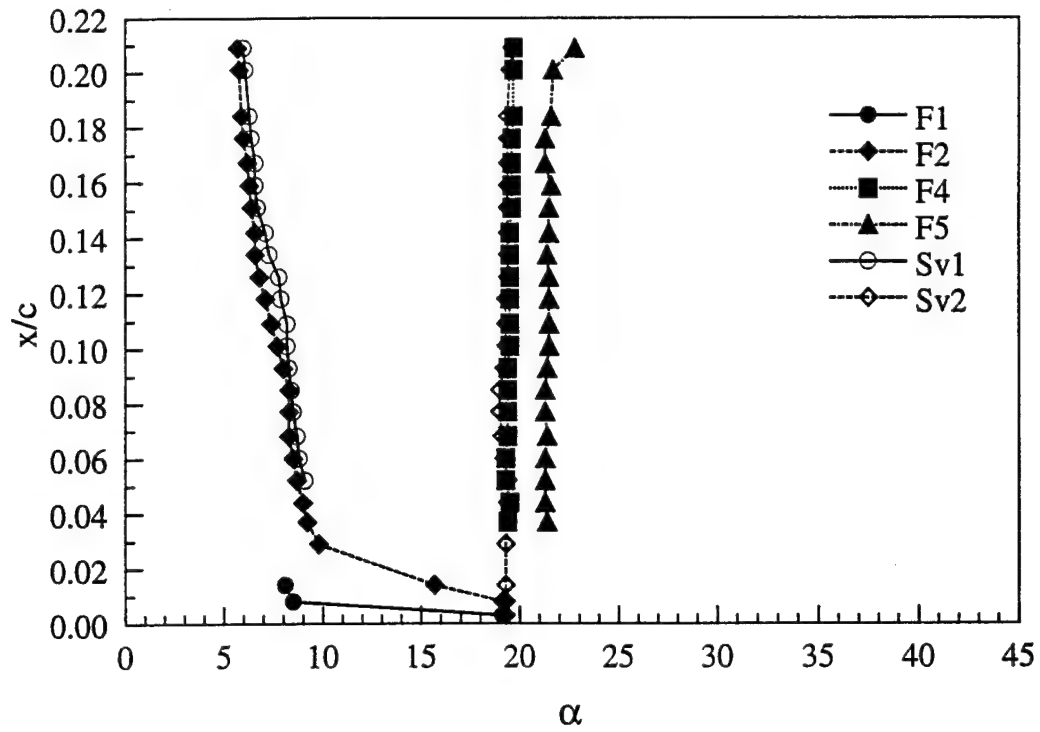


Figure 27 Location and movement of the dominant shear stress and standard deviation features ( $\alpha^+ = 0.010$ ,  $Re_c = 1.0 \times 10^6$ ).

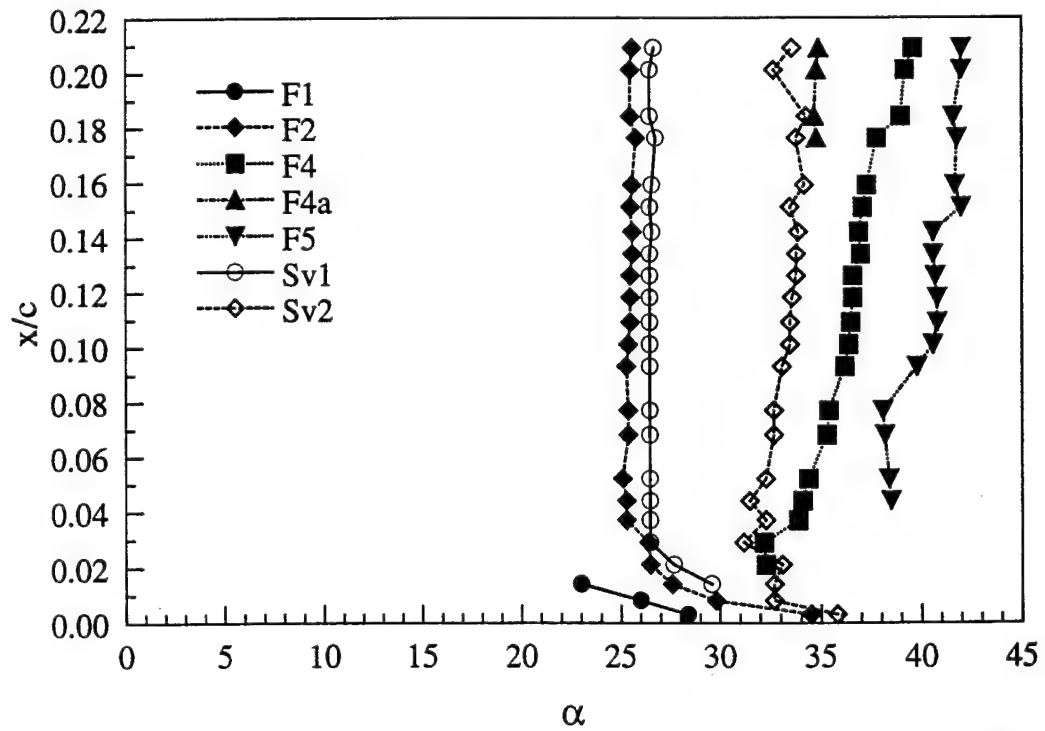


Figure 28 Location and movement of the dominant shear stress and standard deviation features ( $\alpha^+ = 0.150$ ,  $Re_c = 1.0 \times 10^6$ ).

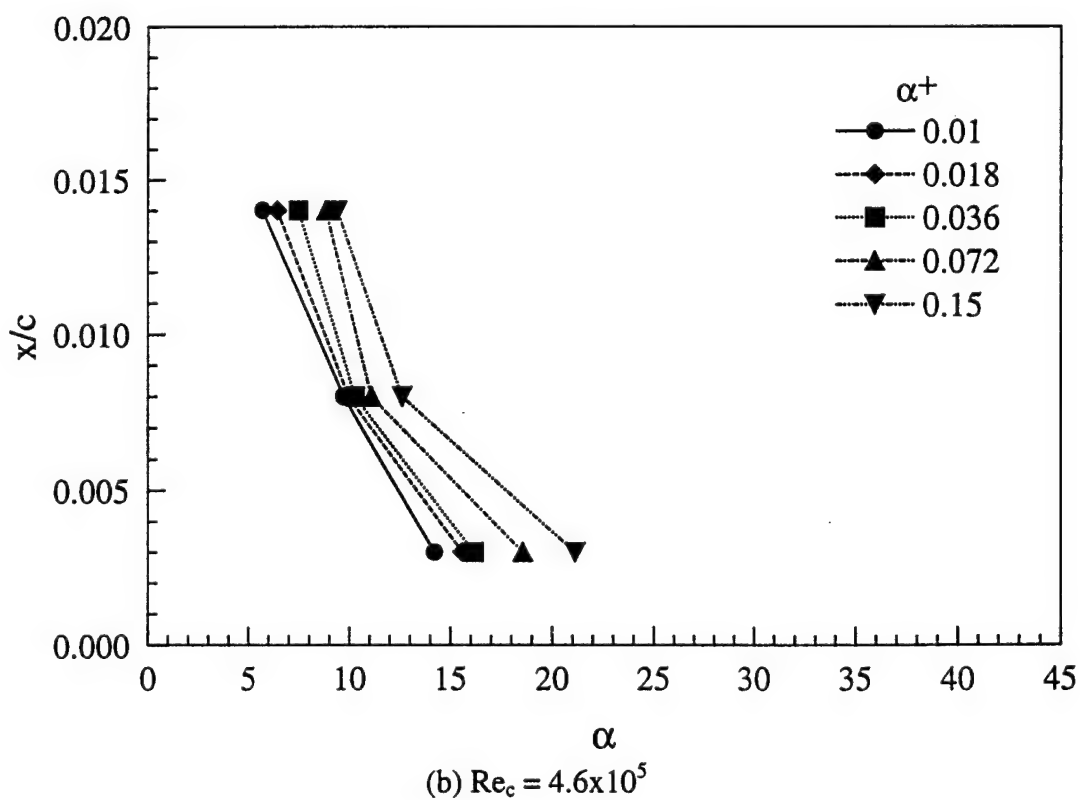
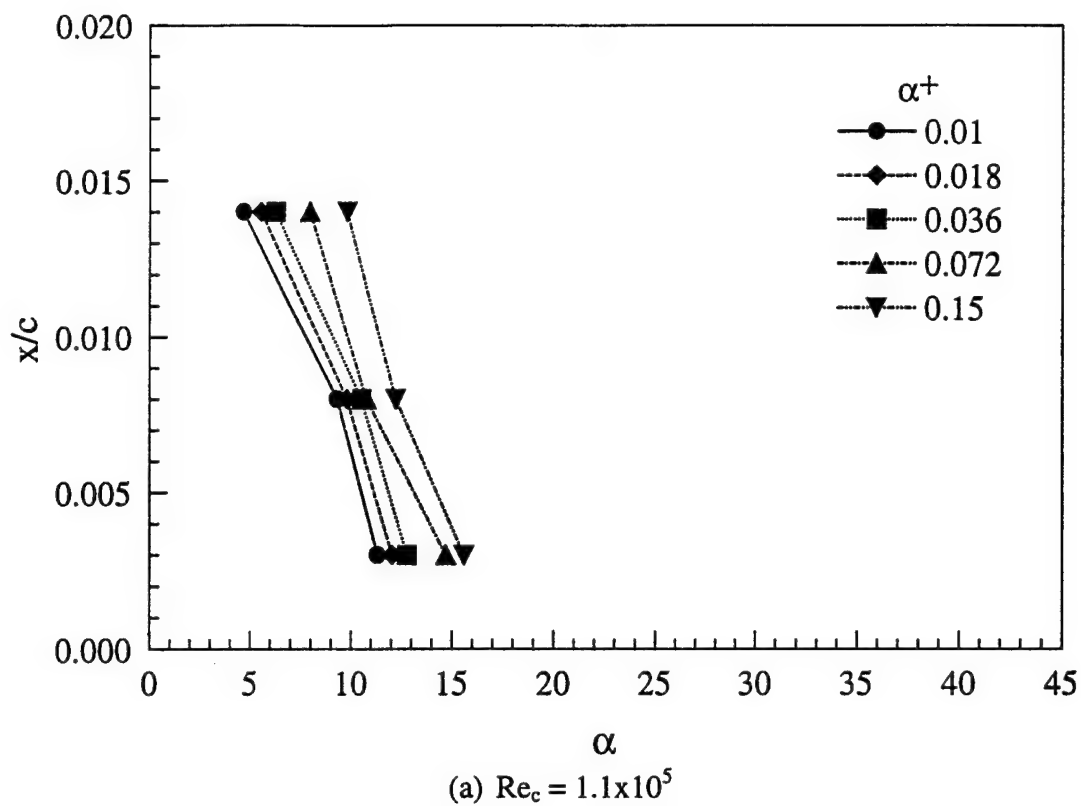
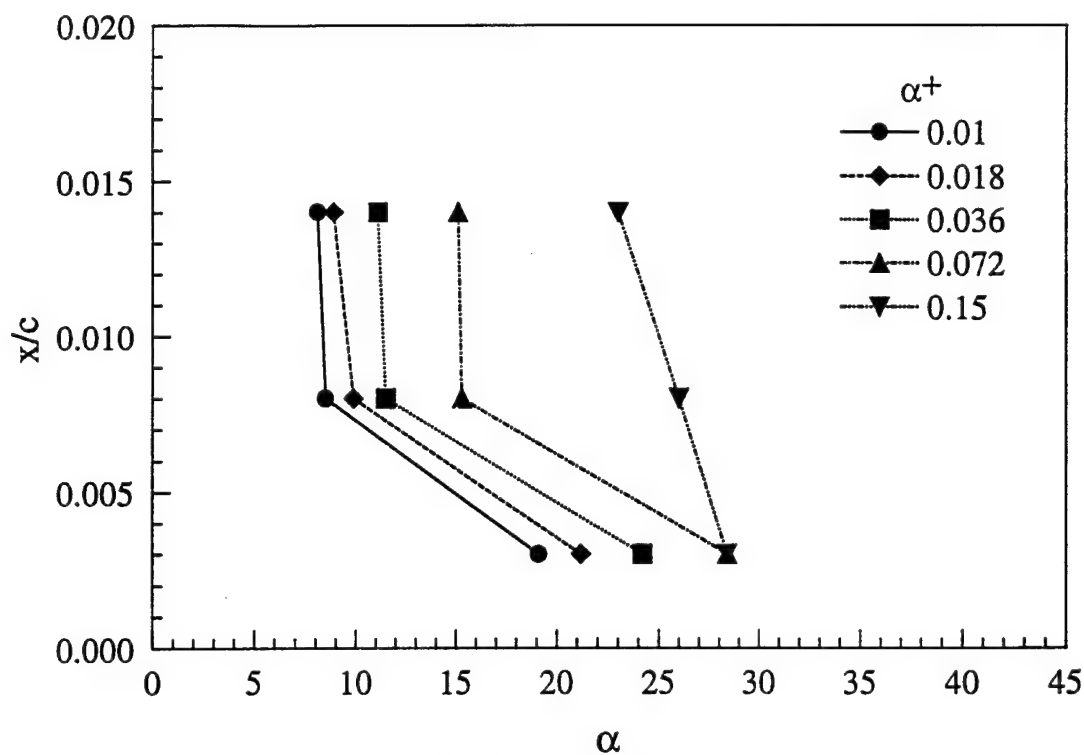
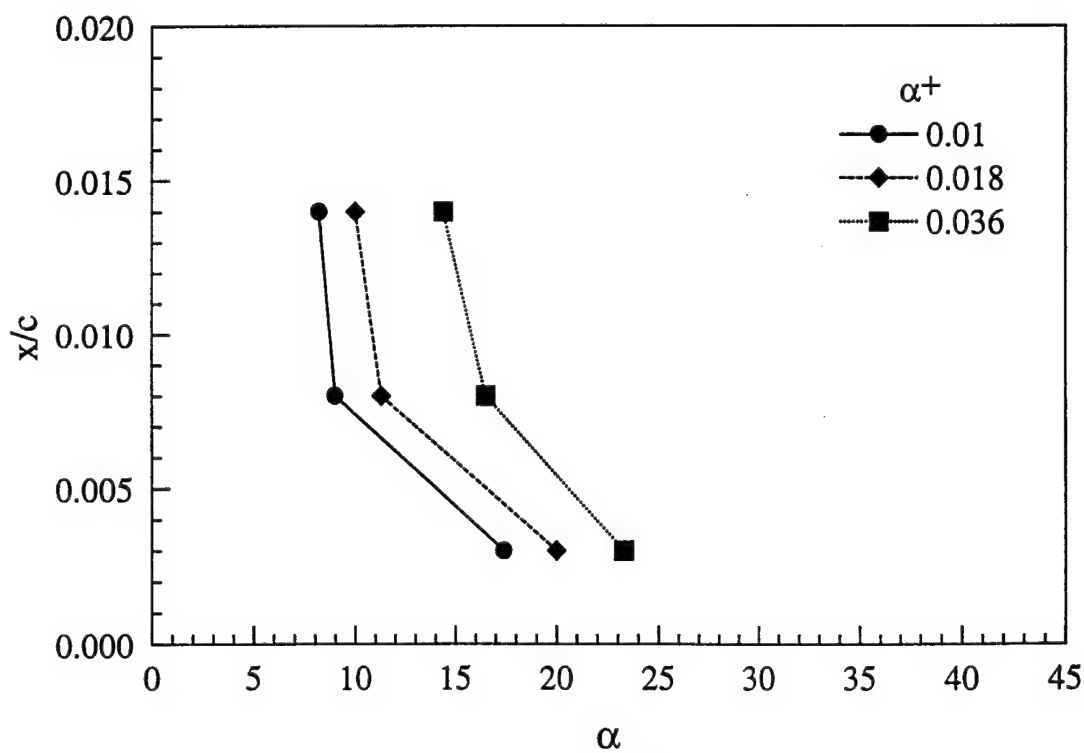


Figure 29 Behavior of shear stress feature 1 with varying pitch rate.

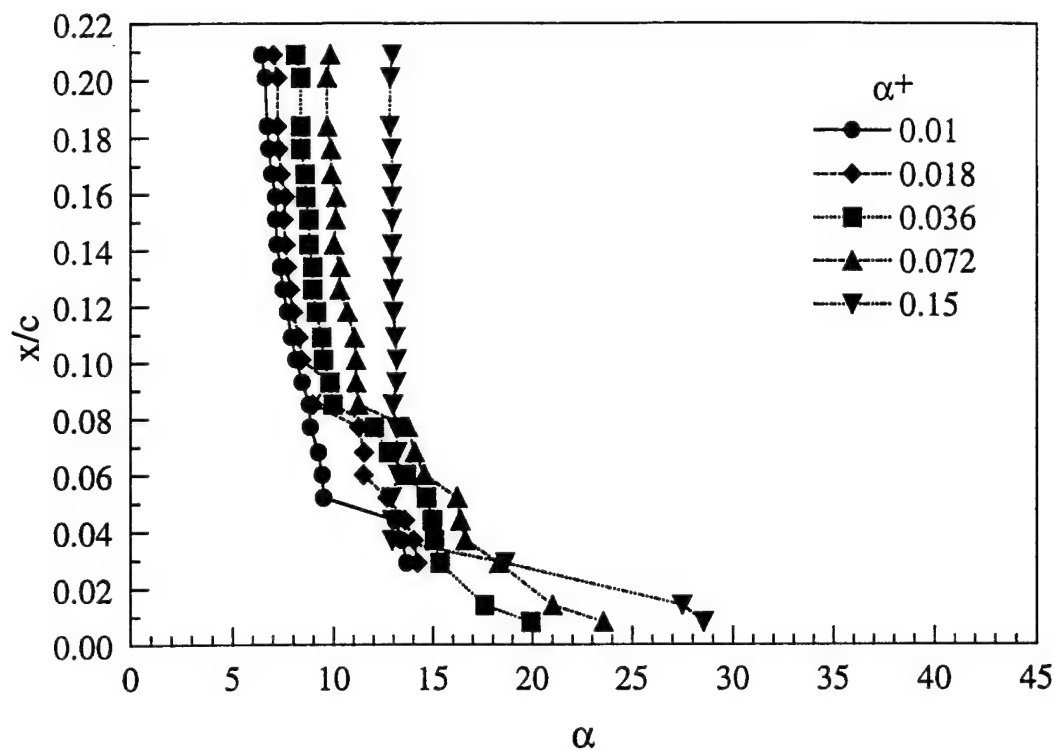


(c)  $Re_c = 1.0 \times 10^6$

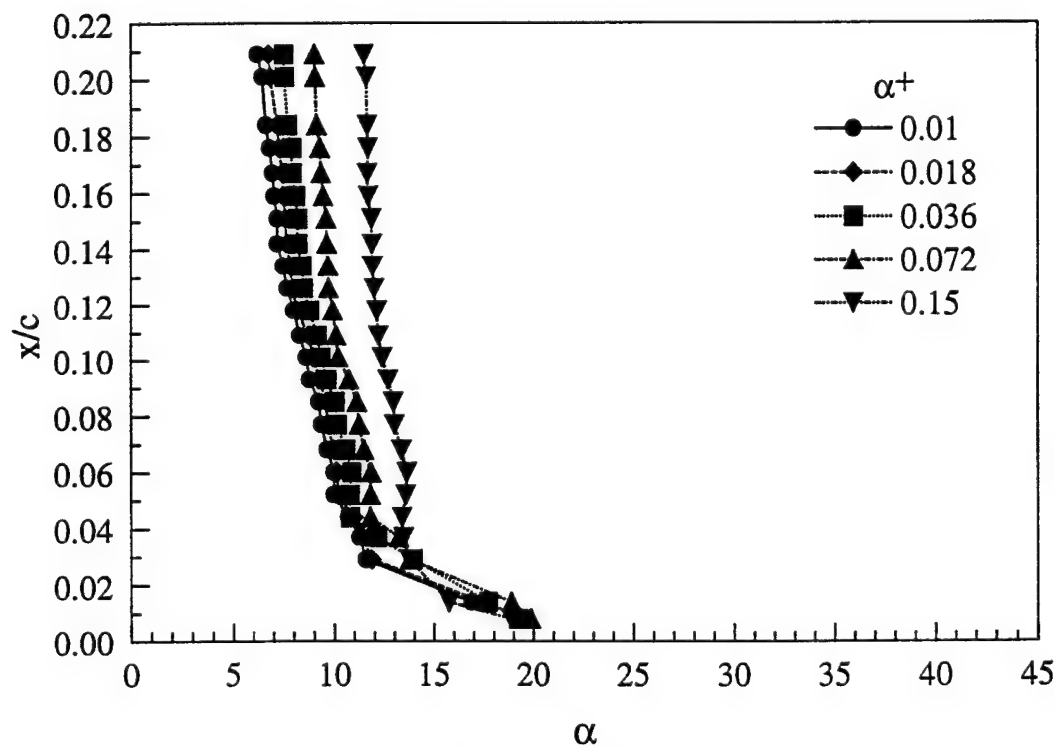


(d)  $Re_c = 2.0 \times 10^6$

Figure 29 (concluded).



(a)  $Re_c = 1.1 \times 10^5$



(b)  $Re_c = 4.6 \times 10^5$

Figure 30 Behavior of shear stress feature 2 with varying pitch rate.

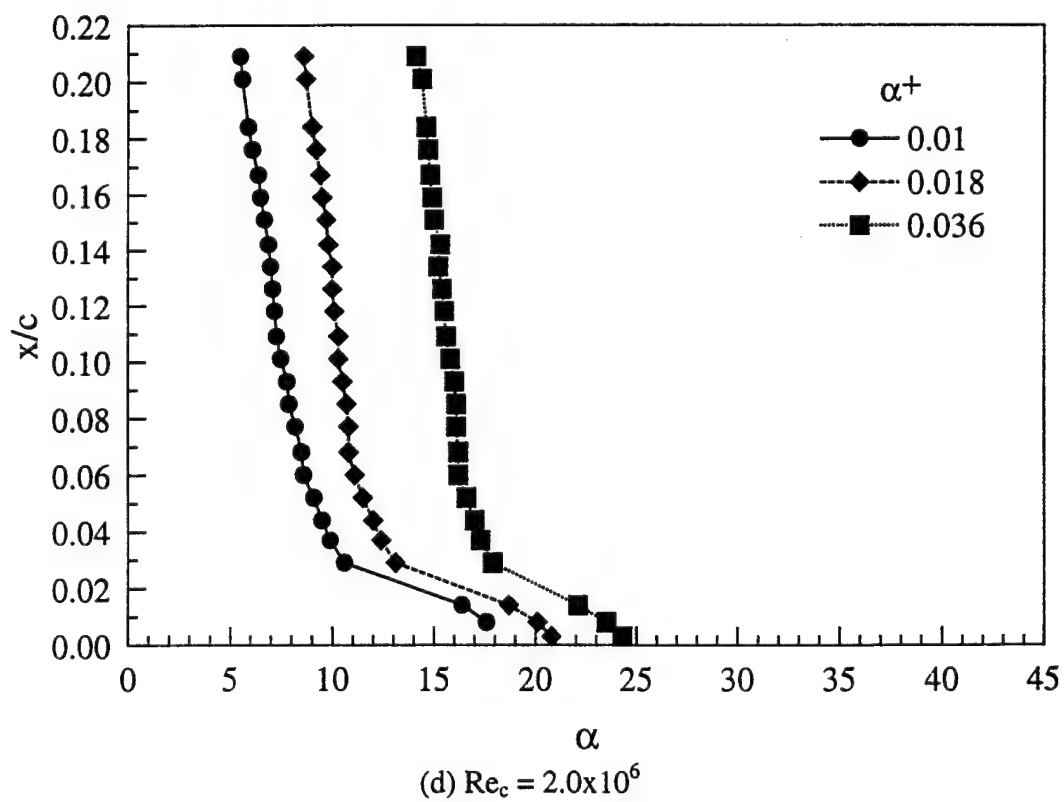
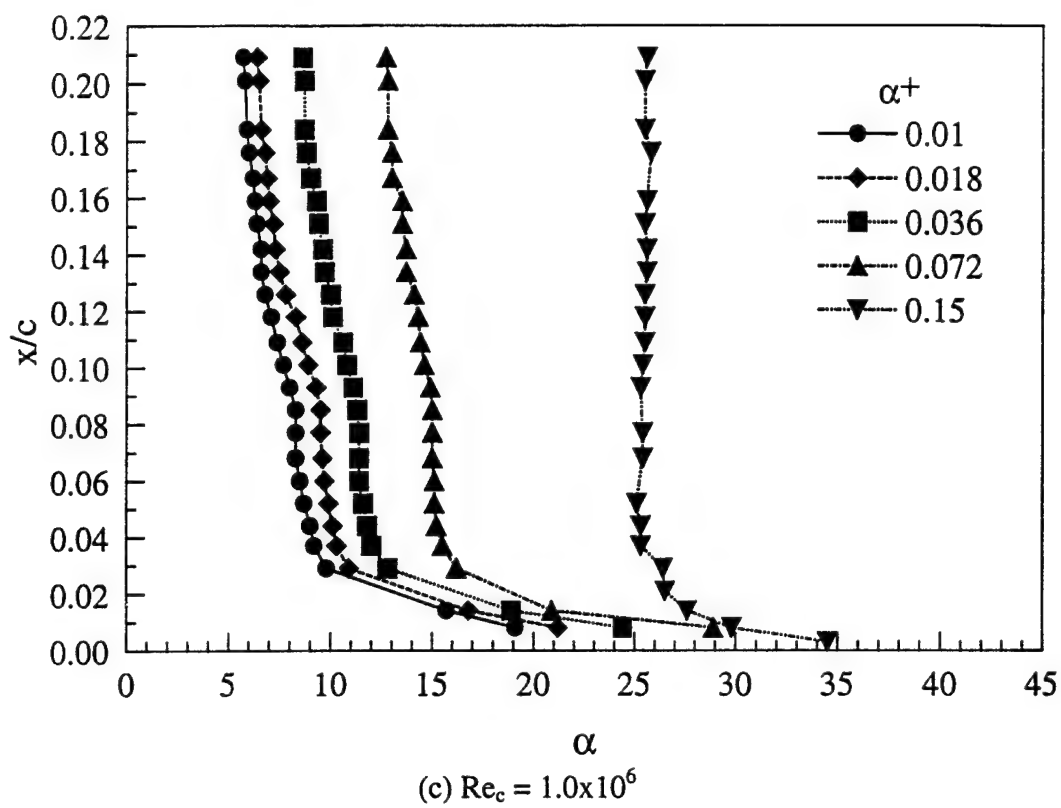
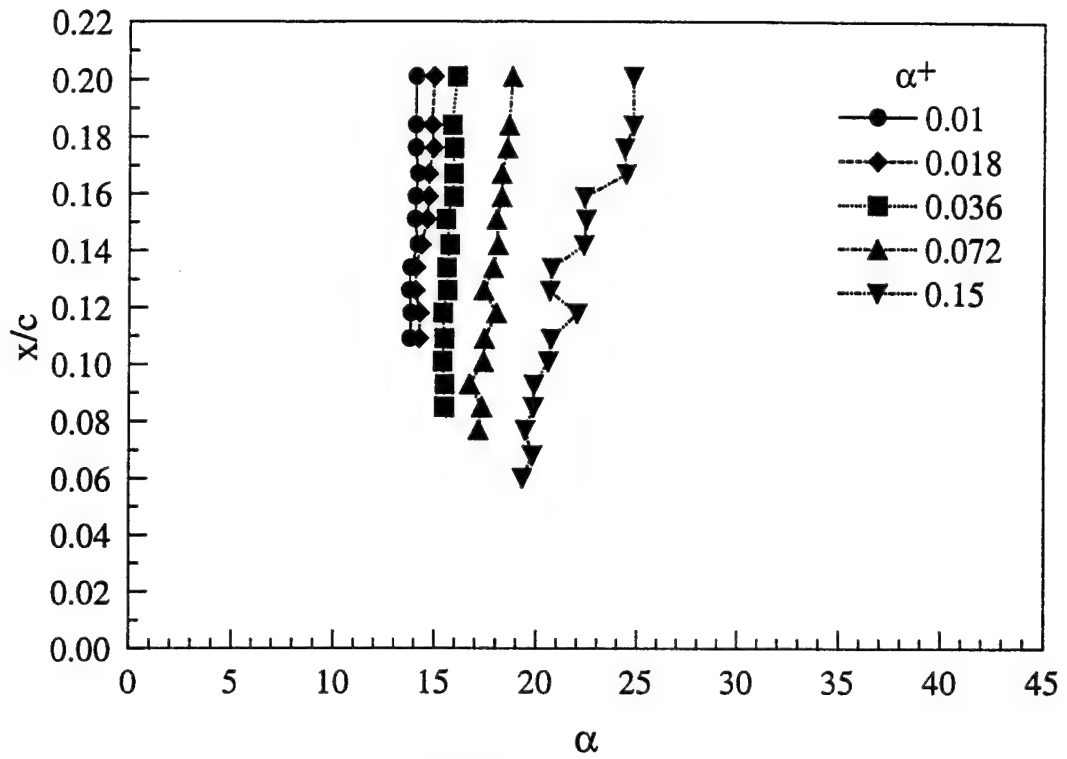
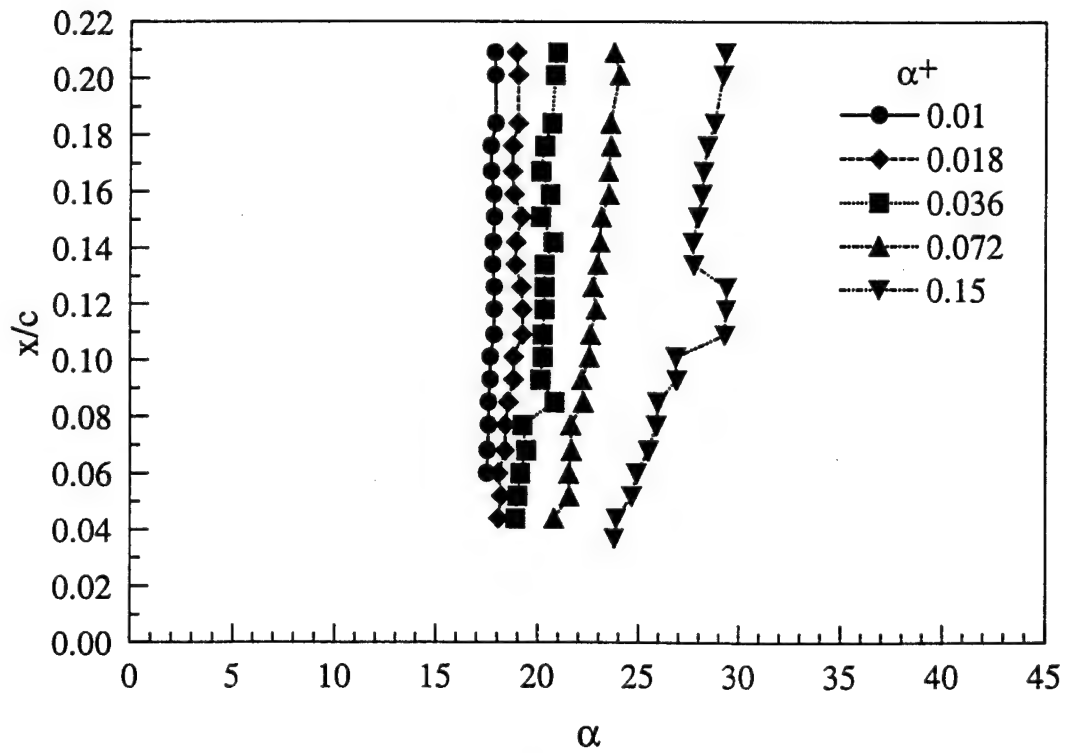


Figure 30 (concluded).



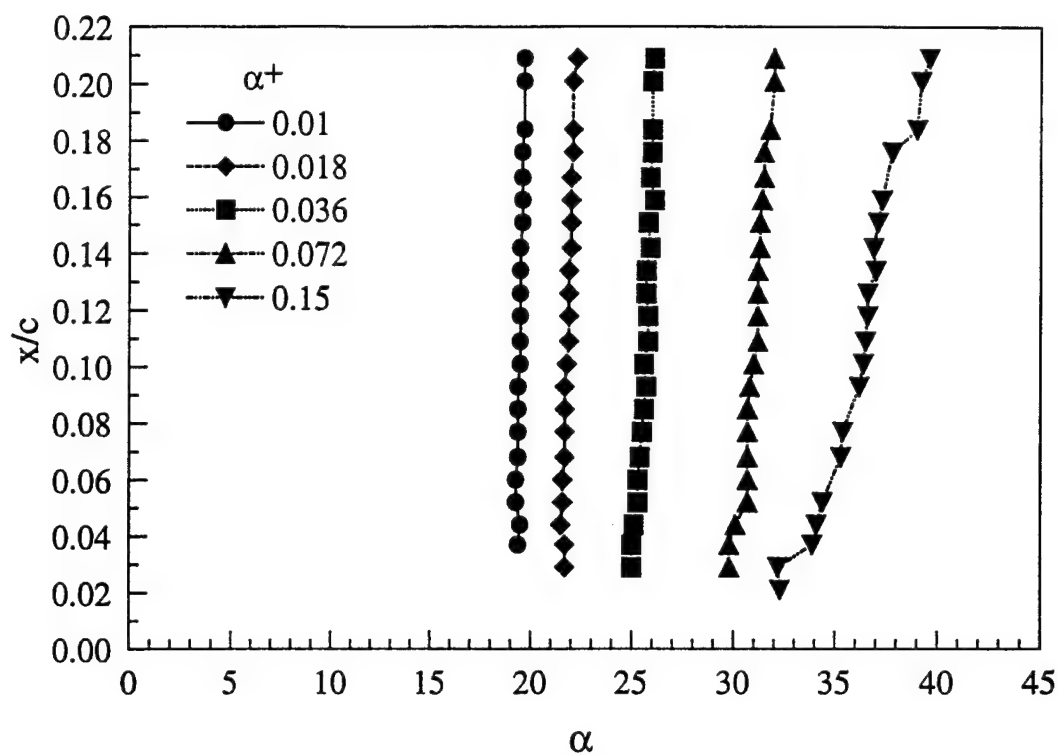
(a)  $Re_c = 1.1 \times 10^5$



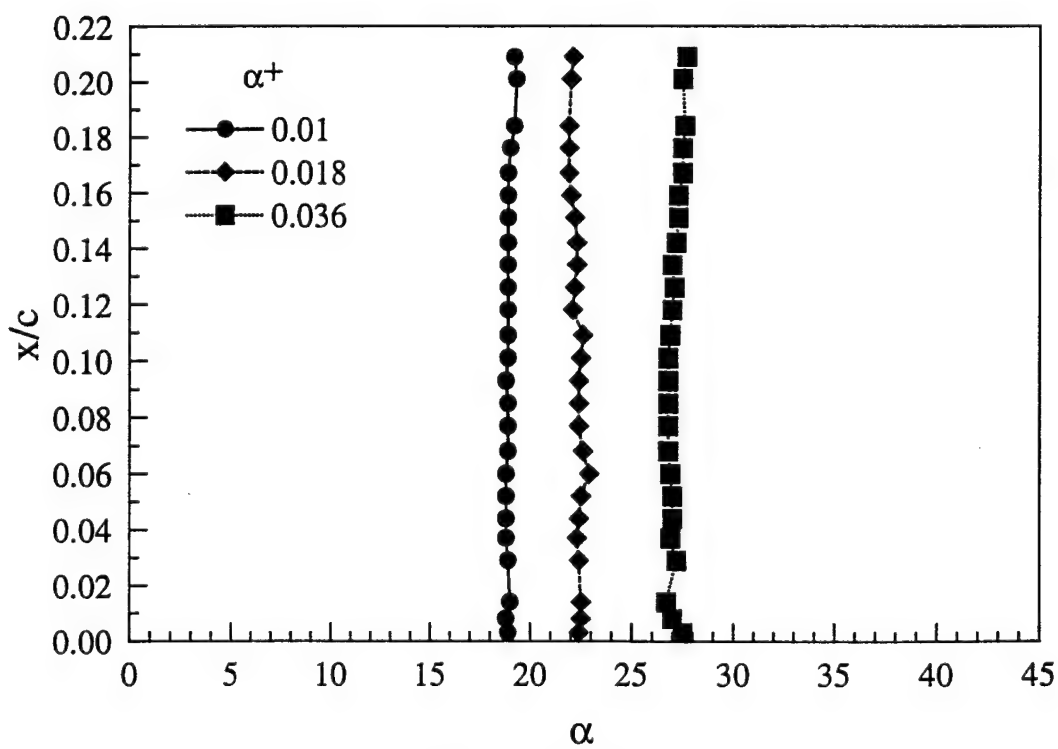
(b)  $Re_c = 4.6 \times 10^5$

Figure 31 Behavior of shear stress feature 4 with varying pitch rate.



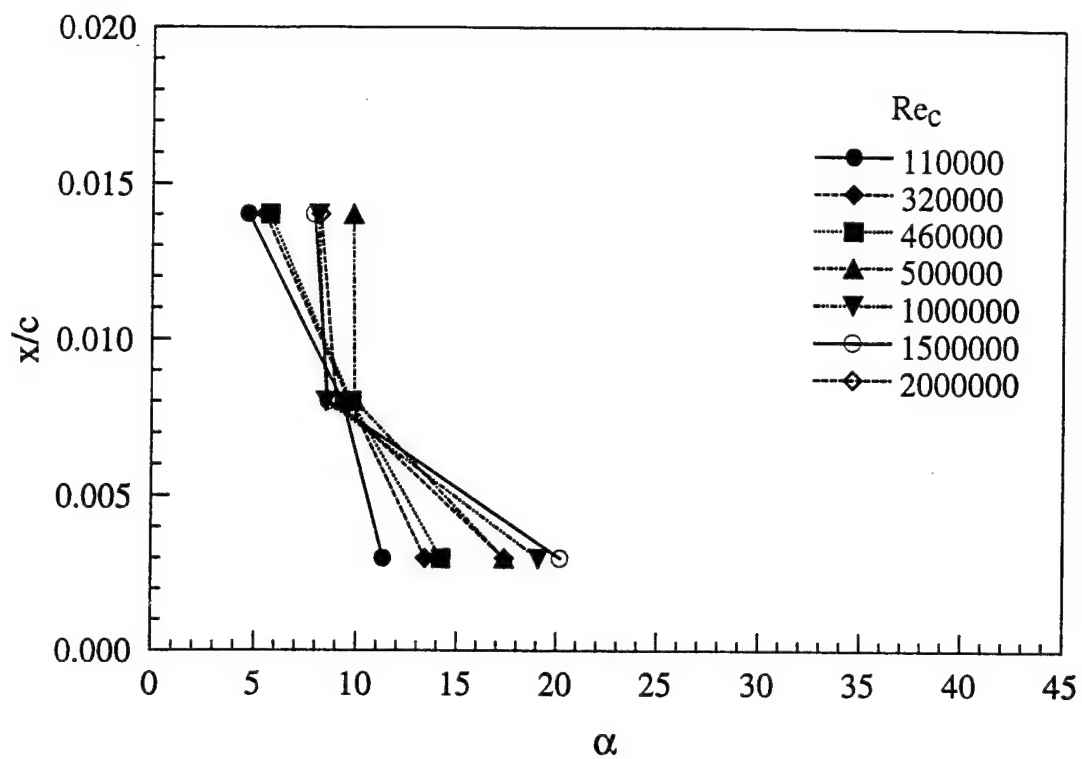


(c)  $Re_c = 1.0 \times 10^6$

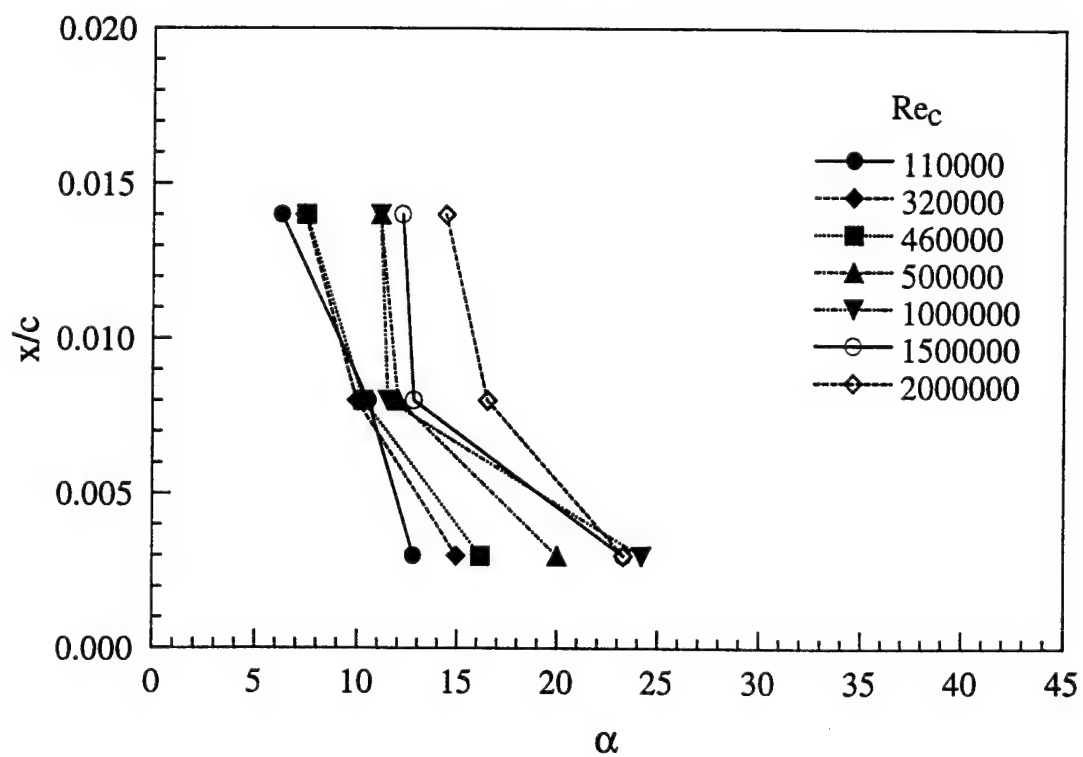


(d)  $Re_c = 2.0 \times 10^6$

Figure 31 (concluded).



(a)  $\alpha^+ = 0.010$



(b)  $\alpha^+ = 0.036$

Figure 32 Behavior of shear stress feature 1 with varying Reynolds number.

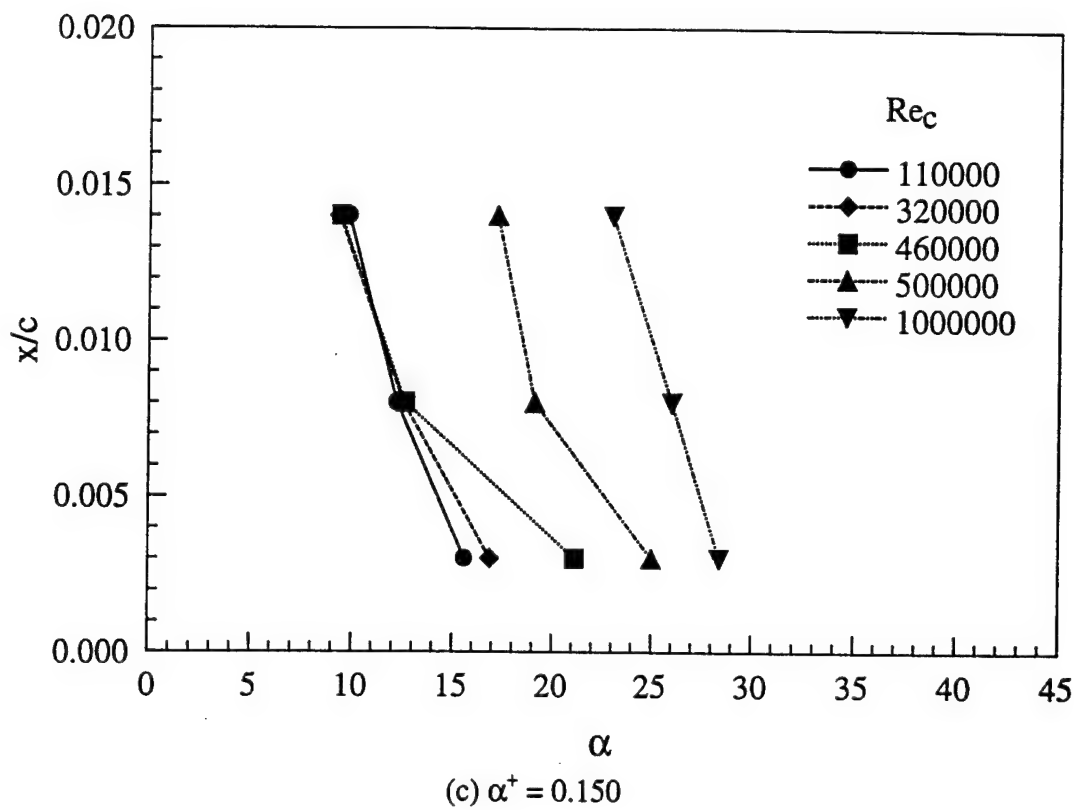
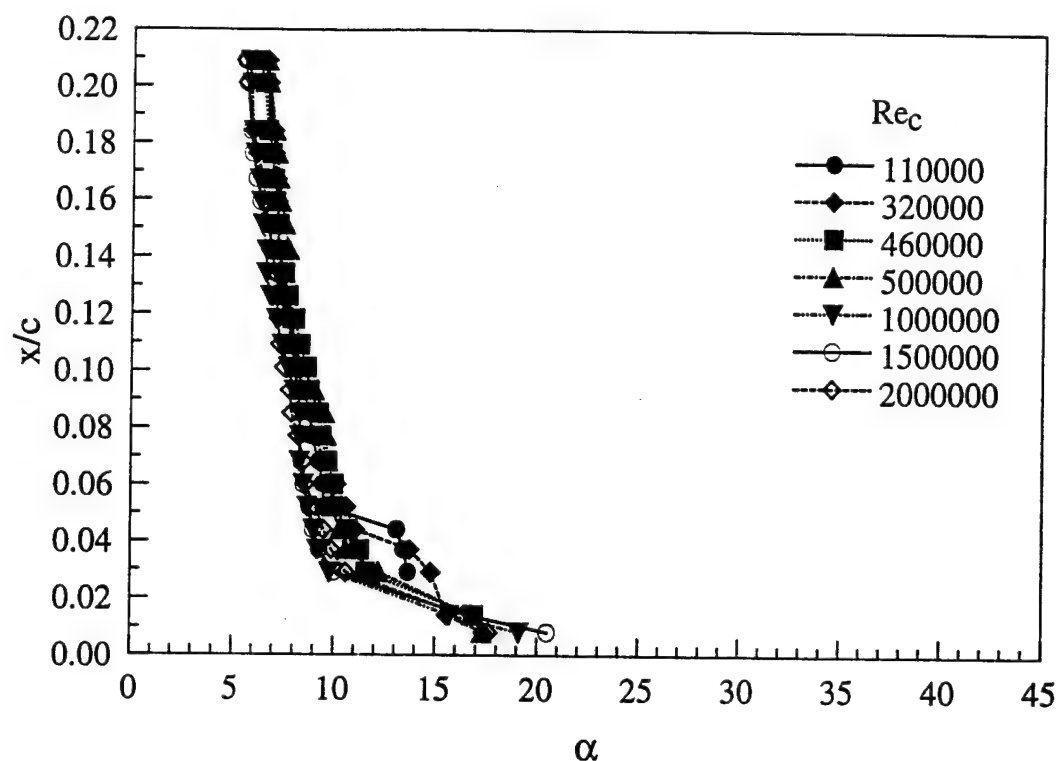
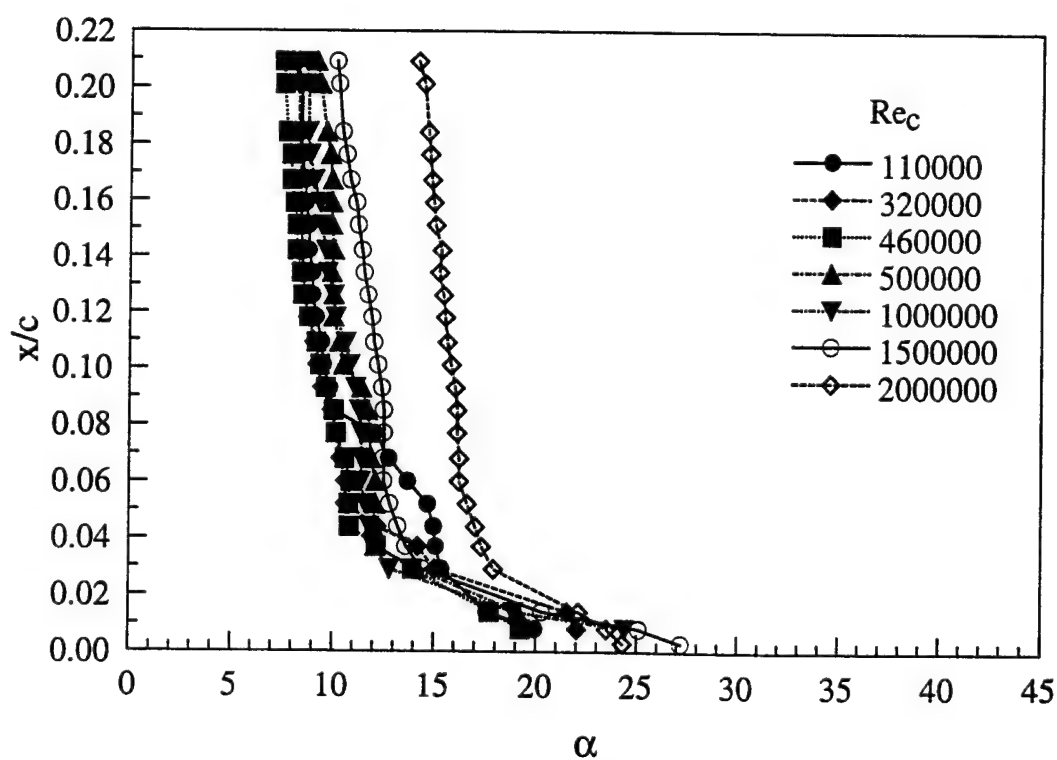


Figure 32 (concluded).

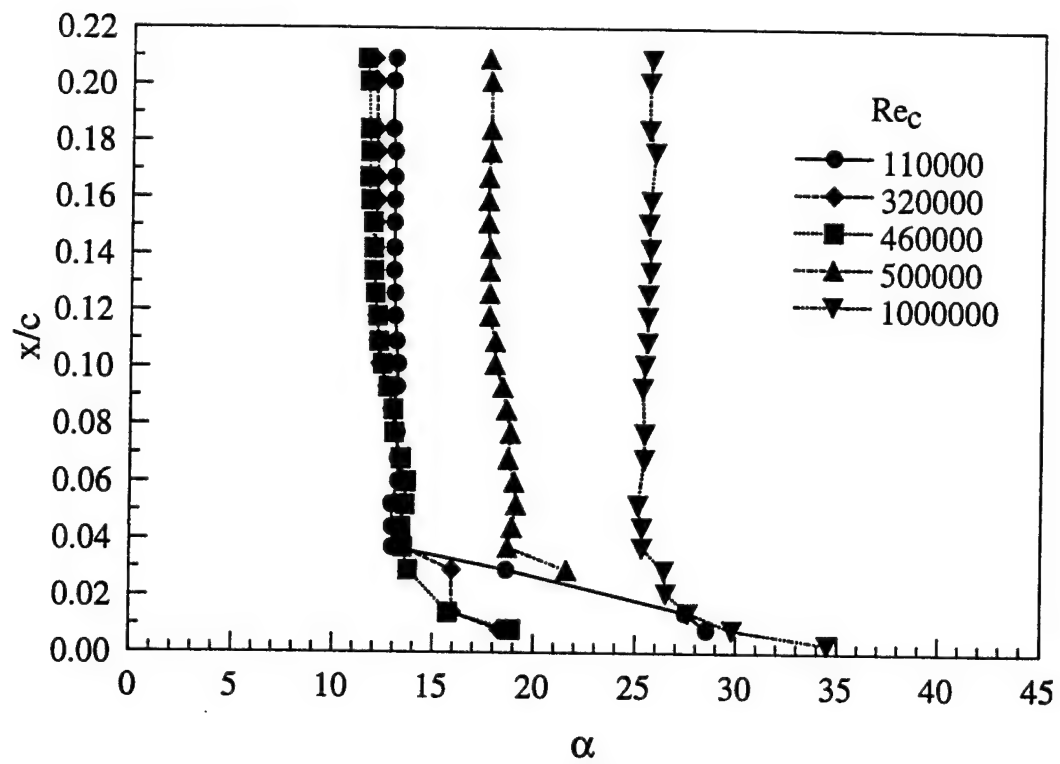


(a)  $\alpha^+ = 0.010$



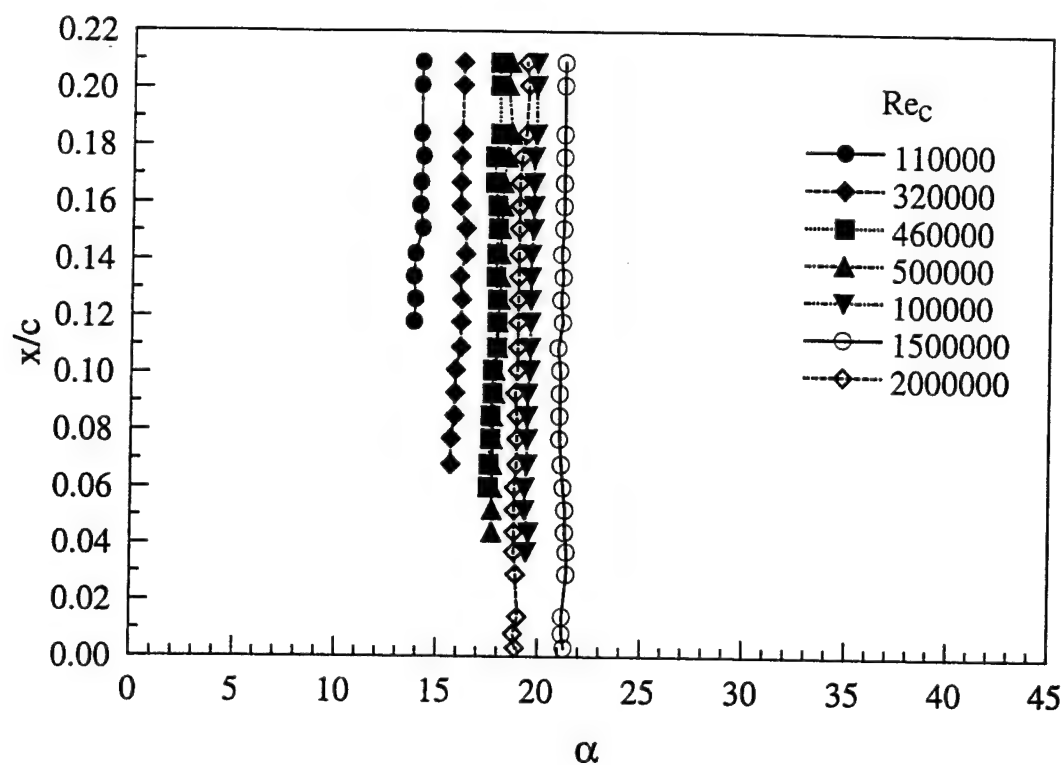
(b)  $\alpha^+ = 0.036$

Figure 33 Behavior of shear stress feature 2 with varying Reynolds number.

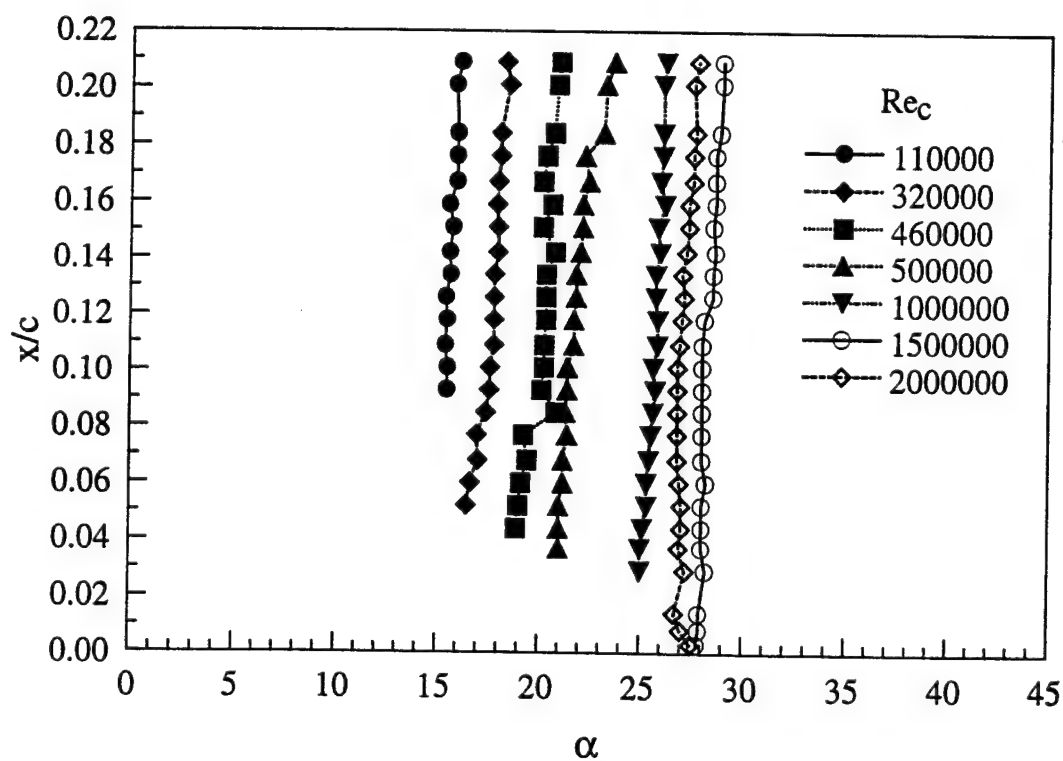


(c)  $\alpha^+ = 0.150$

Figure 33 (concluded).

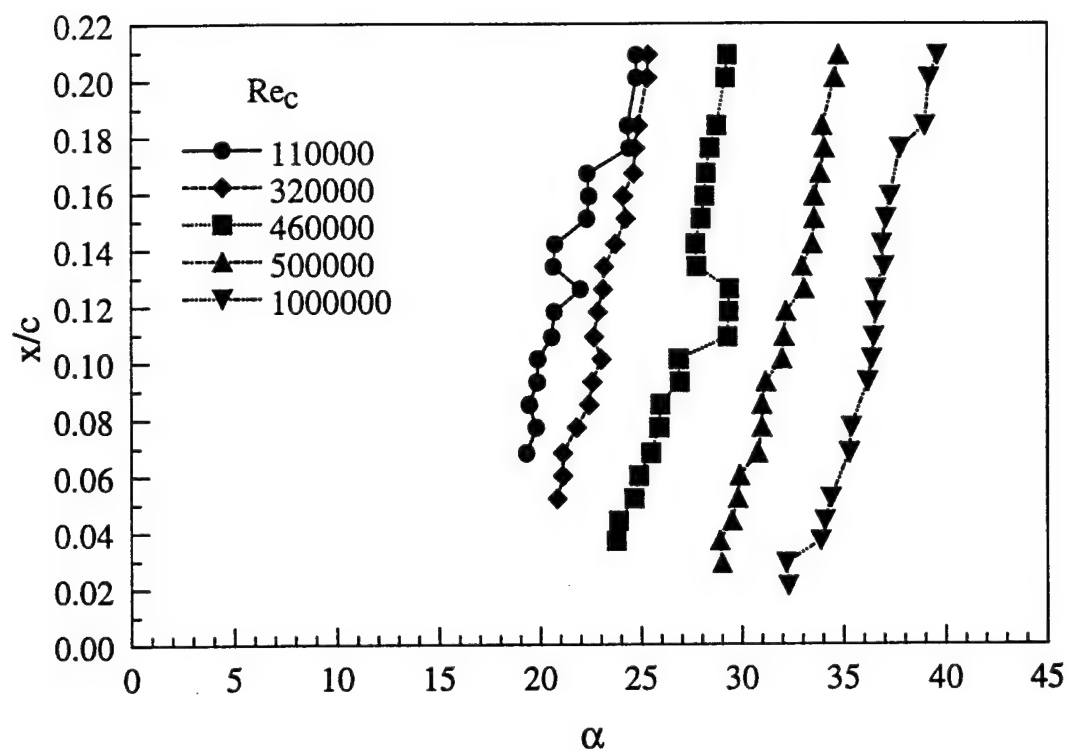


(a)  $\alpha^+ = 0.010$



(b)  $\alpha^+ = 0.036$

Figure 34 Behavior of shear stress feature 4 with varying Reynolds number.



(c)  $\alpha^+ = 0.150$

Figure 34 (concluded).

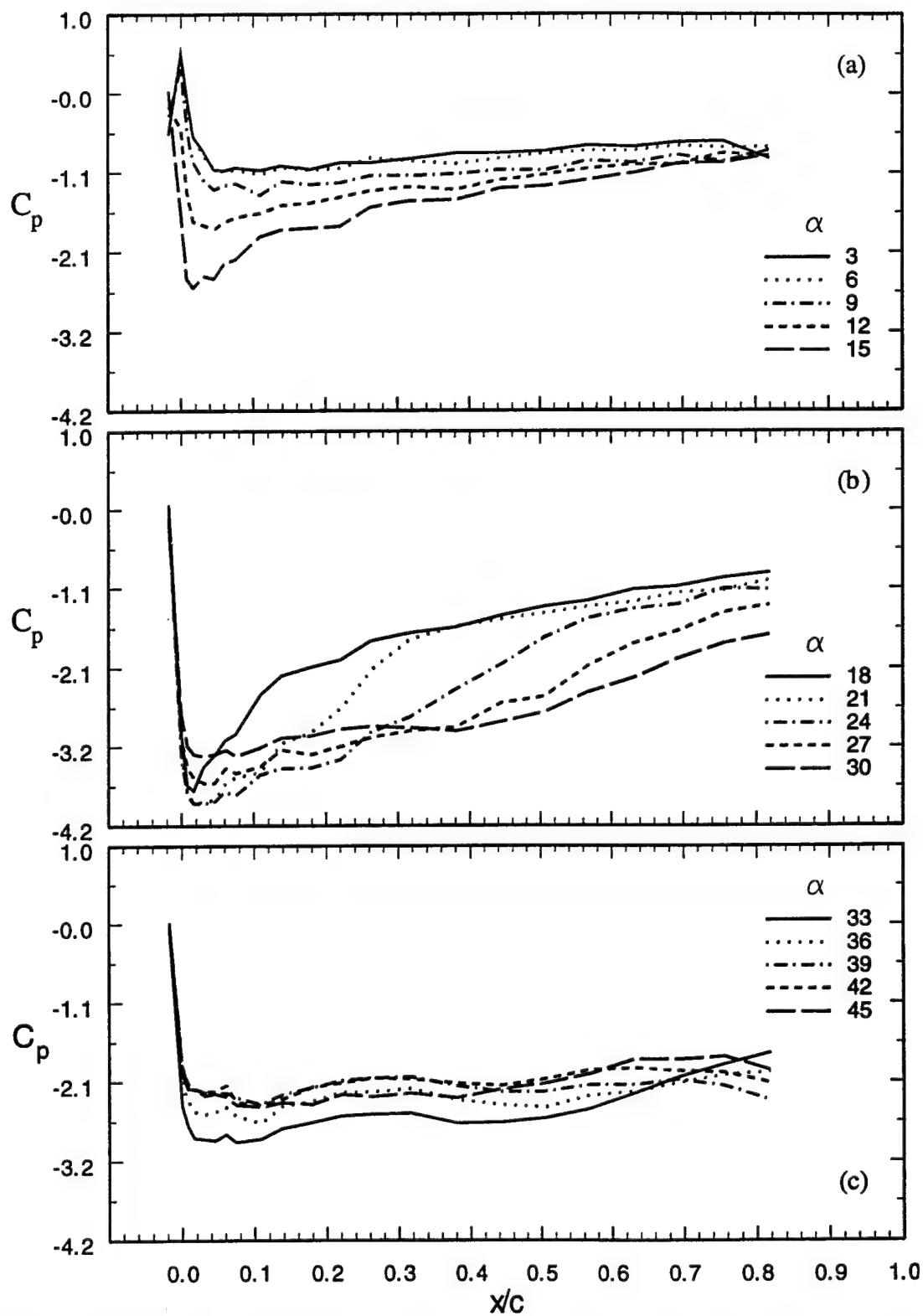


Figure 35 Pressure coefficient distributions on the airfoil suction surface during pitch-up ( $\alpha^+ = 0.150$ ,  $Re_c = 0.5 \times 10^6$ ).



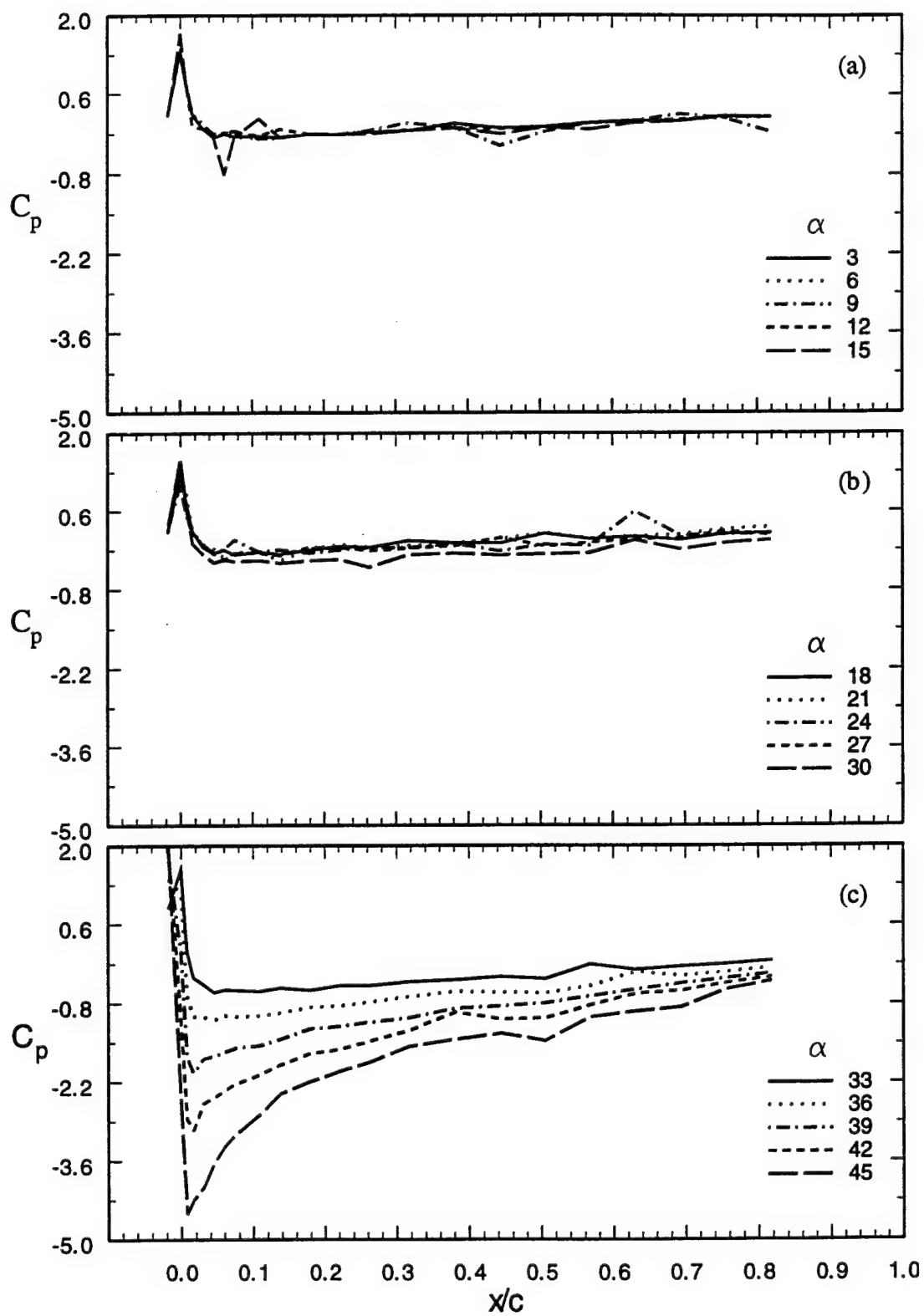


Figure 36 Pressure coefficient distributions on the airfoil suction surface during pitch-up ( $\alpha^+ = 0.150$ ,  $Re_c = 1.0 \times 10^6$ ).

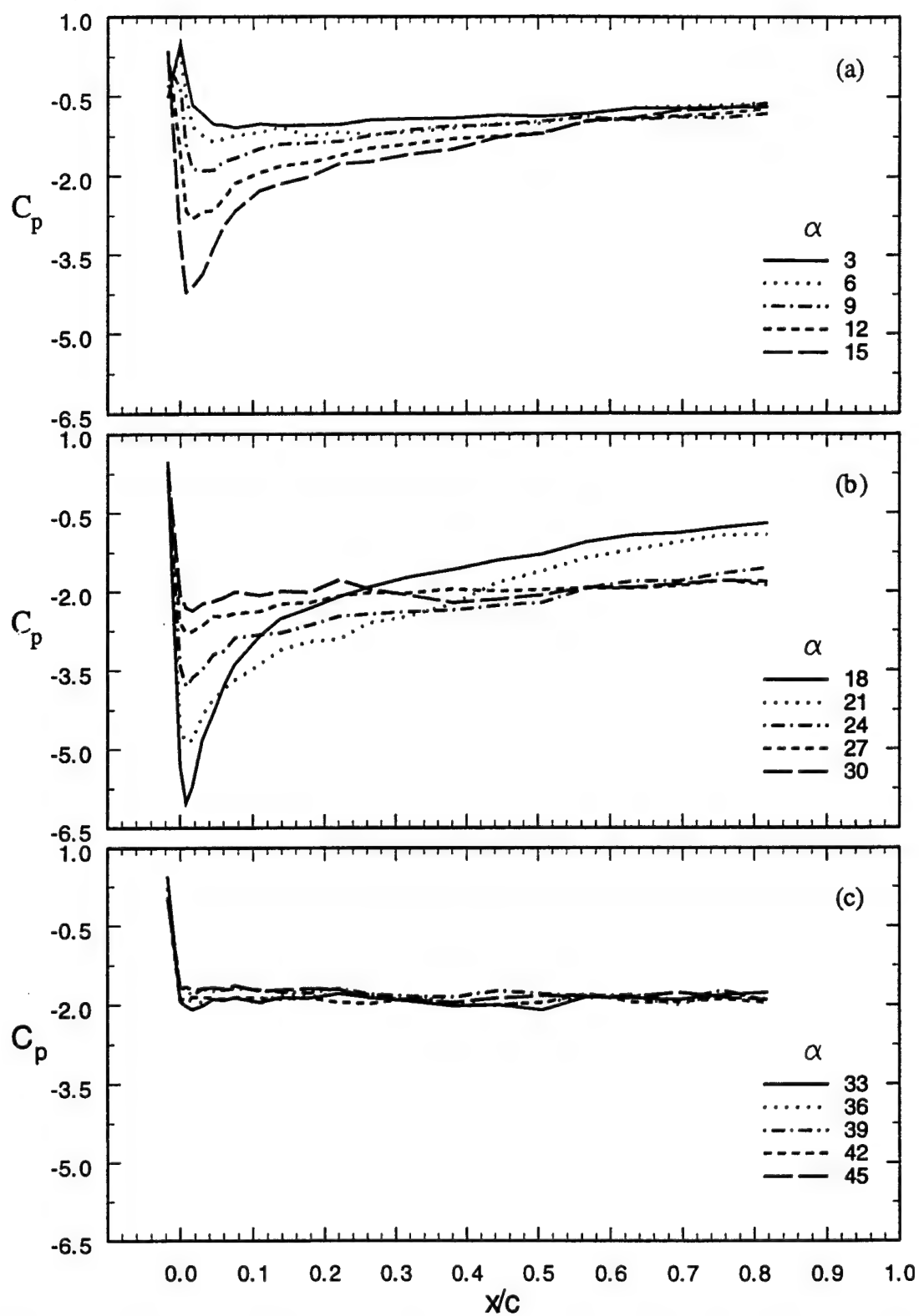


Figure 37 Pressure coefficient distributions on the airfoil suction surface during pitch-up ( $\alpha^+ = 0.036$ ,  $Re_c = 0.5 \times 10^6$ ).

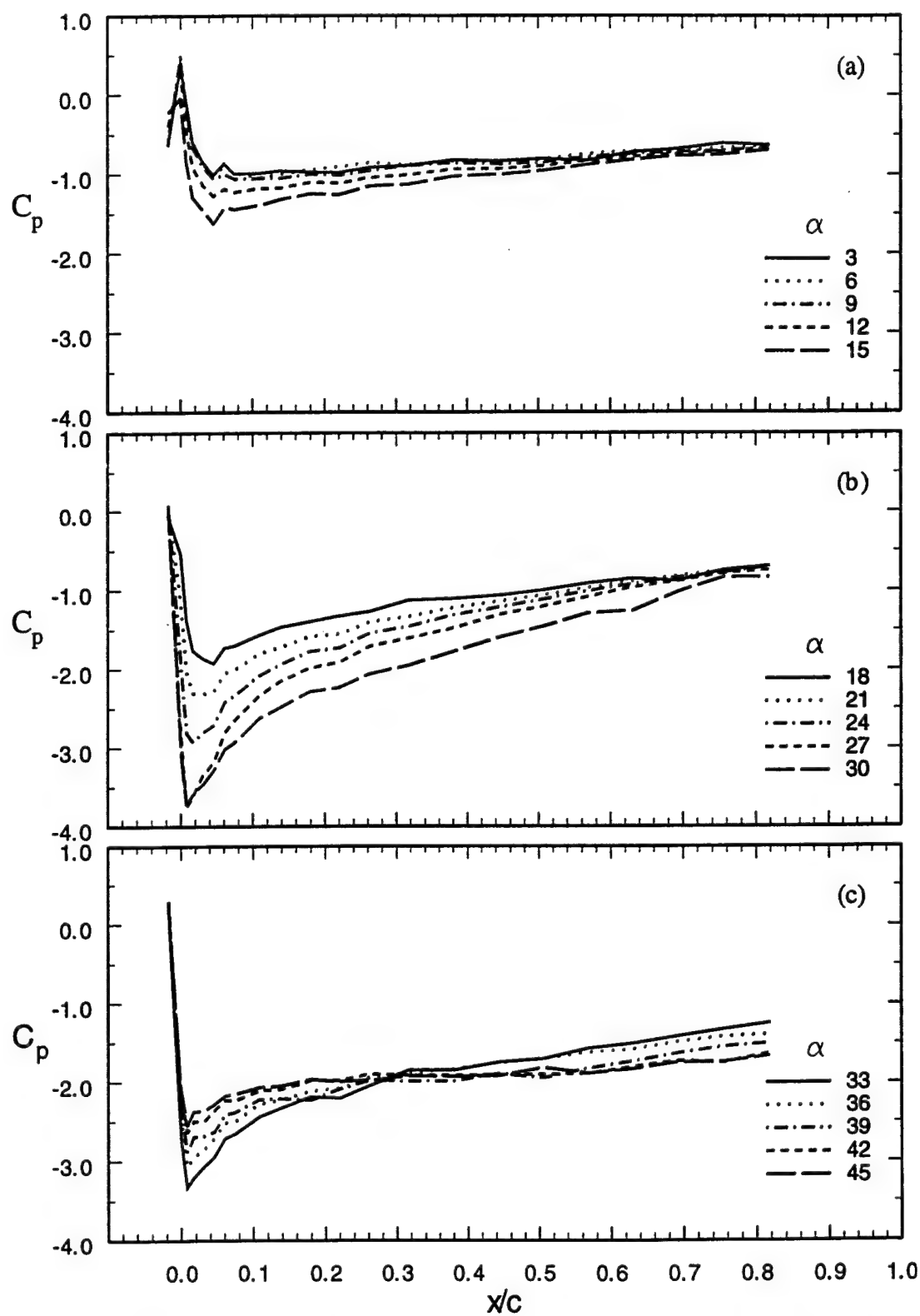


Figure 38 Pressure coefficient distributions on the airfoil suction surface during pitch-up ( $\alpha^+ = 0.036$ ,  $Re_c = 1.0 \times 10^6$ ).

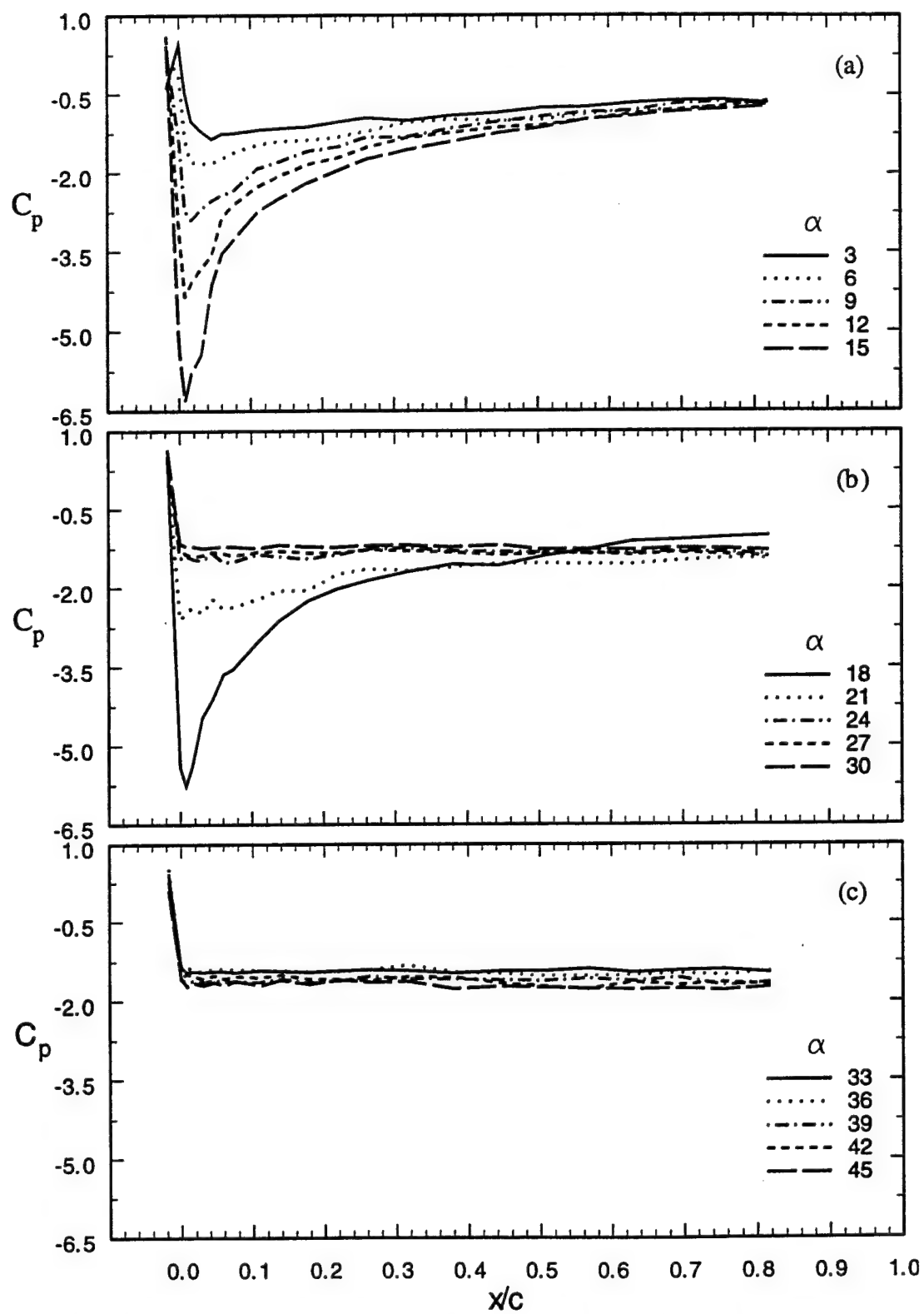


Figure 39 Pressure coefficient distributions on the airfoil suction surface during pitch-up ( $\alpha^+ = 0.010$ ,  $Re_c = 0.5 \times 10^6$ ).

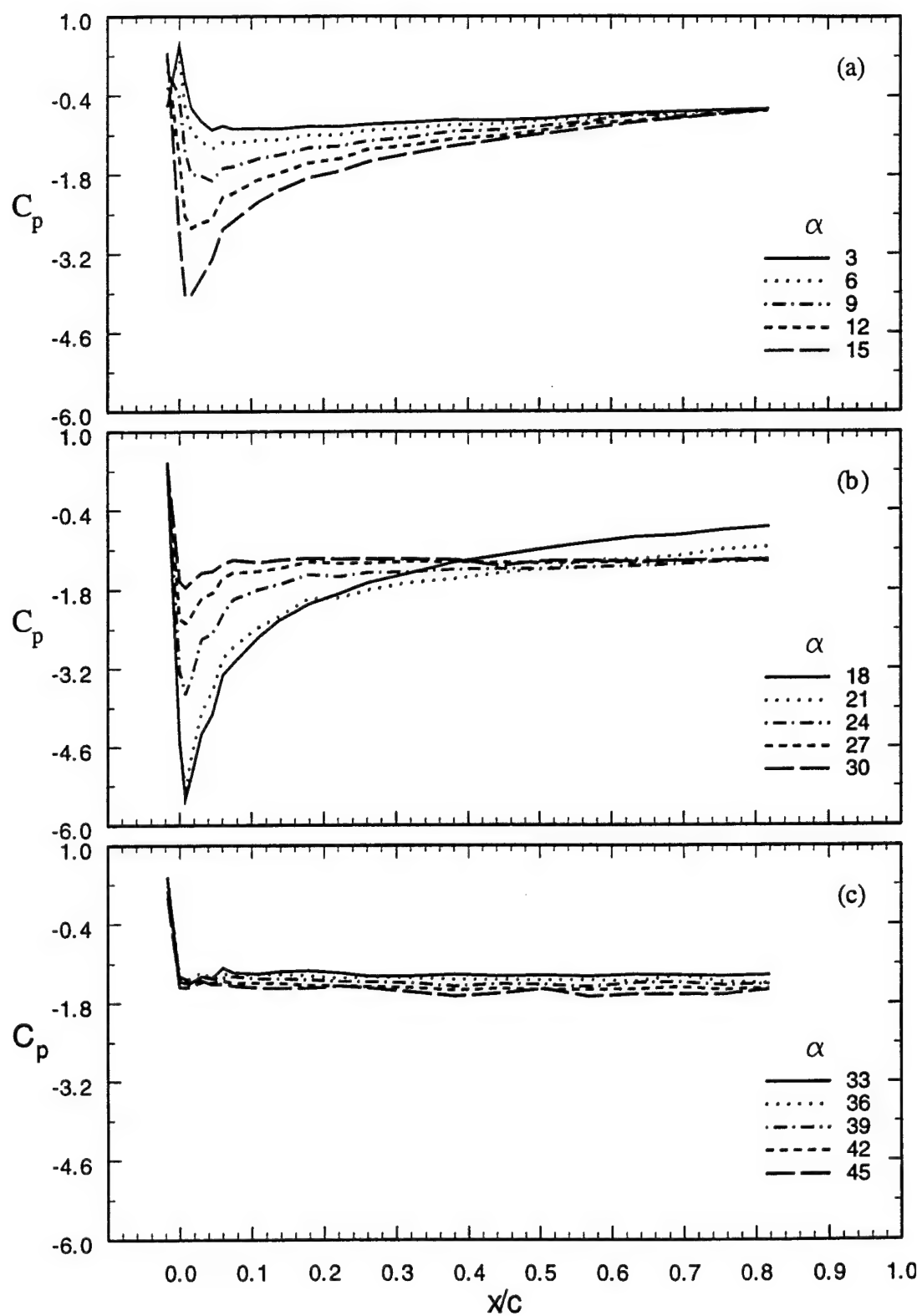


Figure 40 Pressure coefficient distributions on the airfoil suction surface during pitch-up ( $\alpha^+ = 0.010$ ,  $Re_c = 1.0 \times 10^6$ ).

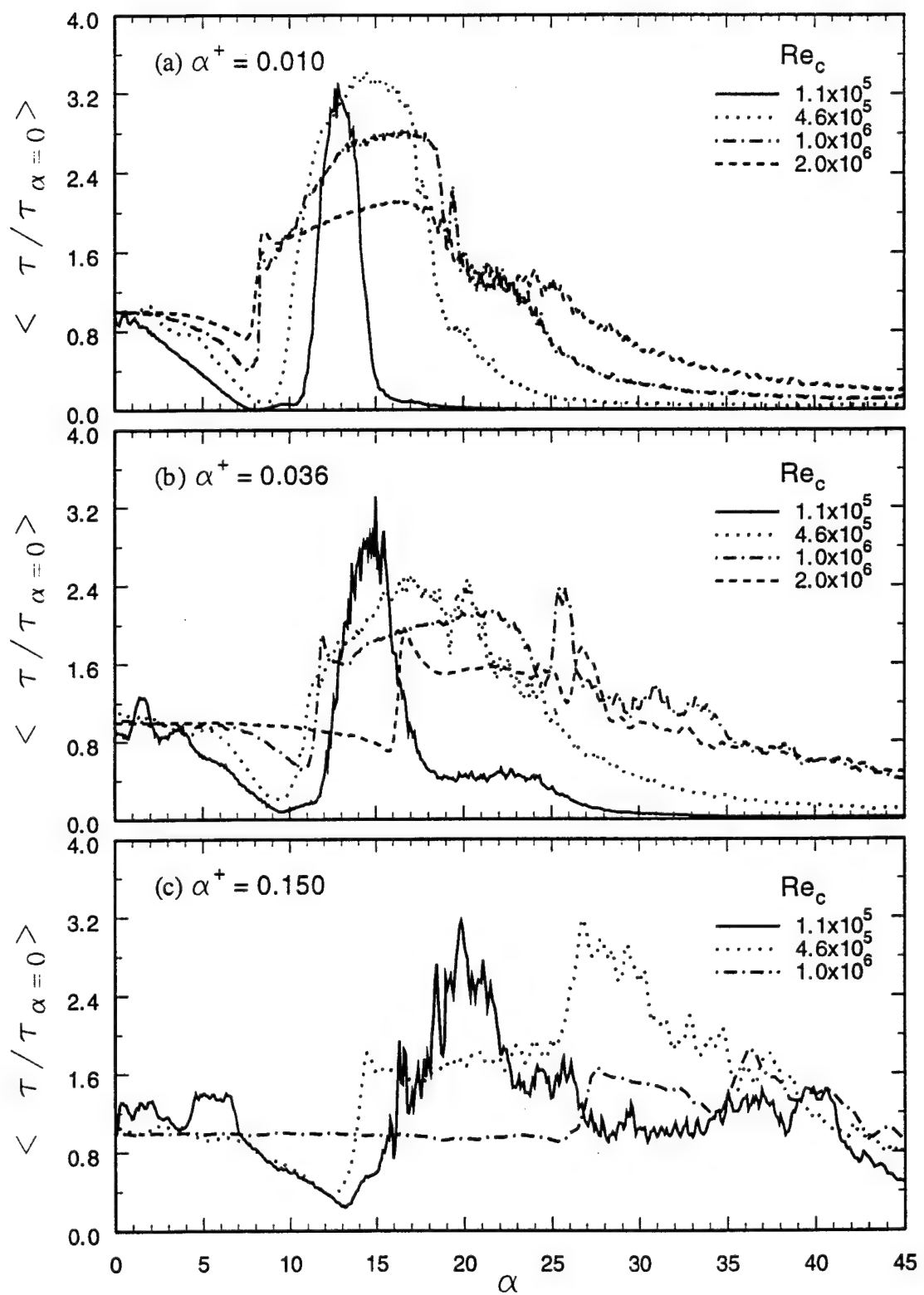


Figure 41 Changes in the normalized shear-stress variations during pitch-up with increasing Reynolds number at  $x/c = 0.101$ .

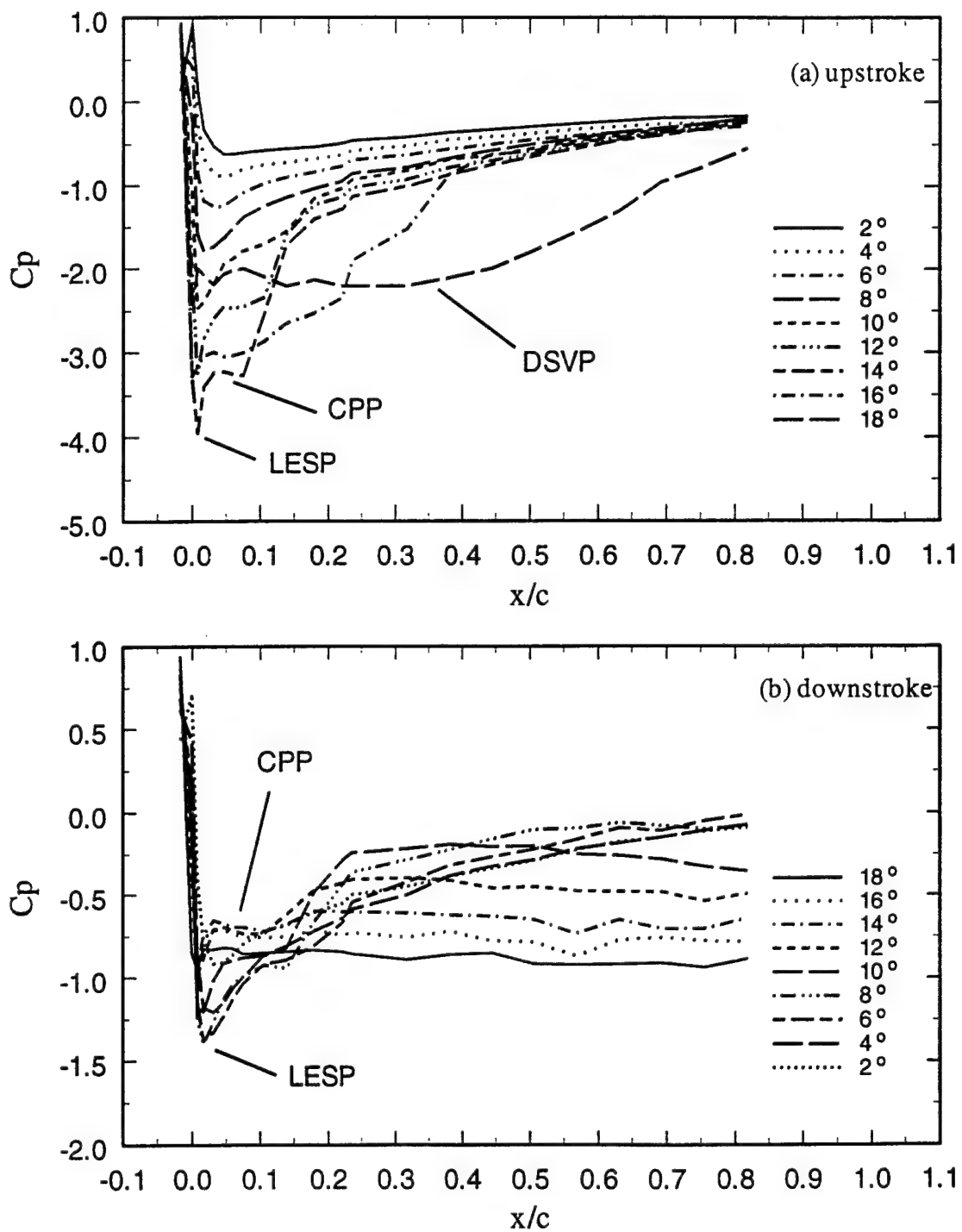


Figure 42 Chordwise pressure distribution over an oscillating 2-D airfoil at selected angles for  $Re_c = 1.1 \times 10^5$ ,  $k = 0.1$ ,  $\alpha_o = 10^\circ$ ,  $\alpha_m = 10^\circ$ .

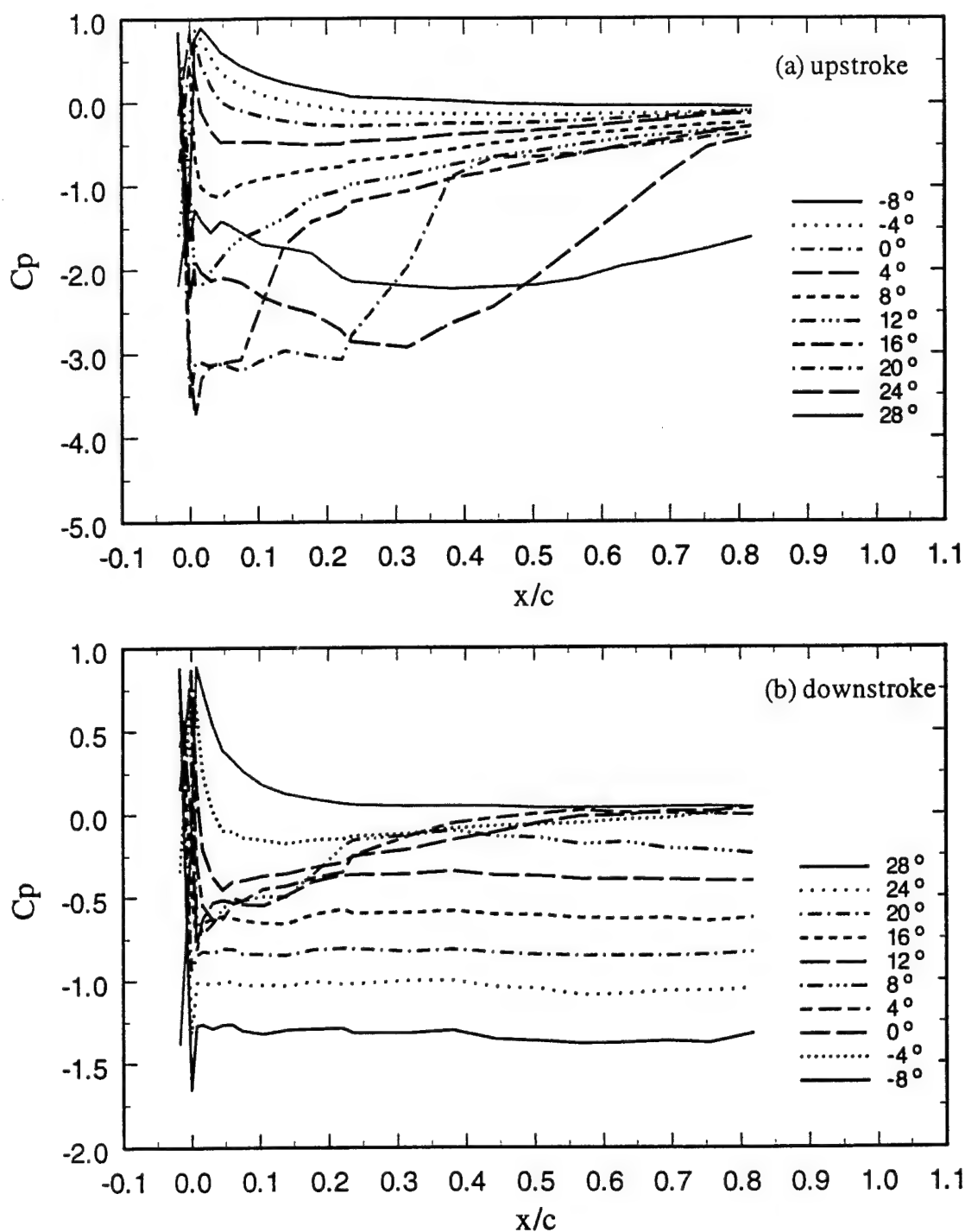


Figure 43 Chordwise pressure distribution over an oscillating 2-D airfoil at selected angles for  $Re_c = 1.1 \times 10^5$ ,  $k = 0.1$ ,  $\alpha_o = 10^\circ$ ,  $\alpha_m = 20^\circ$ .



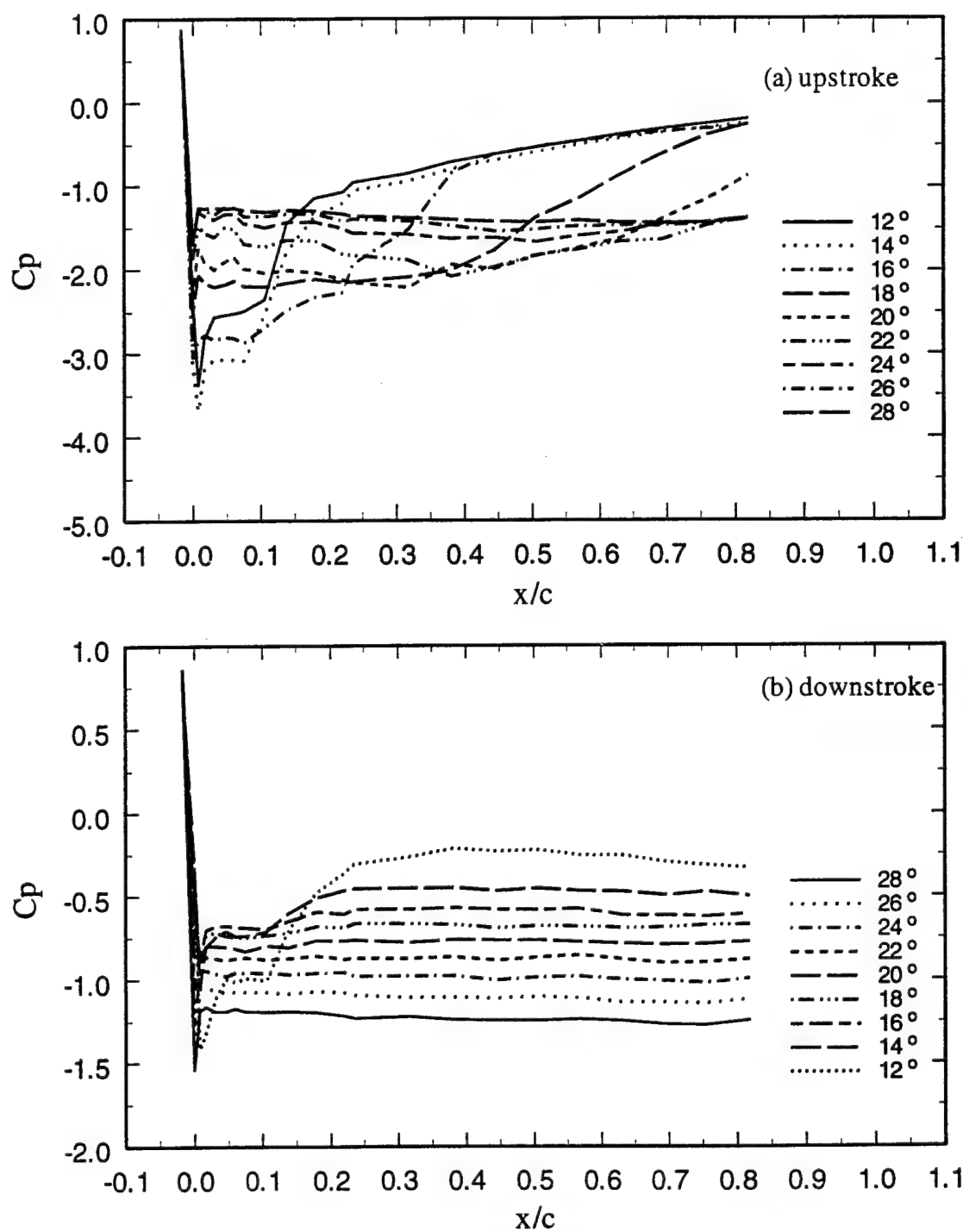


Figure 44 Chordwise pressure distribution over an oscillating 2-D airfoil at selected angles for  $Re_c = 1.1 \times 10^5$ ,  $k = 0.1$ ,  $\alpha_o = 20^\circ$ ,  $\alpha_m = 10^\circ$ .

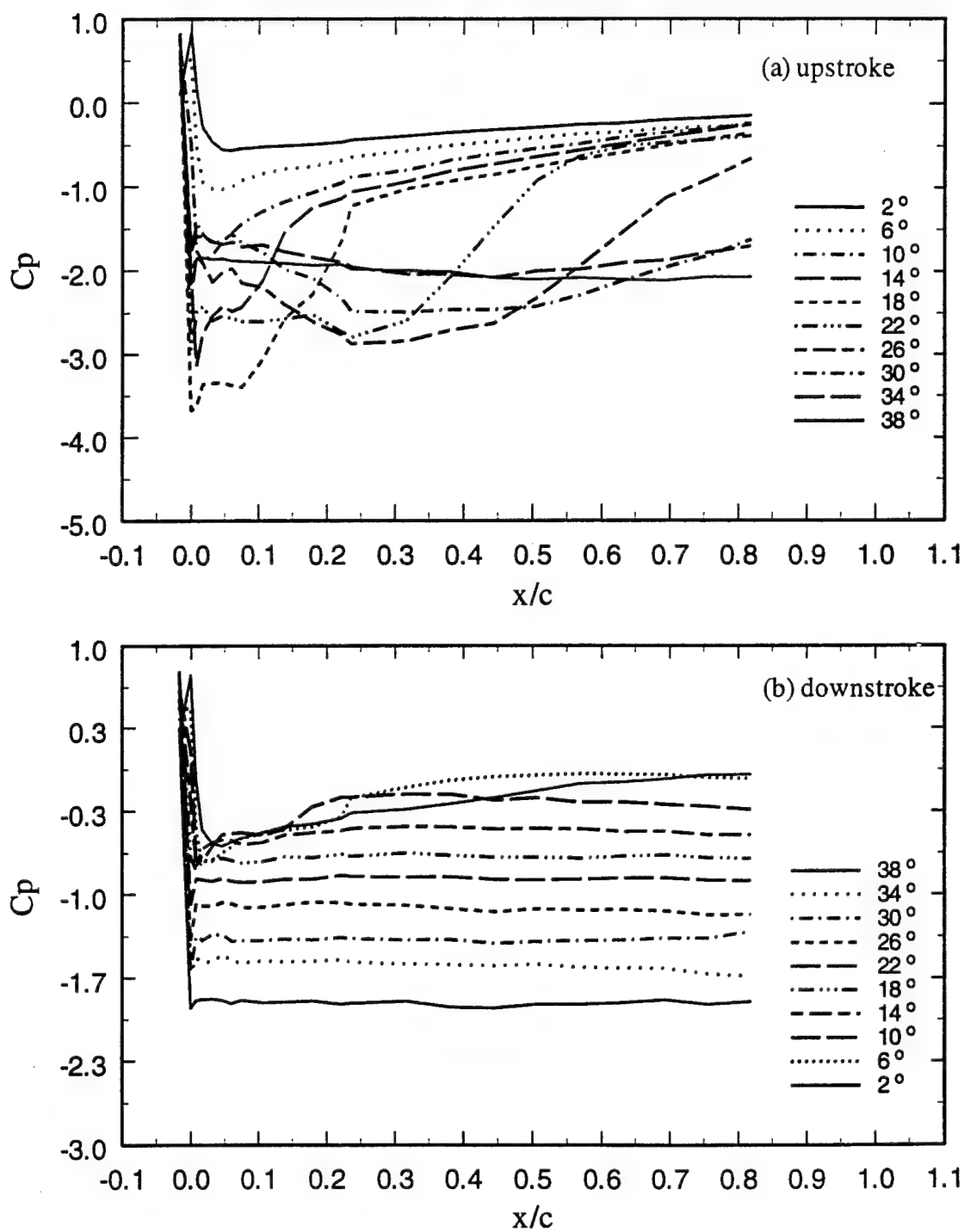


Figure 45 Chordwise pressure distribution over an oscillating 2-D airfoil at selected angles for  $Re_c = 1.1 \times 10^5$ ,  $k = 0.1$ ,  $\alpha_o = 20^\circ$ ,  $\alpha_m = 20^\circ$ .

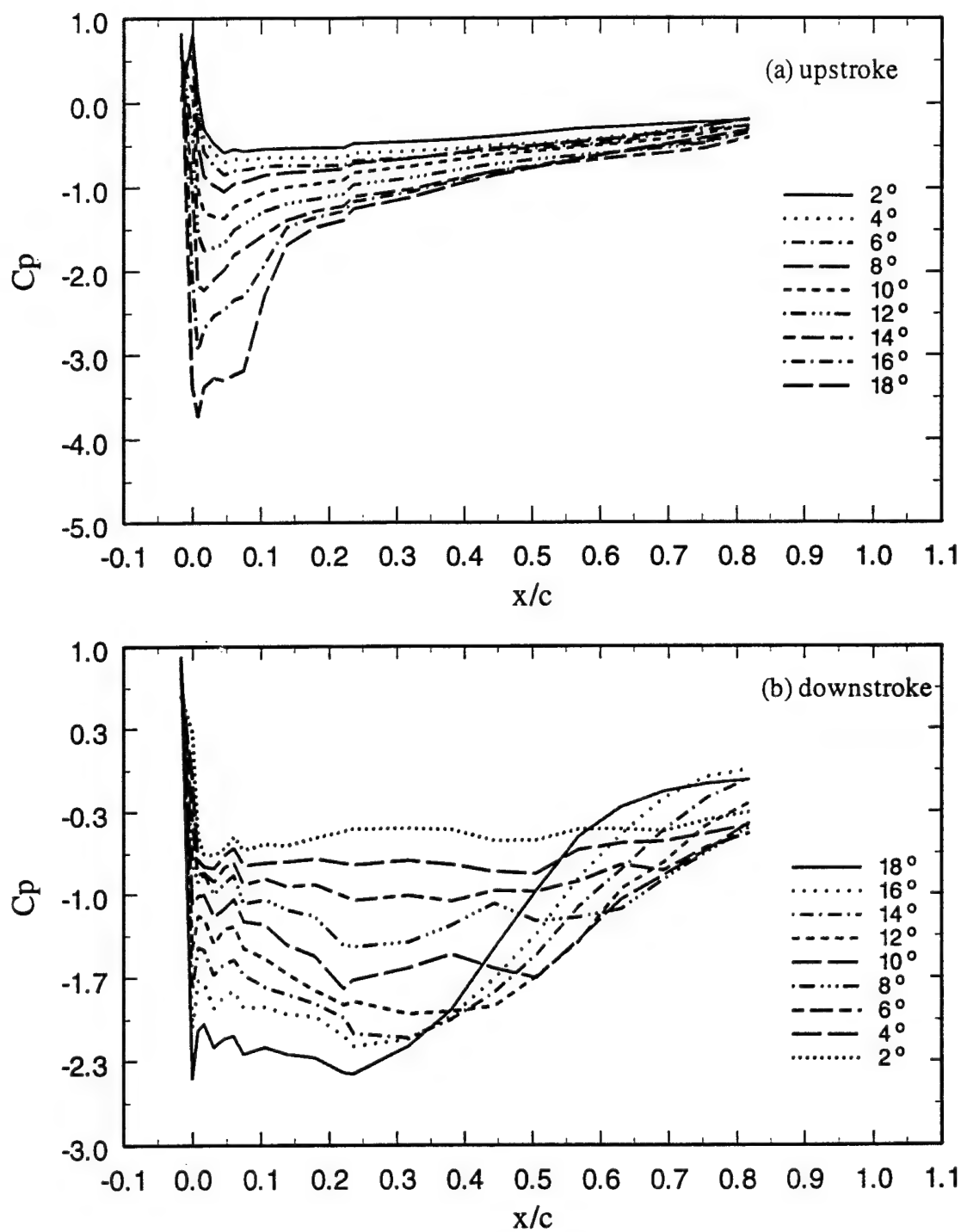


Figure 46 Chordwise pressure distribution over an oscillating 2-D airfoil at selected angles for  $Re_c = 1.1 \times 10^5$ ,  $k = 0.4$ ,  $\alpha_o = 10^\circ$ ,  $\alpha_m = 10^\circ$ .

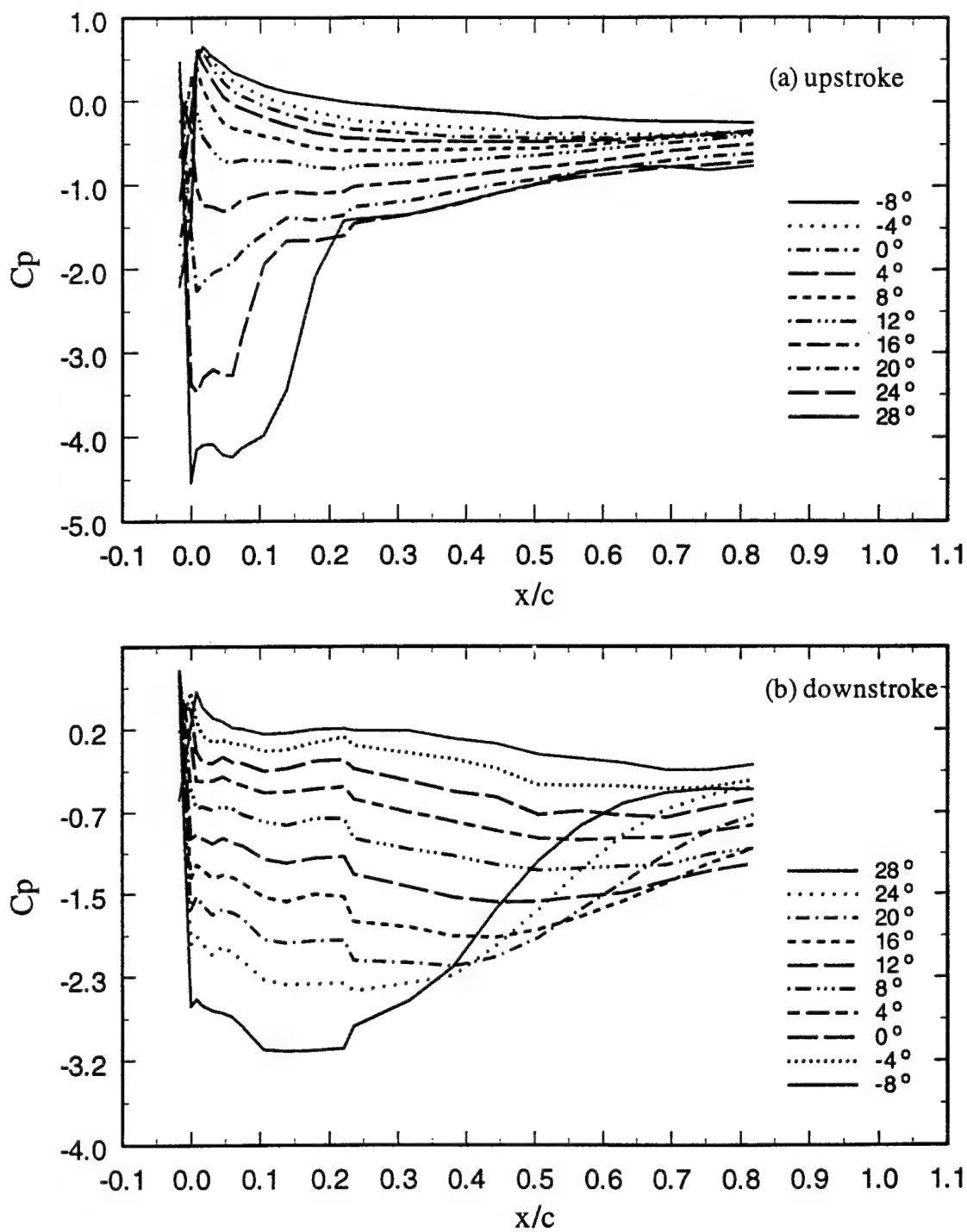


Figure 47 Chordwise pressure distribution over an oscillating 2-D airfoil at selected angles for  $Re_c = 1.1 \times 10^5$ ,  $k = 0.4$ ,  $\alpha_o = 10^\circ$ ,  $\alpha_m = 20^\circ$ .

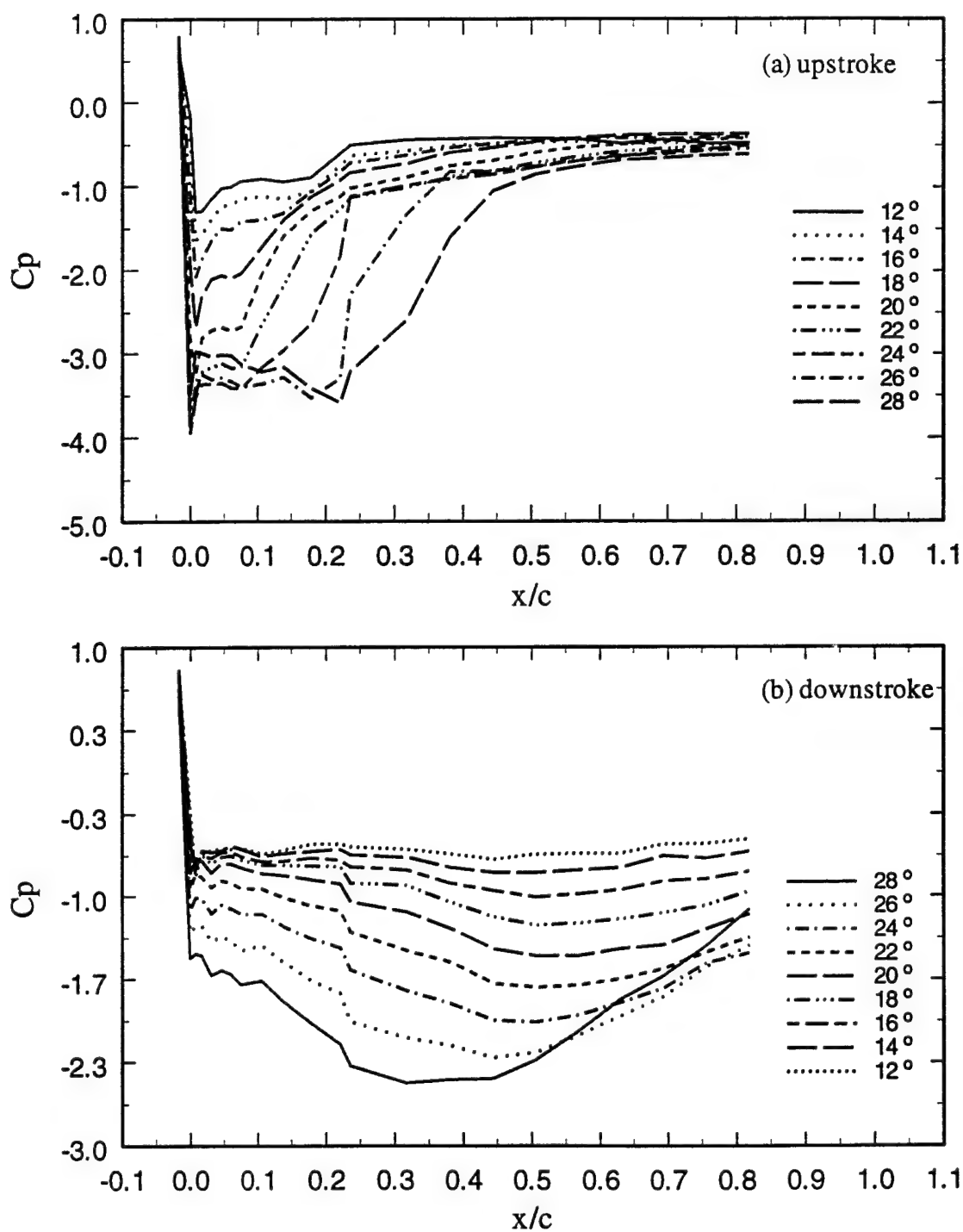


Figure 48 Chordwise pressure distribution over an oscillating 2-D airfoil at selected angles for  $Re_c = 1.1 \times 10^5$ ,  $k = 0.4$ ,  $\alpha_o = 20^\circ$ ,  $\alpha_m = 10^\circ$ .

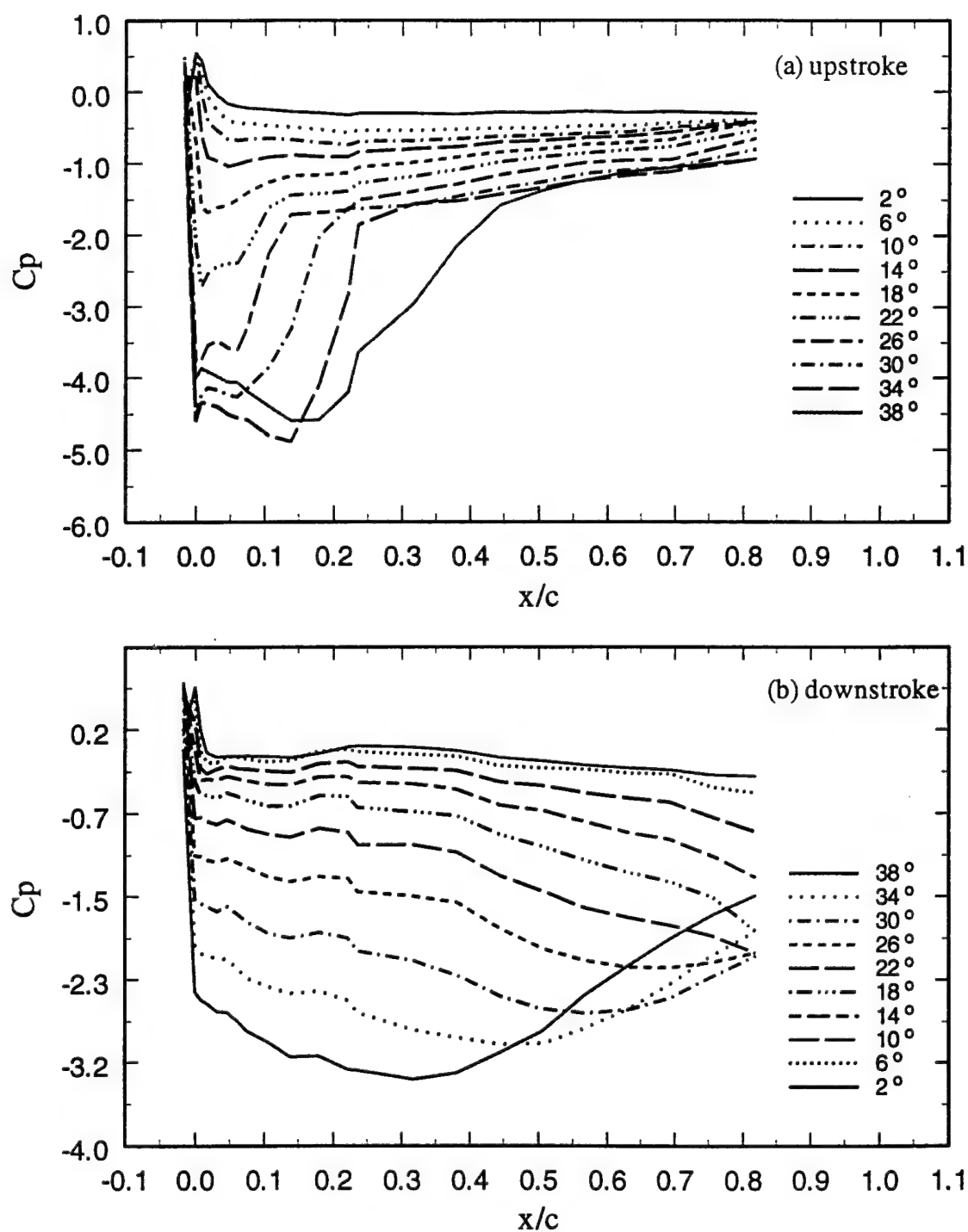


Figure 49 Chordwise pressure distribution over an oscillating 2-D airfoil at selected angles for  $Re_c = 1.1 \times 10^5$ ,  $k = 0.4$ ,  $\alpha_o = 20^\circ$ ,  $\alpha_m = 20^\circ$ .

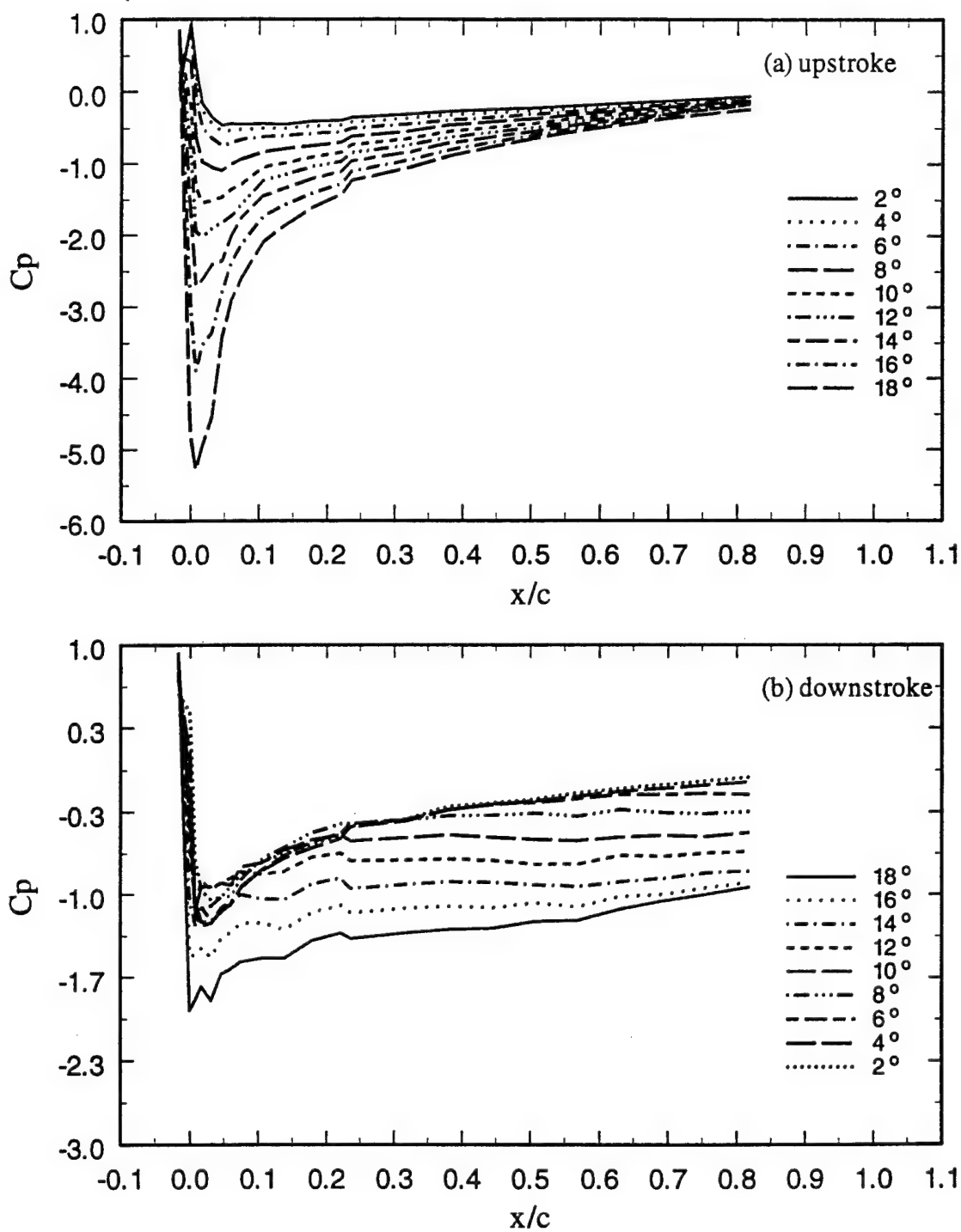


Figure 50 Chordwise pressure distribution over an oscillating 2-D airfoil at selected angles for  $Re_c = 4.6 \times 10^5$ ,  $k = 0.1$ ,  $\alpha_o = 10^\circ$ ,  $\alpha_m = 10^\circ$ .

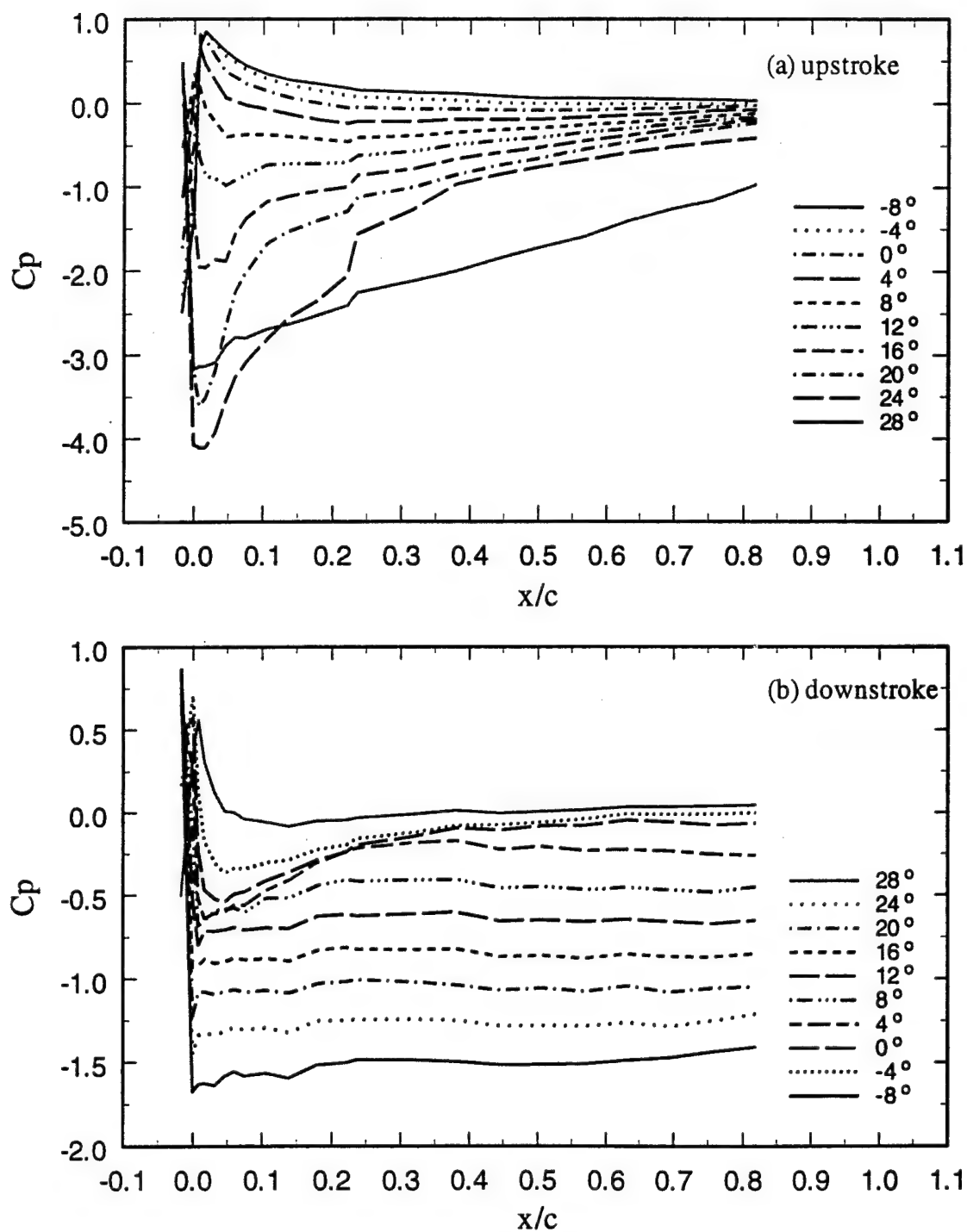


Figure 51 Chordwise pressure distribution over an oscillating 2-D airfoil at selected angles for  $Re_c = 4.6 \times 10^5$ ,  $k = 0.1$ ,  $\alpha_o = 10^\circ$ ,  $\alpha_m = 20^\circ$ .



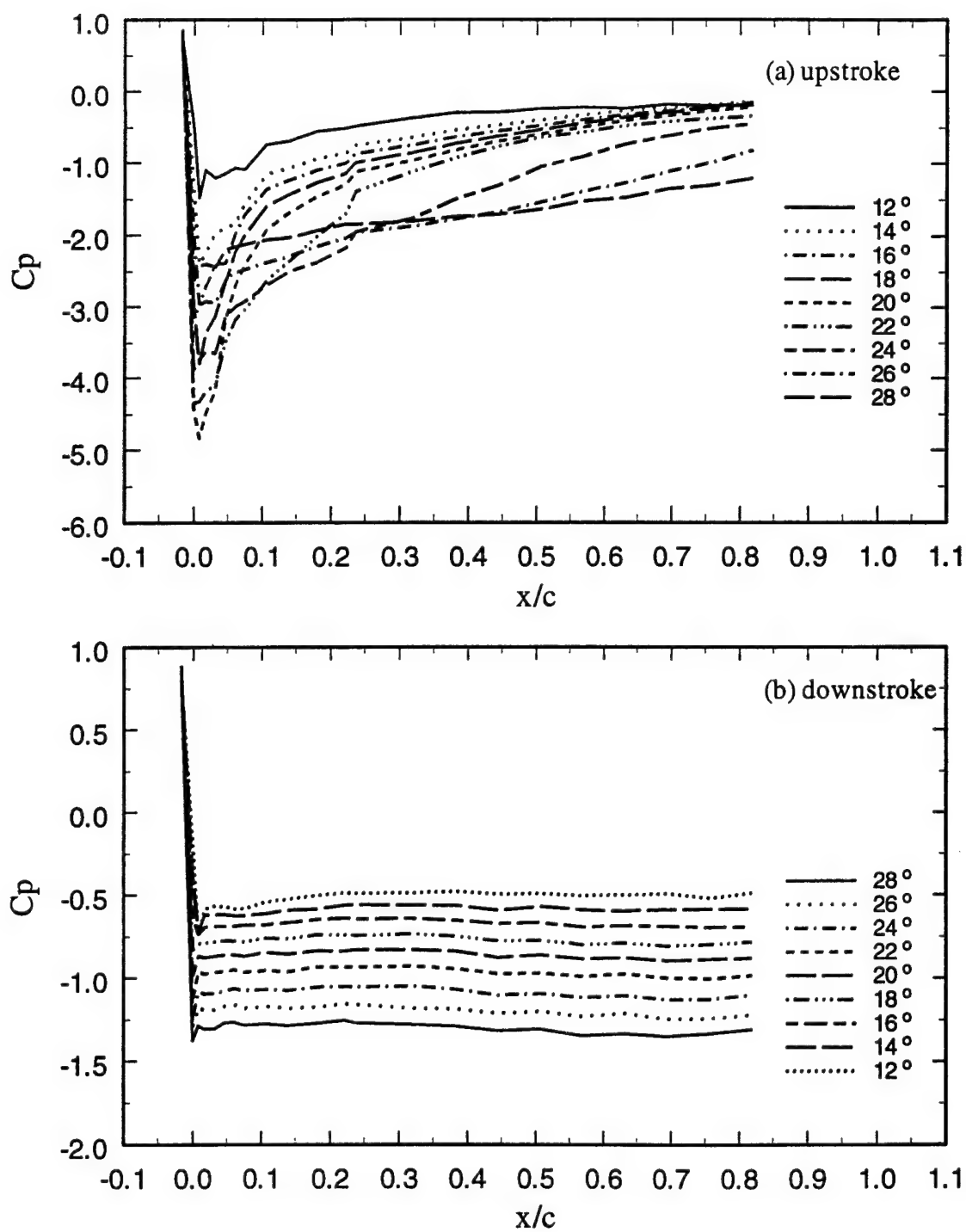


Figure 52 Chordwise pressure distribution over an oscillating 2-D airfoil at selected angles for  $Re_c = 4.6 \times 10^5$ ,  $k = 0.1$ ,  $\alpha_o = 20^\circ$ ,  $\alpha_m = 10^\circ$ .

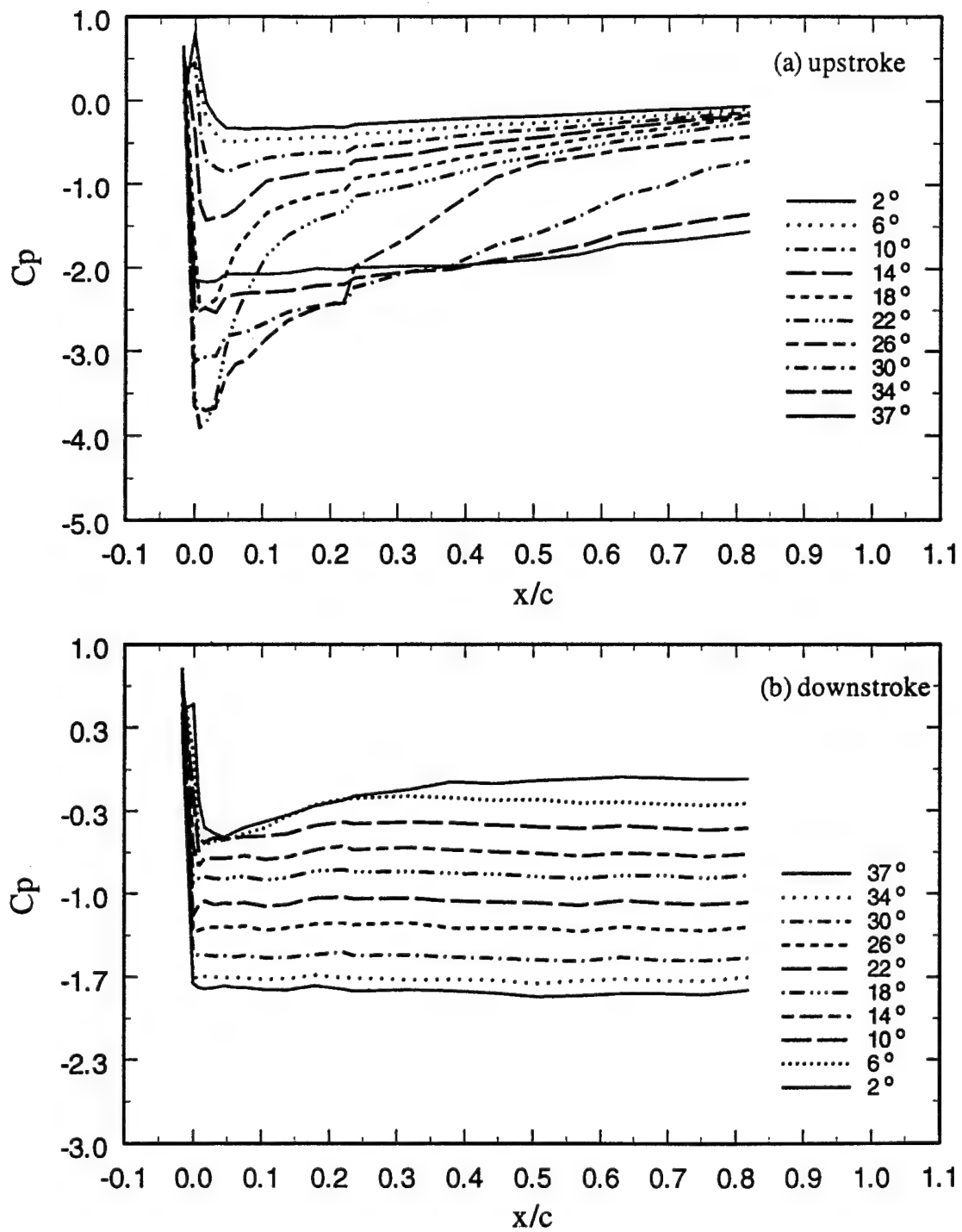


Figure 53 Chordwise pressure distribution over an oscillating 2-D airfoil at selected angles for  $Re_c = 4.6 \times 10^5$ ,  $k = 0.1$ ,  $\alpha_0 = 20^\circ$ ,  $\alpha_m = 20^\circ$ .

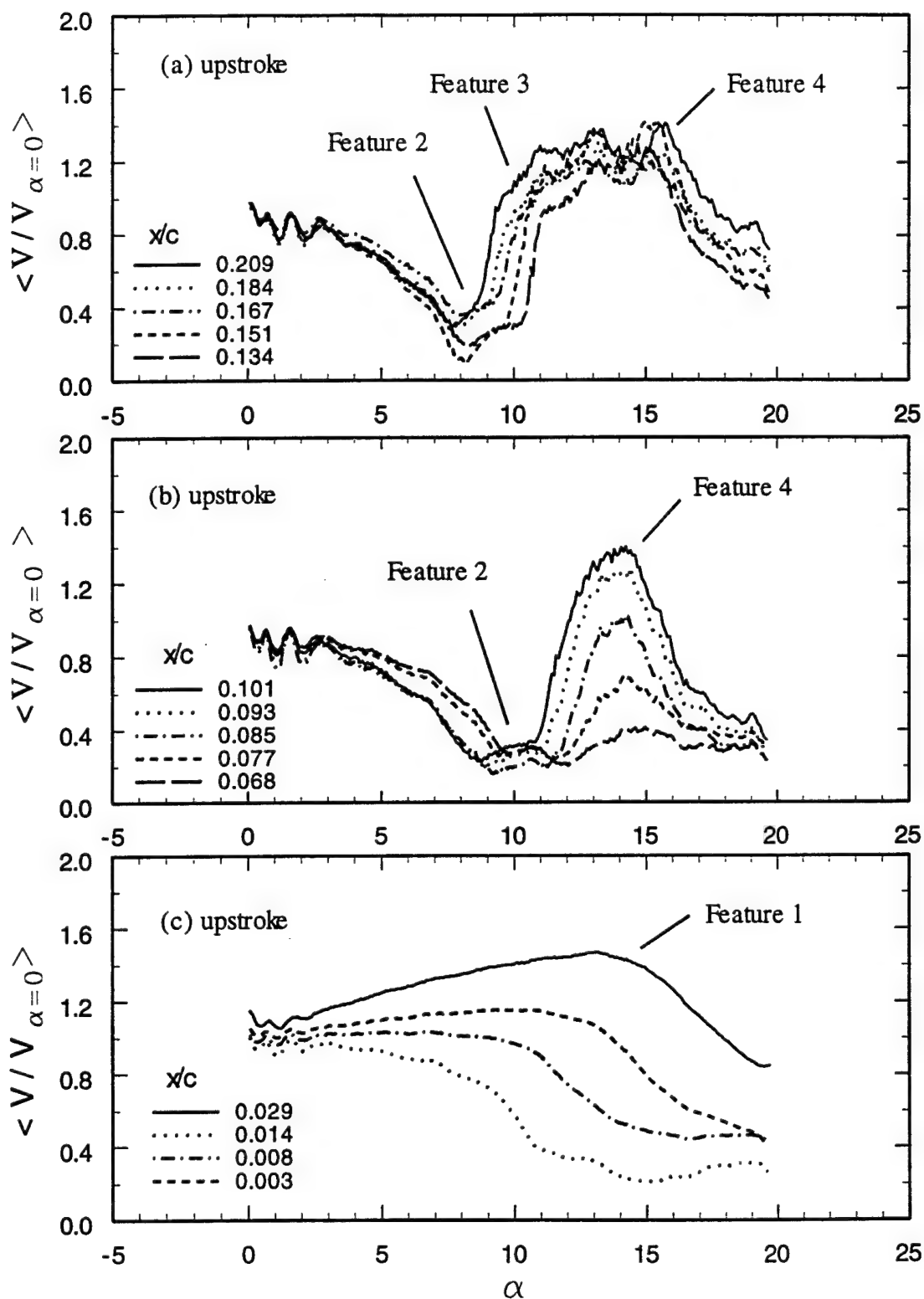


Figure 54 Typical voltage output of hot-film sensors over an oscillating 2-D airfoil at selected chordwise locations for  $Re_c = 1.1 \times 10^5$ ,  $k = 0.1$ ,  $\alpha_o = 10^\circ$ ,  $\alpha_m = 10^\circ$  (page 1 of 2).

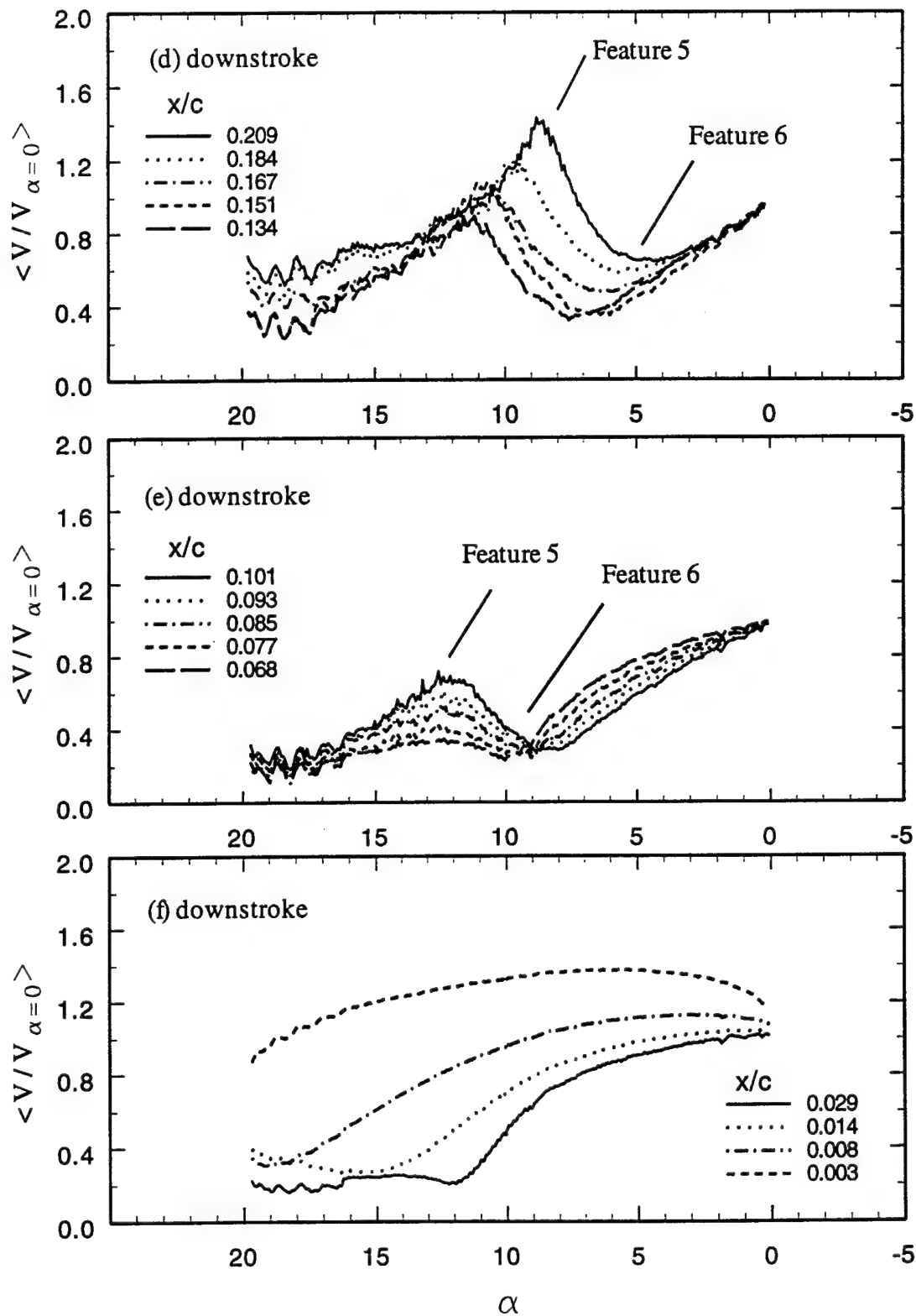


Figure 54 (concluded).

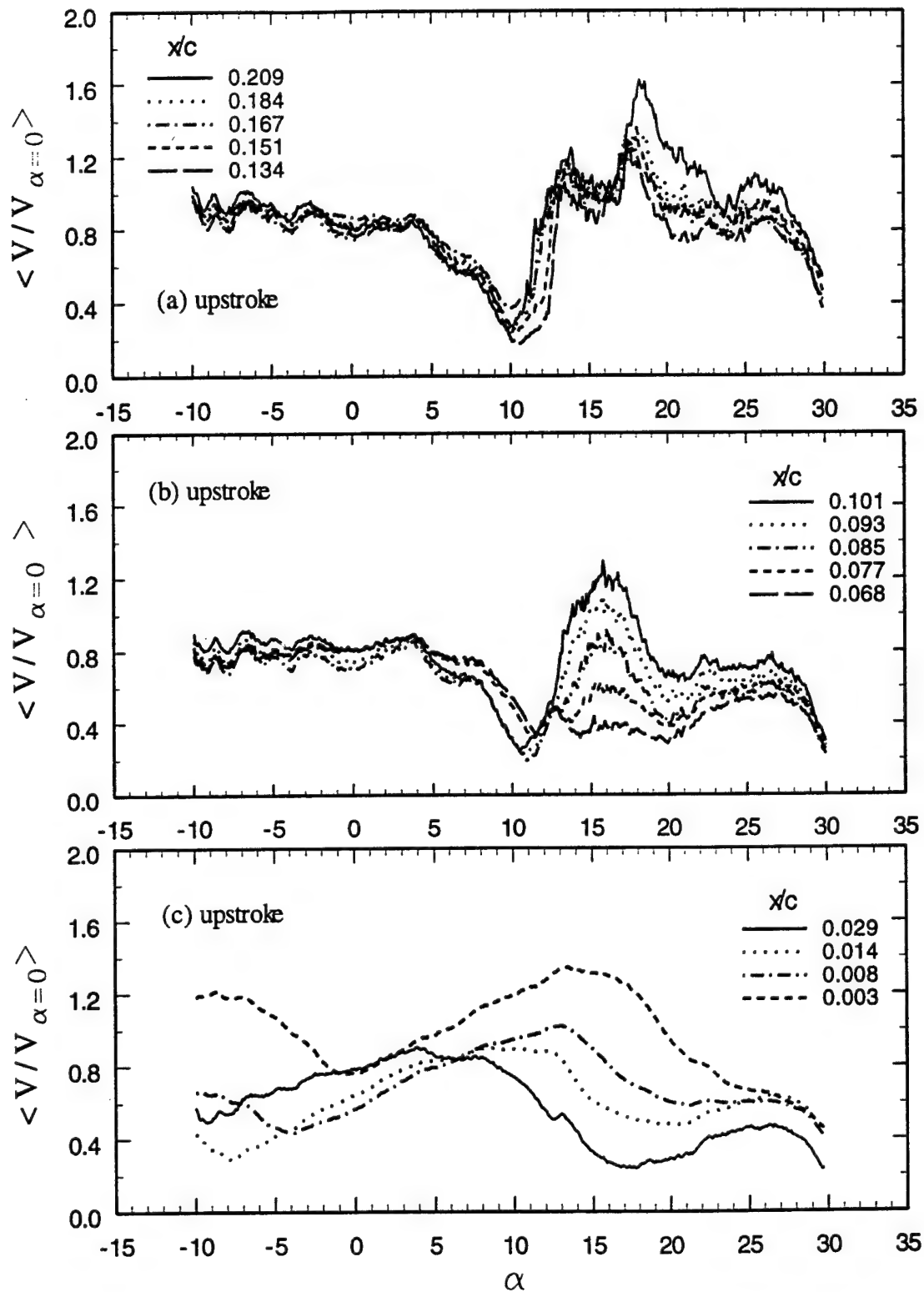


Figure 55 Typical voltage output of hot-film sensors over an oscillating 2-D airfoil at selected chordwise locations for  $Re_c = 1.1 \times 10^5$ ,  $k = 0.1$ ,  $\alpha_o = 10^\circ$ ,  $\alpha_m = 20^\circ$  (page 1 of 2).

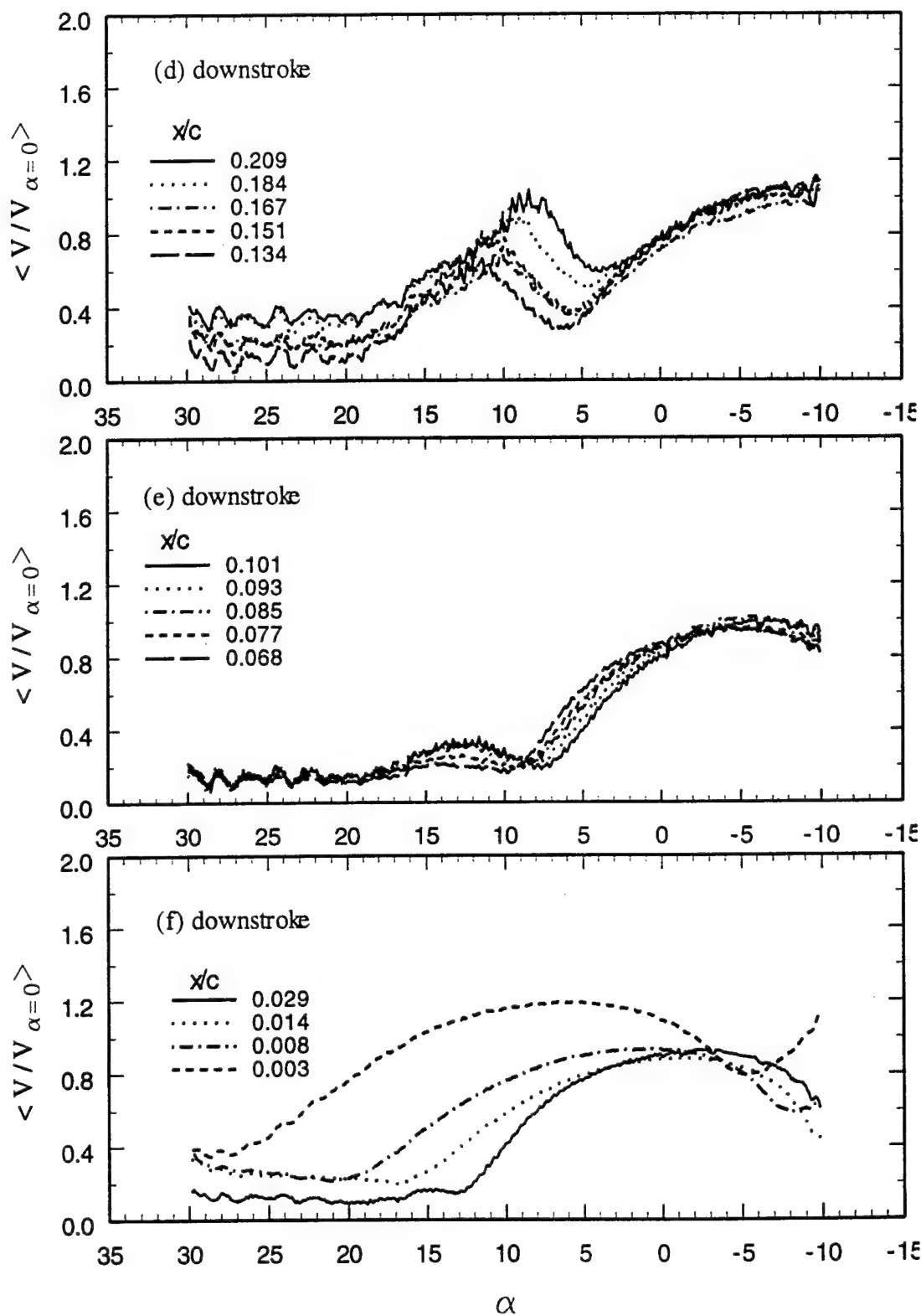


Figure 55 (concluded).

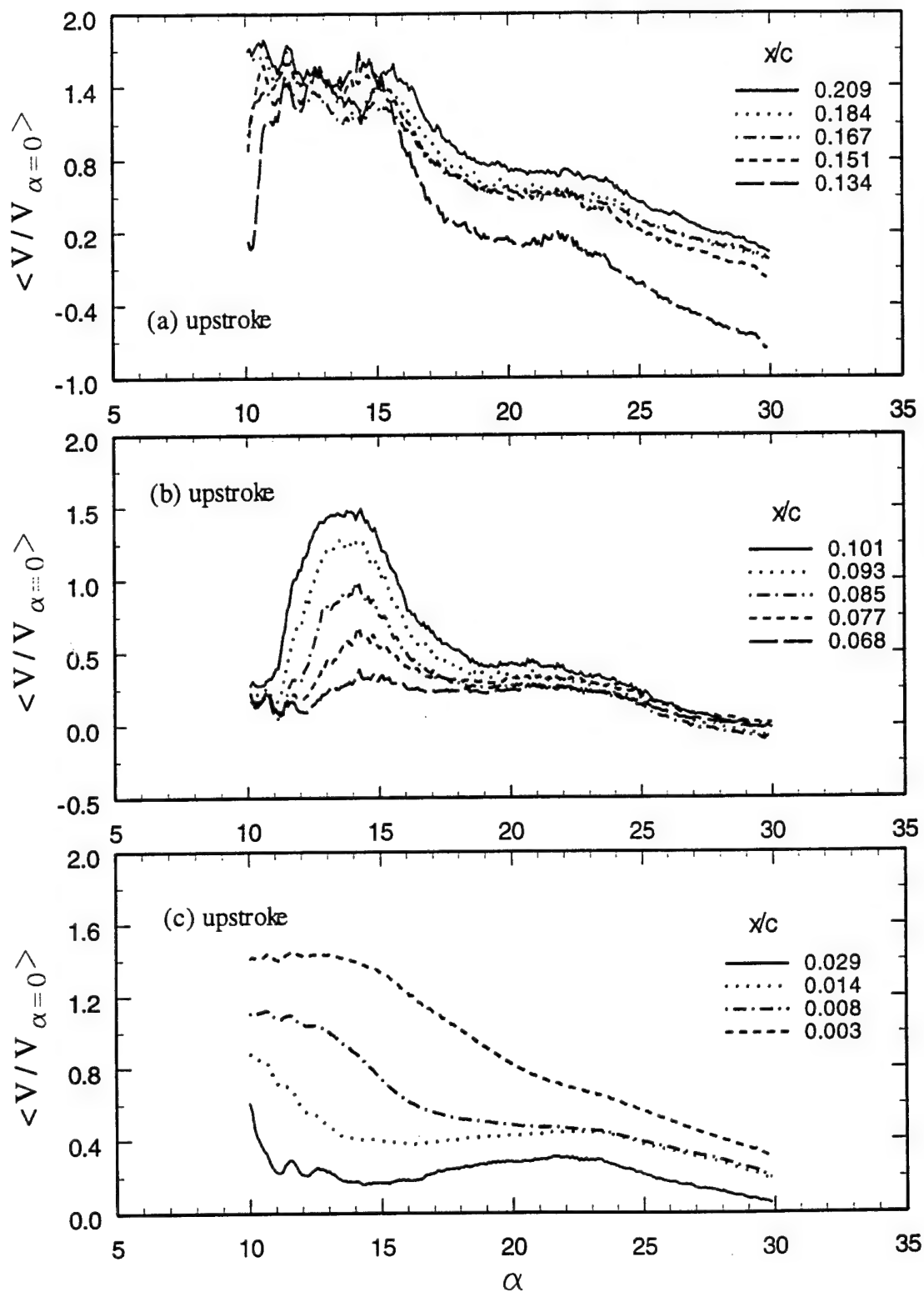


Figure 56 Typical voltage output of hot-film sensors over an oscillating 2-D airfoil at selected chordwise locations for  $Re_c = 1.1 \times 10^5$ ,  $k = 0.1$ ,  $\alpha_o = 20^\circ$ ,  $\alpha_m = 10^\circ$  (page 1 of 2).

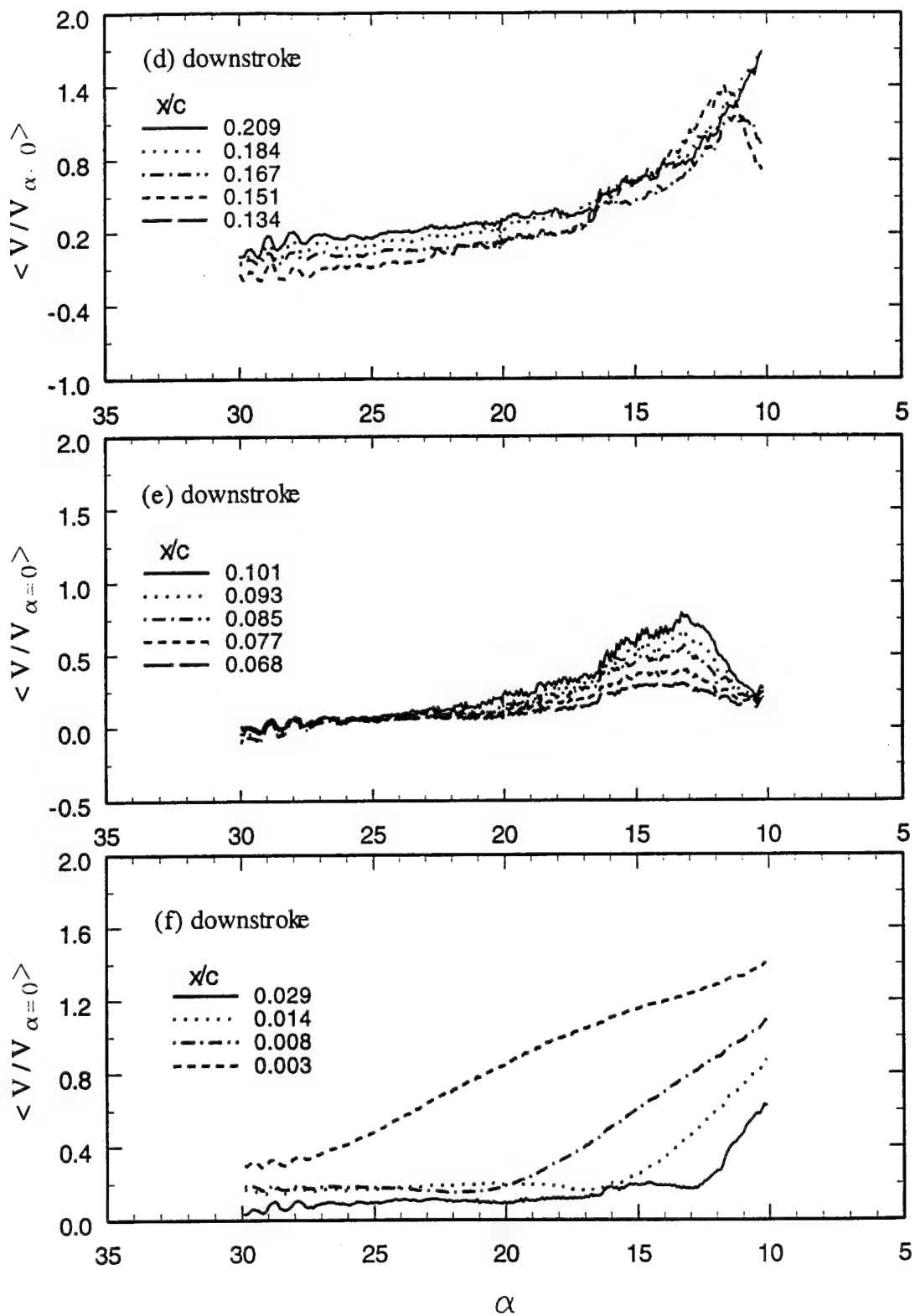


Figure 56 (concluded).



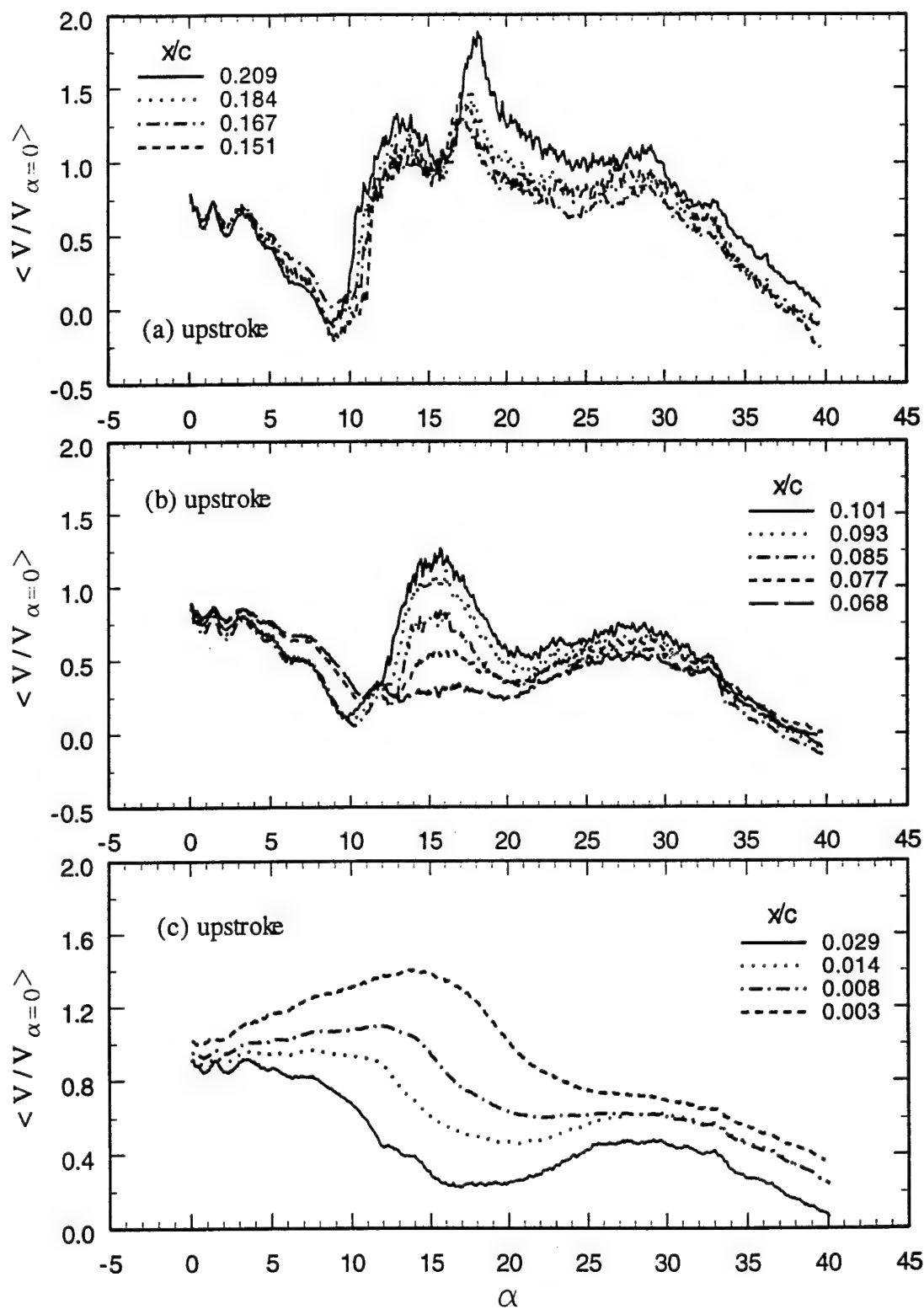


Figure 57 Typical voltage output of hot-film sensors over an oscillating 2-D airfoil at selected chordwise locations for  $Re_c = 1.1 \times 10^5$ ,  $k = 0.1$ ,  $\alpha_o = 20^\circ$ ,  $\alpha_m = 20^\circ$  (page 1 of 2).

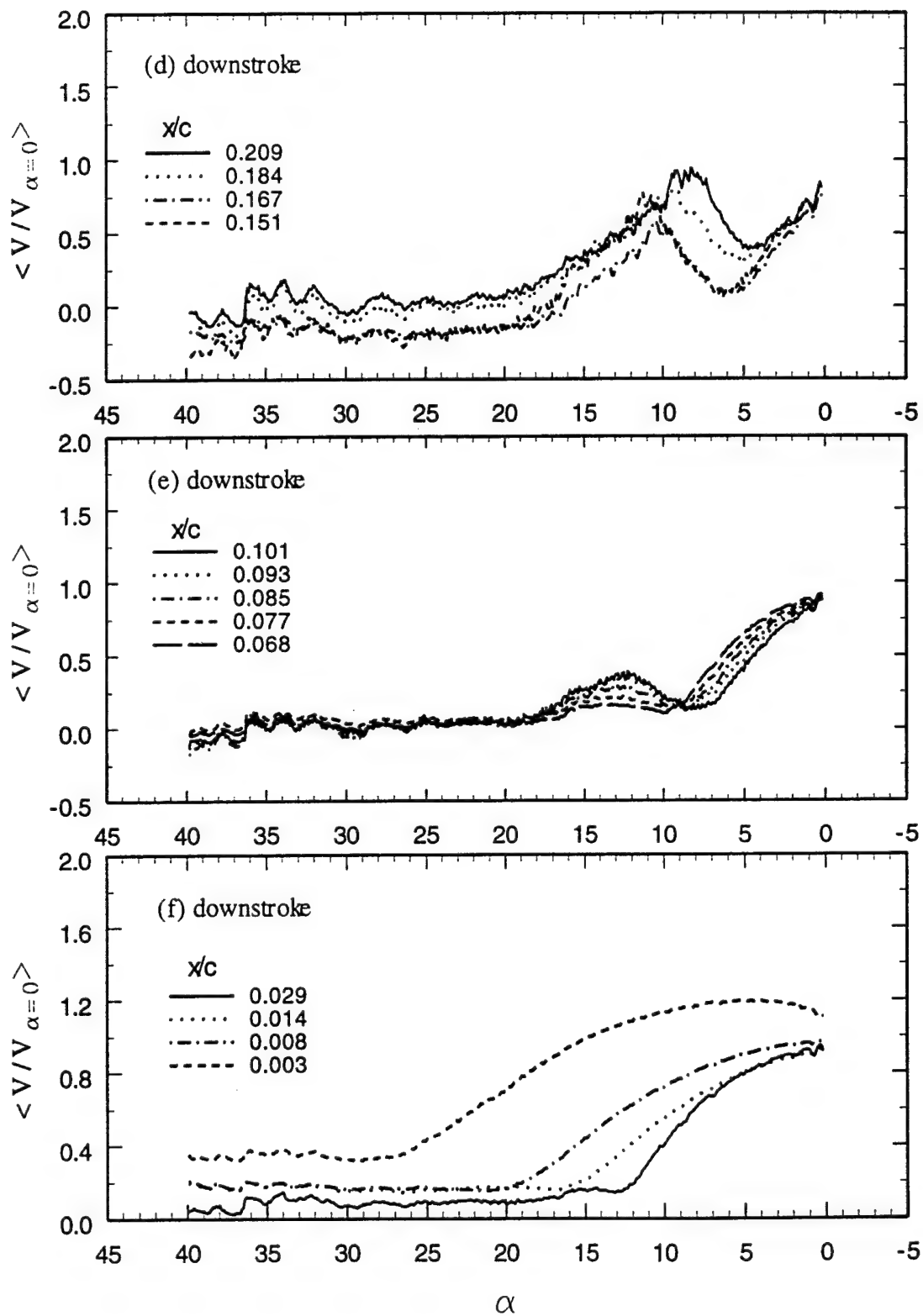


Figure 57 (concluded).

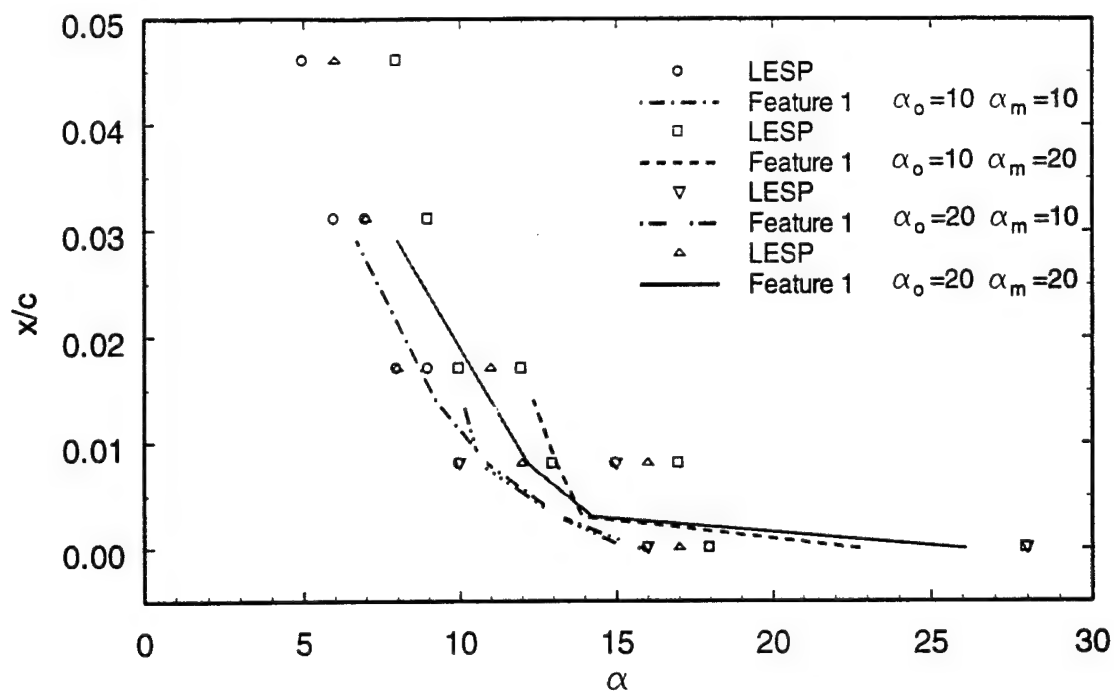


Figure 58 Chordwise location and movement of Feature 1 for  $Re_c = 1.1 \times 10^5$ ,  $k = 0.1$ .

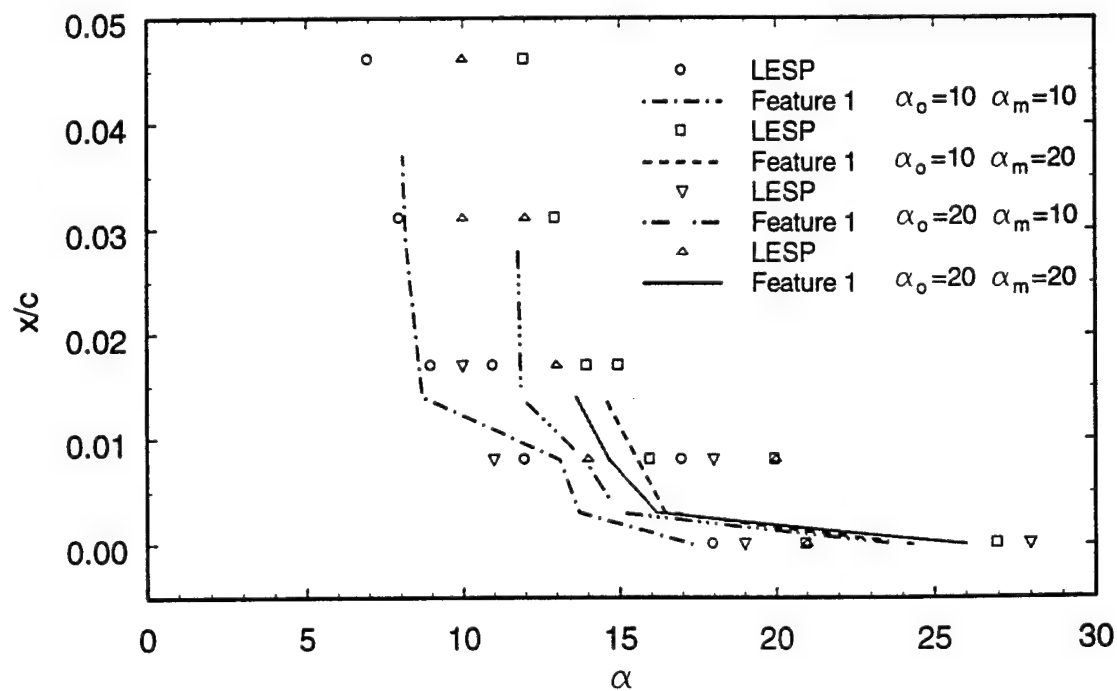


Figure 59 Chordwise location and movement of Feature 1 for  $Re_c = 1.1 \times 10^5$ ,  $k = 0.2$ .

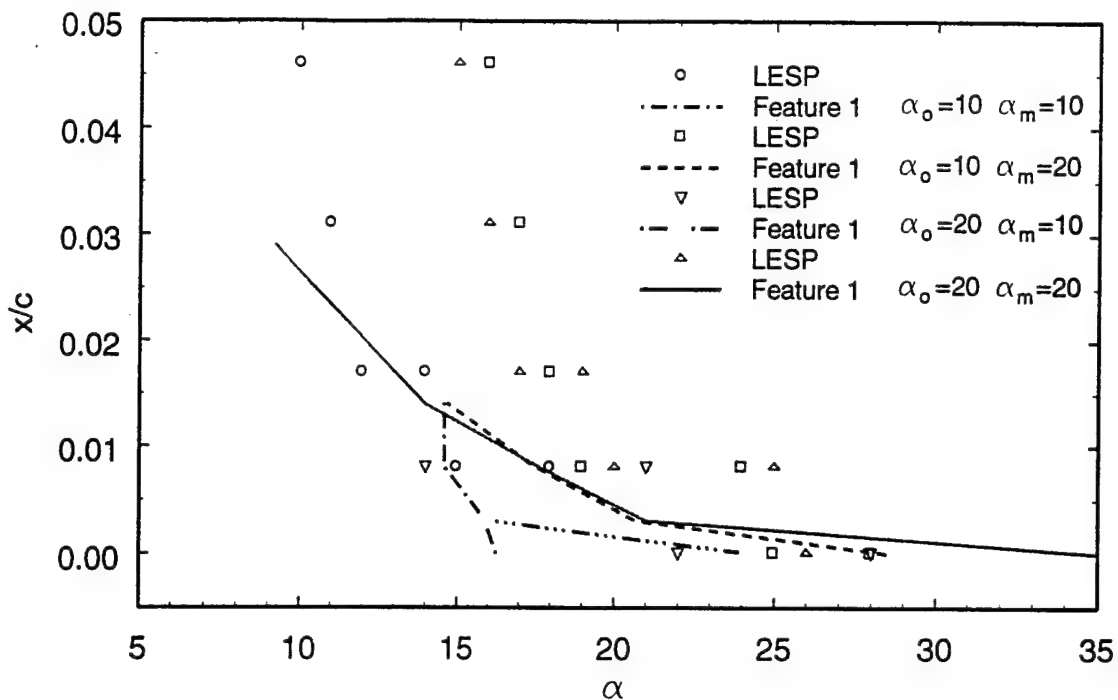


Figure 60 Chordwise location and movement of Feature 1 for  $Re_c = 1.1 \times 10^5$ ,  $k = 0.4$ .

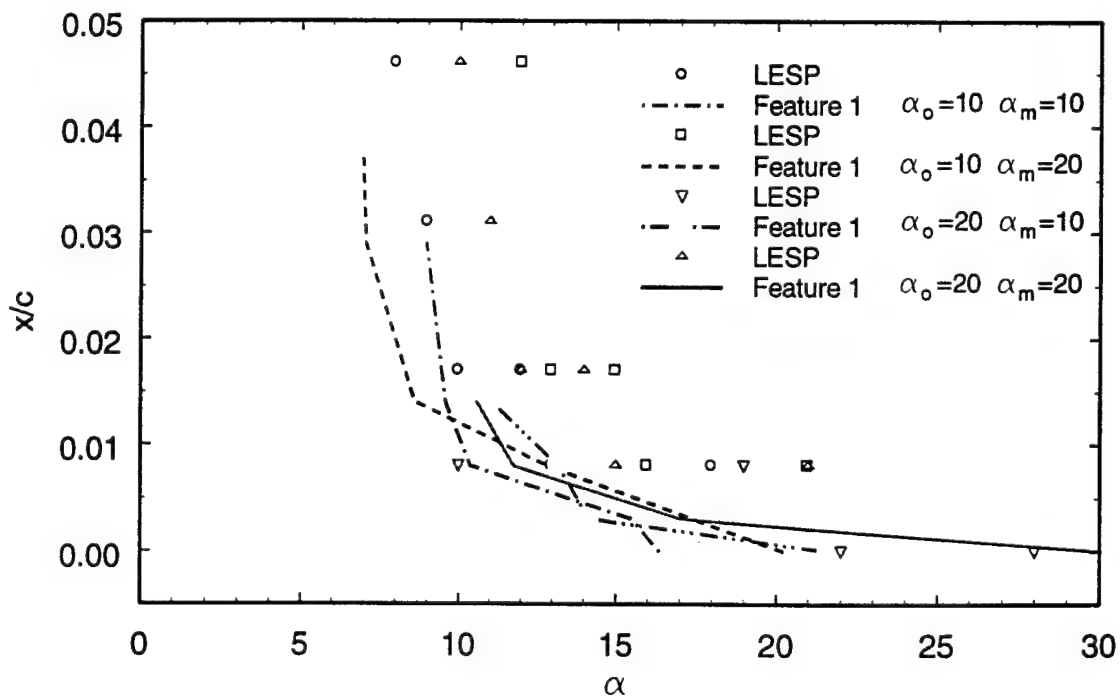


Figure 61 Chordwise location and movement of Feature 1 for  $Re_c = 3.2 \times 10^5$ ,  $k = 0.1$ .

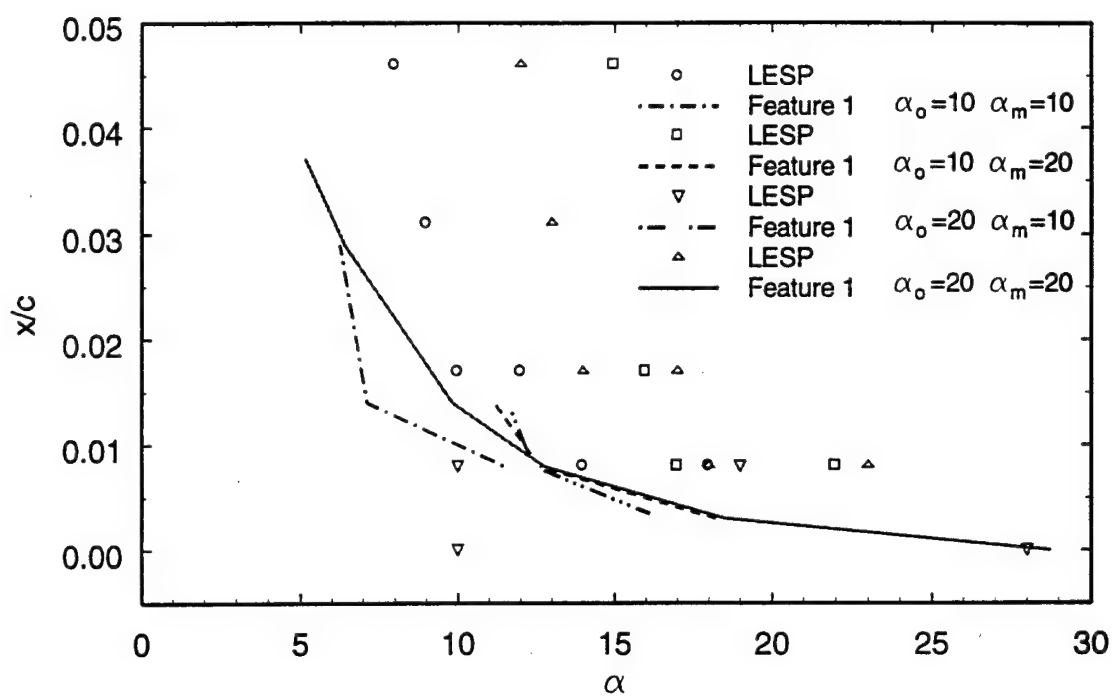


Figure 62 Chordwise location and movement of Feature 1 for  $Re_c = 4.6 \times 10^5$ ,  $k = 0.1$ .

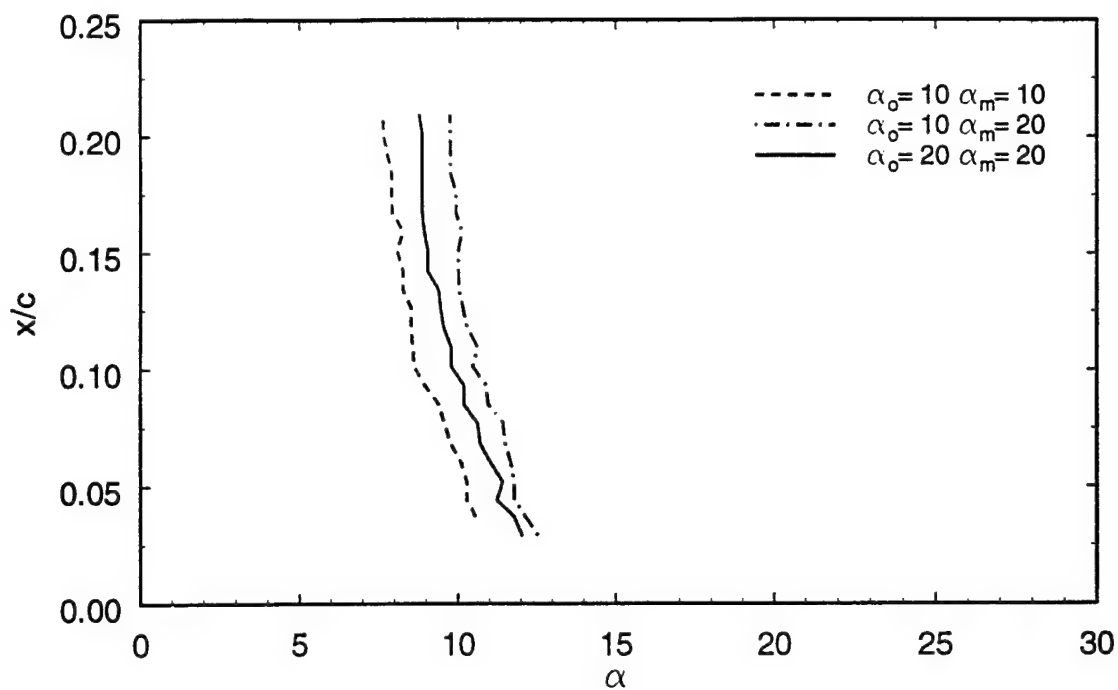


Figure 63 Chordwise location and movement of Feature 2 for  $Re_c = 1.1 \times 10^5$ ,  $k = 0.1$ .

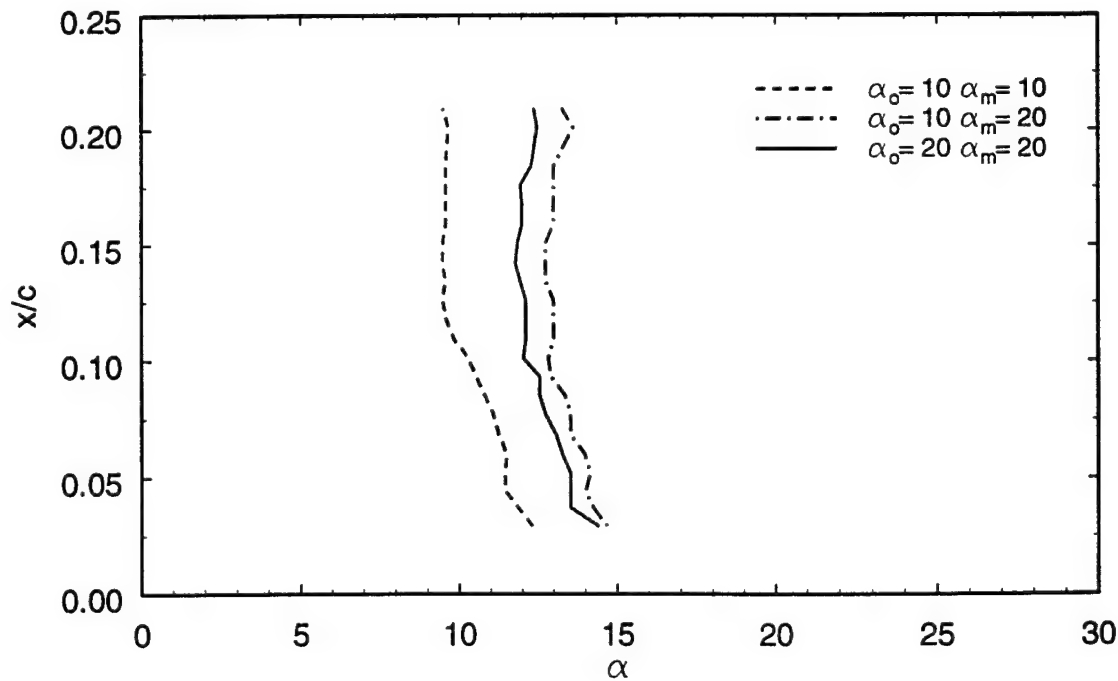


Figure 64 Chordwise location and movement of Feature 2 for  $Re_c = 1.1 \times 10^5$ ,  $k = 0.2$ .

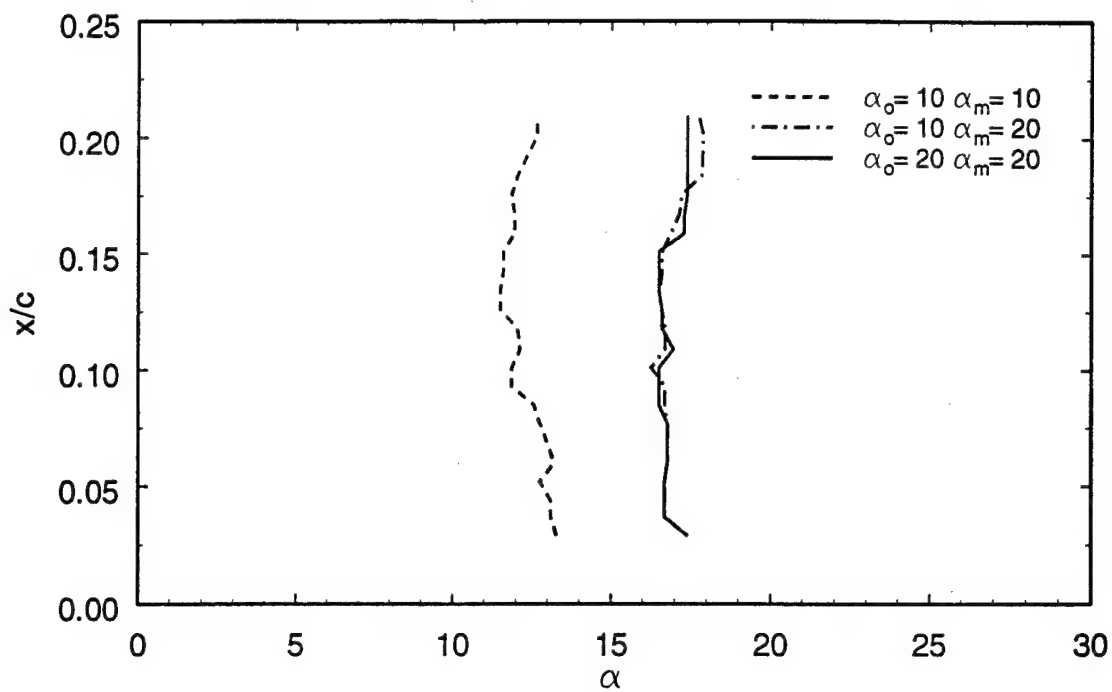


Figure 65 Chordwise location and movement of Feature 2 for  $Re_c = 1.1 \times 10^5$ ,  $k = 0.4$ .

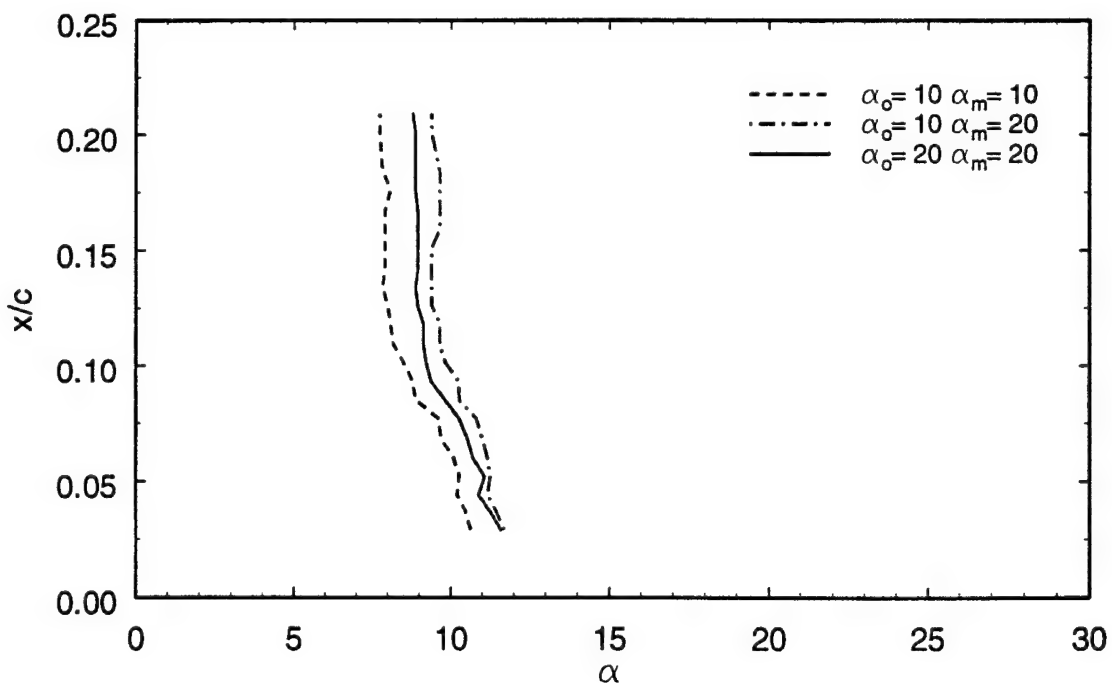


Figure 66 Chordwise location and movement of Feature 2 for  $Re_c = 3.2 \times 10^5$ ,  $k = 0.1$ .

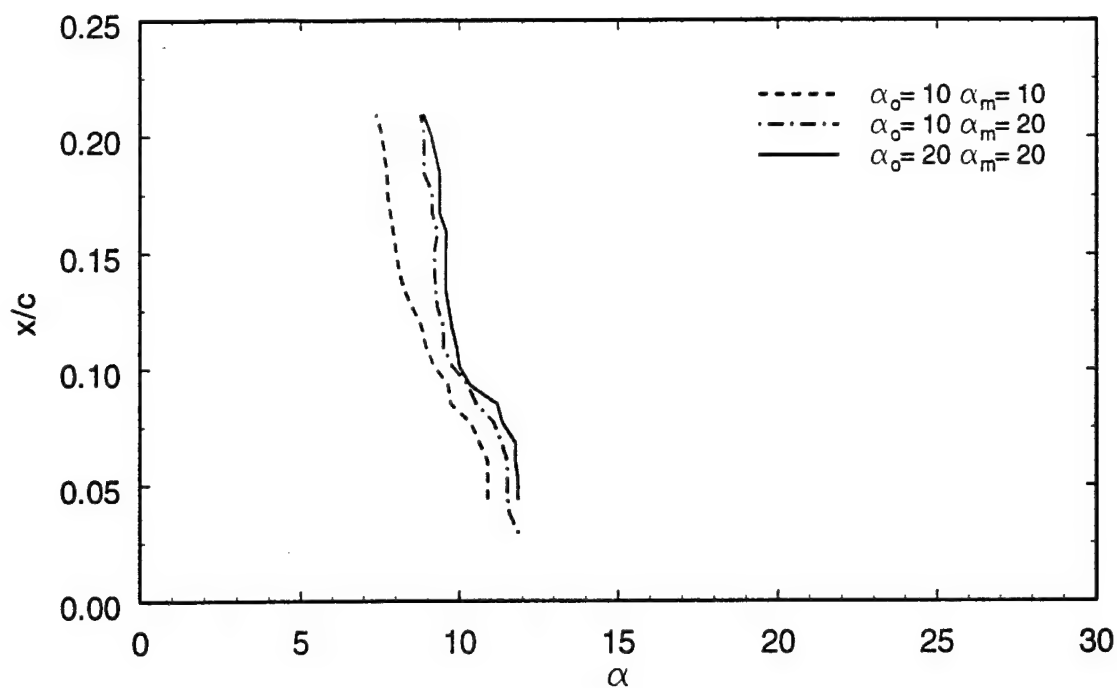


Figure 67 Chordwise location and movement of Feature 2 for  $Re_c = 4.6 \times 10^5$ ,  $k = 0.1$ .

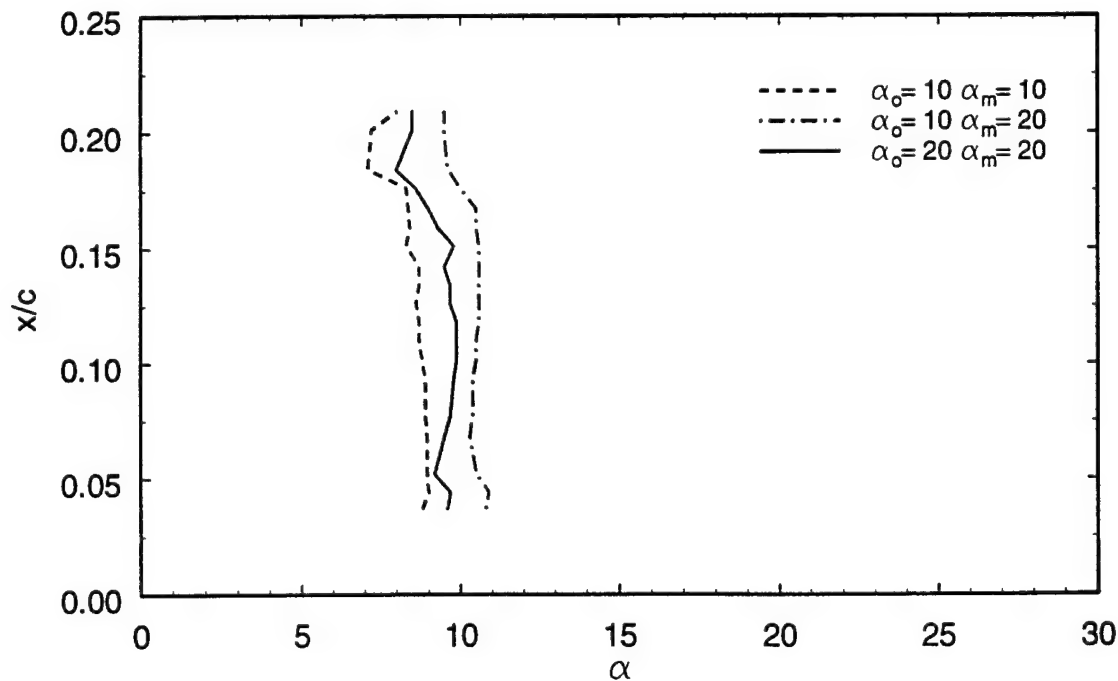


Figure 68 Chordwise location and movement of Feature 2 for  $Re_c = 0.5 \times 10^6$ ,  $k = 0.1$ .



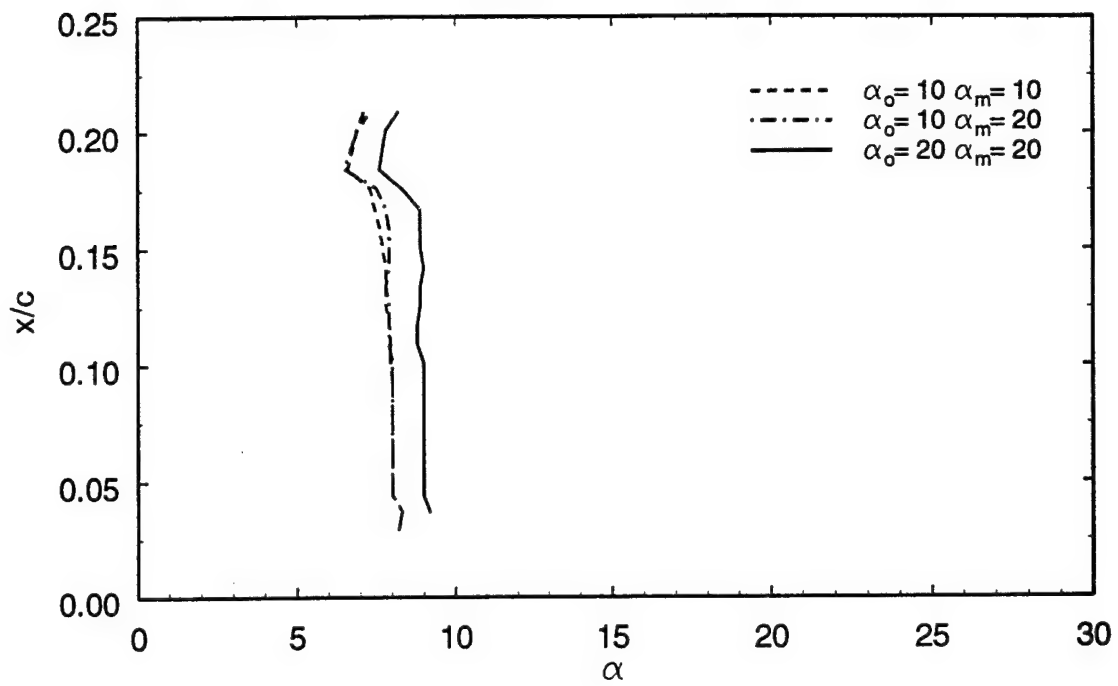


Figure 69 Chordwise location and movement of Feature 2 for  $Re_c = 1.0 \times 10^6$ ,  $k = 0.1$ .

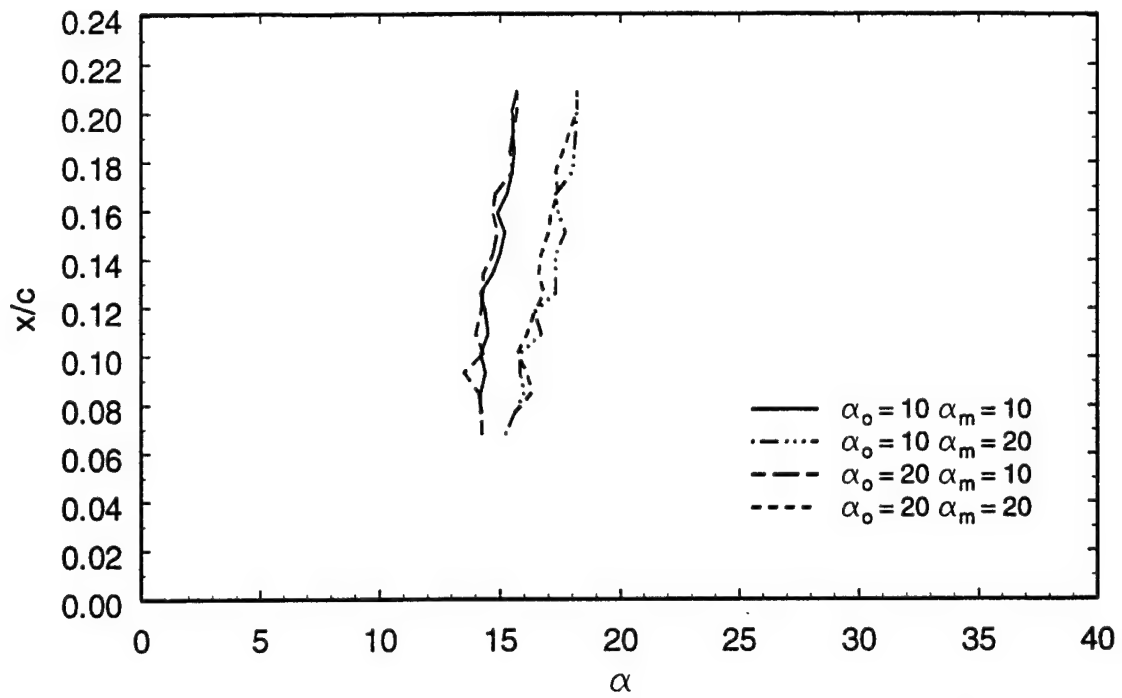


Figure 70 Chordwise location and movement of Feature 4 for  $Re_c = 1.1 \times 10^5$ ,  $k = 0.1$ .

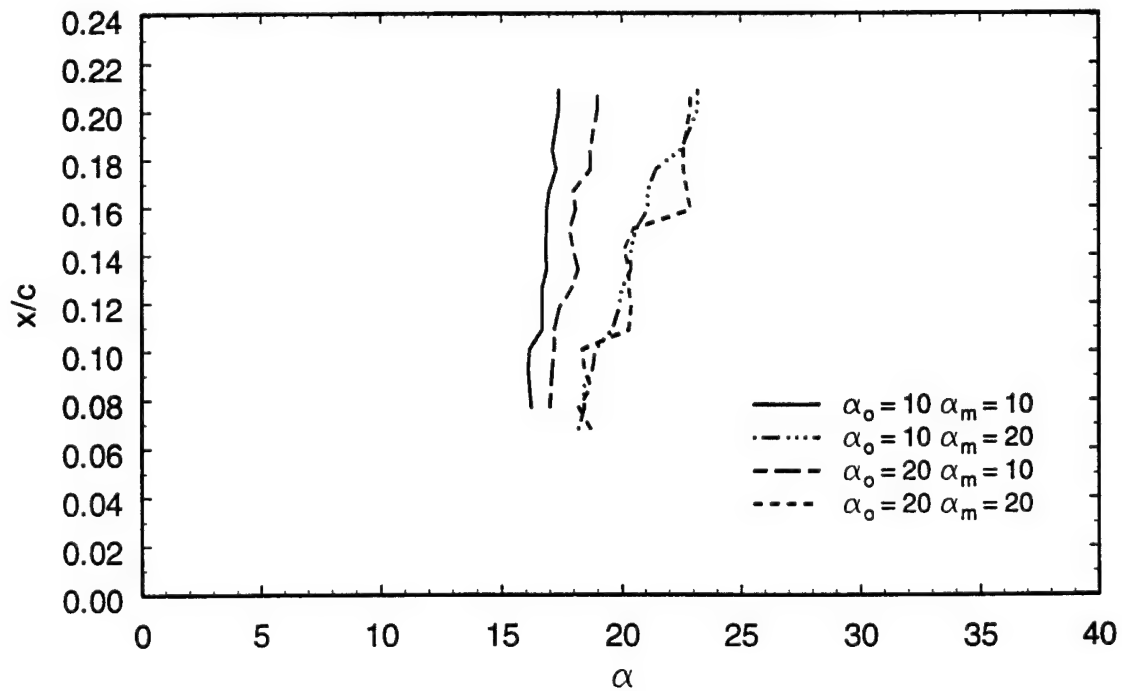


Figure 71 Chordwise location and movement of Feature 4 for  $Re_c = 1.1 \times 10^5$ ,  $k = 0.2$ .

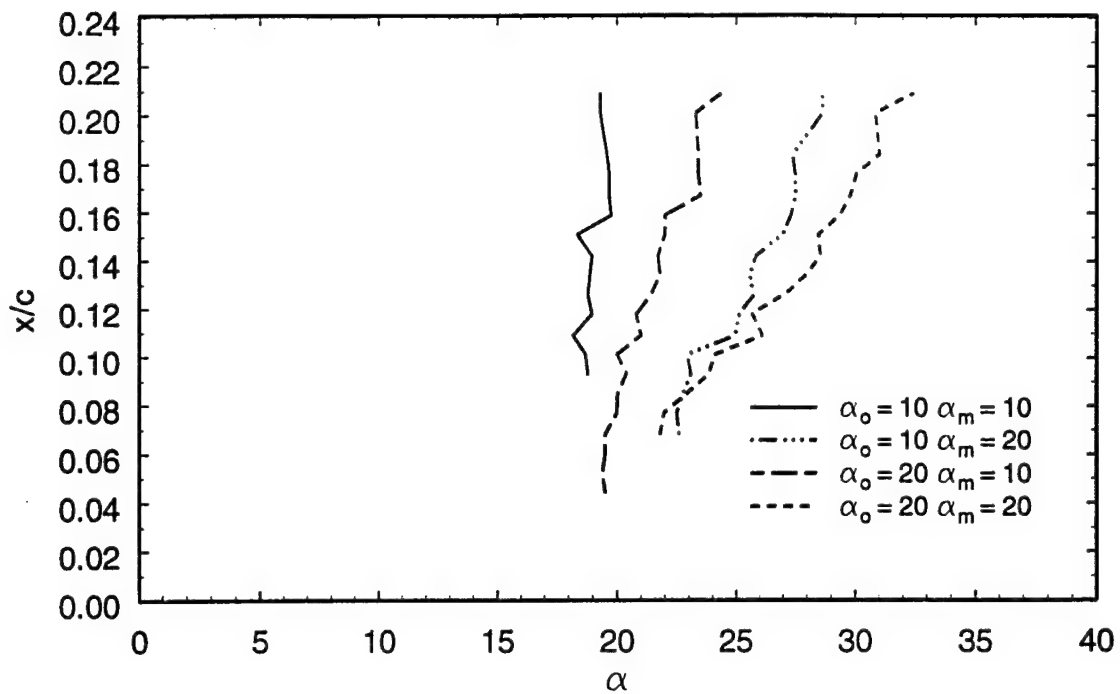


Figure 72 Chordwise location and movement of Feature 4 for  $Re_c = 1.1 \times 10^5$ ,  $k = 0.4$ .

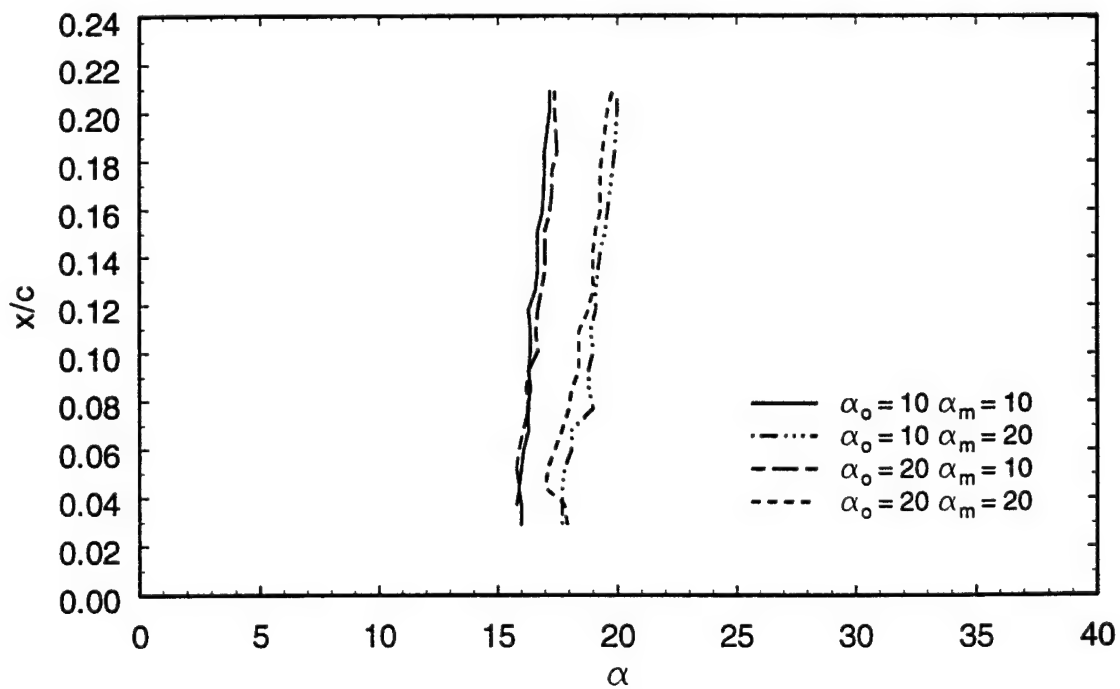


Figure 73 Chordwise location and movement of Feature 4 for  $Re_c = 3.2 \times 10^5$ ,  $k = 0.1$ .

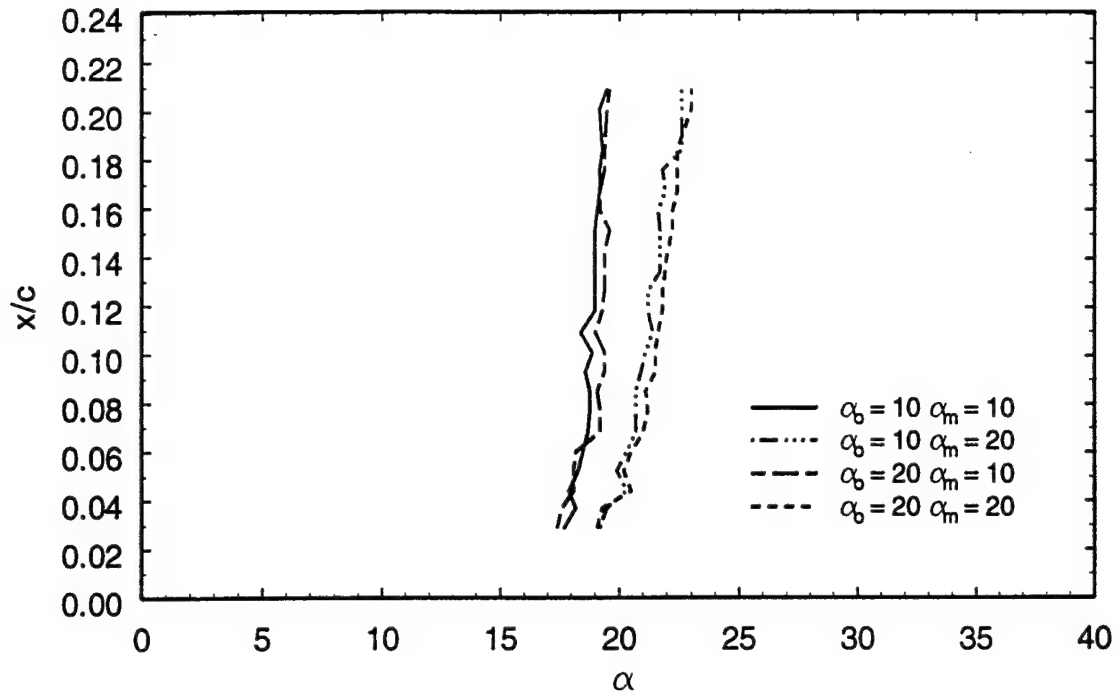


Figure 74 Chordwise location and movement of Feature 4 for  $Re_c = 4.6 \times 10^5$ ,  $k = 0.1$ .

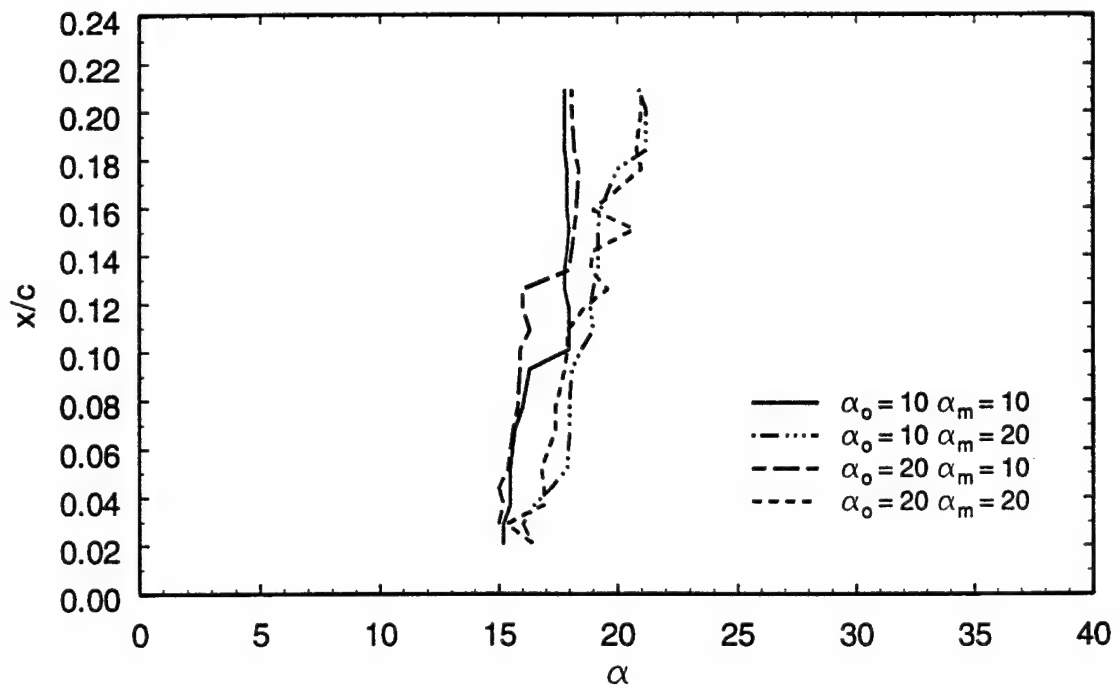


Figure 75 Chordwise location and movement of Feature 4 for  $Re_c = 0.5 \times 10^6$ ,  $k = 0.1$ .

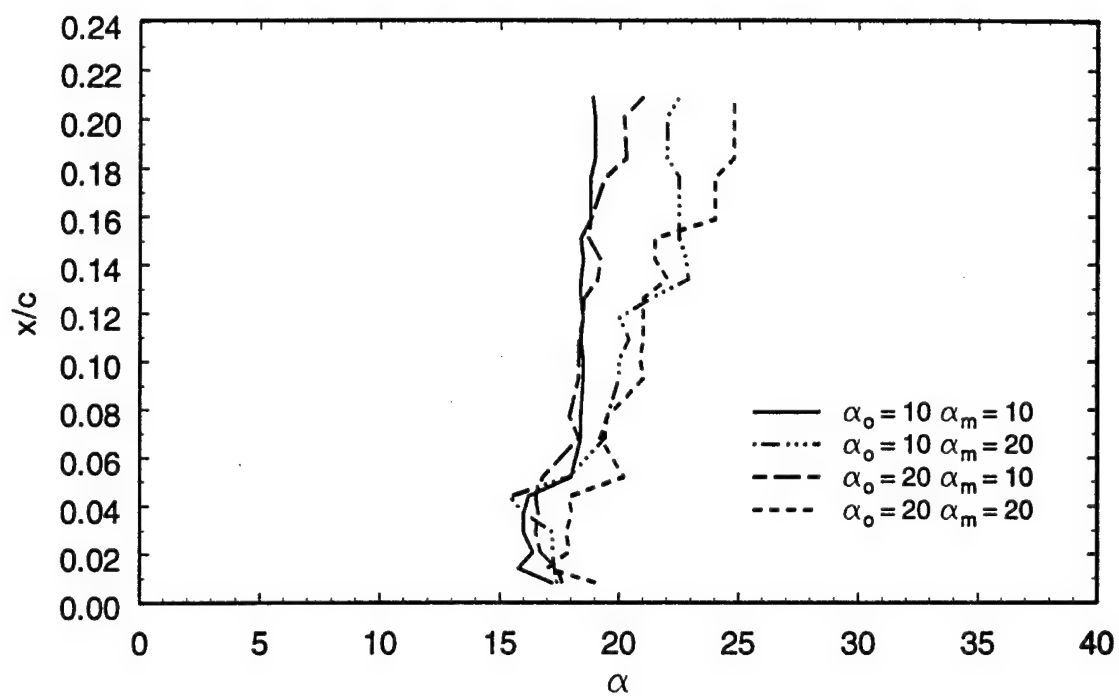


Figure 76 Chordwise location and movement of Feature 4 for  $Re_c = 1.0 \times 10^6$ ,  $k = 0.1$ .

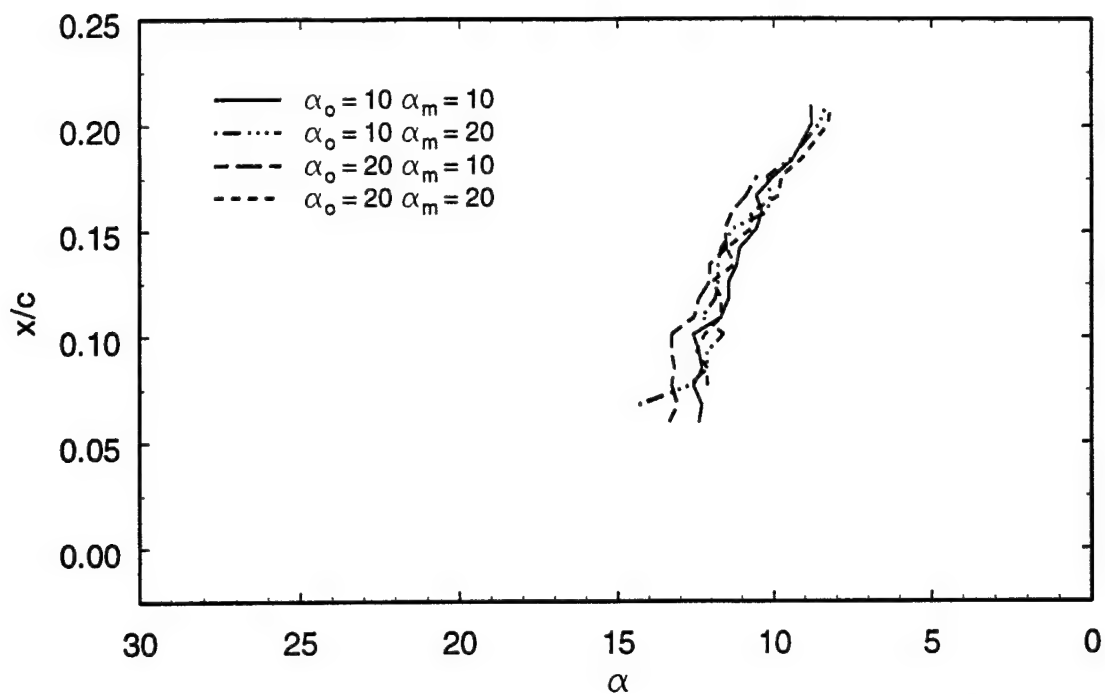


Figure 77 Chordwise location and movement of Feature 5 for  $Re_c = 1.1 \times 10^5$ ,  $k = 0.1$ .

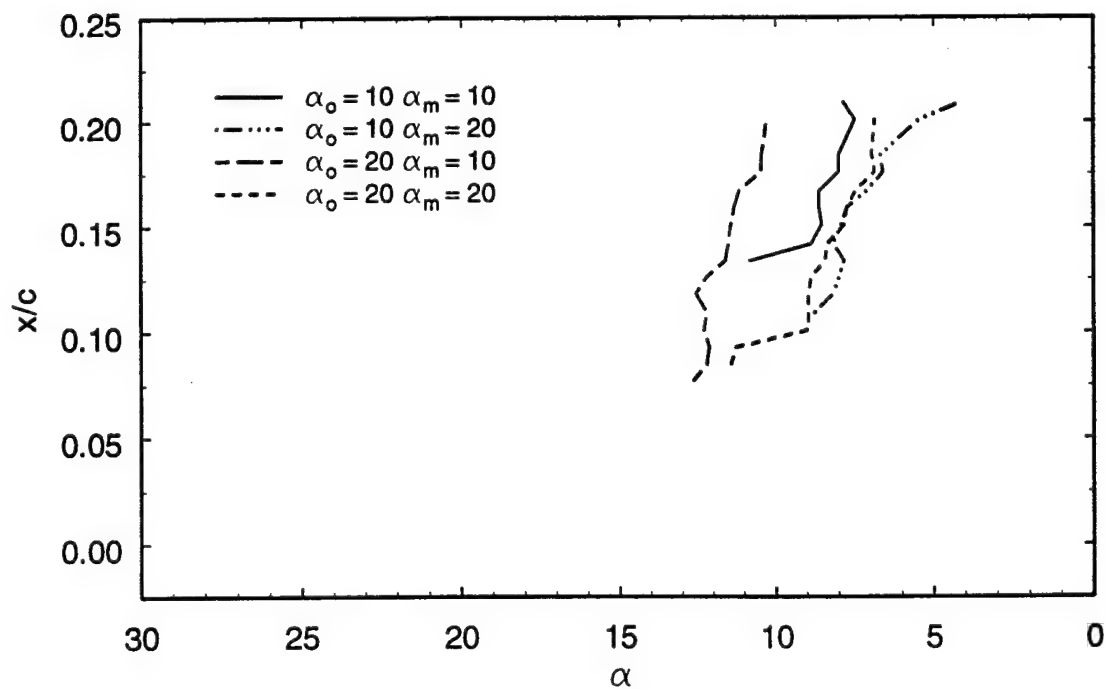


Figure 78 Chordwise location and movement of Feature 5 for  $Re_c = 1.1 \times 10^5$ ,  $k = 0.2$ .

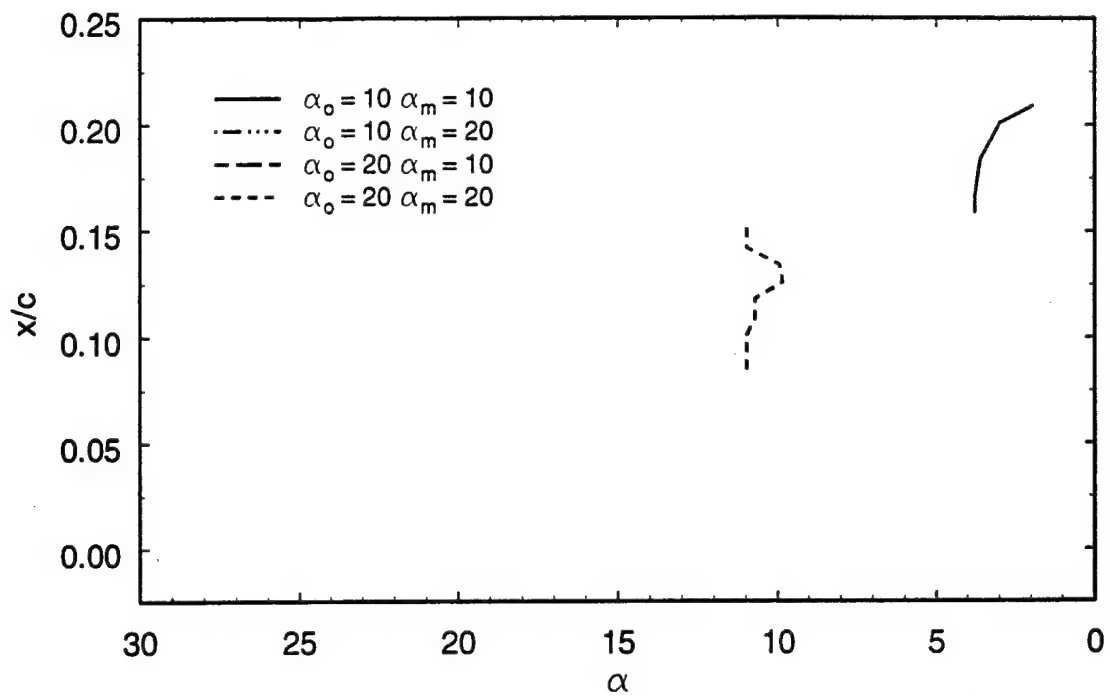


Figure 79 Chordwise location and movement of Feature 5 for  $Re_c = 1.1 \times 10^5$ ,  $k = 0.4$ .

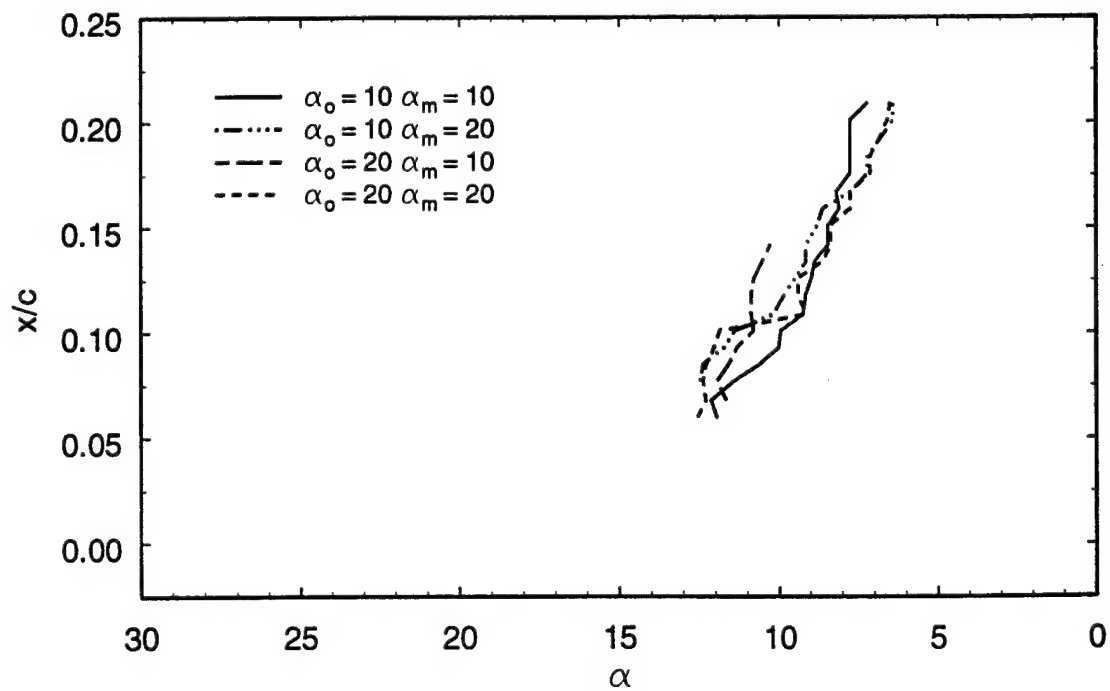


Figure 80 Chordwise location and movement of Feature 5 for  $Re_c = 3.2 \times 10^5$ ,  $k = 0.1$ .

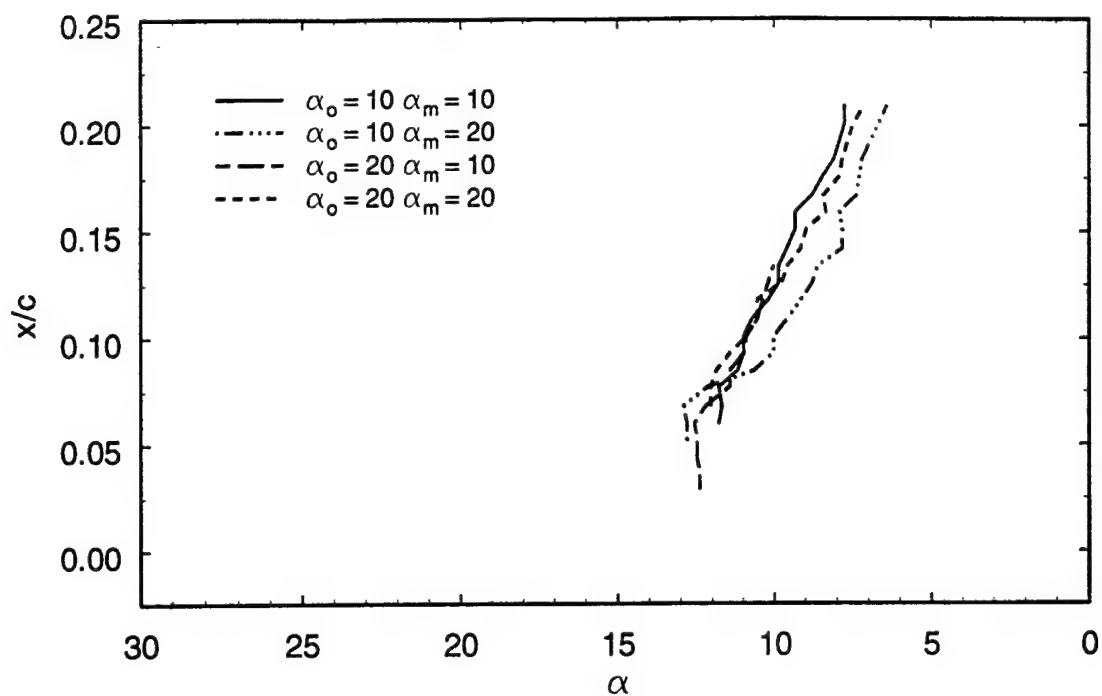


Figure 81 Chordwise location and movement of Feature 5 for  $Re_c = 4.6 \times 10^5$ ,  $k = 0.1$ .

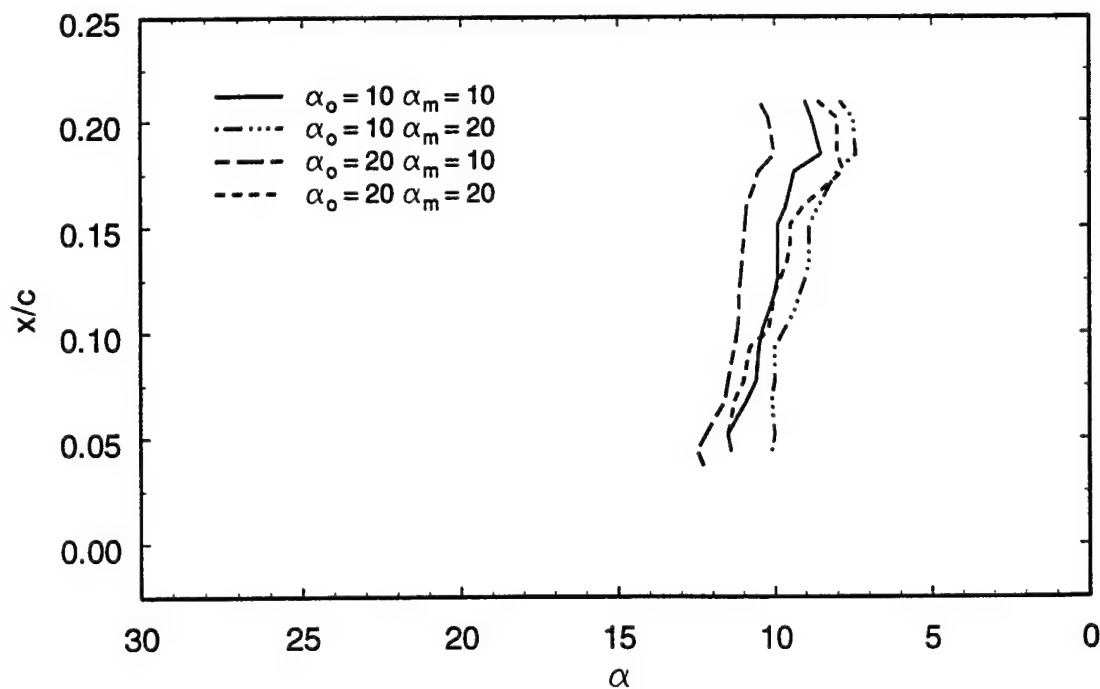


Figure 82 Chordwise location and movement of Feature 5 for  $Re_c = 0.5 \times 10^6$ ,  $k = 0.1$ .



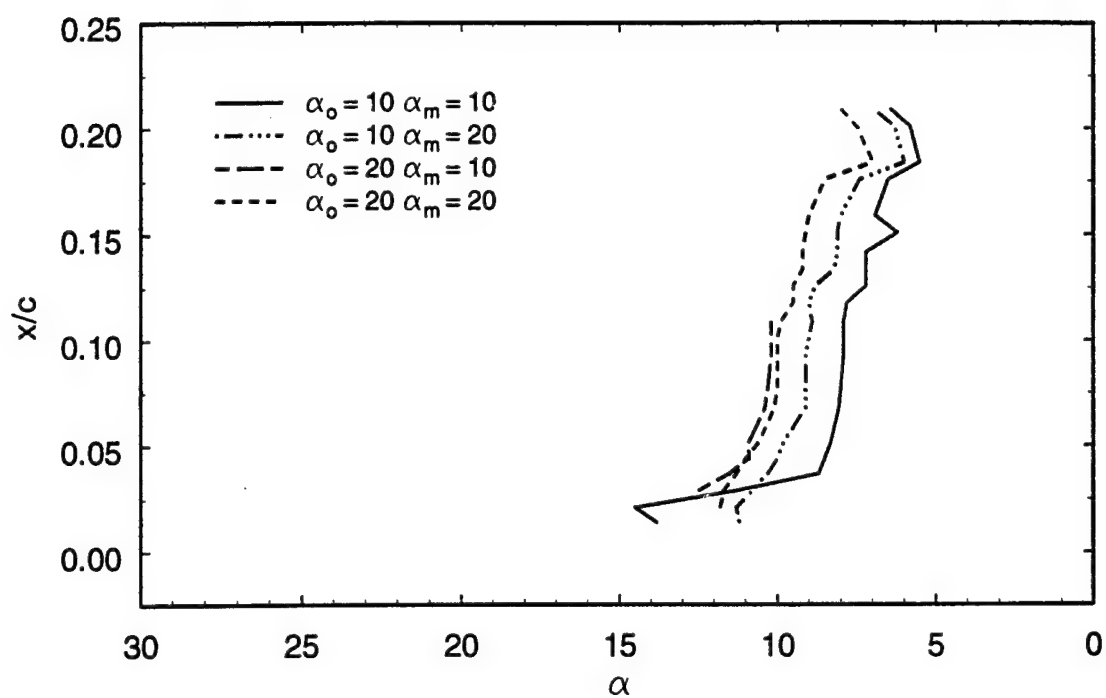


Figure 83 Chordwise location and movement of Feature 5 for  $Re_c = 1.0 \times 10^6$ ,  $k = 0.1$ .

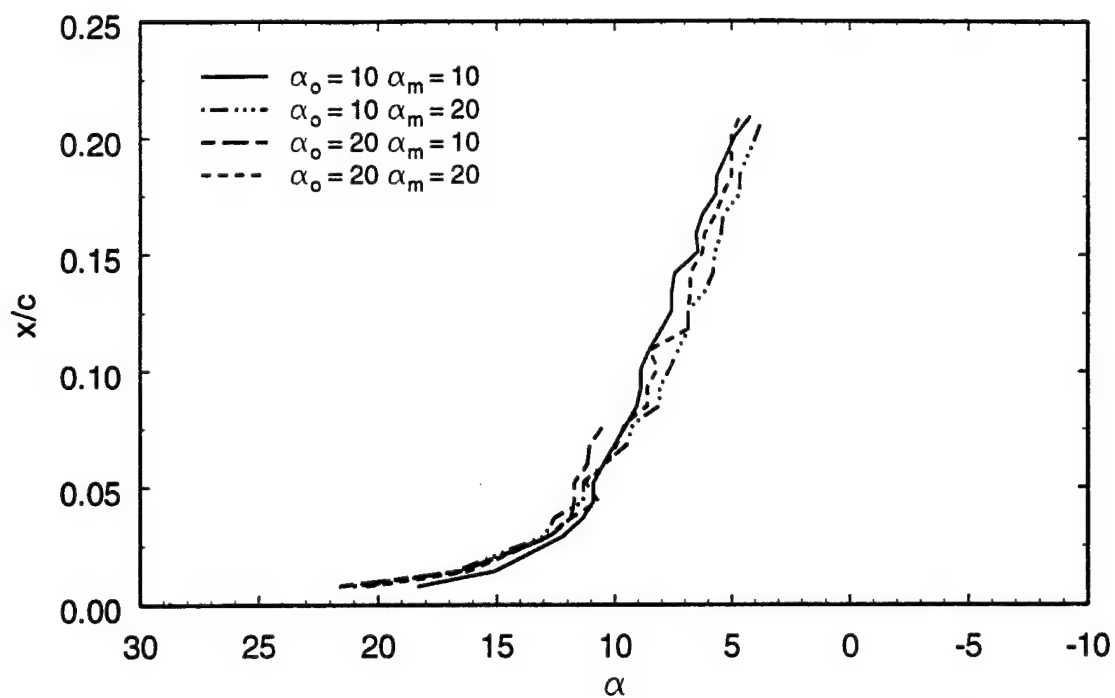


Figure 84 Chordwise location and movement of Feature 6 for  $Re_c = 1.1 \times 10^5$ ,  $k = 0.1$ .

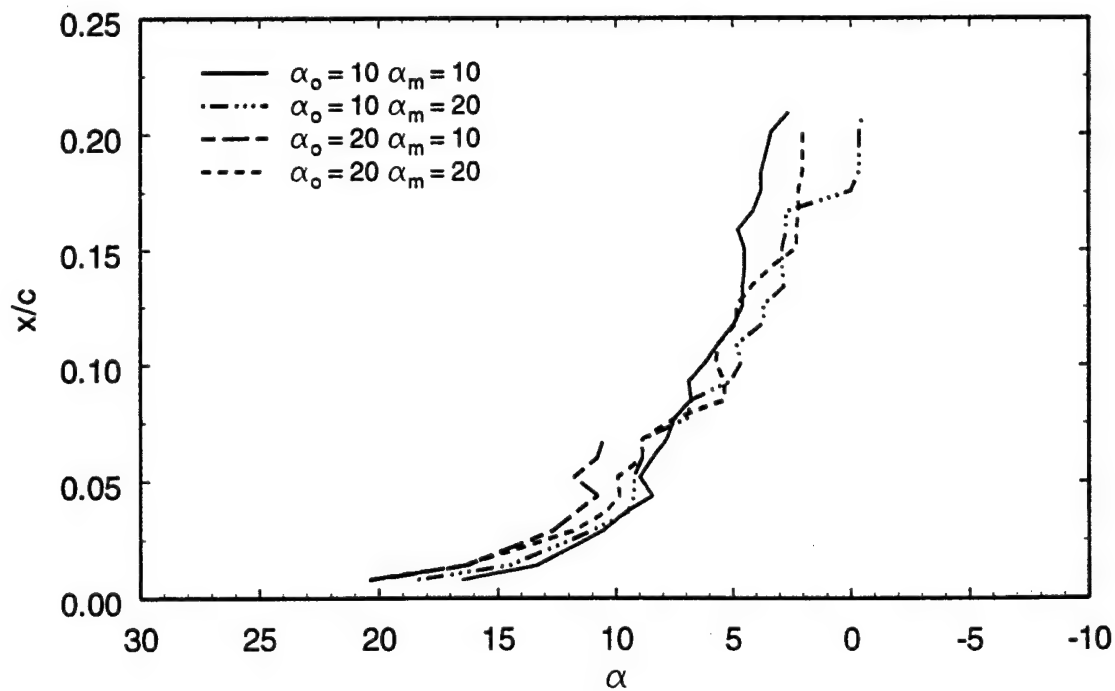


Figure 85 Chordwise location and movement of Feature 6 for  $Re_c = 1.1 \times 10^5$ ,  $k = 0.2$ .

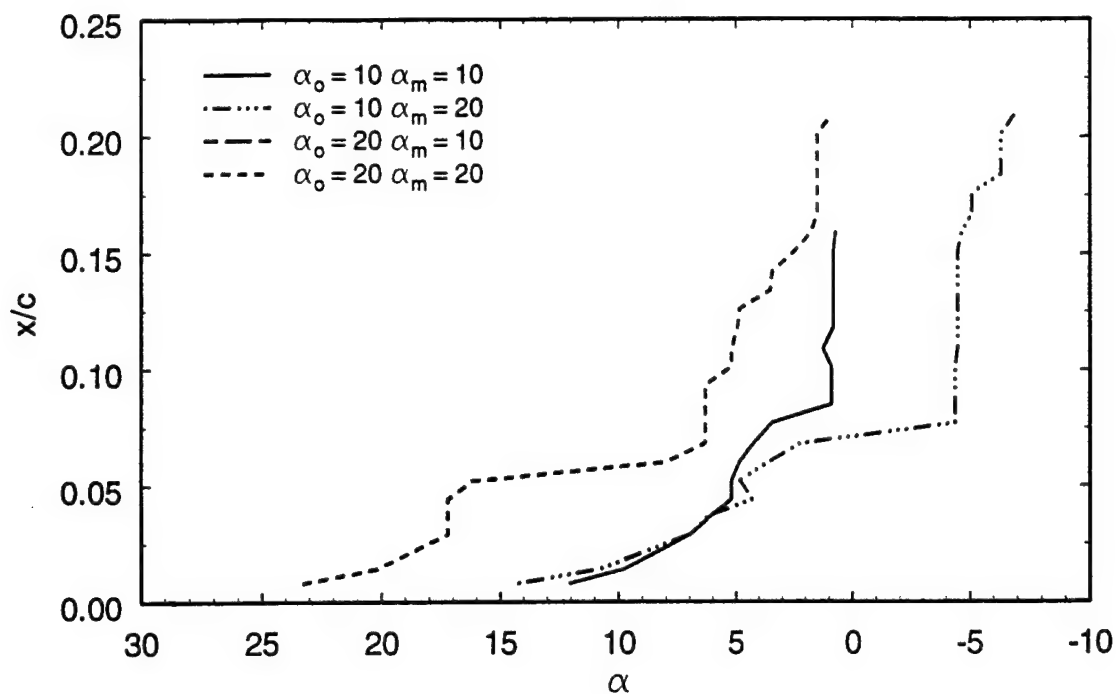


Figure 86 Chordwise location and movement of Feature 6 for  $Re_c = 1.1 \times 10^5$ ,  $k = 0.4$ .

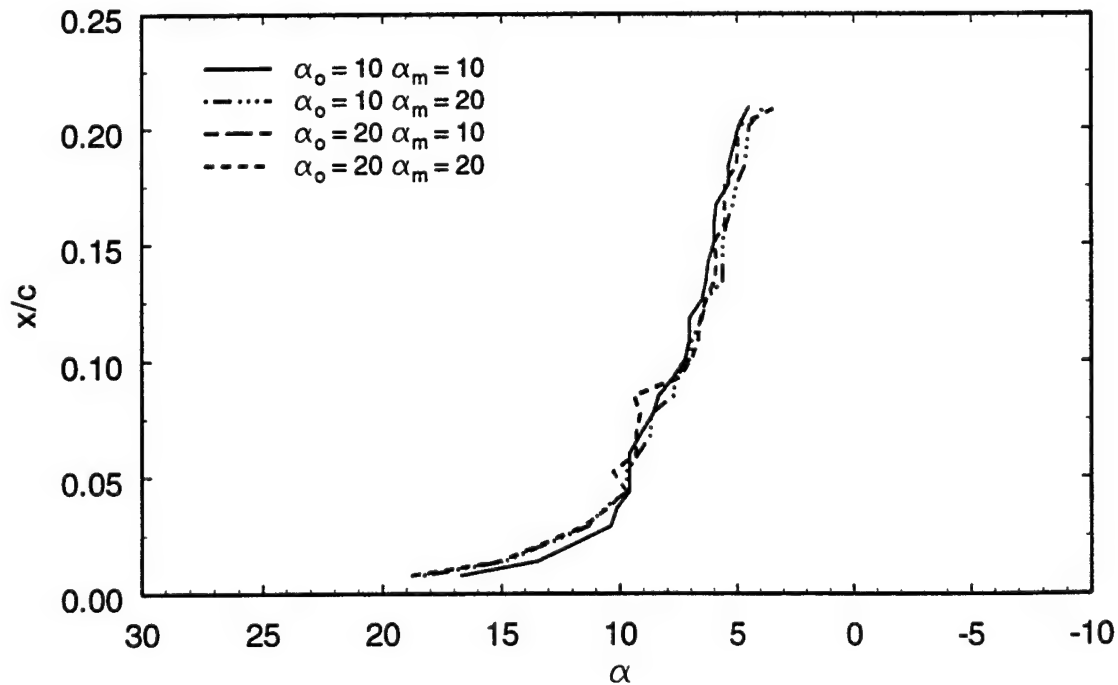


Figure 87 Chordwise location and movement of Feature 6 for  $Re_c = 3.2 \times 10^5$ ,  $k = 0.1$ .

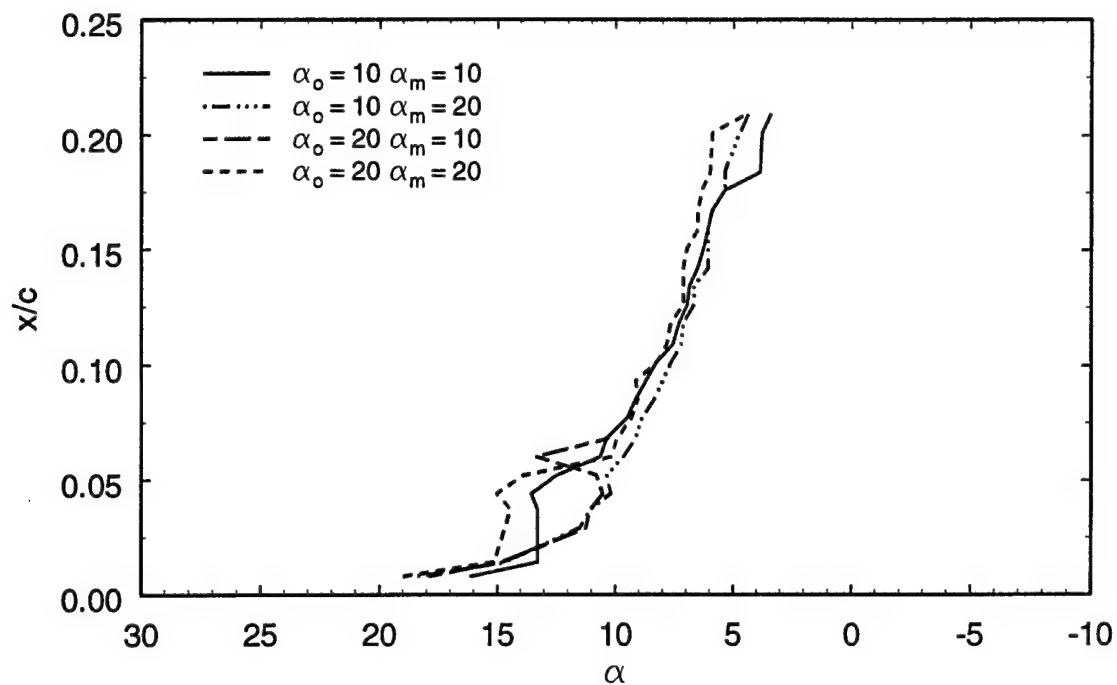


Figure 88 Chordwise location and movement of Feature 6 for  $Re_c = 4.6 \times 10^5$ ,  $k = 0.1$ .

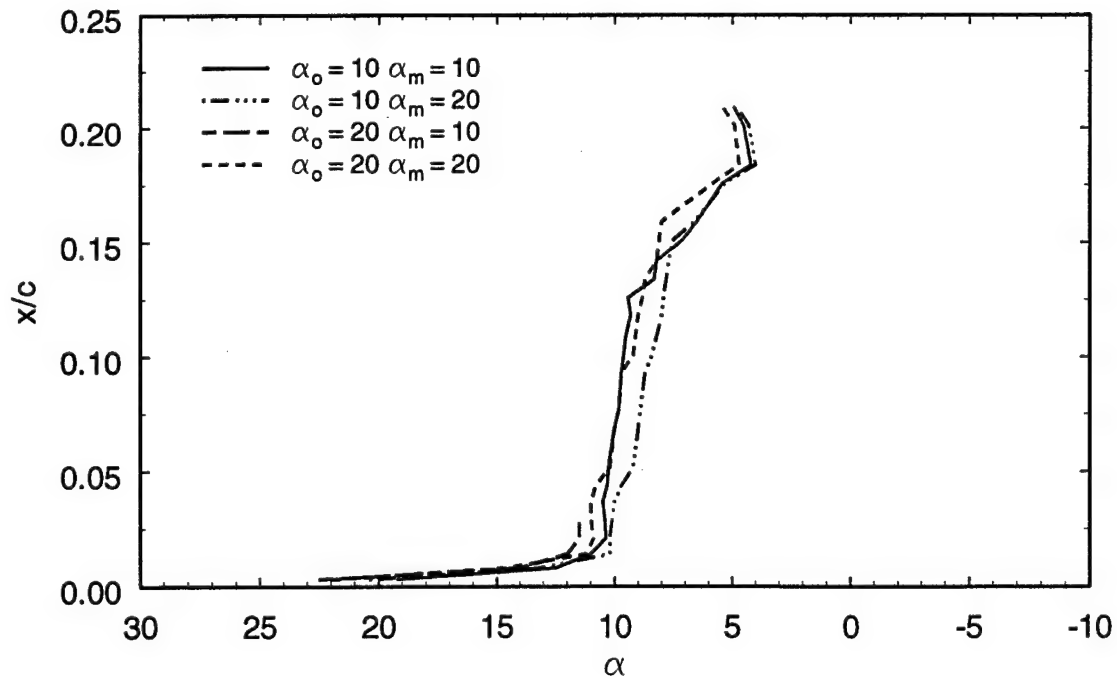


Figure 89 Chordwise location and movement of Feature 6 for  $Re_c = 0.5 \times 10^6$ ,  $k = 0.1$ .

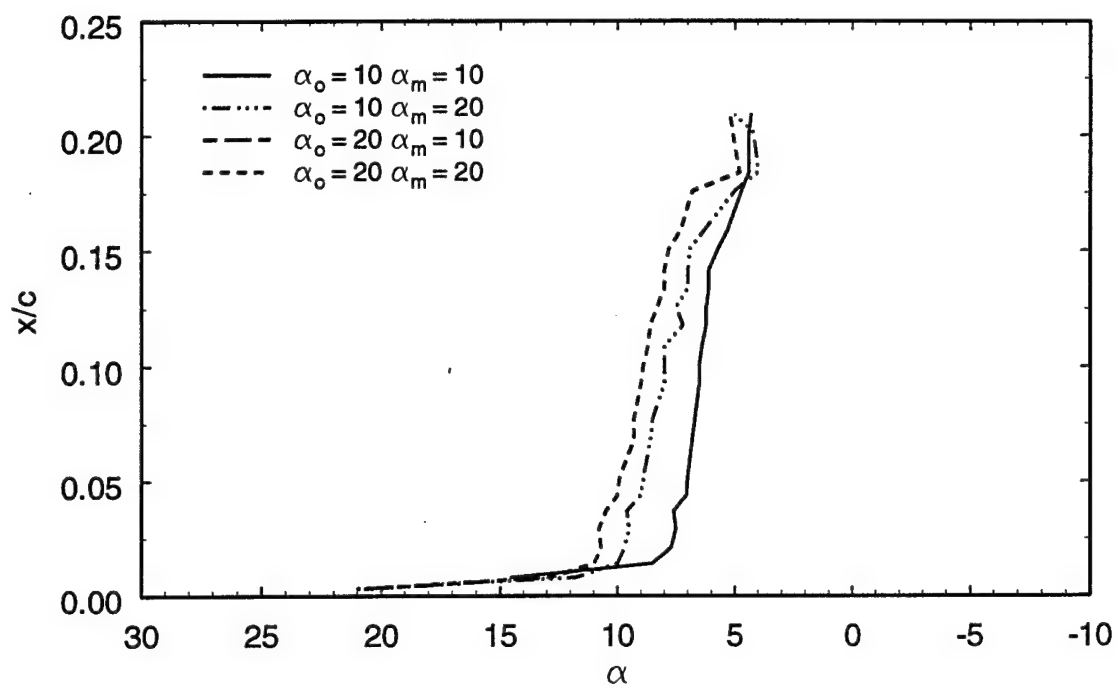


Figure 90 Chordwise location and movement of Feature 6 for  $Re_c = 1.0 \times 10^6$ ,  $k = 0.1$ .

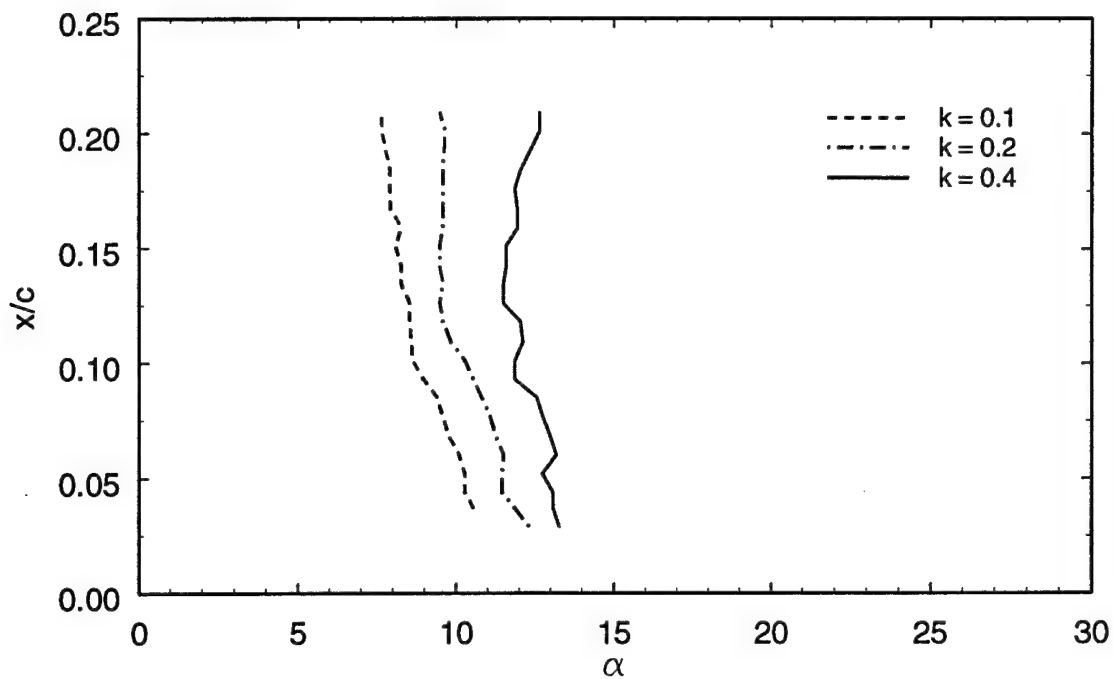


Figure 91 Effects of reduced frequency on Feature 2 for  $Re_c = 1.1 \times 10^5$   
 $\alpha_o = 10^\circ$ ,  $\alpha_m = 10^\circ$ .

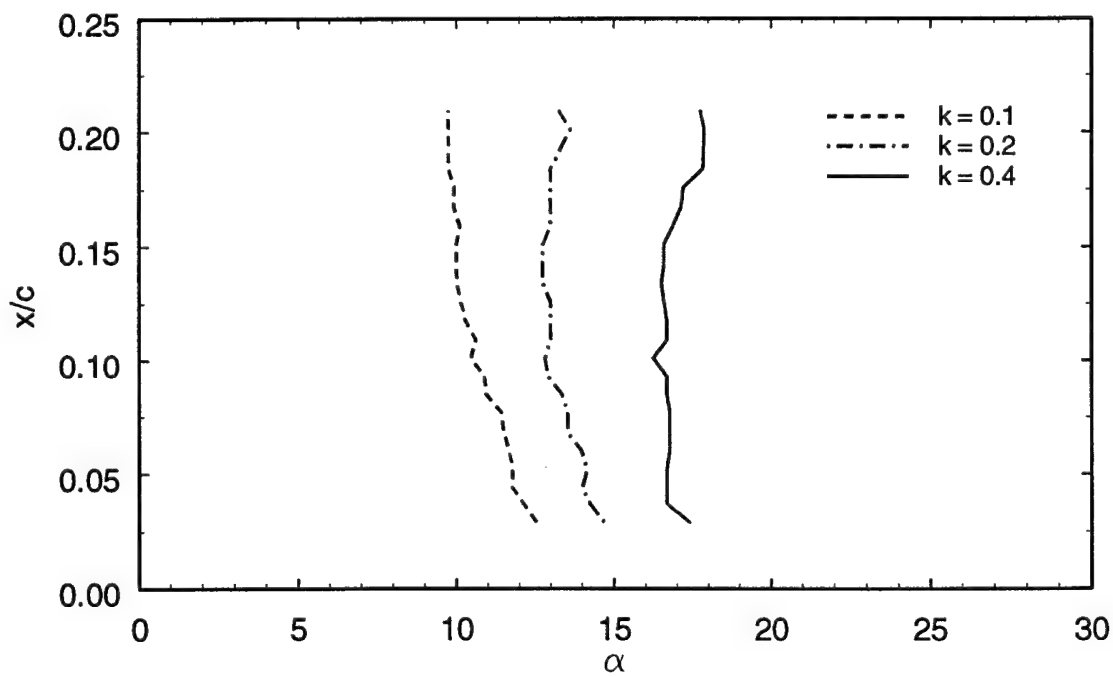


Figure 92 Effects of reduced frequency on Feature 2 for  $Re_c = 1.1 \times 10^5$   
 $\alpha_o = 10^\circ$ ,  $\alpha_m = 20^\circ$ .

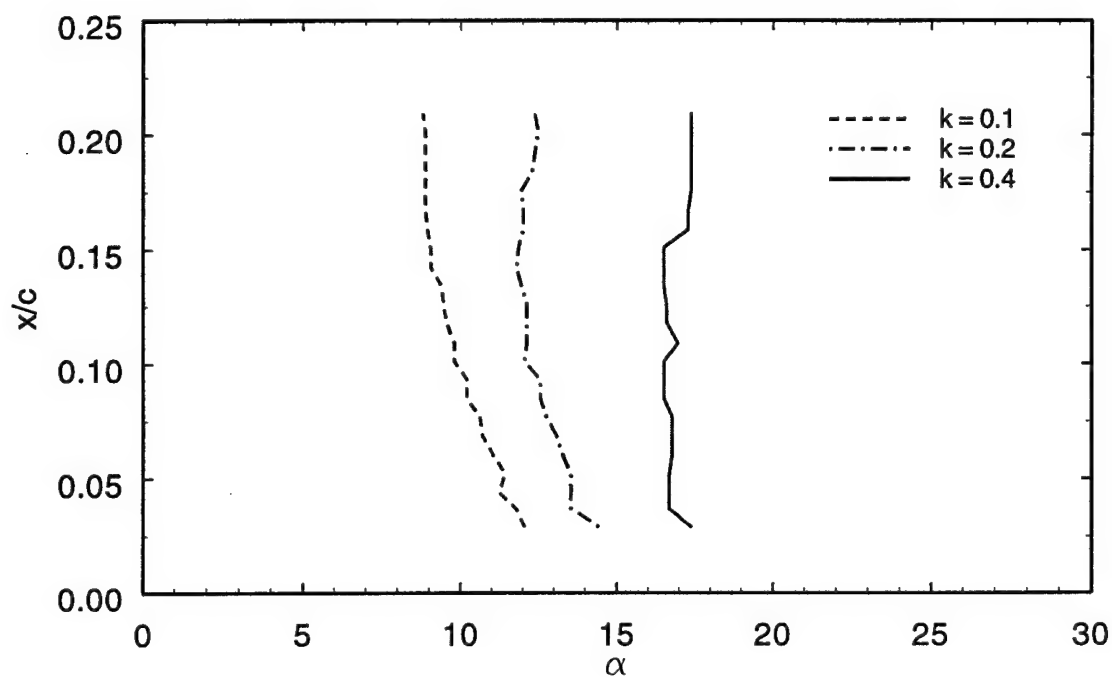


Figure 93 Effects of reduced frequency on Feature 2 for  $Re_c = 1.1 \times 10^5$   
 $\alpha_o = 20^\circ$ ,  $\alpha_m = 20^\circ$ .

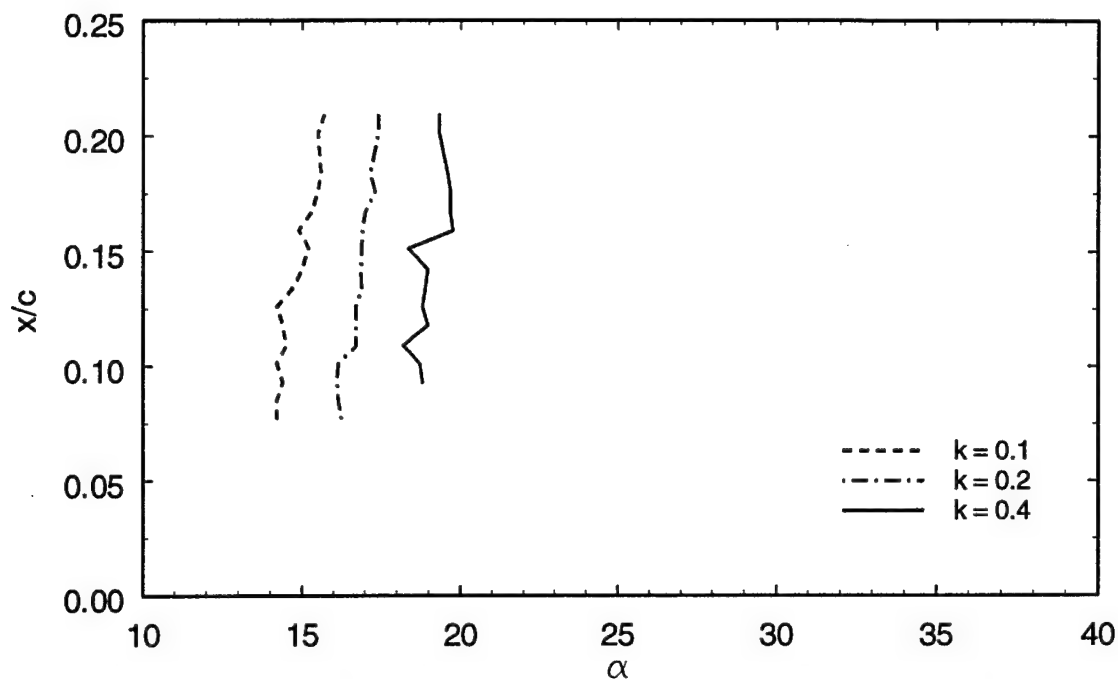


Figure 94 Effects of reduced frequency on Feature 4 for  $Re_c = 1.1 \times 10^5$   
 $\alpha_o = 10^\circ$ ,  $\alpha_m = 10^\circ$ .

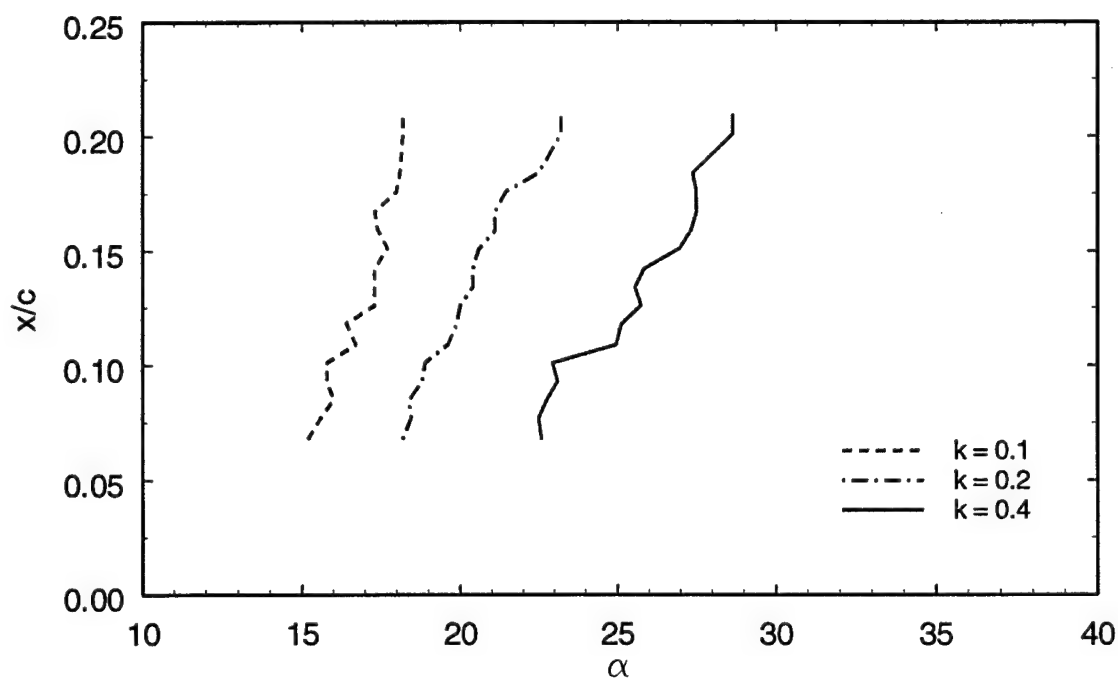


Figure 95 Effects of reduced frequency on Feature 4 for  $Re_c = 1.1 \times 10^5$   
 $\alpha_o = 10^\circ$ ,  $\alpha_m = 20^\circ$ .



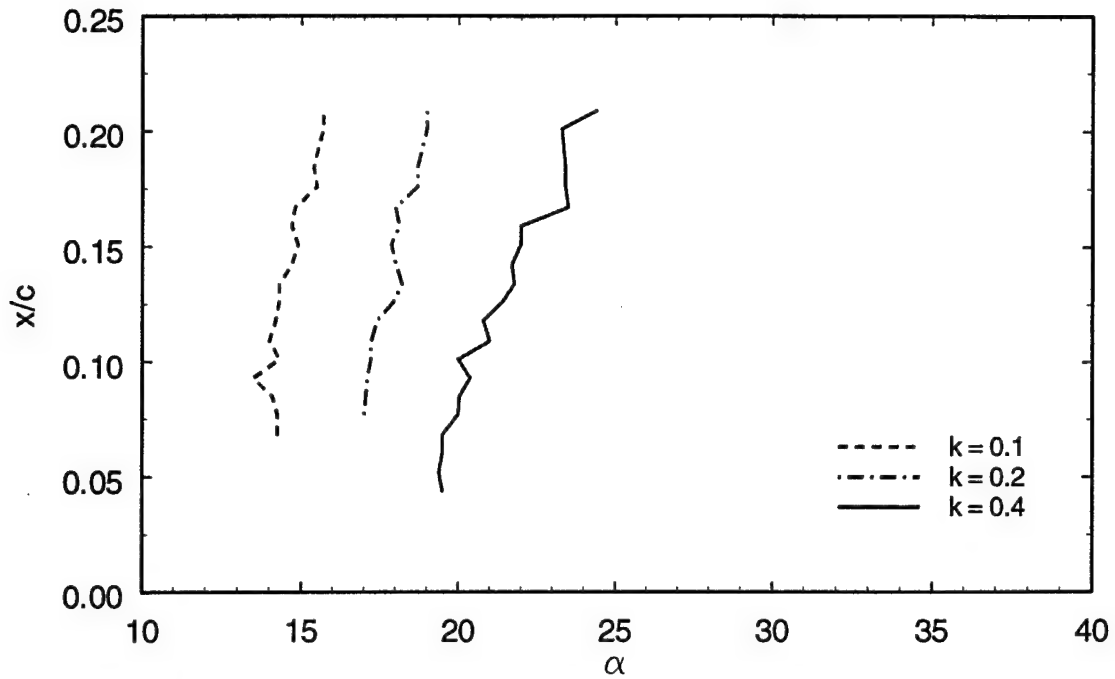


Figure 96 Effects of reduced frequency on Feature 4 for  $Re_c = 1.1 \times 10^5$   
 $\alpha_0 = 20^\circ$ ,  $\alpha_m = 10^\circ$ .

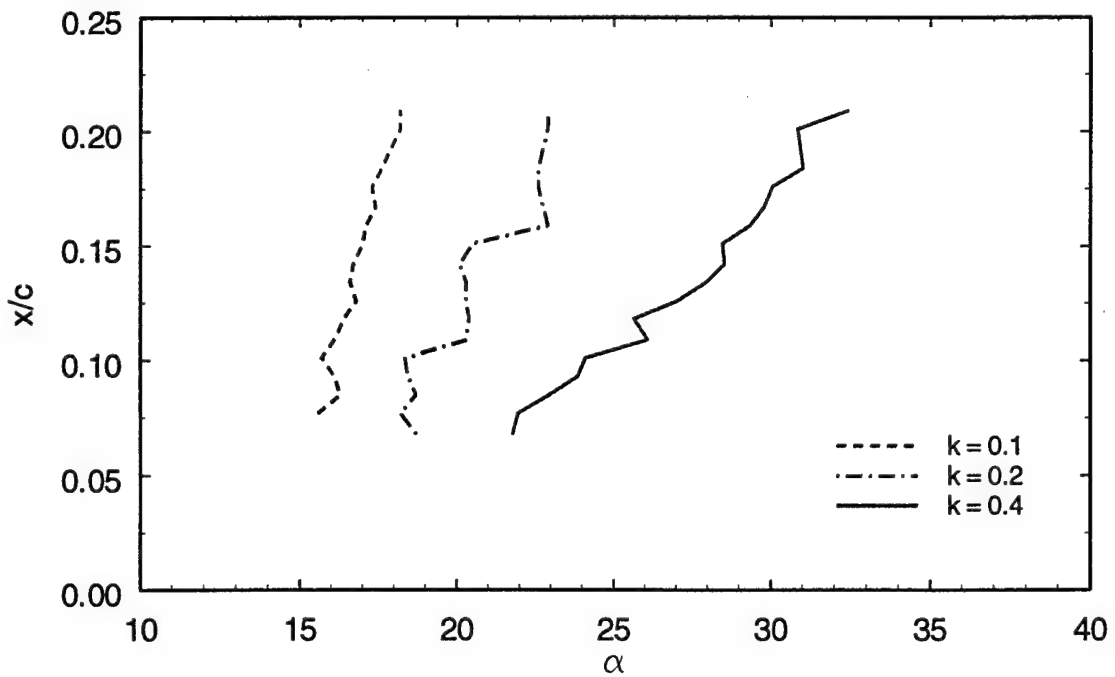


Figure 97 Effects of reduced frequency on Feature 4 for  $Re_c = 1.1 \times 10^5$   
 $\alpha_0 = 20^\circ$ ,  $\alpha_m = 20^\circ$ .

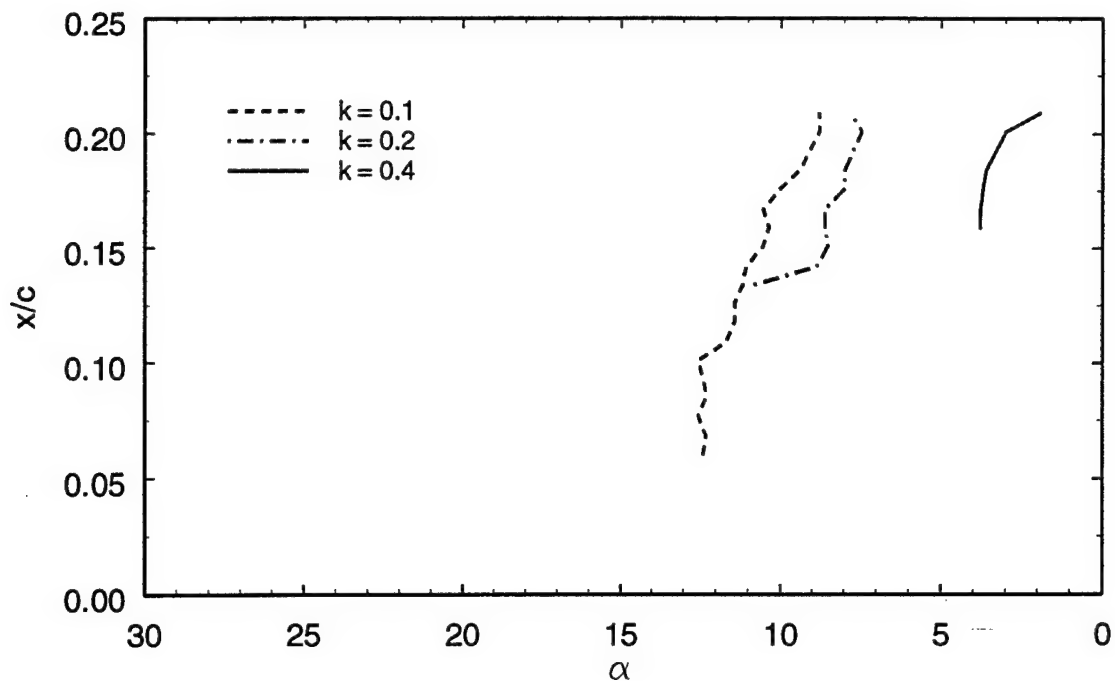


Figure 98 Effects of reduced frequency on Feature 5 for  $Re_c = 1.1 \times 10^5$   
 $\alpha_o = 10^\circ$ ,  $\alpha_m = 10^\circ$ .

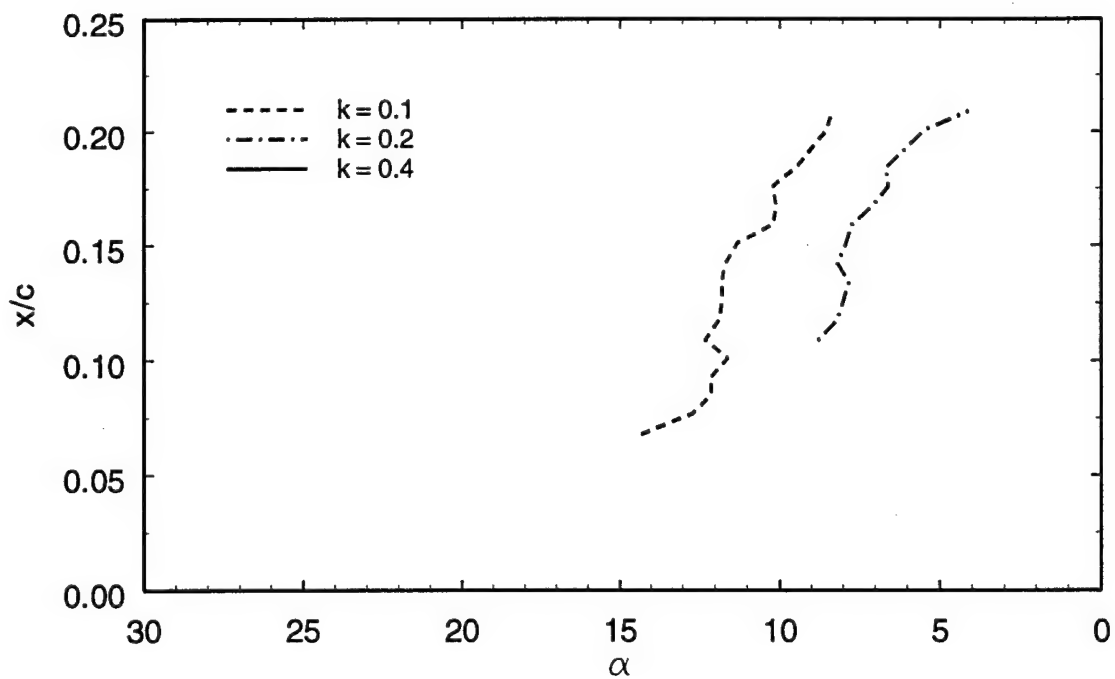


Figure 99 Effects of reduced frequency on Feature 5 for  $Re_c = 1.1 \times 10^5$   
 $\alpha_o = 10^\circ$ ,  $\alpha_m = 20^\circ$ .

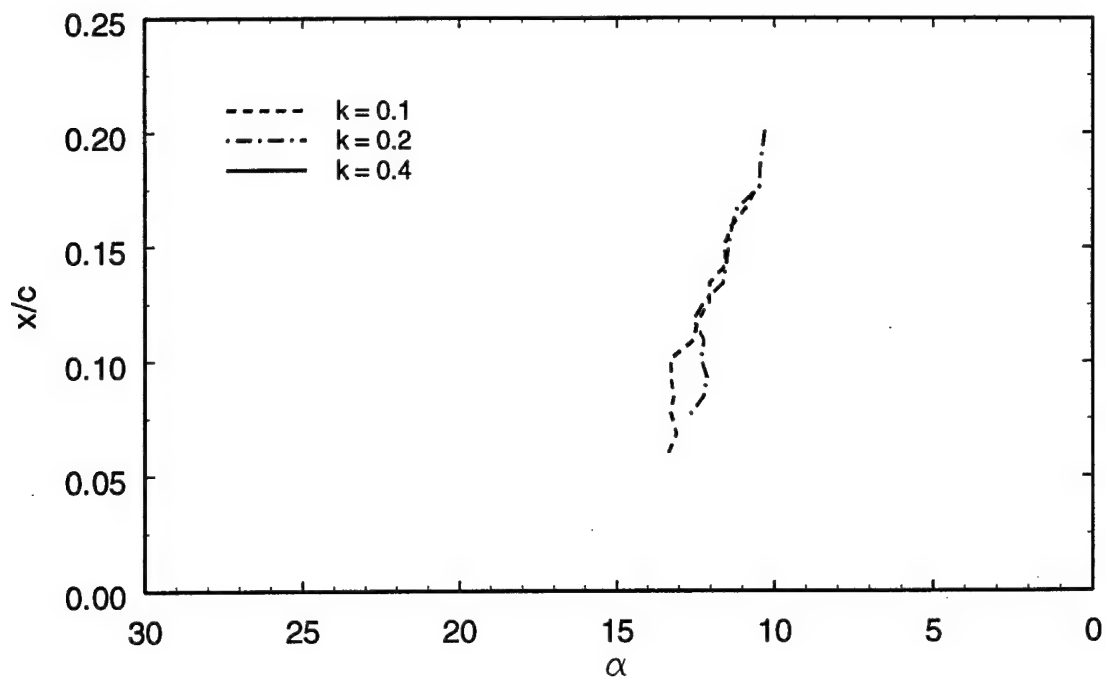


Figure 100 Effects of reduced frequency on Feature 5 for  $Re_c = 1.1 \times 10^5$   
 $\alpha_o = 20^\circ$ ,  $\alpha_m = 10^\circ$ .

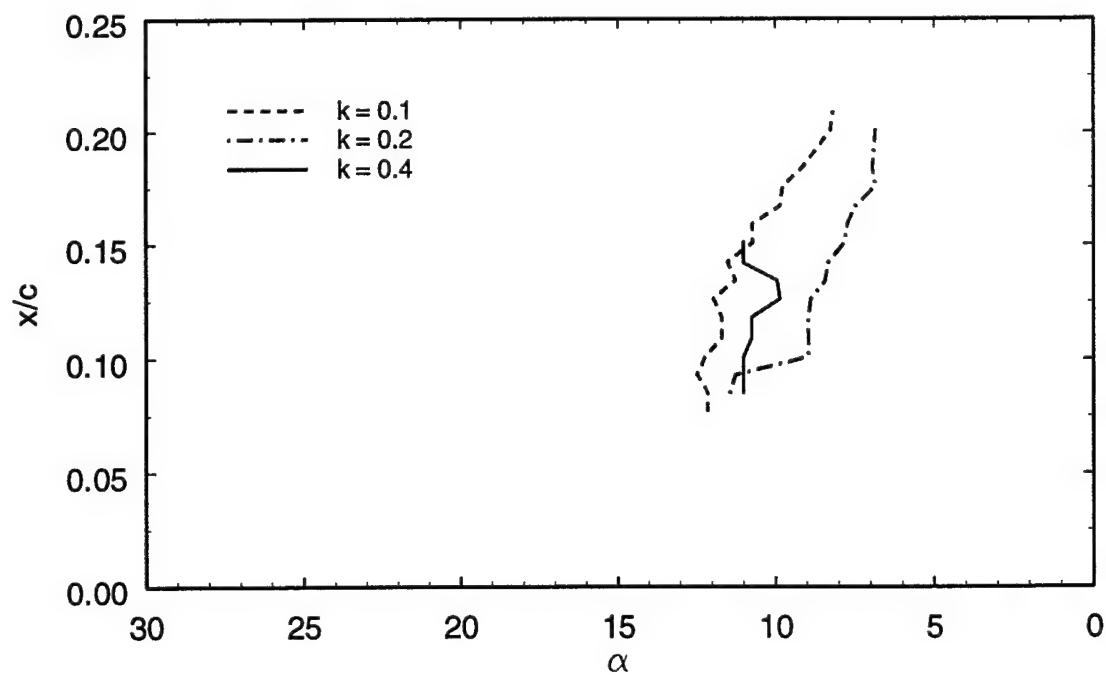


Figure 101 Effects of reduced frequency on Feature 5 for  $Re_c = 1.1 \times 10^5$   
 $\alpha_o = 20^\circ$ ,  $\alpha_m = 20^\circ$ .

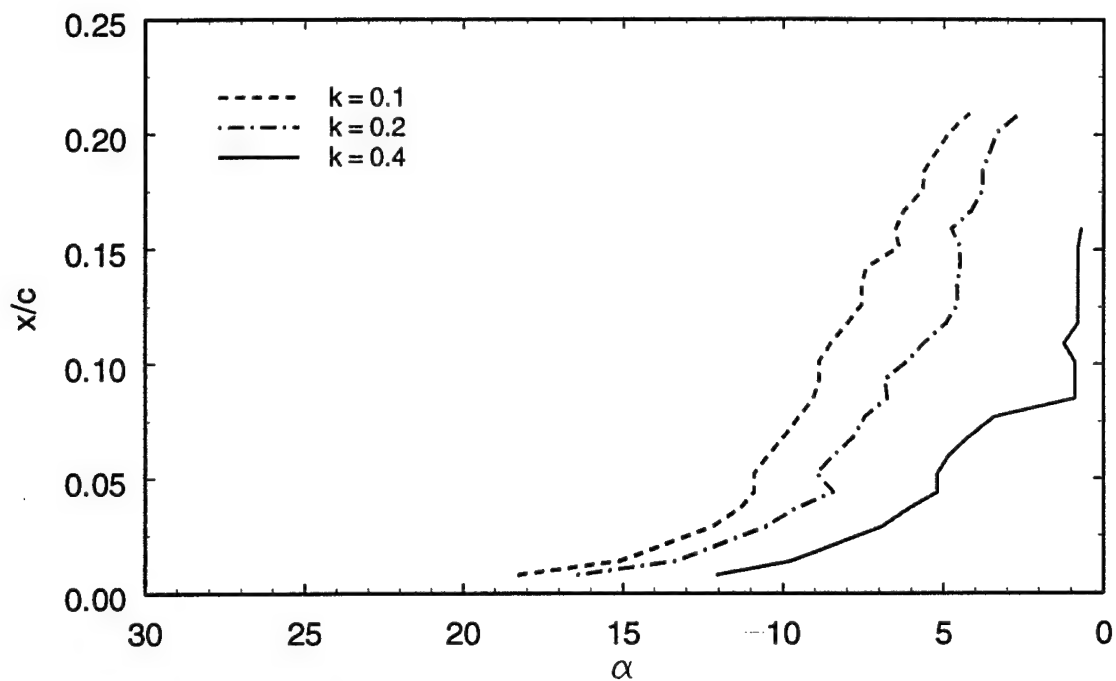


Figure 102 Effects of reduced frequency on Feature 6 for  $Re_c = 1.1 \times 10^5$   
 $\alpha_0 = 10^\circ$ ,  $\alpha_m = 10^\circ$ .

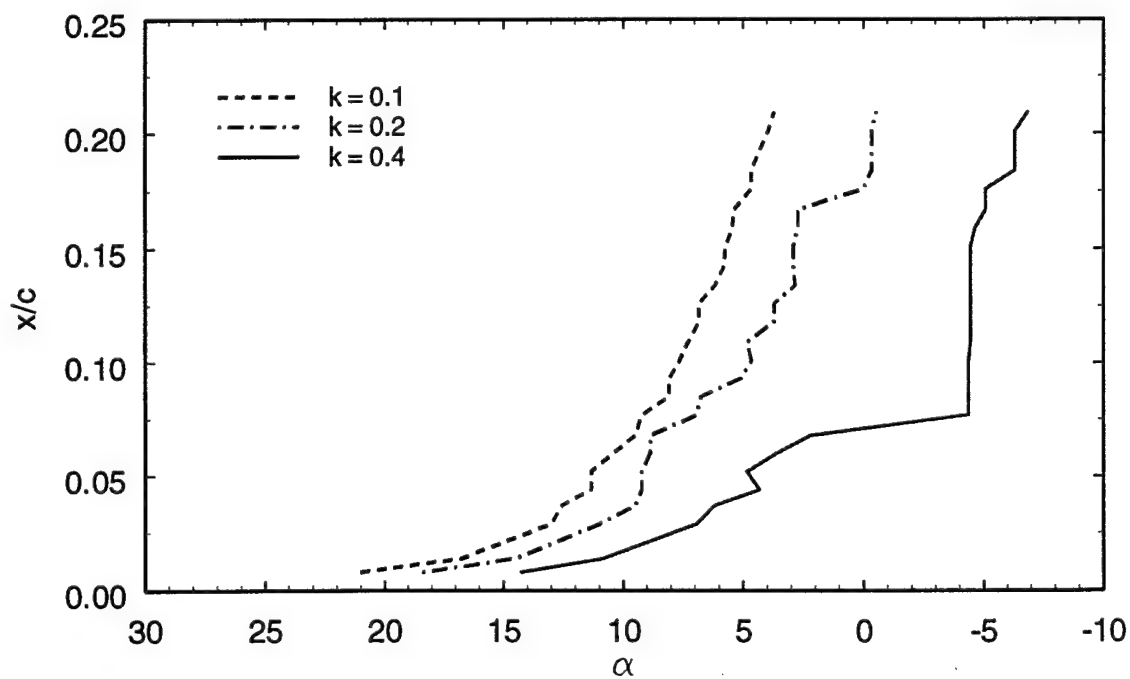


Figure 103 Effects of reduced frequency on Feature 6 for  $Re_c = 1.1 \times 10^5$   
 $\alpha_0 = 10^\circ$ ,  $\alpha_m = 20^\circ$ .

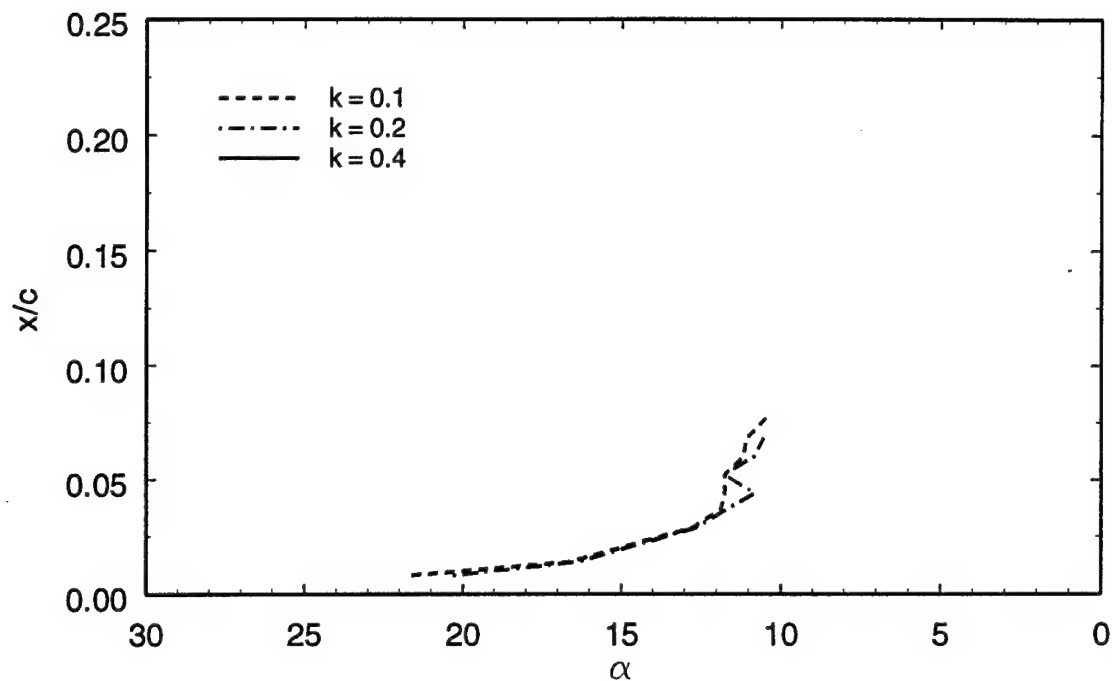


Figure 104 Effects of reduced frequency on Feature 6 for  $Re_c = 1.1 \times 10^5$   
 $\alpha_o = 20^\circ$ ,  $\alpha_m = 10^\circ$ .

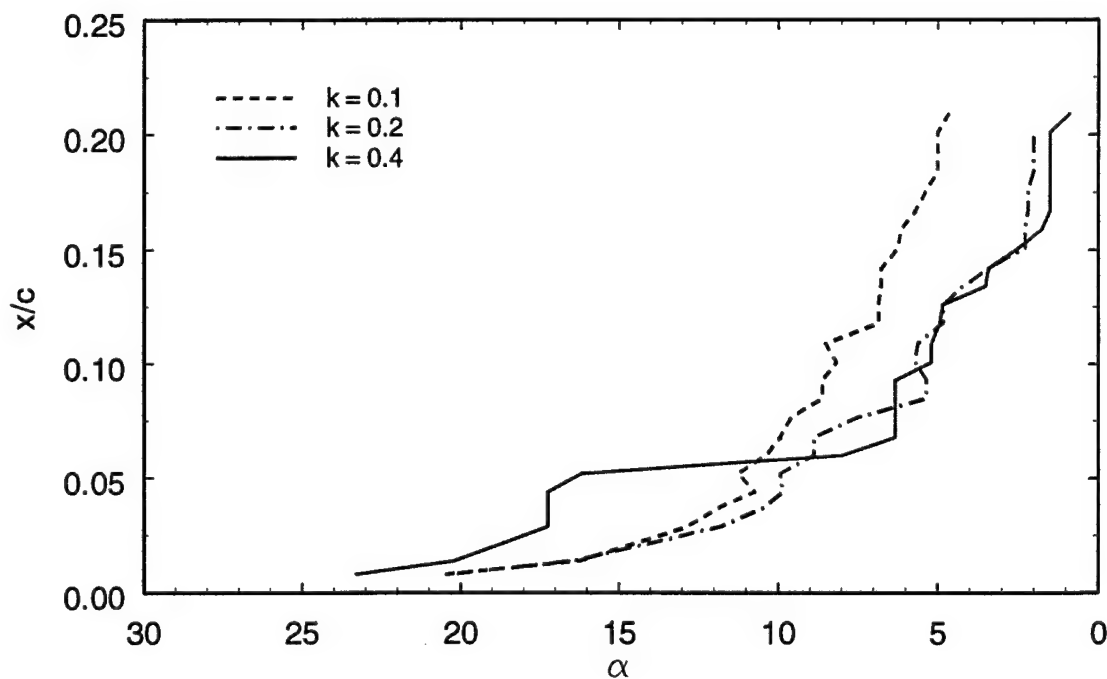


Figure 105 Effects of reduced frequency on Feature 6 for  $Re_c = 1.1 \times 10^5$   
 $\alpha_o = 20^\circ$ ,  $\alpha_m = 20^\circ$ .

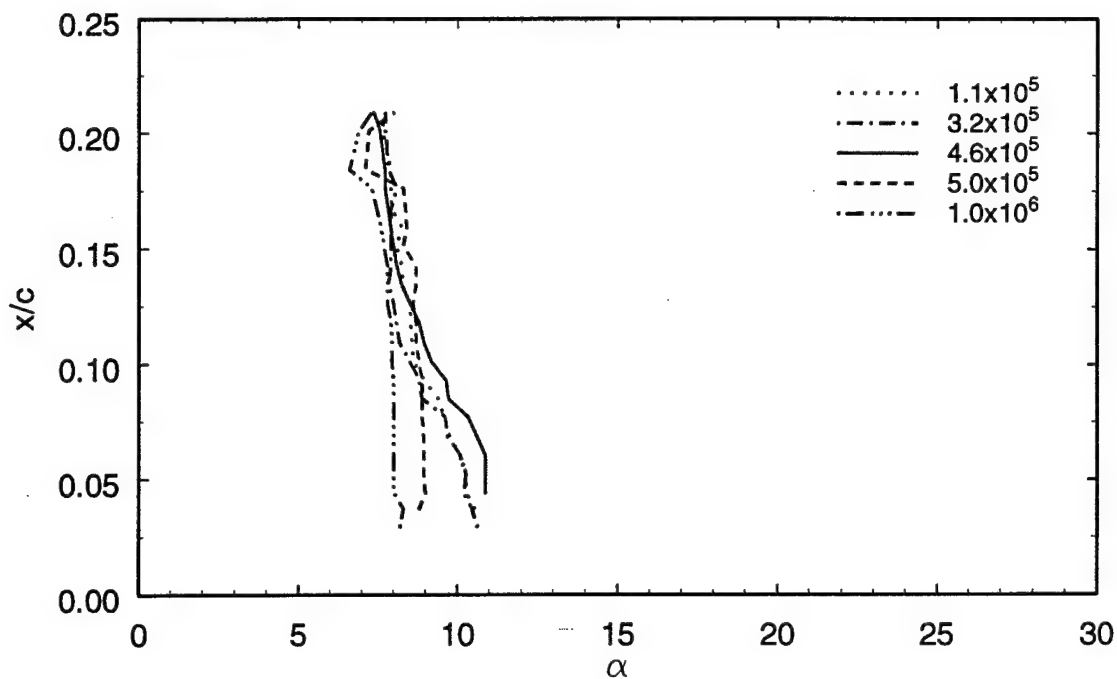


Figure 106 Effects of Reynolds number on Feature 2 for  $k = 0.1$   
 $\alpha_0 = 10^\circ$ ,  $\alpha_m = 10^\circ$ .

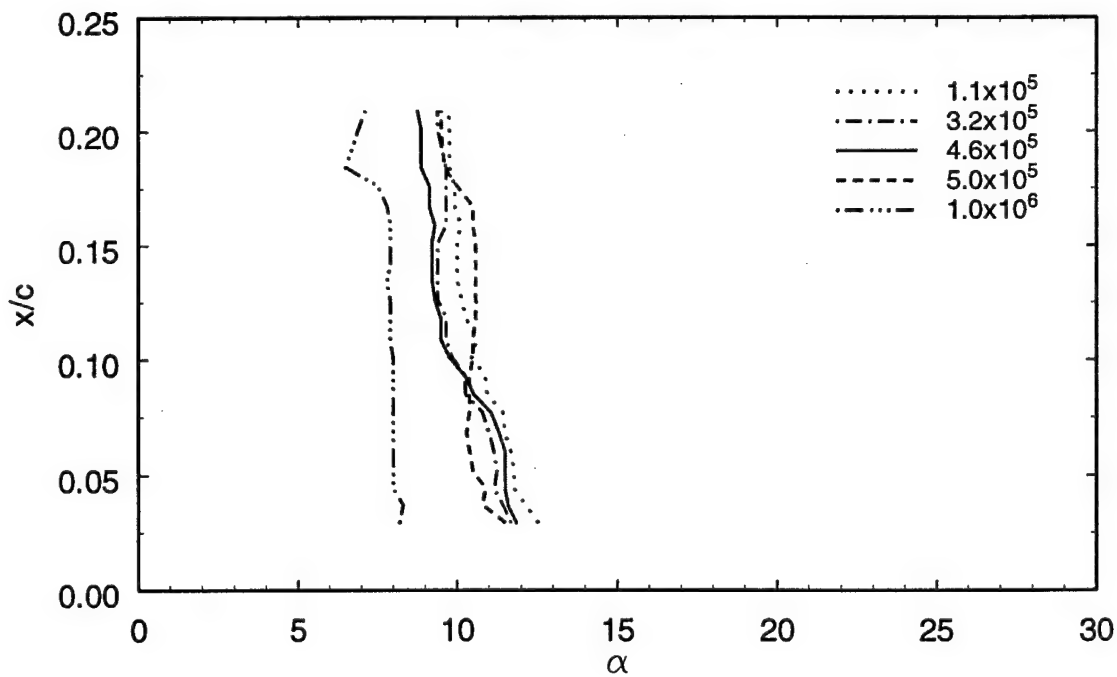


Figure 107 Effects of Reynolds number on Feature 2 for  $k = 0.1$   
 $\alpha_0 = 20^\circ$ ,  $\alpha_m = 10^\circ$ .

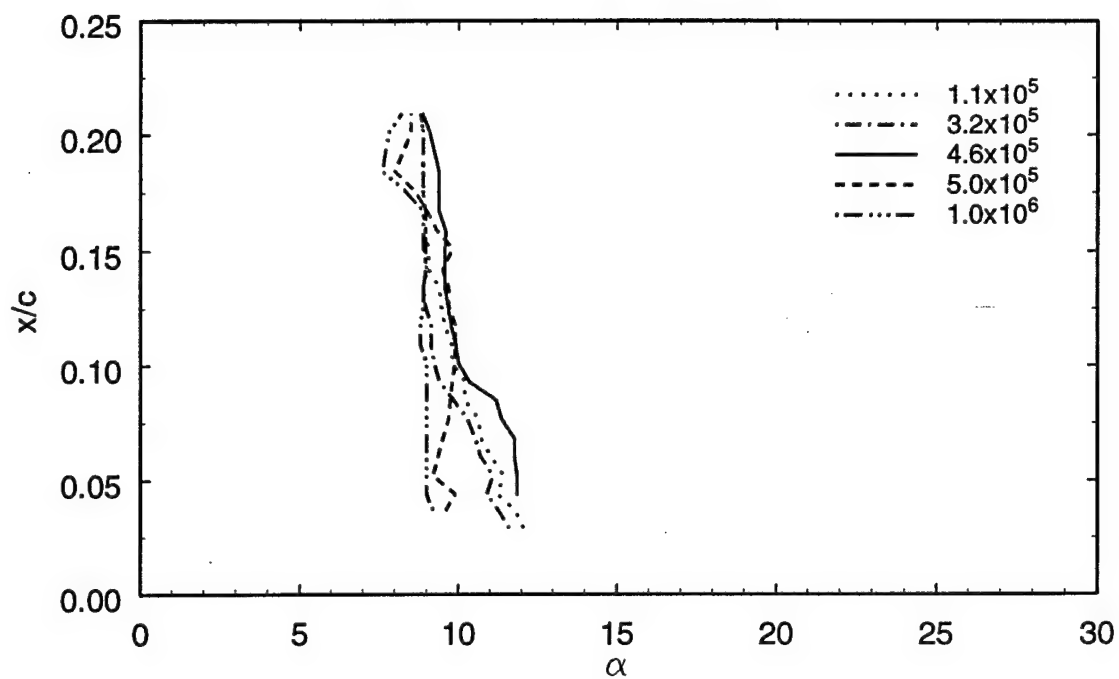


Figure 108 Effects of Reynolds number on Feature 2 for  $k = 0.1$   
 $\alpha_o = 20^\circ$ ,  $\alpha_m = 20^\circ$ .

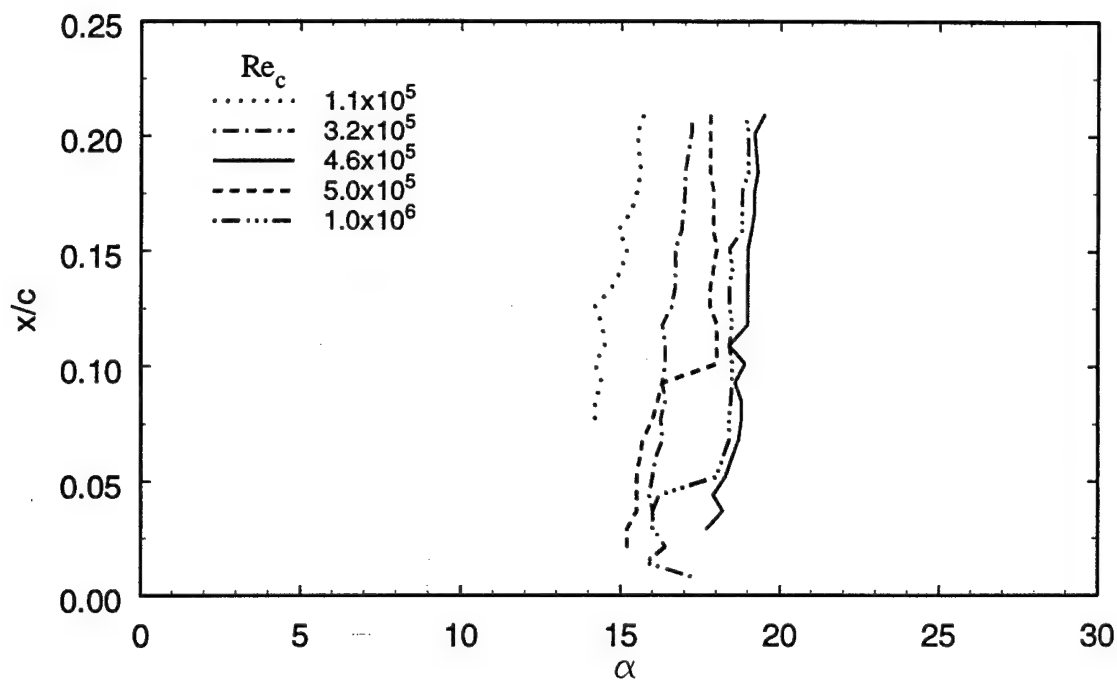


Figure 109 Effects of Reynolds number on Feature 4 for  $k = 0.1$   
 $\alpha_o = 10^\circ$ ,  $\alpha_m = 10^\circ$ .

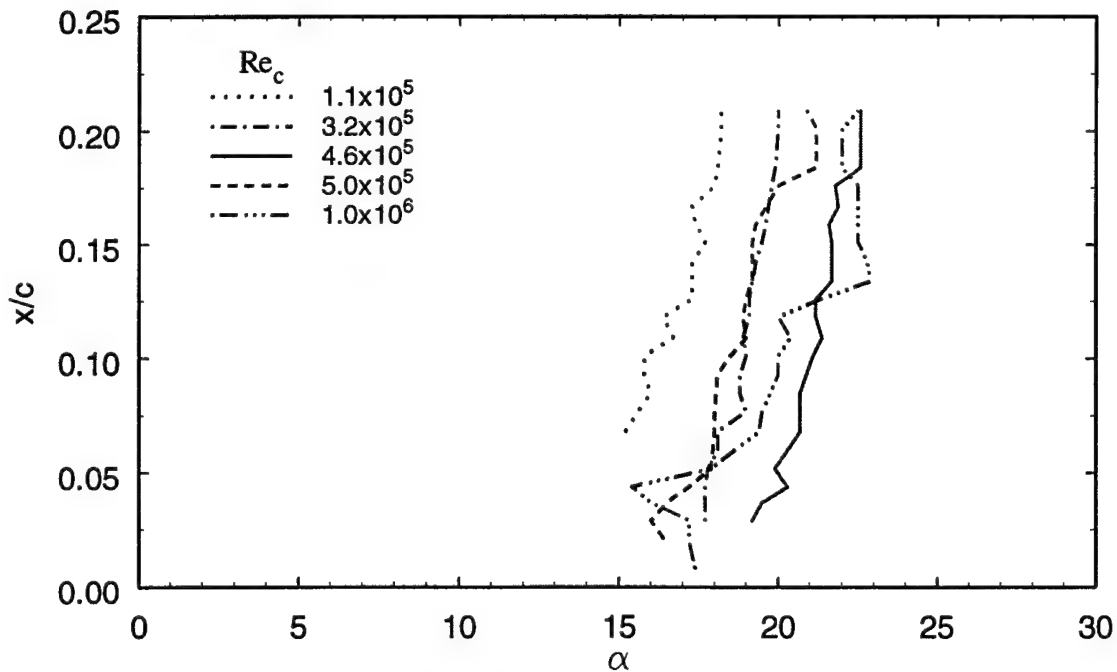


Figure 110 Effects of Reynolds number on Feature 4 for  $k = 0.1$   
 $\alpha_o = 10^\circ$ ,  $\alpha_m = 20^\circ$ .



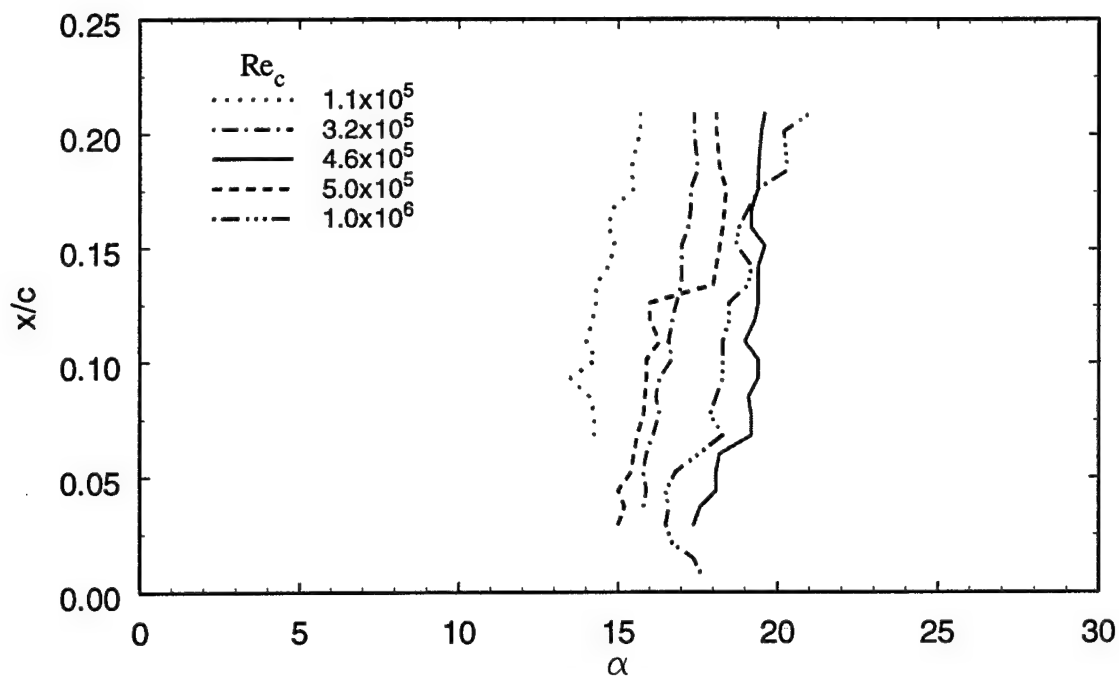


Figure 111 Effects of Reynolds number on Feature 4 for  $k = 0.1$   
 $\alpha_o = 20^\circ$ ,  $\alpha_m = 10^\circ$ .

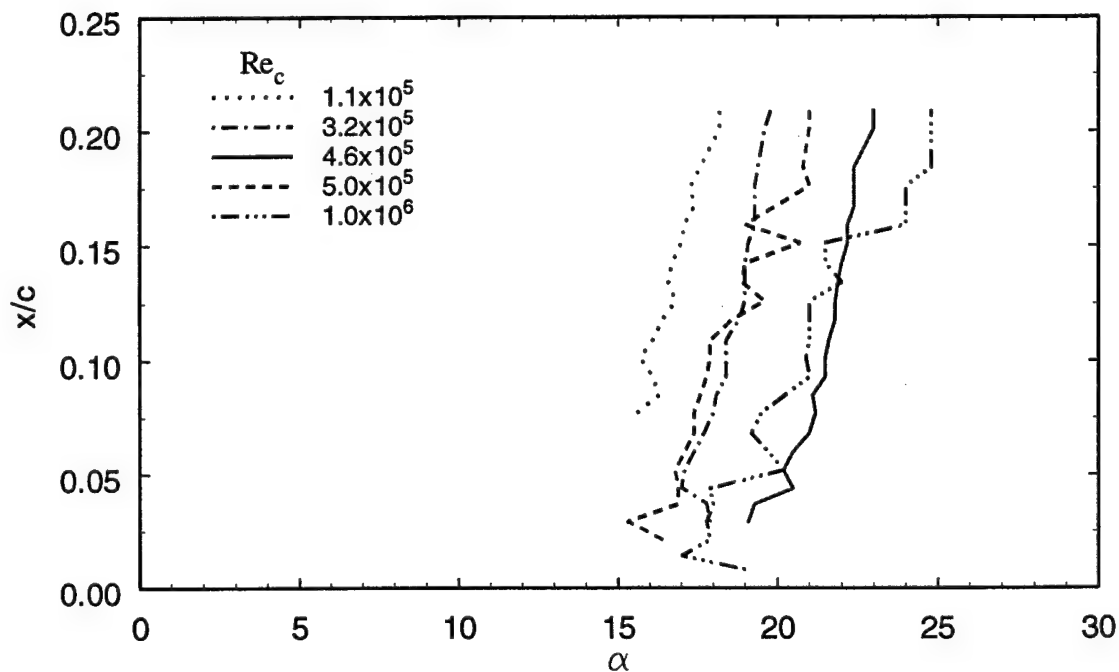


Figure 112 Effects of Reynolds number on Feature 4 for  $k = 0.1$   
 $\alpha_o = 20^\circ$ ,  $\alpha_m = 20^\circ$ .

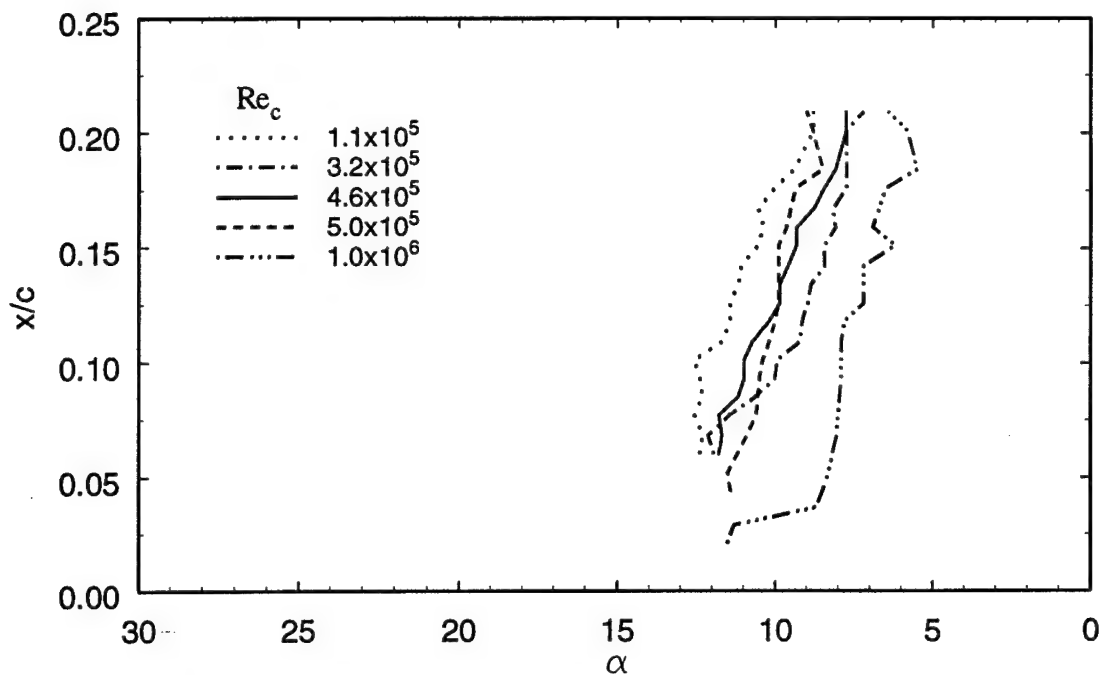


Figure 113 Effects of Reynolds number on Feature 5 for  $k = 0.1$   
 $\alpha_0 = 10^\circ$ ,  $\alpha_m = 10^\circ$ .

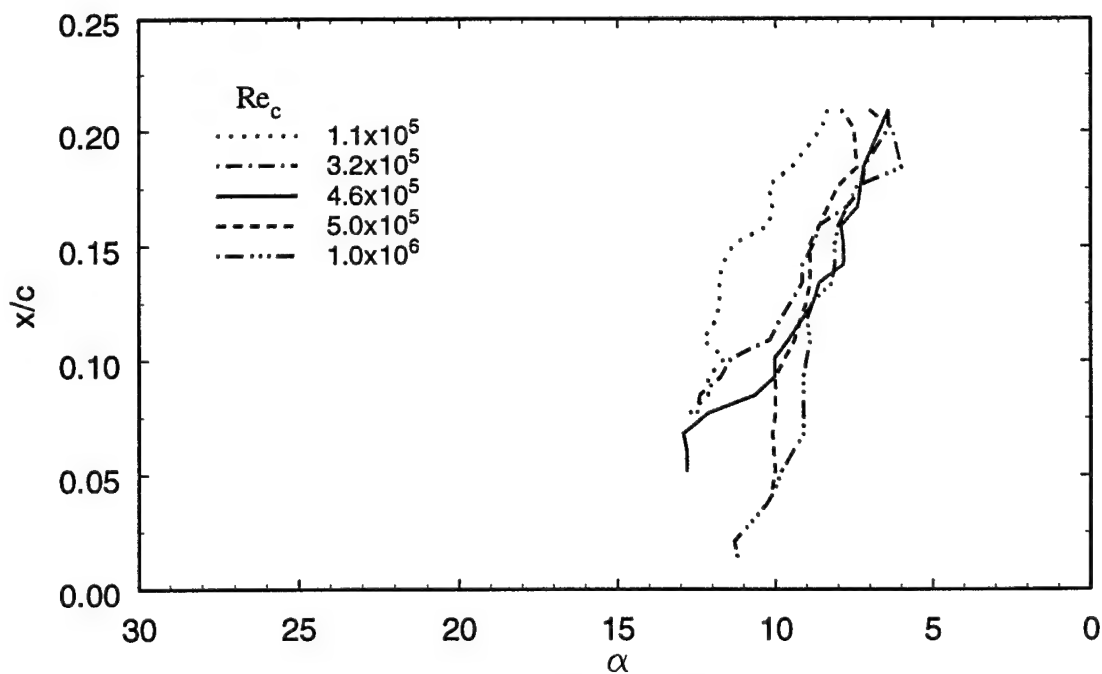


Figure 114 Effects of Reynolds number on Feature 5 for  $k = 0.1$   
 $\alpha_0 = 10^\circ$ ,  $\alpha_m = 20^\circ$ .

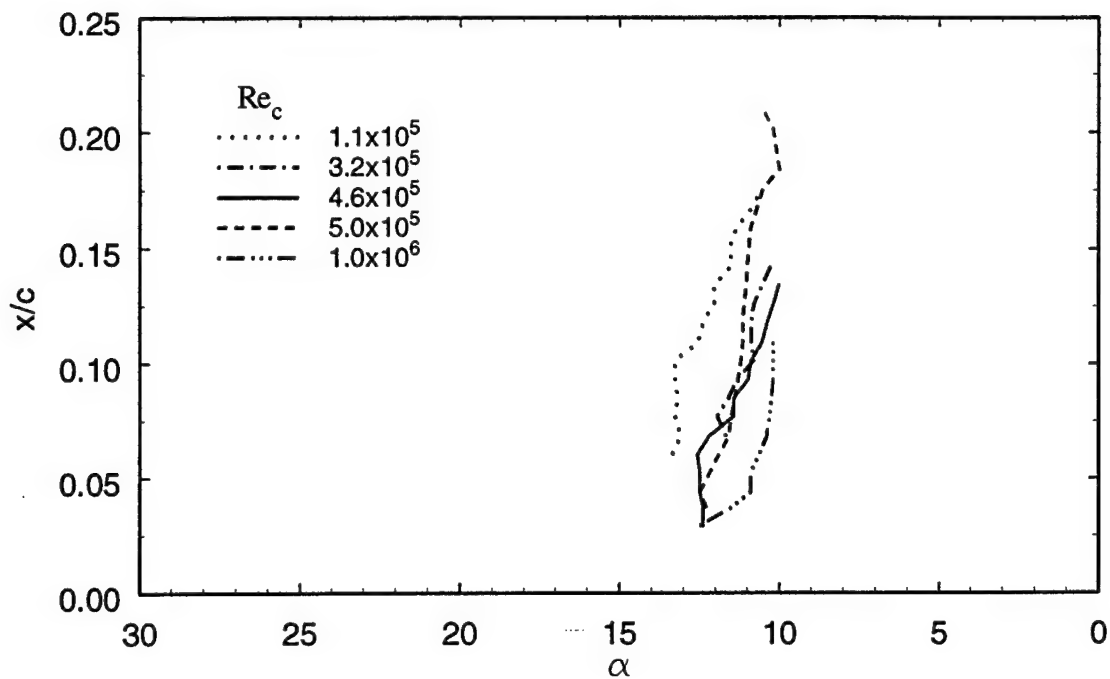


Figure 115 Effects of Reynolds number on Feature 5 for  $k = 0.1$   
 $\alpha_o = 20^\circ$ ,  $\alpha_m = 10^\circ$ .

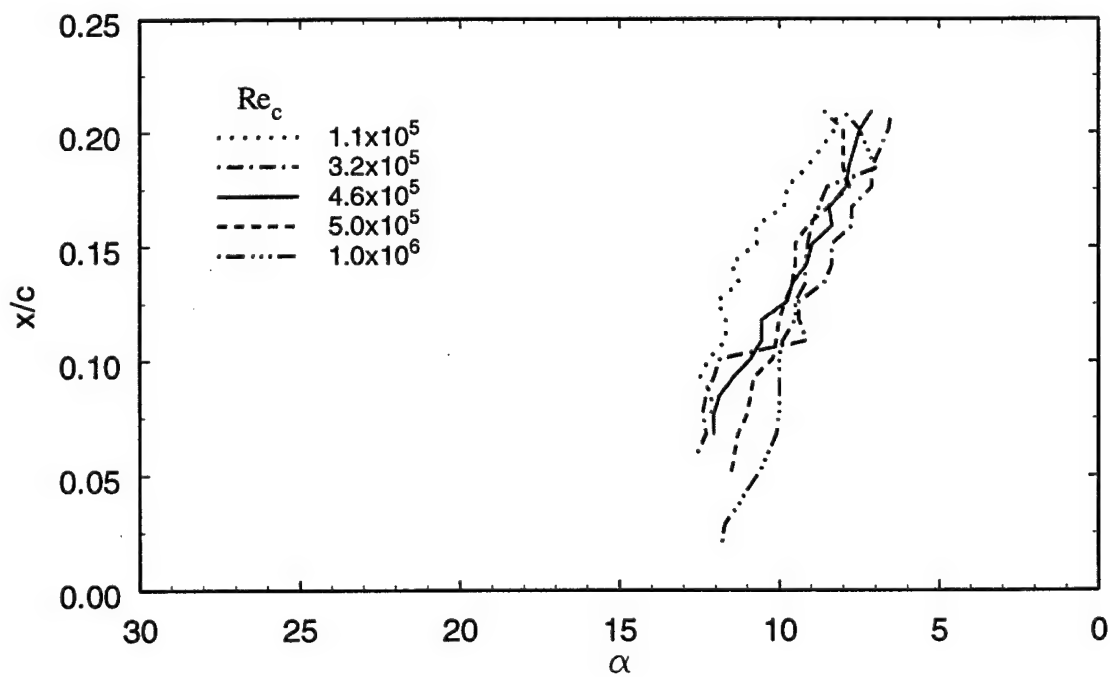


Figure 116 Effects of Reynolds number on Feature 5 for  $k = 0.1$   
 $\alpha_o = 20^\circ$ ,  $\alpha_m = 20^\circ$ .

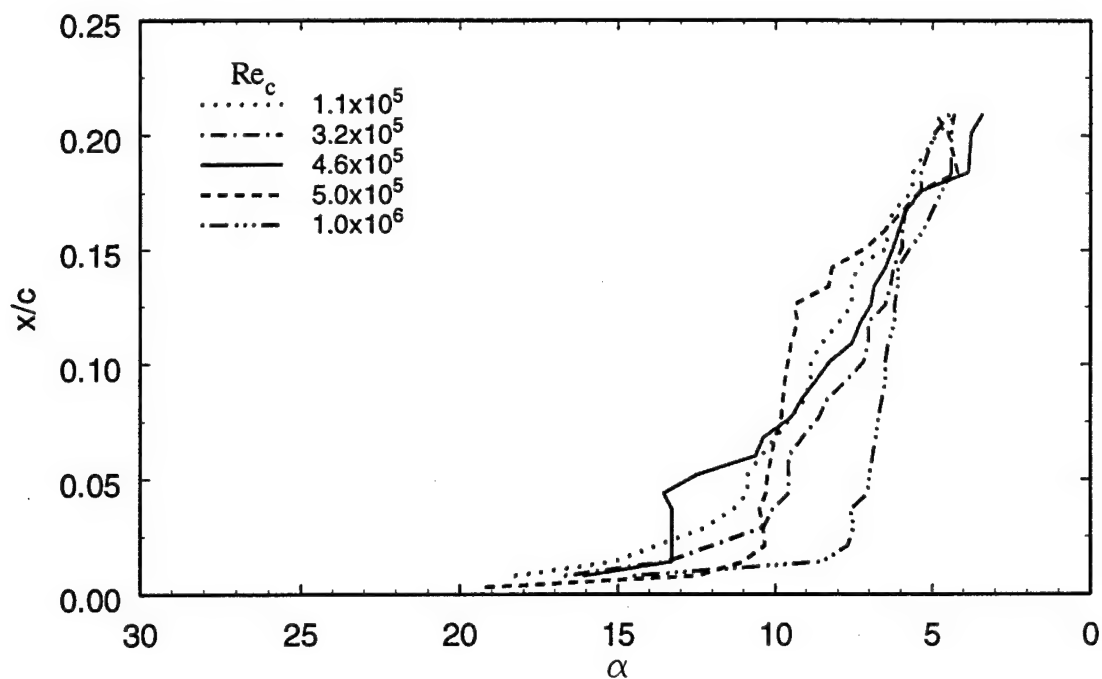


Figure 117 Effects of Reynolds number on Feature 6 for  $k = 0.1$   
 $\alpha_o = 10^\circ$ ,  $\alpha_m = 10^\circ$ .

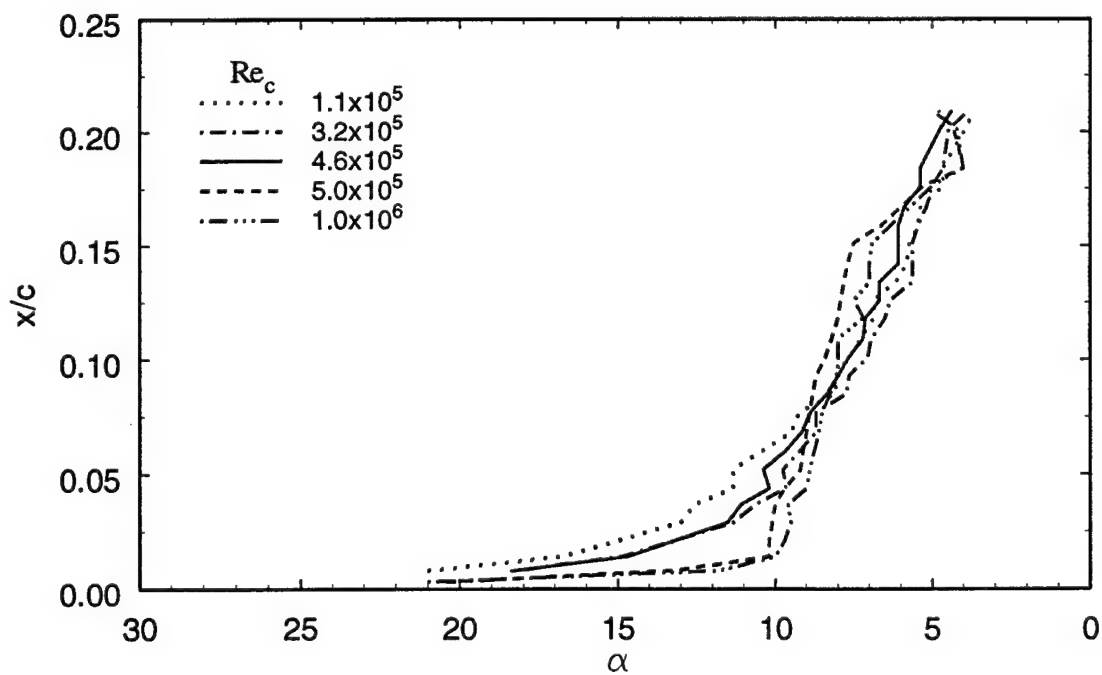


Figure 118 Effects of Reynolds number on Feature 6 for  $k = 0.1$   
 $\alpha_o = 10^\circ$ ,  $\alpha_m = 20^\circ$ .

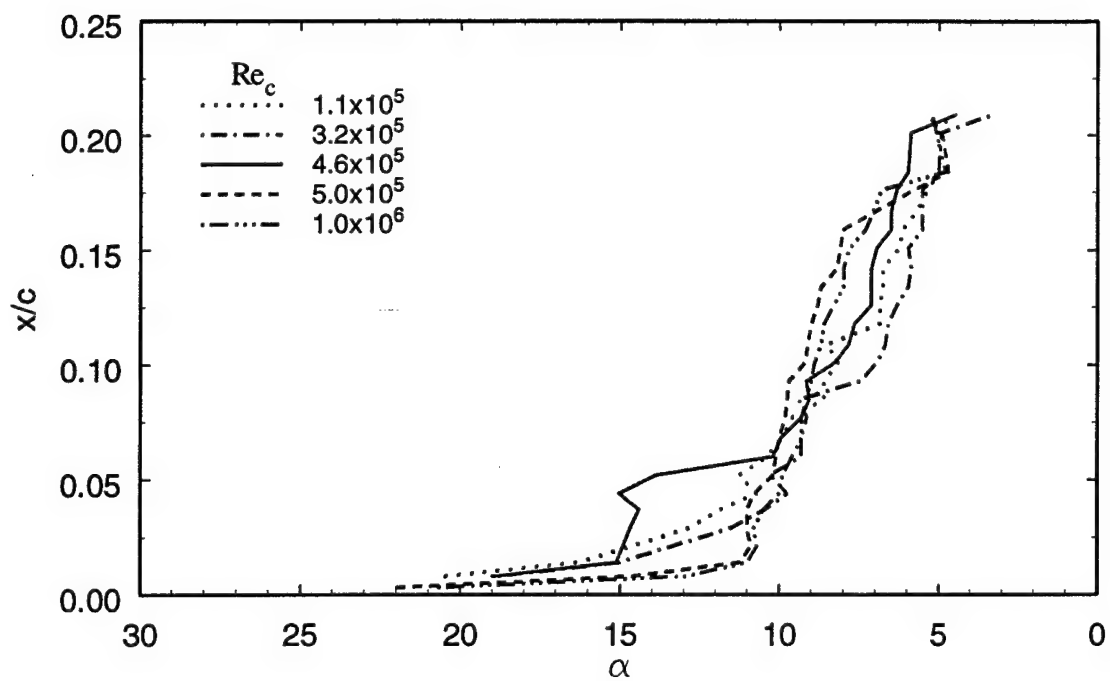


Figure 119 Effects of Reynolds number on Feature 6 for  $k = 0.1$   
 $\alpha_o = 20^\circ$ ,  $\alpha_m = 20^\circ$ .

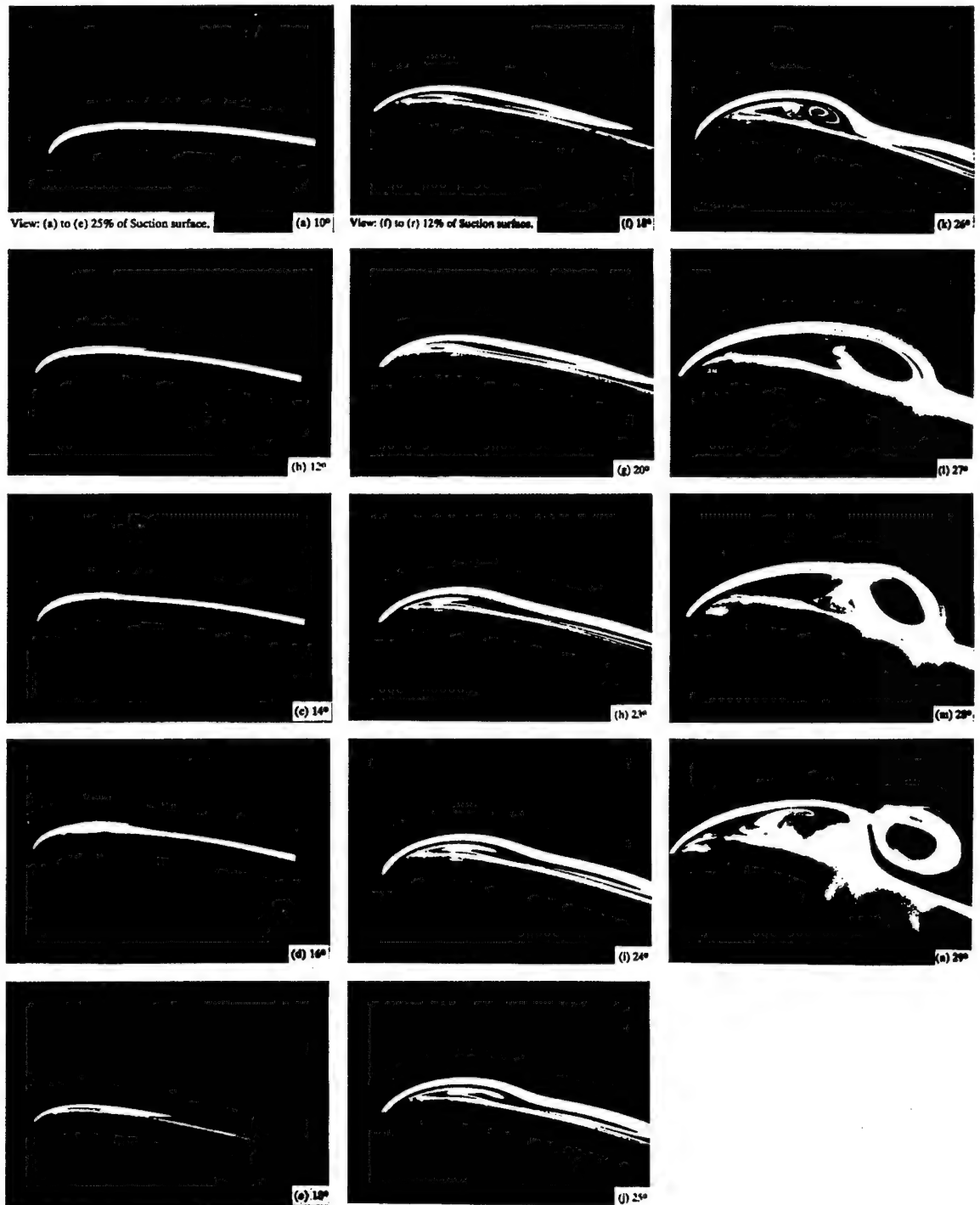


Figure 120 Flow visualization showing development of the DSV over a pitching airfoil in laminar flow ( $\alpha^+ = 0.31$ ,  $Re_c = 30,000$ , spanwise smoke wire positioned at nose) (Karim<sup>12</sup>, 1992).

## BIBLIOGRAPHY

1. McCroskey, W. J., "Unsteady Airfoils," Annual Review of Fluid Mechanics, Vol. 14, 1982, pp. 285-331.
2. Gad-el-Hak, M., "Unsteady Separation on Lifting Surfaces," Applied Mechanics Review, Vol. 40, No. 4, 1987, pp. 441-452.
3. Ericsson, L. E. and Reding, J. P., "Fluid Dynamics of Unsteady Separated Flow. Part H. Lifting Surfaces," Progress in Aerospace Sciences, Vol. 24, 1987, pp. 249-356.
4. Doligalski, T. L., Smith, C. R., and Walker, J. D. A., "Vortex Interaction with Walls," Annual Review of Fluid Mechanics, Vol. 26, 1994, pp. 573-616.
5. Karim, M. A. and Acharya, M., "Suppression of Dynamic-Stall Vortices over Pitching Airfoils by Leading-Edge Suction," AIAA Journal Vol. 32, No. 8, 1994, pp. 1647-1655.
6. Alrefai, M. and Acharya, M., "Controlled Leading-Edge Suction for the Management of Unsteady Separation over Pitching Airfoils," AIAA Journal, Vol. 34, No. 11, pp. 2327-2336 (see also AIAA Paper 95-2188, San Diego, CA, June 1995).
7. Metwally, H. M., Investigation and Control of the Unsteady Flow Over a Pitching Airfoil, Ph. D. Thesis, MAE Dept., Illinois Institute of Technology, December, 1990.
8. Kramer, M., "Increase in the Maximum Lift of an Airfoil due to a Sudden Increase in its Effective Angle of Attack Resulting from a Gust," NASA TM 678, 1932.
9. Johnson, W. and Ham, N. D., "On the Mechanism of Dynamic Stall," Journal of the ASME, Vol. 17, Oct. 1972, pp. 36-45.
10. McCroskey, W. J., Carr, L. W., and McAlister, K. W., "Dynamic Stall Experiments on Oscillating Airfoils," AIAA Journal, Vol. 14, No. 1, 1976, pp. 57-63.
11. McCroskey, W. J., and Carr, L.W., "Water Tunnel Visualizations of Dynamic Stall," Journal of Fluids Engineering, Vol. 101, Sept. 1978, pp. 376-380.
12. Karim, M. A., Experimental Investigation of the Formation and Control of the Dynamic-Stall Vortex over a Pitching Airfoil, M. S. Thesis, MAE Dept., Illinois Institute of Technology, December 1992.

13. Huang, L. S., Bryant, T. D., and Maestrello, L., "Separation Control over Airfoils at High Angles of Attack by Sound Emanating from the Surface," AIAA Paper 87-1261, Honolulu, HA, 1987.
14. Hsiao, F. B., Liu, C. F., and Shyu, J. Y., "Control of Wall-Separated Flow by Internal Acoustic Excitation," AIAA Journal, Vol. 28, No. 8, 1990, pp. 1440-1446, (see also AIAA Paper 89-0974, Tempe, AZ, 1989).
15. Koga, D. J., Control of Separated Flowfields using Forced Unsteadiness, Ph. D. Thesis, MAE Dept., Illinois Institute of Technology, 1983.
16. Montividas, R. E., Acharya, M., and Metwally, H. M., "The Reactive Control of an Unsteady Separating Flow," AIAA Paper 91-0041, Reno, NV, 1991.
17. Moore, F. K., "On The Separation of the Unsteady Laminar Boundary Layer," Boundary Layer Research, ed. H. G. Gortler, Springer-Verlag, Berlin, 1958, pp. 296-310.
18. Rott, N., "Unsteady Flow in the Vicinity of a Stagnation Point," Quarterly Rev. of Applied Math, Vol. 23, 1956, pp. 444-451.
19. Sears, W. R., "Some Recent Developments in Airfoil Theory," Journal of the Aeronautical Sciences, Vol. 23, 1956, pp. 490-499.
20. Reynolds, W. C. and Carr, L. W., "Review of Unsteady, Driven, Separated Flows," AIAA Paper 85-0527, Boulder, Co, 1985.
21. Schreck, S. J., Faller, W., and Helin, H. E., "Pitch Rate and Reynolds Number Effects on Unsteady Boundary Layer Transition and Separation," AIAA Paper 94-2256, June 1994.
22. Chandrasekhara, M. S., Carr, L. W., and Ahmed, S., "Comparison of Pitch Rate History Effects on Dynamic Stall," NASA/AFOSR/ARO Workshop on Physics of Forced Unsteady Separation, 1990.
23. Chandrasekhara, M. S. and Brydges, B. E., "Amplitude Effects on Dynamic Stall of an Oscillating Airfoil," AIAA Paper 91-0575, 1990.
24. Chandrasekhara, M. S., Wilder, M. C., and Carr, L. W., "Reynolds Number Influence on 2-D Compressible Dynamic Stall," AIAA Paper 96-0073, 1996.
25. Ahmed, S. and Chandrasekhara, M. S., "Reattachment Studies of an Oscillating Airfoil Dynamic Stall Flow Field," AIAA Paper 91-3225, 1991.
26. Ekaterinaris, J. A., "Compressible Studies of Dynamic Stall," AIAA Paper 89-0024, 1989.



27. Visbal, M. R., "On Some Physical Aspects of Airfoils Dynamic Stall," ASME Symposium on Steady Fluid Dynamics, Canada, 1990.
28. Ghia, K. N., Yang, J., Osswald, G. A., and Ghia, U., "Study of the Role of Unsteady Separation in the Formation of Dynamic Stall Vortex," AIAA Paper 92-0196, January 1992.
29. Okong'o, N. and Knight, D. D., "Implicit Unstructured Navier-Stokes Simulation of Leading Edge Separation over a Pitching Airfoil," AIAA Paper 97-0657, January 1997.
30. Nelson, C. F., Koga, D. J., and Eaton, J. K., "Control of the Unsteady, Separated Flow Behind an Oscillating, Two-Dimensional Flap," AIAA Paper 89-1027, Tempe, AZ, 1989.
31. Freymuth, P., "Toward Dynamic Separation Without Dynamic Stall," Experiments in Fluids, Vol. 7, 1989, pp. 187-196.
32. Reisenthel, P. H., Reattachment Control Behind A Rearward Facing Step Using Forced Unsteadiness, M. S. Thesis, MAE Dept., Illinois Institute of Technology, 1984.
33. Ramiz, M. A., The Development of a Simple, Non-Intrusive Technique for Flow-State Detection in a Model, Leading-Edge Unsteady Separation, M. S. Thesis, MAE Dept., Illinois Institute of Technology, 1989.
34. Visbal, M. R., "On the Formation and Control of the Dynamic Stall Vortex on a Pitching Airfoil," AIAA Paper 91-0006, January 1991.
35. Alrefai, M., Unsteady Pressure Field and Flow State over a Pitching Airfoil with Leading-Edge Suction, M. S. Thesis, MAE Dept., Illinois Institute of Technology, 1995.
36. Kawthar-Ali, M. H. and Acharya, M., "Artificial Neural Networks for Suppression of the Dynamic Stall Vortex over Pitching Airfoils," AIAA Paper 96-0540, 1996.
37. Karim, M. A., Experimental Investigation of the Three-Dimensional Unsteady Flow Over a Pitching Backward Swept Wing, Ph. D. Thesis, MAE Dept., Illinois Institute of Technology, 1997.
38. Walker, J. M., Seller, F. J., and Chou, D. C., "Forced Unsteady Vortex Flows Driven by Pitching Airfoils," AIAA Paper 87-1331, June 1987.

39. Acharya, M. and Metwally, M. H., "Unsteady Pressure Field and Vorticity Production over a Pitching Airfoil," AIAA Journal, Vol. 30, No. 2, 1992, pp. 403-411.
40. Chandrasekhara, M. S., Ahmed, S., and Carr, L. W., "Schlieren Studies of Compressibility Effects on Dynamic Stall of Transiently Pitching Airfoils," Journal of Aircraft, Vol. 30, No. 2, 1993, pp. 213-220.
41. Koochesfahani, M. M. and Smiljanovski, V., "Initial Acceleration Effects on Flow Evolution around Airfoils Pitching to High Angles of Attack," AIAA Journal, Vol. 31, No. 8, 1993, pp. 1529-1531.
42. Schreck, S. J. and Helin, H. E., "Unsteady Vortex Dynamics and Surface Pressure Topologies on a Pitching Wing," AIAA Paper 93-0435, January 1993.
43. Crisler, W., Krothapalli, A., and Lourenco, L., "PIV Investigation of High Speed Flow over a Pitching Airfoil," AIAA Paper 94-0533, January 1994.
44. Shih, C., Lourenco, L. M., and Krothapalli, A., "Investigation of Flow at Leading and Trailing Edges of Pitching-Up Airfoil," AIAA Journal, Vol. 33, No. 8, 1995, pp. 1369-1376.
45. Visbal, M. R., "Effect of Compressibility on Dynamic Stall of a Pitching Airfoil," AIAA Paper 88-0132, January 1988.
46. Gendrich, C. P., Koochesfahani, M. M., and Visbal, M. R., "Initial Acceleration Effects on the Flow Field Development around Rapidly Pitching Airfoils," AIAA Paper 93-0438, January 1993.
47. Ghosh Choudhuri, P. and Knight, D. D., "Effects of Compressibility, Pitch Rate, and Reynolds Number on Unsteady Incipient Leading-Edge Boundary-Layer Separation over a Pitching Airfoil," Journal of Fluid Mechanics, Vol. 308, 1996, pp. 195-217.
48. Nagib, H., Hites, M., Won, J., and Gravante, S., "Flow Quality Documentation of the National Diagnostic Facility," AIAA Paper 94-2499, June 1994.
49. Mangalam, S. M., Maddalon, D. V., Saric, W. S., and Agarwal, N. K., "Measurement of Crossflow Vortices, Attachment-Line Flow, and Transition Using Microthin Hot Films," AIAA Paper 90-1636, June 1990.
50. Nakayama, A., Stack, J. P., Lin, J. C., and Valarezo, W. O., "Surface Hot-Film Technique for Measurements of Transition, Separation, and Reattachment Points," AIAA Paper 93-2918, July 1993.

51. Sarma, G. R., "Transfer Function Analysis of the Constant Voltage Anemometer," Review of Scientific Instruments, Vol. 69, No. 6, June 1998, pp. 2385-2391.
52. McCroskey, W. J., "Some Current Research in Unsteady Fluid Dynamics," Journal of Fluid Engineering, Vol. 99, 1977, pp. 8-38.
53. Telionis, D. P., "Review – Unsteady Boundary Layers, Separated and Attached," Journal of Fluid Engineering, Vol. 101, 1979, pp. 29-43.
54. Saxena, L. S., An Experimental Investigation of Oscillating Flows over an Airfoil, Ph. D. Thesis, MAE Dept., Illinois Institute of Technology, 1977.
55. Fitzgerald, E. J. and Mueller, T. J., "Measurements in a Separation Bubble on an Airfoil using Laser Velocimetry," AIAA Journal, Vol. 28, No. 4, 1990, pp. 584-592.

Additional References:

- Carr, L. E., "Progress in Analysis and Prediction of Dynamic Stall," Journal of Aircraft, Vol. 25, No. 1, 1988, pp. 6-17.
- Carr, L. W., McAlister, K. W., and McCroskey, W. J., "Analysis of the Development of Dynamic Stall Based on Oscillating Airfoil Experiments," NASA TN-8382, 1977.
- Cebeci, T., Khattab, A. A., and Schimke, S. M., "Separation and Reattachment Near the Leading Edge of a Thin Oscillating Airfoil," Journal of Fluid Mechanics, Vol. 188, 1988, pp. 254-274.
- Chandrasekhara, M. S. and Ahmed, S., "Laser Velocimetry Measurements of Oscillating Airfoil Dynamic Stall Flow Field," AIAA Paper 91-1799, 1991.
- Ericsson, L. E., "Dynamic Airfoil Flows Separation and Reattachment," Journal of Aircraft, Vol. 25, No. 6, 1995, pp. 1171-1197.
- Ericsson, L. E., and Reding, J. P., "Unsteady Airfoil Stall, Review, and Extension," Journal of Aircraft, Vol. 8, No. 8, 1971, pp. 609-616.
- Ericsson, L. E. and Reding, J. P., "Dynamic Stall Analysis in Light of Recent Numerical and Experimental Results," Journal of Aircraft, Vol. 13, No. 4, 1976, pp. 248-255.
- Freytmuth, P., "Progress In Visualizing Unsteady Separation," Workshop II on Unsteady Separated Flow, U.S. Air Force Academy, CO, 1988, pp.197-210.

- Freytmuth, P., "Propulsive Vortical Signature of Plunging and Pitching Airfoils," AIAA Journal, Vol. 26, No. 7, 1988, pp. 881-883.
- Freytmuth, P., Bank, W., and Palmer, M., "Visualization of Accelerating Flow around an Airfoil at High Angles of Attack," Zeitschrift fuer Flugwiss. u. Weltraumforsch., Vol. 7, 1983, pp. 392-395.
- Hajek, T. J., Airfoil Oscillating in Pitch in a Sinusoidally Oscillating Free Stream, M. S. Thesis, MAE Dept., Illinois Institute of Technology, 1979.
- Herbst, W. B., "Supermaneuverability," Proceedings of Workshop on Unsteady Separated Flow, U. S. Air Force Academy, Colorado Springs, CO, 1983, pp. 1-9.
- Hsieh, B. J., Dynamic Stall on Oscillating Airfoils in Oscillating Free-Streams, Ph. D. Thesis, MAE Dept., Illinois Institute of Technology, 1979.
- Kim, J. S. and Park, S. O., "Smoke Wire Visualization of Unsteady Separation over an Oscillating Airfoil," AIAA Journal, Vol. 26, No. 11, 1988, pp. 1408-1410.
- Koromilas, C. A. and Telionis, D. P., "Unsteady Laminar Separation: An Experimental Study," Journal of Fluid Mechanics, Vol. 97, 1980, pp. 347-384.
- Liiva, J., "Unsteady Aerodynamic and Stall Effects on Helicopter Rotor Blade Airfoil Sections," Journal of Aircraft, Vol. 6, No. 1, 1969, pp. 46-51.
- McAlister, K. W., Carr, L. W., and McCroskey, W. J., "Dynamic Stall Experiments on the NACA 0012 Airfoil," NASA TP-1100, Washington DC, 1978.
- McCroskey, W. J., "Introduction to Unsteady Aspects of Separation in Subsonic and Transonic Flow," AGRAD LS-94, 1978, Vol. 6, pp. 1-8.
- McCroskey, W. J. and Philippe, J. J., "Unsteady Viscous Flow on Oscillating Airfoils," AIAA Journal, Vol. 13, No. 1, 1975, pp. 71-79.
- Ohmi, D., Coutanceau, M., Loc, T. P., and Duliieu, A., "Vortex Formation around an Oscillating and Translating Airfoil at Large Incidences," Journal of Fluid Mechanics, Vol. 211, 1990, pp. 37-60.
- O'Meara, M. M. and Mueller, T.J., "Laminar Separation Bubble Characteristics on an Airfoil at Low Reynolds Numbers," AIAA Journal, Vol. 25, No. 3, 1987, pp.1033-1041.
- Schreck, S. J., Faller, W. E., and Luttges, M. W., "Dynamic Reattachment on a Downward Pitching Finite Wing," Journal of Aircraft, Vol. 33, No. 2, 1996, pp. 279-285.

- Smith, F. T., "Steady and Unsteady Boundary-Layer Separation," Annual Review, Fluid Mechanics, Vol. 18, 1986, pp. 197-220.
- Tsahalis, D. J. and Telionis, D. P., "Oscillating Laminar Boundary Layers and Unsteady Separation," AIAA Journal, Vol. 12, No. 11, 1974, pp. 1469-1476.
- Visbal, M. R. and Gordnier, R. G., "Pitch Rate and Pitch-Axis Location Effects on Vortex Breakdown Onset," Journal of Aircraft, Vol. 32, No. 5, 1995, pp. 929-935.
- Walker, J. M., Helin, H. E., and Strickland, J. H., "An Experimental Investigation of an Airfoil Undergoing Large Amplitude Pitching Motions," AIAA Journal, Vol. 23, No.8, 1985, pp. 1141-1142.
- Wernert, P., Geissler, W., Raffel, M., and Kompenhaus, J., "Experimental and Numerical Investigations of Dynamic Stall on a Pitching Airfoil," AIAA Journal, Vol. 34, No. 5, 1996, pp. 982-989.
- Williams, J. C., "Incompressible Boundary-layer Separation," Annual Review of Fluid Mechanics, Vol. 9, 1977, pp. 113-144.
- Williams, J. C. III and Johanson, W. D., "Note on Unsteady Boundary-Layer Separation," AIAA Journal, Vol.12, No. 10, 1974, pp. 1427-1429.
- Zolan, J. J., Dynamic-Stall on Airfoils in Oscillating Flow, M. S. Thesis, MAE Dept., Illinois Institute Technology, 1976.
- Yu, Y. H., Lee, S., McAlister, K. W., and Tung, C., "Dynamic Stall Control for Advanced Rotorcraft Application," AIAA Journal, Vol. 33, No. 2, 1995, pp. 289-295.